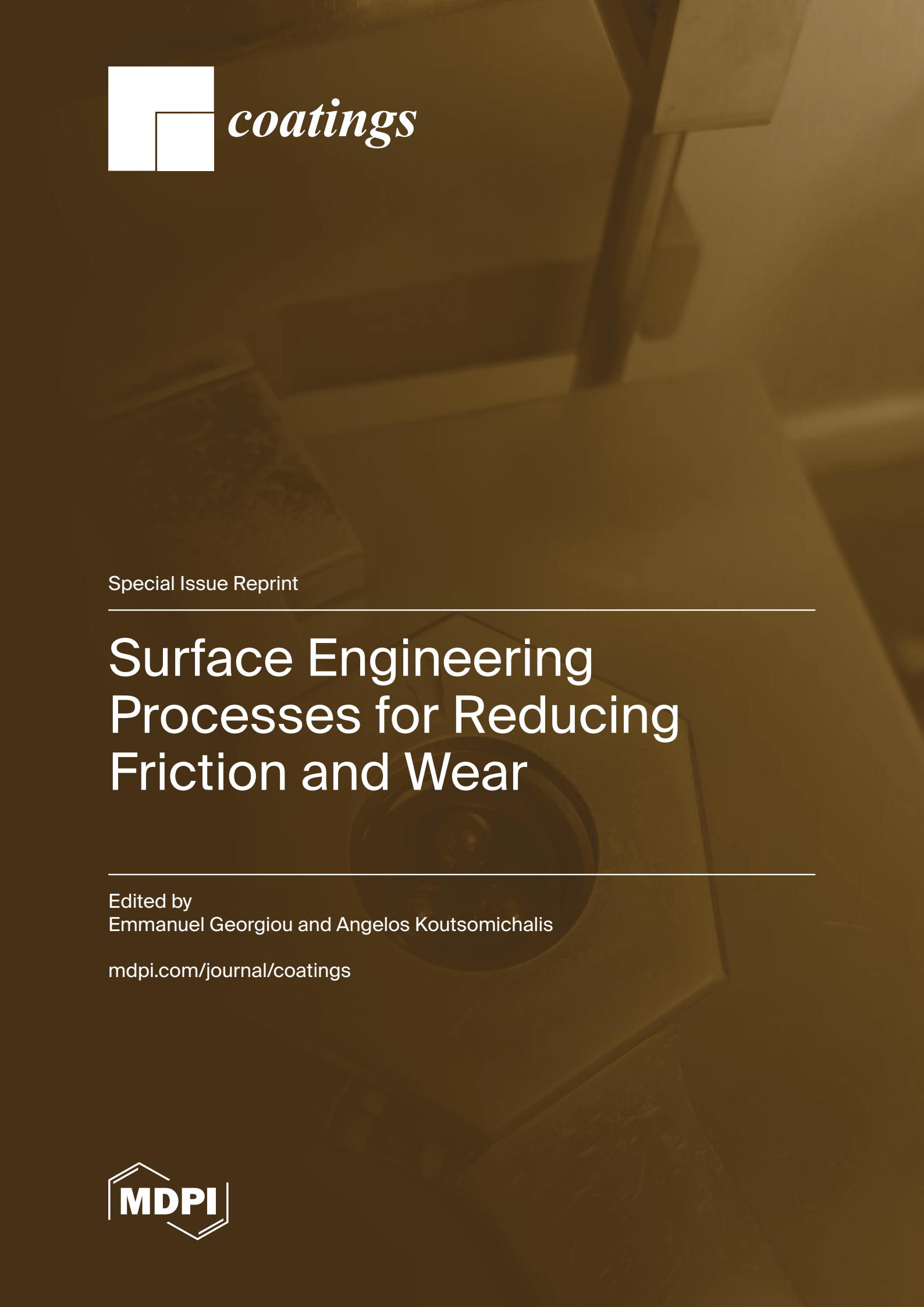


coatings

Special Issue Reprint

Surface Engineering Processes for Reducing Friction and Wear

Edited by
Emmanuel Georgiou and Angelos Koutsomichalis

mdpi.com/journal/coatings

MDPI

Surface Engineering Processes for Reducing Friction and Wear

Surface Engineering Processes for Reducing Friction and Wear

Guest Editors

Emmanuel Georgiou
Angelos Koutsomichalis

MDPI

Basel • Beijing • Wuhan • Barcelona • Belgrade • Novi Sad • Cluj • Manchester

Guest Editors

Emmanuel Georgiou
Department of Aeronautical Sciences
Hellenic Air Force Academy
Attika
Greece

Angelos Koutsomichalis
Department of Aeronautical Sciences
Hellenic Air Force Academy
Attika
Greece

Editorial Office
MDPI AG
Grosspeteranlage 5
4052 Basel, Switzerland

This is a reprint of the Special Issue, published open access by the journal *Coatings* (ISSN 2079-6412), freely accessible at: https://www.mdpi.com/journal/coatings/special_issues/Surface_Friction_Wear.

For citation purposes, cite each article independently as indicated on the article page online and as indicated below:

Lastname, A.A.; Lastname, B.B. Article Title. *Journal Name* **Year**, *Volume Number*, Page Range.

ISBN 978-3-7258-8827-6 (Hbk)
ISBN 978-3-7258-8828-3 (PDF)
https://doi.org/10.3390/books978-3-7258-8828-3

Cover image courtesy of Emmanuel Georgiou

© 2026 by the authors. Articles in this reprint are Open Access and distributed under the Creative Commons Attribution (CC BY) license. The reprint as a whole is distributed by MDPI under the terms and conditions of the Creative Commons Attribution-NonCommercial-NoDerivs (CC BY-NC-ND) license (https://creativecommons.org/licenses/by-nc-nd/4.0/).

Contents

About the Editors . . . . . **vii**

Preface . . . . . **ix**

Juncai Li, Yue Yang, Liaoyuan Chen, Tianbiao Yu, Ji Zhao and Zixuan Wang
Multi-Objective Optimization of Process Parameters in Laser DED Ni-Based Powder on Steel Rail Using Response Surface Design
Reprinted from: *Coatings* **2024**, *14*, 401, https://doi.org/10.3390/coatings14040401 . . . . . **1**

Saima Yaqoob, Jaharah A. Ghani, Nabil Jouini and Afifah Z. Juri
Performance Evaluation of PVD and CVD Multilayer-Coated Tools in Machining High-Strength Steel
Reprinted from: *Coatings* **2024**, *14*, 865, https://doi.org/10.3390/coatings14070865 . . . . . **17**

Ioannis Karagiannidis, Athanasios Tzanis, Dirk Drees, Lais Lopes, Georgios Chondrakis, Maria Myrto Dardavila, et al.
Friction and Wear Behavior of 3D-Printed Inconel 718 Alloy under Dry Sliding Conditions
Reprinted from: *Coatings* **2024**, *14*, 1029, https://doi.org/10.3390/coatings14081029 . . . . . **34**

Zihan Wang, Xiaolei Chong, Lei Liang, Zhenglei Chen and Chaojia Liu
Design and Application of Driving Resistance Test Device for Aircraft Tire and Soil Pavement
Reprinted from: *Coatings* **2024**, *14*, 1208, https://doi.org/10.3390/coatings14091208 . . . . . **46**

Yuanyuan Kang, Guowei Zhang, Yanling Hu and Yue Liu
Interfacial Diffusion and Copper Alloy Layer Wear Mechanism in Cu-20Pb-5Sn/45 Steel Bimetallic Composites
Reprinted from: *Coatings* **2025**, *15*, 1072, https://doi.org/10.3390/coatings15091072 . . . . . **62**

Bauyrzhan Rakhadilov, Nurtoleu Magazov, Aidar Kengesbekov, Manarbek Kylyshkanov and Arystanbek Kussainov
Study of Surface Wear of Punches and Molds for Optimization of Nuclear Fuel Production
Reprinted from: *Coatings* **2025**, *15*, 1088, https://doi.org/10.3390/coatings15091088 . . . . . **74**

Chuanyong Yu, Peng Zhang, Min Wei, Qiwei Wang and Wei Zhang
POSS-Grafted PI/MoS_2 Gradient Composite Coatings with Enhanced Tribological Properties Under Atomic Oxygen Irradiation
Reprinted from: *Coatings* **2026**, *16*, 73, https://doi.org/10.3390/coatings16010073 . . . . . **88**

Konstantinos Antonopoulos, Athanasios Tzanis, Dirk Drees, Michalis Vardavoulias, Emmanuel Georgiou, Angelos Koutsomichalis, et al.
Tribological Performance and Microstructural Analysis of NiAl–Inconel 625 Composite Coating Produced by Wire Arc Spraying
Reprinted from: *Coatings* **2026**, *16*, 609, https://doi.org/10.3390/coatings16050609 . . . . . **106**

About the Editors

Emmanuel Georgiou

Emmanuel Georgiou is Assistant Professor at the Hellenic Air Force Academy (Greece), working in the fields of Materials Processing and Tribology. His research interests focus on surface engineering, friction and wear, materials characterization, and the tribological performance of engineering materials. He has participated in and managed numerous European and industrial R&D projects related to surface technologies and tribological testing. He previously worked at KU Leuven (Belgium) and at Falex Tribology (Belgium), as Project Manager. He is the author or co-author of more than 140 scientific publications, conference papers, and book chapters in Materials Science and Tribology.

Angelos Koutsomichalis

Angelos Koutsomichalis is Professor at the Hellenic Air Force Academy (Greece), where he serves at the Department of Aeronautical Sciences as Head of the Manufacturing, Materials Technology and Planning Sector and Director of the Materials Technology Laboratory. His research interests include surface engineering, thermal spray and thin-film coatings, wear and fracture behavior, composite materials, and materials for aerospace applications. He has participated in numerous national and international research projects funded by organizations including Horizon Europe and NATO. His achievements include more than 120 scientific publications and extensive experience in research management, industrial innovation, and the design and evaluation of large-scale European development and technology programs.

Preface

This volume presents recent advances in tribology and surface engineering, with contributions addressing friction, wear, surface modification, coated tools, additive manufacturing, and laser-based repair technologies. Together, the chapters highlight current approaches to improving component performance and durability.

Emmanuel Georgiou and Angelos Koutsomichalis
Guest Editors

coatings

Article

Multi-Objective Optimization of Process Parameters in Laser DED Ni-Based Powder on Steel Rail Using Response Surface Design

Juncai Li [1,2,3], Yue Yang [1,2], Liaoyuan Chen [1,2], Tianbiao Yu [1,2,*], Ji Zhao [1,2,*] and Zixuan Wang [1,2]

[1] School of Mechanical Engineering and Automation, Northeastern University, Shenyang 110819, China
[2] Liaoning Provincial Key Laboratory of High-End Equipment Intelligent Design and Manufacturing Technology, Shenyang 110819, China
[3] Key Laboratory of Data Analytics and Optimization for Smart Industry (Northeastern University), Ministry of Education, Shenyang 110819, China
* Correspondence: tianbiaoyudyx@gmail.com (T.Y.); jzhao@mail.neu.edu.cn (J.Z.)

Abstract: With the rise of global industrialization, the requirements for the operating speed and carrying capacity of high-speed trains are increasingly higher. Because the wear and tear of rails gradually increases during the running of high-speed trains, strengthening or repairing rail surfaces is of paramount significance. Laser-directed energy deposition (DED) exhibits significant advantages in improving surface hardness, corrosion resistance, and abrasion resistance. Because of the multiple interacting optimization objectives, the development of a multi-objective optimization method for process parameters is significant for improving DED deposition quality. Response surface design employs multivariate quadratic regression equations to fit the functional relationship between the factors and the responses, which can be employed to find the optimal process parameters and solve multivariate problems. This study develops a multi-objective optimization model with response surface design and 2D process mappings to visually analyze the effects of scanning speed, laser power, and powder feed rate on aspect ratio, dilution rate, and microhardness. The optimal combination of process parameters for Ni-based alloys on U71Mn rail is a laser power of 431 W, a scanning speed of 5.34 mm/s, and a powder feed rate of 1.03 r/min. In addition, a multi-physics field finite element model is developed to analyze the evolution mechanism of the microstructure from the bottom to the top of the single track. This study can provide theoretical and technical support for the surface strengthening or repair of U71Mn rail.

Keywords: laser-directed energy deposition; U71Mn rail; multi-objective optimization; response surface design; geometrical characteristics; microstructure evolution

1. Introduction

The rail transition is an economic artery closely related to daily life and pivotal in the economy and society [1,2]. Rails are one of the critical components of the wheel and rail transportation system and the basis for train operations. With the development of rail transportation technology, the maximum running speed of high-speed trains has been gradually increased from 100 to 300 km/h. The rail loading environment is becoming more complex and demanding, resulting in harsher working conditions for the wheel–rail friction pair. The rail surface is susceptible to wear, corrosion, and failure under the conditions of side grinding and crushing, which decreases the smoothness and safety of train operation [3]. Therefore, it is essential to employ surface-strengthening technology to improve the hardness, wear resistance, and corrosion resistance of rails, thus prolonging their service life. It is of essential practical value and practical significance for reducing the difficulty of railroad maintenance, reducing the cost of railroad maintenance, and guaranteeing the efficiency of train operation [4].

Laser-directed energy deposition (DED) is a new surface repair or modification technology that has emerged over recent years [5,6]. The deposition material and substrate surface material on the rail are rapidly melted by laser energy to form a molten pool. Under the self-cooling effect of the rail substrate, the molten pool solidifies quickly to form a coating metallurgically bonded to the substrate. Therefore, by designing the composition of the deposited powder, the microhardness, wear resistance, and resistance to high temperatures of the rail can be significantly improved [3]. Because the DED process is characterized by complex physicochemical behavior, it is crucial to select a suitable combination of process parameters to obtain a high-quality cladding layer [7,8]. In addition, DED is a complex nonlinear process covering the coupling of multiple process parameters, resulting in significant difficulties in qualitatively characterizing the mapping relationship between individual process parameters and the quality of the cladding layer [9,10].

For the multi-objective optimization of process parameters in the DED process, many scholars have conducted research on orthogonal experimental design, response surface analysis, and gray correlation analysis. Ma et al. [11] first explored the factors affecting the morphology of the cladding layer by the orthogonal experimental method and obtained the combination of process parameters under optimal quality by polar analysis and calculation of gray correlation degree prediction. The results showed that laser power and scanning speed affected the forming quality among the various influencing factors. Ansari et al. [12] presented an empirical statistical model for DED optimization for In718 and analyzed the effects of key process parameters on the geometric characteristics of single tracks. Processing diagrams are practically usable for selecting appropriate processing parameters for specific equipment and materials. Intelligent optimization methods are on-the-fly search algorithms based on artificial intelligence or natural phenomena that allow various behaviors to be abstracted into quantifiable key indicators and transformed into mathematical problems to be solved, mainly including BP neural networks and particle swarm algorithms [13,14]. Based on the experimental data of laser powder deposition of iron-based alloy coatings on ASTM36 substrate, Sohrabpoor [15] developed an adaptive neuro-fuzzy inference model to predict the geometrical characteristics of the deposited layers. The results indicate that an artificial neural network (ANN) can effectively solve the multi-objective optimization problem related to process parameters in the DED process. To obtain the optimal parameters of cobalt-based alloy coatings, Guo et al. [16] trained experimental data using the BP neural network to determine the mapping relationship between process parameters and mechanical performance. Comparing the predicted and experimental results, the average relative error was not more than 10%. This proves the feasibility of the model and demonstrates the optimization of the process parameters. However, this method requires a large amount of experimental data. Ma et al. [11] employed a particle swarm algorithm to optimize the laser power, scanning speed, and defocus amount to fabricate coatings with a low dilution rate and residual stress. However, the intelligent optimization method not only requires a large amount of data to be trained and validated but also suffers from the problems of slow convergence, tedious and cumbersome processes, and a lack of explicit function expression.

Overall, response surface methodology represents certain advantages in dealing with nonlinear problems containing multiple factors and enables more experimental information to be obtained with a limited number of trials [17,18]. It is possible to obtain the relationship between one or more response targets and input responses, thereby obtaining the optimal multivariate parameters more reliably [19]. Therefore, this study selected the commonly used modified rail steel U71Mn steel as the deposition substrate. Due to the high corrosion resistance required of the repaired steel rail and the ability of Ni and Fe atoms to replace each other, the nickel-based self-soluble powder Ni45 was selected as the deposited material. Local repair of damaged guide rails can reduce the consumption of Ni-based alloys and the waste of rare and precious metals. The response surface method was employed to optimize the laser power (P), scanning speed (Vs), and powder feed rate (V_f) of the Ni-based powder

coated on the rail surface to obtain a suitable process combination. This study aims to provide a foundation for the repair or strengthening of high-speed rails.

2. Optimization Process

The central composite test design comprises a zero-level main test point, an axial test point, and a cubic test point [20]. The regression relationship between process parameters and response indicators can be expressed as follows:

$$y_u = \phi(x_{1u}, x_{2u}, \cdots x_{ku}) + \varepsilon_u \tag{1}$$

where μ denotes the number of designed experiments; k denotes the number of process parameters; $x_{k\mu}$ indicates the level of the kth factor at the uth test; and the Φ is the response function.

This study developed a second-order polynomial regression model to fit the experimental data to assess the effect of process parameters and response indexes. The functional relationship can be expressed as follows:

$$y_u = \beta_0 + \beta_1 x_{1u} + \beta_2 x_{2u} + \beta_{11} x_{1u}^2 + \beta_{22} x_{2u}^2 + \beta_{12} x_{1u} x_{2u} + \varepsilon_u \tag{2}$$

where y is the predicted response value; β_0 is the intercept; β_i, β_{ii}, and β_{ij} are the regression coefficients; and ε is the test error.

To evaluate the regression credibility, it is necessary to analyze the variance (ANOVA) of the established regression model by assessing its significance. The detailed process is as follows:

(1) Calculate the sum of squares of the deviations

The factor variable total sum of squares (SS_t), the factor variable residual sum of squares (SS_e), and the factor regression sum of squares (SS_r) can be expressed as follows:

$$\begin{cases} SS_t = \sum_{i=1}^{n} (y_i - \overline{y})^2 = SS_e + SS_r \\ SS_e = \sum_{i=1}^{n} (y_i - \hat{y}_i)^2 \\ SS_r = \sum_{i=1}^{n} (\hat{y}_i - \overline{y})^2 \end{cases} \tag{3}$$

where y_i is the experimental value of the response, $\overline{y}$ is the mean value of the reaction, and $\hat{y}_i$ is the regression estimate of the response.

(2) Calculate freedom degrees

The degrees of freedom corresponding to each type of sum of squares are df_t, df_e, df_r, and their expressions are as follows:

$$\begin{cases} df_t = n - 1 \\ df_r = 2p + p(p-1)/2 \\ df_e = f_t - f_r \end{cases} \tag{4}$$

where n denotes the sum of the degrees of freedom.

(3) Calculate average mean square

The average mean squared error (MS) indicates the ratio of each sum of squares to its degrees of freedom, and R^2 is employed to indicate the correlation of the regression model. If the value of R^2 is closer, it means that the regression model correlation is better, and its expression is as follows:

$$MS = \frac{SS_t}{df_e} \tag{5}$$

(4) Calculate *F*- and *p*-values

The *F*-value, also known as the *F*-test statistic, is designed to characterize the goodness of fit of a regression model. A larger *F*-value indicates a better fit and better significance. The *F*-value expression is as follows:

$$F = \frac{SS_r/df_r}{SS_e/df_e} \sim F(df_r, df_e) \tag{6}$$

The *p*-value indicates the probability that the difference between the factors resulted from sample error, which can be applied to determine the significance of the model, taking the significance level of 0.05. When *p* is greater than 0.05, the regression model is not significant. When *p* is less than 0.05, the model is effective. Moreover, smaller *p*-values indicate that the process parameter exerts a more significant effect on the corresponding target.

The aspect ratio and dilution rate are the two leading indicators that affect the deposition and bonding strength of the solidified coating. When the aspect ratio is less than 2, the clad height is large, and the melt pool edge is prone to collapse. On the contrary, when the aspect ratio exceeds 2, the clad lies flat on the substrate, with fewer defects in the lapping zone and high deposition quality. In addition, microhardness is an essential indicator for evaluating the mechanical properties of the coating. The dilution rate is employed to characterize the extent to which the melting of the substrate results in a variation in the composition of the clad. Too large a dilution rate weakens the performance of the single track. However, too low a dilution rate can lead to poor metallurgical bonding between the clad and the substrate, resulting in peeling from the substrate. In this study, based on the multi-objective optimization theory, the maximum aspect ratio, maximum microhardness, and minimum dilution rate were expected. The process parameter level ranges were set as constraints to achieve a multi-objective optimization study of DED process parameters with the aid of the Design Expert software v11.0. The detailed flow of the optimization process is shown in Figure 1.

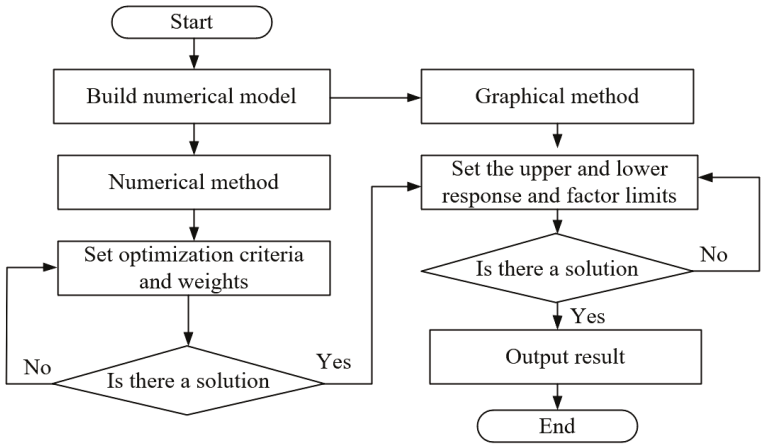


Figure 1. Multi-objective optimization flow of process parameters based on response surface design.

3. Experimental

Standard high-specification U71Mn rails are shown in Figure 2a. A substrate of $100 \times 70 \times 10$ mm^3 was machined by wire EDM technology, and the ground substrate is shown in Figure 2b. Ni45 self-fusing alloy was chosen as the deposited material because of its effective resistance to corrosion, abrasion, and impermissibility with rail steel. The scanning electron microscopy (SEM) images of Ni45 self-fluxing powder are shown in Figure 2c. The chemical compositions of U71Mn rail and Ni45 powder are shown in Table 1.

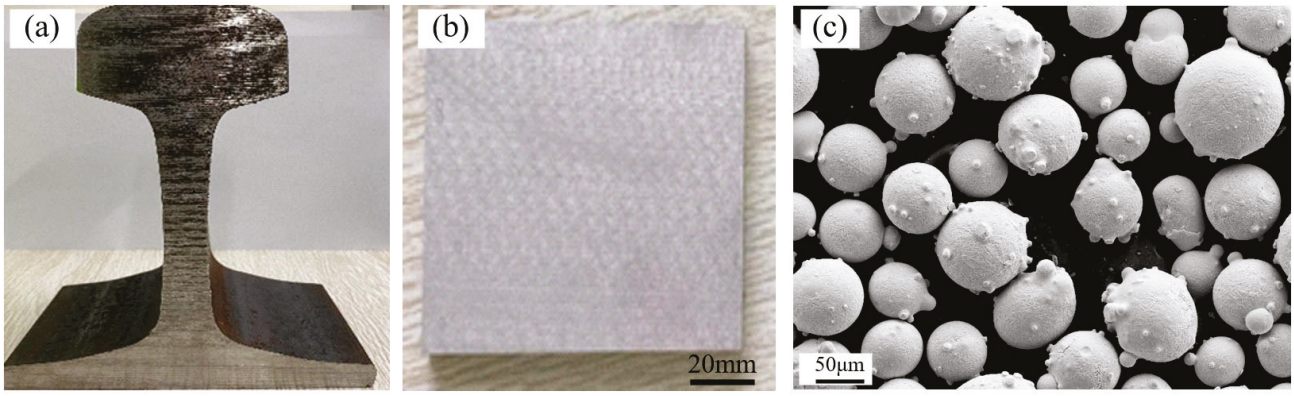


Figure 2. Experimental material: (**a**) U71Mn rail, (**b**) ground substrate, and (**c**) Ni45 powder.

Table 1. Chemical composition of Ni45 powder and U71Mn steel.

Element	C	Cr	Si	Fe	B	Mn	P	S	Ni
Ni-based powder	0.45	12.00	4.0	10.00	2.40	0.10	-	-	Bal.
U71Mn steel	0.65–0.76	-	0.15–0.35	Bal.	-	1.10–1.40	≤0.030	≤0.030	-

Based on the pre-completed one-factor experiments, the process parameters were optimized for the single tracks, and the levels of the process parameters are shown in Table 2. Based on a central composite design with a factor of 2 and a level of 5, 20 group experiments were designed, as shown in Table 3.

Table 2. The level of process parameters for the response surface.

Parameters	Unit	Levels				
		−1.68	**−1**	**0**	**+1**	**+1.68**
Laser Power (*P*)	(W)	409.77	420	435	450	460.23
Sanning speed (*Vs*)	(mm/s)	3.32	4	5	6	6.68
Power feed rate (V_f)	(r/min)	0.83	0.9	1	1.10	1.17

Table 3. Central composite trial design and measured results.

Std	Run	Laser Power *P* (W)	Scanning Speed V_s (mm/s)	Power Feed Rate V_f (r/min)	Aspect Ratio ζ	Dilution Ratio η	Microhardness ($HV_{0.3}$)
#1	11	420.00	4.00	0.90	2.26	0.3354	428.55
#2	9	450.00	4.00	0.90	2.34	0.3427	417.13
#3	13	420.00	6.00	0.90	2.18	0.3512	455.53
#4	6	450.00	6.00	0.90	2.77	0.4174	435.4
#5	19	420.00	4.00	1.10	2.25	0.2845	438.92
#6	8	450.00	4.00	1.10	2.12	0.3351	420.23
#7	10	420.00	6.00	1.10	2.34	0.3256	462.11
#8	3	450.00	6.00	1.10	2.71	0.3871	450.19
#9	7	409.77	5.00	1.00	2.01	0.3064	434.19
#10	4	460.23	5.00	1.00	2.34	0.3812	412.81
#11	2	435.00	3.32	1.00	2.42	0.3342	428.08
#12	18	435.00	6.68	1.00	2.98	0.3878	470.26
#13	17	435.00	5.00	0.83	2.24	0.3423	442.79
#14	15	435.00	5.00	1.17	2.25	0.3115	447.82
#15	5	435.00	5.00	1.00	2.98	0.3434	446.82
#16	14	435.00	5.00	1.00	2.99	0.3426	461.49

Table 3. *Cont.*

Std	Run	Laser Power P (W)	Scanning Speed V_s (mm/s)	Power Feed Rate V_f (r/min)	Aspect Ratio ζ	Dilution Ratio η	Microhardness ($HV_{0.3}$)
#17	20	435.00	5.00	1.00	2.94	0.3189	460.78
#18	1	435.00	5.00	1.00	3.04	0.3494	459.63
#19	16	435.00	5.00	1.00	3.22	0.3266	453.31
#20	12	435.00	5.00	1.00	2.74	0.3328	460.8

The experiments were conducted on a laser DED system, as shown in Figure 3a. The DED system consisted of the following key components: a KUKA robot, a cladding head, a controller, a water cooler, a powder feeder, and an electrical control cabinet. The laser generator provided enough energy to melt the substrate and the deposited material to form a molten pool, which rapidly solidified to form the clad, as shown in Figure 3b. The process mainly consisted of the following steps: drying the powder, writing the program, conducting the experiments, and characterizing the results.

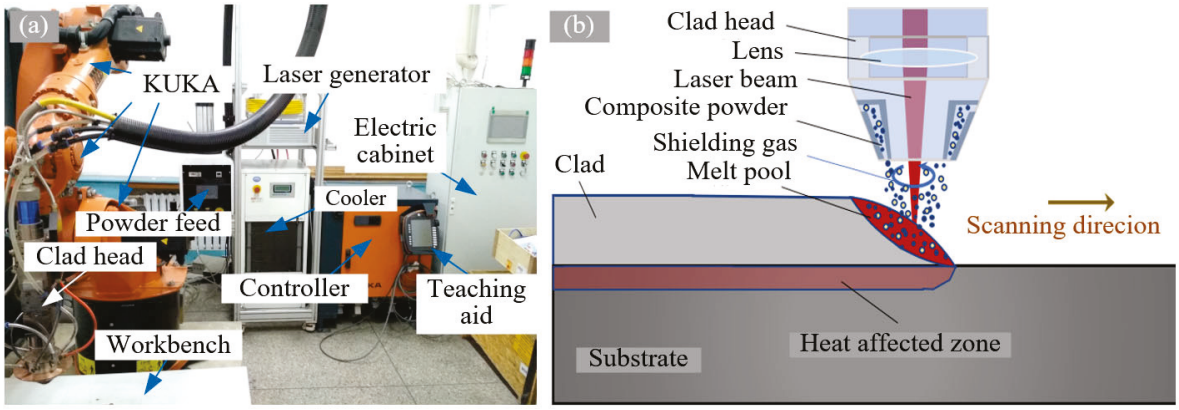


Figure 3. Experimental equipment: (**a**) actual and (**b**) schematic.

After the experiment, the cross section of single tracks was obtained by cutting the substrate perpendicular to the scanning direction using EDM technology. The cross section was ground alternately by sandpaper of 240 to 2000 grit, followed by metallurgical polishing to achieve a mirror-like finish. The cross-sectional morphology of the single track was obtained by 3D laser confocal microscopy (Japan) as well as the measurement of the height, width, and depth of the melt pool by the integrated software, as shown in Figure 4a. The aspect ratio (ξ) and dilution rate (D) can be calculated as follows:

$$\xi = W/H \tag{7}$$

$$D = \frac{h}{H+h} \tag{8}$$

where W is the clad width, H is the clad height, and h is the pool depth.

The polished specimens were etched by aqua regia for 30 s. The grain characteristics at different locations of the single track were gathered by laser confocal microscopy, as shown in Figure 4a. The Vickers hardness tester (China) was used to obtain the micro-hardness of a single track, and the mean value of three selected points on the fusion cladding was considered the average micro-hardness, as shown in Figure 4b. The optical cross-sectional morphology of the single tracks is shown in Figure 5. It can be noticed that a good metallurgical bond was formed between all single tracks and the substrate. Under the strong Marangoni convection in the molten pool, the high-temperature liquid on the surface of the molten pool flowed towards the bottom of the molten pool, increasing

the dilution rate and bond strength. In addition, as a result of the large surface tension coefficient at the gas–liquid interface of the molten pool, the single-pass track surface at the end of solidification exhibited a rounded shape, which is beneficial for improving the quality of the multi-pass overlap in the laser cladding repair process. The experimental results of the aspect ratio, dilution rate, and microhardness of the single tracks are shown in Table 3.

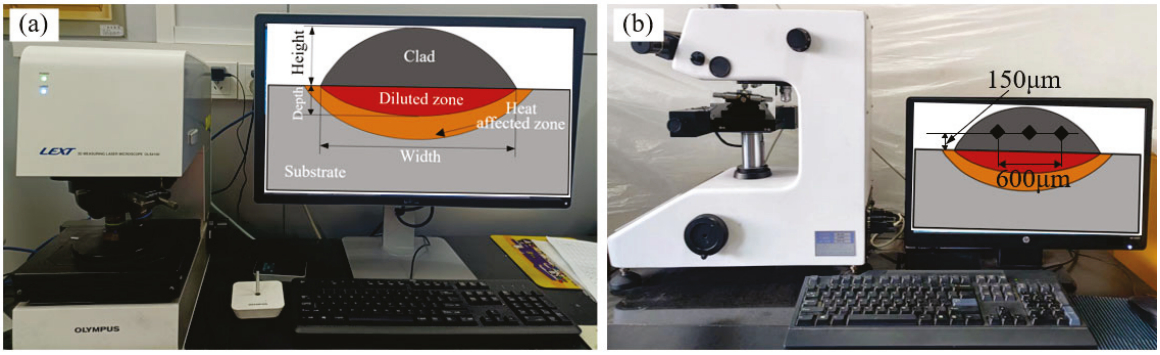


Figure 4. Characterization equipment: (**a**) 3D laser confocal microscopy and (**b**) Vickers hardness tester.

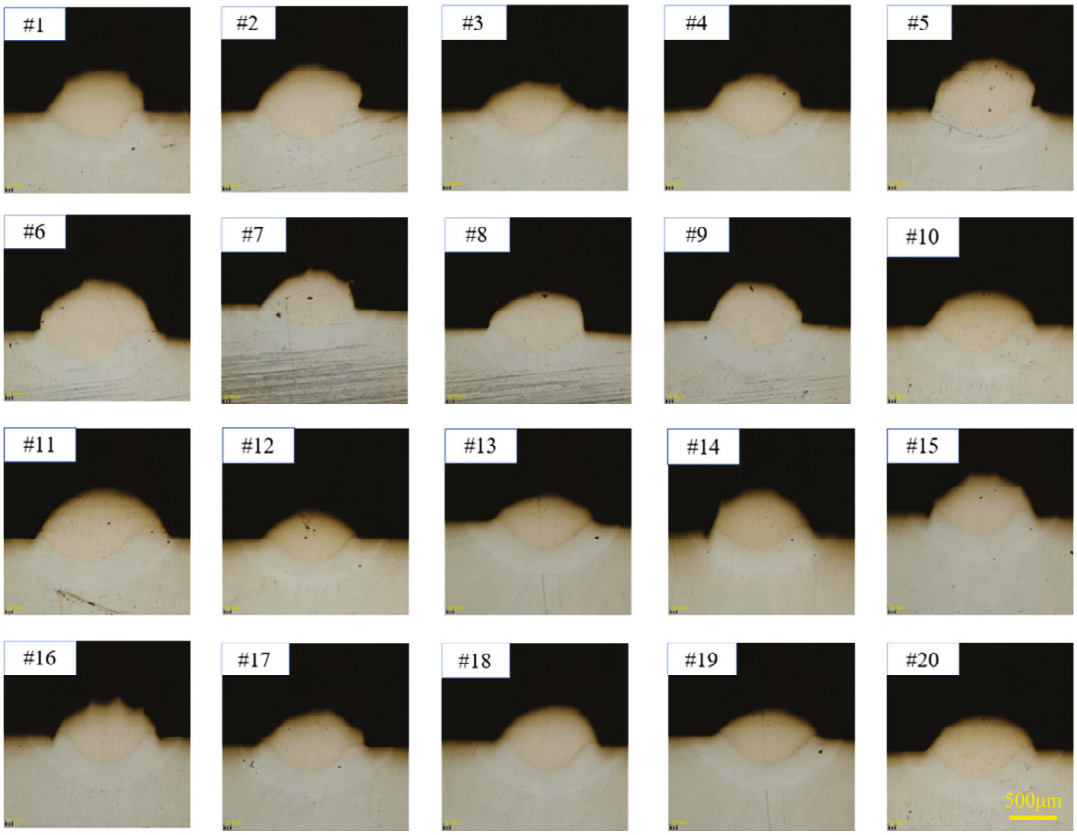


Figure 5. Cross-sectional morphologies of single tracks.

4. Results and Discussion

4.1. Response Surface Analysis for Aspect Ratio

The process parameters and aspect ratios were analyzed by ANOVA, and the results are shown in Table 4. It can be seen that the *F*-value is 22.12 with a *p*-value less than 0.0001, indicating that the established quadratic regression model for aspect ratio is valid and highly significant. Its loss of fit is not significant, proving the fitted equation is reliable. The signal-to-noise ratio of 12.169 is more than 4, indicating high precision and accuracy [21,22].

The R^2 value is 0.8877, indicating a good correlation. Figure 6a presents the residual plot of the aspect ratio model. No abnormal values exist, indicating that the model is credible. Figure 6b shows the measured and predicted values of the aspect ratio. It can be noticed that the experimental values are more centrally distributed on both sides of the fitted straight line, which also indicates the accuracy of the model [23]. In summary, the insignificant factors in the model were removed to develop a quadratic regression model for the effect of process parameters on the aspect ratio. The final regression model for the aspect ratio is as follows:

$$\xi = 2.98 + 0.11A + 0.14B - 0.28A^2 - 0.093B^2 - 0.25C^2 \quad (9)$$

where A, B, and C in Equation (9) can be found in Table 4.

Table 4. ANOVA for the aspect ratio.

	Sum of Square	Freedom Degrees	Mean Squares	*F*-Value	*p*-Value	
Model	2.34	5	0.47	22.12	<0.0001	Significant
A Laser power	0.16	1	0.16	7.43	0.0164	
B Scanning speed	0.28	1	0.28	13.46	0.0025	
A^2	1.12	1	1.12	53.02	<0.0001	
B^2	0.13	1	0.13	5.94	0.0288	
C^2	0.93	1	0.93	44.03	<0.0001	
Residual	0.3	14	0.021			
Anomaly	0.18	9	0.02	0.81	0.6306	Not significant
Pure error	0.12	5	0.024			
Sum of all	2.64	19				
Standard deviation	0.15		R^2	0.8877		
Mean	2.56		Adjusted R^2	0.8475		
Variation coefficient	5.69		Projected R^2	0.8151		
Predicting the residual sum of squares	0.49		Signal-to-noise ratio	12.169		

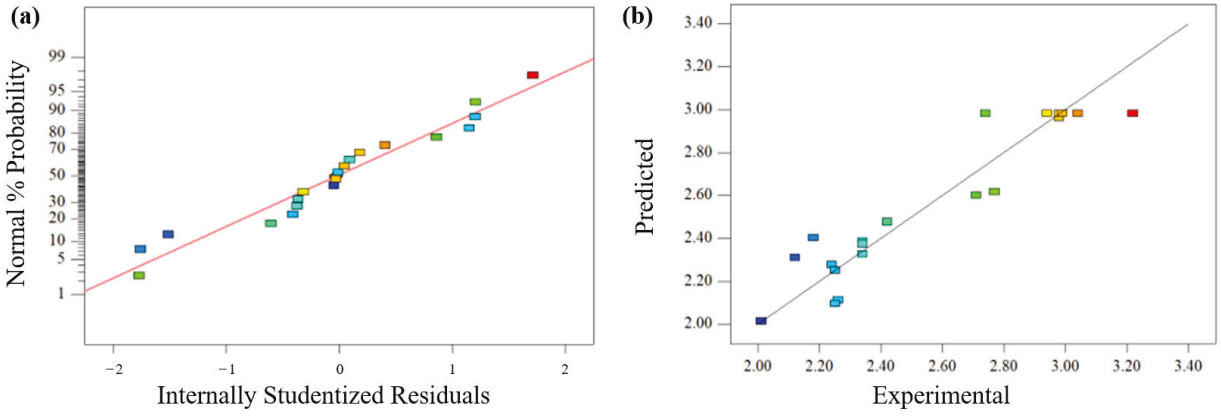


Figure 6. Fitting of process parameters to the aspect ratio: (**a**) residual and (**b**) comparison of measured and predicted values.

The *p*-values regarding laser power and scanning speed are less than 0.05, indicating that both factors significantly affect the aspect ratio. In contrast, the effect of powder feed rate on the aspect ratio is insignificant. Therefore, contour plots and 3D response surface plots of scanning speed and laser power concerning aspect ratio were developed. Figure 7 shows that the aspect ratio increases gradually as the laser power decreases and the scanning speed increases. The decrease in laser power and increase in scanning speed can decrease the laser energy and powder density. As a result, the height and width of the single-pass deposition are significantly reduced. At the same time, the liquid at the

center of the melt pool flows toward its edges due to negative surface tension [24,25]. This behavior results in an increase in width and a decrease in height, increasing the aspect ratio.

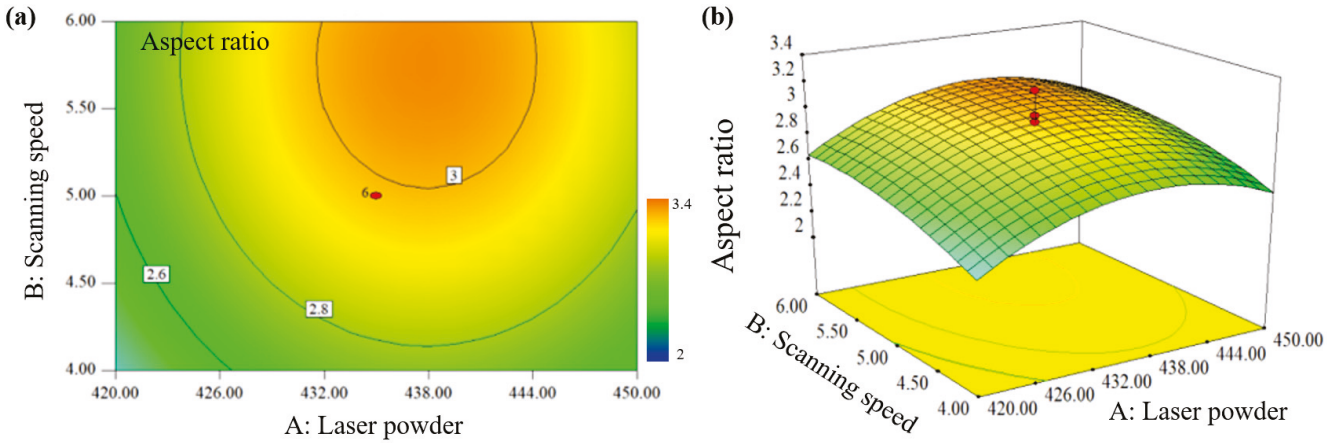


Figure 7. Response of laser power and scanning speed to the aspect ratio: (**a**) contour plot, (**b**) 3D surface.

4.2. Response Surface Analysis for the Dilution Rate

Table 5 lists the ANOVA results of the process parameters on the dilution rate. It can be seen that the *F*-value is 25.68 with a *p*-value of less than 0.0001, indicating that the established quadratic regression model for dilution rate is valid and highly significant. Its fit loss is insignificant, proving that the fitted equation is reliable. The signal-to-noise ratio of 17.668 is more than 4, indicating a high degree of accuracy and precision. The R^2 value of 0.8726 indicates a strong correlation [17]. The residual plot for the dilution rate model is shown in Figure 8a. The absence of abnormal values indicates a high confidence level in the model. Figure 8b compares the measured and predicted values of the dilution rate. It can be seen that the measured values are more centrally distributed on both sides of the fitted straight line, which also suggests that the proposed model is highly accurate [10,26]. In summary, the insignificant factors in the model were removed to develop a quadratic regression model for the effect of process parameters on the dilution rate. The final regression model for the dilution rate is as follows:

$$\eta = 0.34 + 0.023A + 0.020B - 0.012C + 9.505 \times 10^{-3} \times B^2 \quad (10)$$

where A, B, and C in Equation (10) can be found in Table 5.

Table 5. ANOVA for the dilution rate.

	Sum of Square	Freedom Degrees	Mean Squares	*F*-Value	*p*-Value	
A Laser power	0.016	4	3.984×10^{-3}	25.68	<0.0001	Significant
B Scanning speed	7.100×10^{-3}	1	7.100×10^{-3}	45.77	<0.0001	
A^2	5.487×10^{-3}	1	5.487×10^{-3}	35.37	<0.0001	
B^2	2.023×10^{-3}	1	2.023×10^{-3}	13.04	0.0026	
C^2	1.326×10^{-3}	1	1.326×10^{-3}	8.55	0.0105	
Residual	2.327×10^{-3}	15	1.551×10^{-4}			
Anomaly	1.659×10^{-3}	10	1.659×10^{-4}	1.24	0.4289	Not significant
Pure error	6.680×10^{-4}	5	1.336×10^{-4}			
Sum of all	0.018	19				
Standard deviation	0.012		R^2	0.8726		
Mean	0.34		Adjusted R^2	0.8386		
Variation coefficient	3.63		Projected R^2	0.7616		
Predicting the residual sum of squares	4.353×10^{-3}		Signal-to-noise ratio	17.668		

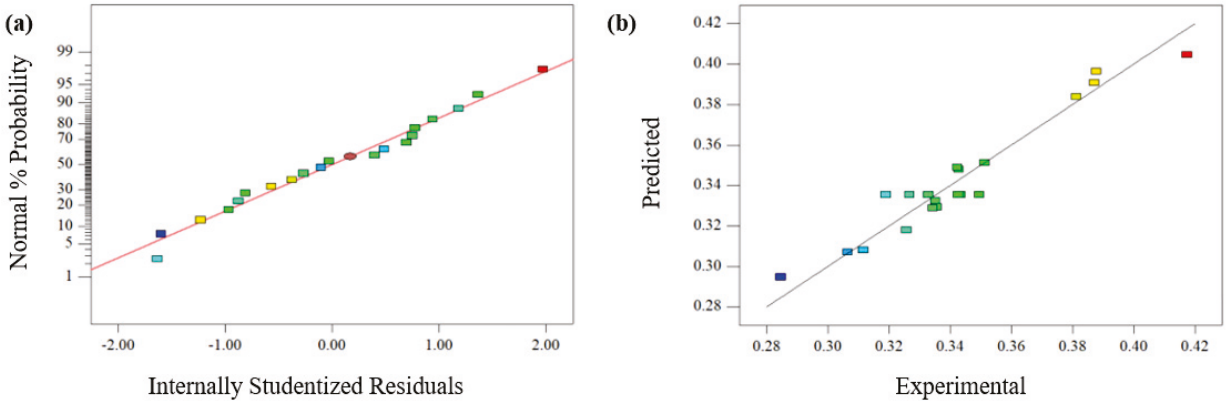


Figure 8. Fitting of process parameters to dilution ratio: (**a**) residual and (**b**) comparison of measured and predicted.

As can be seen from Table 5, the *p*-values of laser power, scanning speed, and powder feed rate are all less than 0.05, and the *p*-values of the first two parameters are less than 0.0001, indicating that the effects of these two parameters are most significant. Figure 9a shows the response of laser power and scanning speed to the dilution rate. As the laser power and scanning speed decrease, the dilution rate gradually decreases. During the DED process, the diminished laser power would reduce the melting of the substrate and decrease the depth of the melt pool [8,27]. Decreasing the scanning speed can increase the amount of molten pool powder injected per unit of time, increasing the deposition height and thus reducing the dilution rate [28]. Therefore, a smaller dilution rate can be obtained by increasing the powder feed rate and decreasing the laser power, as shown in Figure 9b.

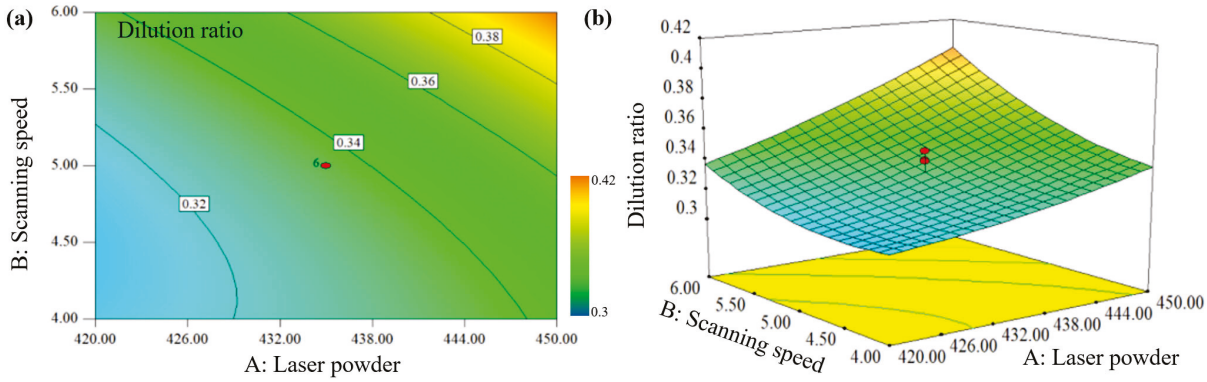


Figure 9. Response of laser power and scanning speed to dilution ratio: (**a**) contour plot, (**b**) 3D surface.

4.3. Response Surface Analysis for Microhardness

The ANOVA results for the effect of process parameters on microhardness are shown in Table 6. It can be seen that the *F*-value is 45.15 with a *p*-value of less than 0.0001, indicating that the established quadratic regression model for microhardness is valid and highly significant. Its misfit is not substantial, proving that the fitted equation is reliable. The signal-to-noise ratio of 22.800 is more than 4, indicating a high degree of precision and accuracy. The R^2 value of 0.9542 indicates a robust correlation. The residual plots of the microhardness model are shown in Figure 10a. No anomalous values are found in the plot, which suggests that the model has a high degree of confidence. Figure 10b plots the measured microhardness values against the predicted values [29,30]. It can be seen that the measured values are more centrally distributed on both sides of the fitted straight line, which also indicates the high accuracy of the regression model [31]. In summary, the

insignificant factors in the model were removed to construct a quadratic regression model for the effect of process parameters on microhardness. The fitting equation is shown below:

$$HV_{0.3} = 457.13 - 7.18A + 12.40B + 3.17C - 11.84A^2 - 2.76B^2 - 4.13C^2 \quad (11)$$

where A, B, and C in Equation (11) can be found in Table 6.

Table 6. ANOVA for the microhardness.

	Sum of Square	Freedom Degrees	Mean Squares	*F*-Value	*p*-Value	
Model	5113.74	6	852.29	45.15	<0.0001	Significant
A Laser power	704.91	1	704.91	37.34	<0.0001	
B Sanning speed	2099.71	1	2099.71	111.23	<0.0001	
C Powder feed rate	137.28	1	137.28	7.27	0.0183	
A^2	2019.38	1	2019.38	106.97	<0.0001	
B^2	109.92	1	109.92	5.82	0.0313	
C^2	245.60	1	245.60	13.01	0.0032	
Residual	245.41	13	18.88			
Anomaly	72.47	8	9.06	0.26	0.9541	Not significant
Pure error	172.94	5	34.59			
Sum of all	5359.15	19				
Standard deviation	4.34		R^2	0.9542		
Mean	444.34		Adjusted R^2	0.9331		
Variation coefficient	0.98		Projected R^2	0.9097		
Predicting the residual sum of squares	484.01		Signal-to-noise ratio	22.800		

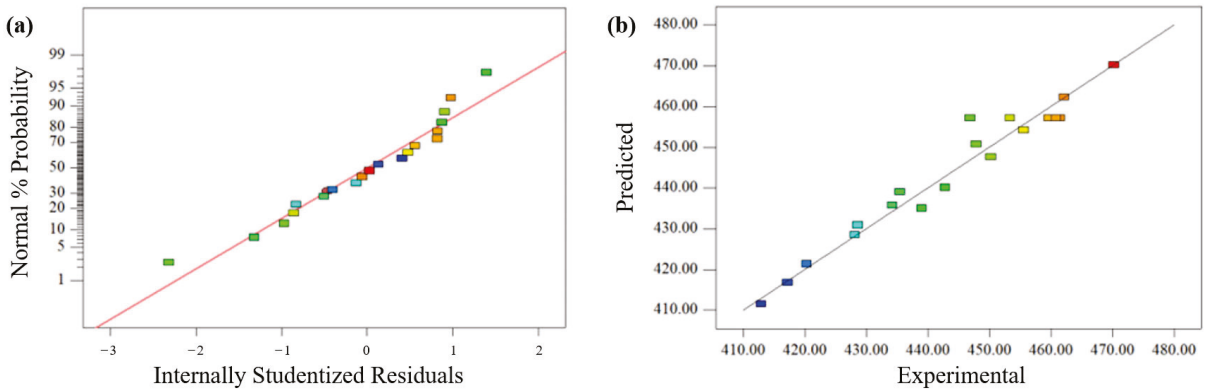


Figure 10. Fitting of process parameters to microhardness: (**a**) residual and (**b**) comparison of measured and predicted.

It can be seen from Table 6 that the *p*-values of laser power, scanning speed, and powder feed rate are less than 0.05, indicating that the effect of these three parameters on microhardness is significant. The scanning speed has the largest *F*-value, suggesting that it is the most significant essential factor. Figure 11a shows the contour plots and 3D response surfaces of the effects of process parameters on microhardness. The microhardness of the single tracks decreases as the laser power increases. However, the microhardness gradually increases with increasing scanning speed. On the one hand, as the laser power increases, the single-track height gradually increases, and the dilution rate decreases. On the other hand, as the scanning speed increases, the dilution rate gradually decreases. Because the microhardness of the deposited material is significantly higher than that of the substrate, the dilution of the molten pool by the substrate material decreases, and the microhardness of the single tracks increases significantly, as shown in Figure 11b.

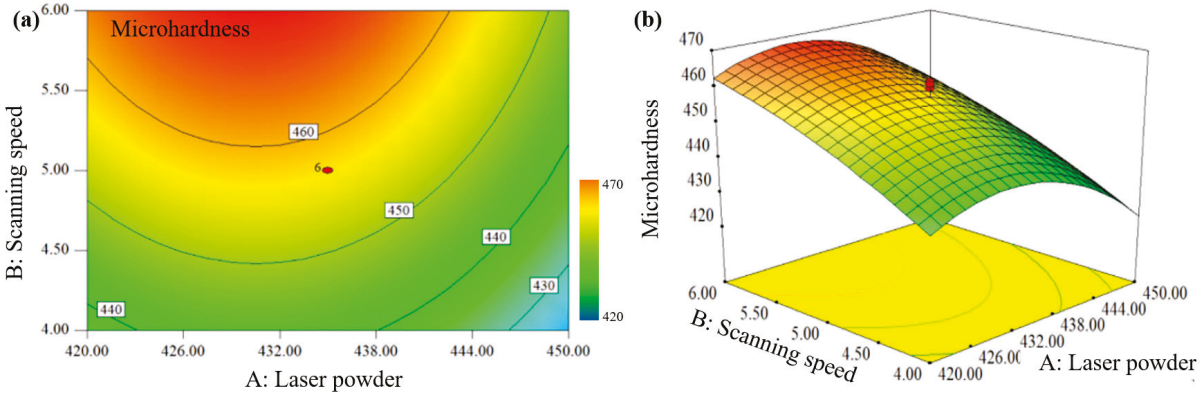


Figure 11. Response of laser power and scanning speed to microhardness: (**a**) contour plot, (**b**) 3D surface.

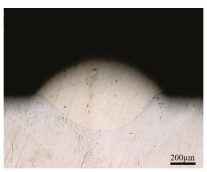
4.4. Multi-Response Optimization of Process Parameters

Based on the multi-objective optimization theory, this study aimed to obtain the maximum aspect ratio, the maximum microhardness, and the minimum dilution rate. A range of process parameter levels was set as the constraints, and the multi-objective optimization of laser cladding process parameters was realized with the help of the Design Expert software. The settings and weights for each process parameter and response target are shown in Table 7. The optimal combination of process parameters for laser cladding Ni-based powder on U71Mn rails obtained by the response surface method is a laser power of 431 W, a scanning speed of 5.34 mm/s, and a powder feed rate of 1.03 r/min. Based on the combination of the above process parameters, a single-pass cladding experiment was carried out. The measurements of each index were repeated three times to obtain the average value, and the results are shown in Table 8. The error between the theoretical prediction and the measured value is not more than 10%, and the experimental results align with the expected requirements. The above analysis demonstrates the high accuracy of the response surface model in predicting the experimental results and further illustrates the reliability of this model.

Table 7. Optimization criteria and targets.

Constraints					
Items	**Target**	**Lower Limit**	**Upper Limit**	**Weights**	**Significant**
A: Laser power	Inside the range	409.77	460.23	1	3
B: Scanning speed	Inside the range	3.32	6.68	1	3
C: Powder feed rate	Within range	0.83	1.17	1	3
Aspect ratio	Maximum value	2.01	3.22	1	3
Dilution ratio	Minimum value	0.2845	0.4174	1	3
Microhardness	Maximum value	412.81	470.26	1	3

Table 8. Comparison between predicted optimization and experimental validation.

	Predicted	**Experimental**	**Optimized Sectional Morphology**
Laser power (W)	431	431	
Powder feed (r/min)	5.34	5.34	
Scanning speed (mm/s)	1.03	1.03	
Aspect ratio	2.93	3.12	
Dilution ratio	0.330	0.354	
Microhardness ($HV_{0.3}$)	462.9	470.8	

4.5. Clad Microstructure Analysis

The temperature field distribution during the laser DED process affects the solidification behavior of the molten pool, where the temperature gradient (*G*) and the solidification

rate (R) are the key parameters that determine solidified grain morphology [32,33]. We have previously developed a finite element model [24] that mainly includes heat and mass transfer, material properties, solution region, and boundary condition settings to simulate the laser cladding process for Ni-based powder on U71Mn rail steel. The G and R can be represented as follows:

$$G = \nabla T \cdot \vec{n_s} \tag{12}$$

$$R = V_s \cos\theta \tag{13}$$

where θ denotes the angle between the normal to the solidification front and the scanning speed, as shown in Figure 12. As solidification proceeds, the θ decreases, indicating a gradual increase in the R from the bottom to the top of the melt pool.

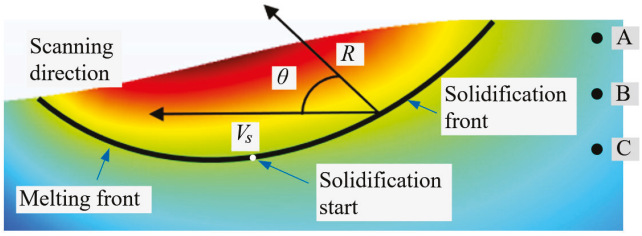


Figure 12. Schematic diagram of solidification rate versus scanning speed.

According to the theory of rapid solidification, the morphology and size of the grains in the cladding layer are subject to the combined effect of G and R [34]. The detailed pattern is shown in Figure 13. It can be seen from Figure 13 that as G/R decreases, the microstructure morphology transforms from planar grains to cellular, columnar, and equiaxial grains. Moreover, the size of the microstructure decreases gradually with an increase in R.

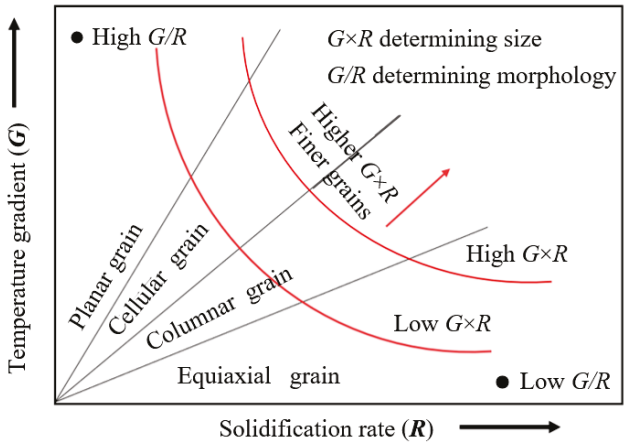


Figure 13. Temperature gradient vs. solidification rate plot defining the grain morphology during solidification [35,36].

The curves of temperature variation with time at three points A, B, and C at the top, middle, and bottom locations of the cross section (Figure 12) were obtained, and the results are shown in Figure 14. It can be seen in Figure 14 that the maximum cooling rates at points A and C during solidification are 3080 and 795 K/s, respectively. Because the surface of the melt pool is closer to the laser heat source than other locations, the G gradually increases from the top to the bottom, and the R of the cladding layer gradually decreases from the surface to the bottom [37].

The grain morphologies at different locations (points A, B, and C) of the optimized single-track, shown in Figure 15. At the top position of the cladding (point A), because G/S is low and $G \times S$ is high, the microstructure in this region exists mainly in the form of refined equiaxed grains. At the middle position of the cladding (point B), the microstructure

primarily exists in the form of equiaxial grains and some columnar grains. However, the full planar grains as well as cellular grains are observed at the bottom position of the cladding layer (point C). This experimental result verifies the above simulation predictions. In addition, it can also be seen that a good metallurgical bond is formed between the cladding layer and the substrate [38].

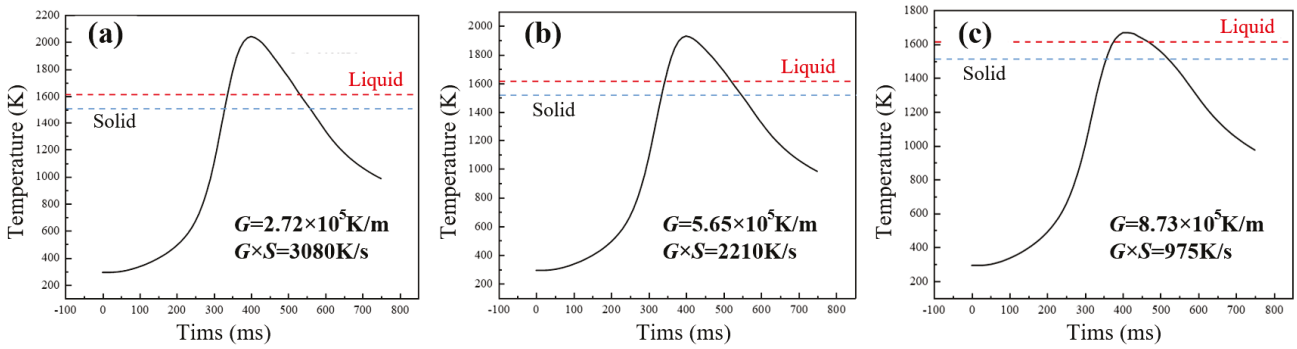


Figure 14. Curve of temperature variation with time: (**a**) point A, (**b**) point B, and (**c**) point C.

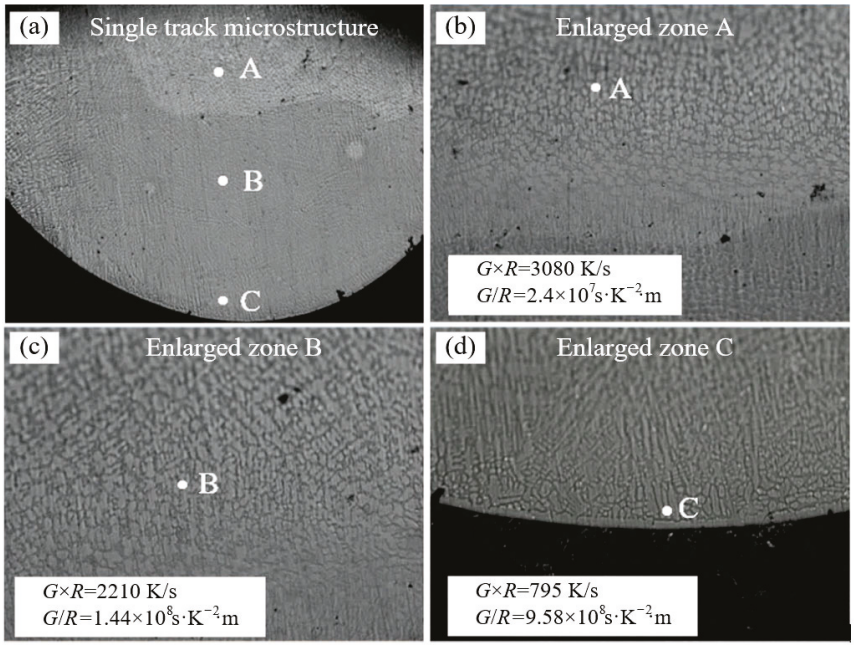


Figure 15. The positions of points A, B, and C in the cladding layer and their corresponding grains.

5. Conclusions

This study developed a quadratic regression model on the relationship between response targets (aspect ratio, dilution rate, and microhardness) and process parameters with the help of ANOVA. The response surface was employed to optimize the process parameters and a suitable combination of process parameters for laser DED deposition of Ni-based alloys on U71Mn steel. The multi-objective optimization of the geometrical morphology and microhardness of the single tracks was realized. The main conclusions are as follows:

1. ANOVA and 3D response surface plots indicate that scanning speed has the most significant effect on aspect ratio. At the same time, the dilution ratio and microhardness are mainly driven by the laser power and scanning speed.
2. The response objectives (aspect ratio, dilution rate, and microhardness) were transformed into single goals to be optimized by response surface design. The optimized

combination of process parameters to satisfy the response objectives was obtained and experimentally verified.

3. The error between the predicted and experimental response targets is not more than 10%, which also indicates the validity and reliability of the model. The optimal combination of process parameters is a laser power of 431 W, a scanning speed of 5.34 mm/s, and a powder feed rate of 1.03 r/min. The microhardness of the clad fabricated by these process parameters is 470.8 HV.
4. During the solidification of the single track, the cooling rate gradually increases from 795 to 3080 K/s from the bottom to the top, while the solidification rate gradually increases from 0.0039 to 0.011 m/s. As a result, the microstructure morphology transforms from planar grains to a mixture of cellular and columellar grains, and the size of the grains decreases.

Author Contributions: Methodology, J.L., T.Y., J.Z. and Z.W.; Software, L.C.; Validation, Y.Y. and L.C.; Investigation, Z.W.; Resources, Y.Y.; Writing—original draft, J.L.; Writing—review & editing, J.L.; Supervision, T.Y.; Project administration, T.Y. and J.Z.; Funding acquisition, J.Z. All authors have read and agreed to the published version of the manuscript.

Funding: This work is supported by the National Natural Science Foundation of China (52075088) and 111Project (B16009).

Institutional Review Board Statement: Not applicable.

Informed Consent Statement: Not applicable.

Data Availability Statement: Data are contained within the article.

Conflicts of Interest: We declare that we have no financial or personal relationships with other people or organizations that can inappropriately influence our work. There is no professional or other personal interest of any nature or kind in any product, service, or company that could be construed as influencing the position presented in, or the review of, the manuscript entitled "Multi-Objective Optimization of Process Parameters in Laser DED Ni-Based Powder on Steel Rail Using Response Surface Design".

References

1. Clare, A.; Oyelola, O.; Folkes, J.; Farayibi, P. Laser cladding for railway repair and preventative maintenance. *J. Laser Appl.* **2012**, *24*, 32004. [CrossRef]
2. Ding, H.; Yang, T.; Wang, W.; Zhu, Y.; Lin, Q.; Guo, J.; Xiao, Q.; Gan, L.; Liu, Q. Optimization and wear behaviors of 316L stainless steel laser cladding on rail material. *Wear* **2023**, *523*, 204830. [CrossRef]
3. Pointner, P. High strength rail steels—The importance of material properties in contact mechanics problems. *Wear* **2008**, *265*, 1373–1379. [CrossRef]
4. Lai, Q.; Abrahams, R.; Yan, W.; Qiu, C.; Mutton, P.; Paradowska, A.; Soodi, M. Investigation of a novel functionally graded material for the repair of premium hypereutectoid rails using laser cladding technology. *Compos. Part B Eng.* **2017**, *130*, 174–191. [CrossRef]
5. DebRoy, T.; Wei, H.L.; Zuback, J.S.; Mukherjee, T.; Elmer, J.W.; Milewski, J.O.; Beese, A.M.; Wilson-Heid, A.; De, A.; Zhang, W. Additive manufacturing of metallic components–Process, structure and properties. *Prog. Mater. Sci.* **2018**, *92*, 112–224. [CrossRef]
6. Svetlizky, D.; Das, M.; Zheng, B.; Vyatskikh, A.L.; Bose, S.; Bandyopadhyay, A.; Schoenung, J.M.; Lavernia, E.J.; Eliaz, N. Directed energy deposition (DED) additive manufacturing: Physical characteristics, defects, challenges and applications. *Mater. Today* **2021**, *49*, 271–295. [CrossRef]
7. Chen, L.; Zhao, Y.; Chen, X.; Yu, T.; Xu, P. Repair of spline shaft by laser-cladding coarse TiC reinforced Ni-based coating: Process, microstructure and properties. *Ceram. Int.* **2021**, *47*, 30113–30128. [CrossRef]
8. Chen, L.; Yu, T.; Xu, P.; Zhang, B. In-situ NbC reinforced Fe-based coating by laser cladding: Simulation and experiment. *Surf. Coat. Technol.* **2021**, *412*, 127027. [CrossRef]
9. Morville, S.; Carin, M.; Peyre, P.; Gharbi, M.; Carron, D.; Le Masson, P.; Fabbro, R. 2D longitudinal modeling of heat transfer and fluid flow during multilayered direct laser metal deposition process. *J. Laser Appl.* **2012**, *24*, 032008. [CrossRef]
10. Singh, A.K.; Sadhu, A.; Das, A.K.; Pratihar, D.K.; Choudhury, A.R. An approach towards energy and material efficient additive manufacturing: Multi-objective optimization of stellite-6 deposition on SS304. *Opt. Laser Technol.* **2021**, *148*, 107799. [CrossRef]
11. Ma, M.; Xiong, W.; Lian, Y.; Han, D.; Zhao, C.; Zhang, J. Modeling and optimization for laser cladding via multi-objective quantum-behaved particle swarm optimization algorithm. *Surf. Coat. Technol.* **2019**, *381*, 125129. [CrossRef]

12. Ansari, M.; Razavi, R.S.; Barekat, M. An empirical-statistical model for coaxial laser cladding of NiCrAlY powder on Inconel 738 superalloy. *Opt. Laser Technol.* **2016**, *86*, 136–144. [CrossRef]
13. Alimardani, M.; Toyserkani, E. Prediction of laser solid freeform fabrication using neuro-fuzzy method. *Appl. Soft Comput.* **2008**, *8*, 316–323. [CrossRef]
14. Chen, L.; Bi, G.; Yao, X.; Tan, C.; Su, J.; Ng, N.P.H.; Chew, Y.; Liu, K.; Moon, S.K. Multisensor fusion-based digital twin for localized quality prediction in robotic laser-directed energy deposition. *Robot. Comput. Manuf.* **2023**, *84*, 102581. [CrossRef]
15. Sohrabpoor, H. Analysis of laser powder deposition parameters: ANFIS modeling and ICA optimization. *Optik* **2016**, *127*, 4031–4038. [CrossRef]
16. Guo, S.; Chen, Z.; Cai, D.; Zhang, Q.; Kovalenko, V.; Yao, J. Prediction of Simulating and Experiments for Co-based Alloy Laser Cladding by HPDL. *Phys. Procedia* **2013**, *50*, 375–382. [CrossRef]
17. Wu, Z.; Li, T.; Li, Q.; Shi, B.; Li, X.; Wang, X.; Lu, H.; Zhang, H.-C. Process optimization of laser cladding Ni60A alloy coating in remanufacturing. *Opt. Laser Technol.* **2019**, *120*, 105718. [CrossRef]
18. Javid, Y. Multi-response optimization in laser cladding process of WC powder on Inconel 718. *CIRP J. Manuf. Sci. Technol.* **2020**, *31*, 406–417. [CrossRef]
19. Meng, G.; Zhu, L.; Zhang, J.; Yang, Z.; Xue, P. Statistical analysis and multi-objective process optimization of laser cladding TiC-Inconel718 composite coating. *Optik* **2021**, *240*, 166828. [CrossRef]
20. Grohol, C.M.; Shin, Y.C.; Frank, A. Laser cladding of aluminum alloy 6061 via off-axis powder injection. *Surf. Coat. Technol.* **2021**, *415*, 127099. [CrossRef]
21. Olakanmi, E.; Nyadongo, S.; Malikongwa, K.; Lawal, S.; Botes, A.; Pityana, S. Multi-variable optimisation of the quality characteristics of fiber-laser cladded Inconel-625 composite coatings. *Surf. Coatings Technol.* **2018**, *357*, 289–303. [CrossRef]
22. Chen, L.; Yu, T.; Chen, X.; Zhao, Y.; Guan, C. Process optimization, microstructure and microhardness of coaxial laser cladding TiC reinforced Ni-based composite coatings. *Opt. Laser Technol.* **2022**, *152*, 108129. [CrossRef]
23. Li, Q.; Chen, J.; Wang, X.; Liu, Y.; Jiang, K.; Yang, S.; Liu, Y. Process, microstructure and microhardness of GH3039 superalloy processed by laser metal wire deposition. *J. Alloys Compd.* **2021**, *877*, 160330. [CrossRef]
24. Chen, L.; Zhao, Y.; Song, B.; Yu, T.; Liu, Z. Modeling and simulation of 3D geometry prediction and dynamic solidification behavior of Fe-based coatings by laser cladding. *Opt. Laser Technol.* **2021**, *139*, 107009. [CrossRef]
25. Li, C.; Yu, Z.; Gao, J.; Zhao, J.; Han, X. Numerical simulation and experimental study of cladding Fe60 on an ASTM 1045 substrate by laser cladding. *Surf. Coat. Technol.* **2018**, *357*, 965–977. [CrossRef]
26. Mondal, S.; Paul, C.P.; Kukreja, L.M.; Bandyopadhyay, A.; Pal, P.K. Application of Taguchi-based gray relational analysis for evaluating the optimal laser cladding parameters for AISI1040 steel plane surface. *Int. J. Adv. Manuf. Technol.* **2012**, *66*, 91–96. [CrossRef]
27. Han, B.; Li, R.; Pi, Q.; Shi, Y.; Qi, H.; Bi, K.; Sun, G. Prediction of deposit characteristics based on the discrete coaxial nozzle during laser direct metal deposition. *Opt. Laser Technol.* **2023**, *163*, 109385. [CrossRef]
28. Wirth, F.; Wegener, K. A physical modeling and predictive simulation of the laser cladding process. *Addit. Manuf.* **2018**, *22*, 307–319. [CrossRef]
29. Sun, Y.; Hao, M. Statistical analysis and optimization of process parameters in Ti6Al4V laser cladding using Nd:YAG laser. *Opt. Lasers Eng.* **2012**, *50*, 985–995. [CrossRef]
30. Farayibi, P.K.; Abioye, T.E.; Clare, A.T. A parametric study on laser cladding of Ti-6Al-4V wire and WC/W2C powder. *Int. J. Adv. Manuf. Technol.* **2016**, *87*, 3349–3358. [CrossRef]
31. Costa, L.; Felde, I.; Réti, T.; Kálazi, Z.; Colaço, R.; Vilar, R.; Verő, B. A Simplified Semi-Empirical Method to Select the Processing Parameters for Laser Clad Coatings. *Mater. Sci. Forum* **2003**, *414–415*, 385–394. [CrossRef]
32. Liu, H.; Li, M.; Qin, X.; Huang, S.; Hong, F. Numerical simulation and experimental analysis of wide-beam laser cladding. *Int. J. Adv. Manuf. Technol.* **2018**, *100*, 237–249. [CrossRef]
33. Jin, K.; Yang, Z.; Chen, P.; Huang, G.; Qiao, X. Dynamic solidification process during laser cladding of IN718: Multi-physics model, solute suppressed nucleation and microstructure evolution. *Int. J. Heat Mass Transf.* **2022**, *192*, 122907. [CrossRef]
34. Wang, H.-Z.; Cheng, Y.-H.; Zhang, X.-C.; Yang, J.-Y.; Cao, C.-M. Effect of laser scanning speed on microstructure and properties of Fe based amorphous/ nanocrystalline cladding coatings. *Mater. Chem. Phys.* **2020**, *250*, 123091. [CrossRef]
35. Chen, L.; Yu, T.; Chen, Y.; Wang, W. Slicing strategy and process of laser direct metal deposition (DMD) of the inclined thin-walled part under open-loop control. *Rapid Prototyp. J.* 2021, *ahead of print*. [CrossRef]
36. Muvvala, G.; Karmakar, D.P.; Nath, A.K. In-process detection of microstructural changes in laser cladding of in-situ Inconel 718/TiC metal matrix composite coating. *J. Alloys Compd.* **2018**, *740*, 545–558. [CrossRef]
37. Mishra, A.K.; Kumar, A. Numerical and experimental analysis of the effect of volumetric energy absorption in powder layer on thermal-fluidic transport in selective laser melting of Ti6Al4V. *Opt. Laser Technol.* **2018**, *111*, 227–239. [CrossRef]
38. Salloom, R.; Joshi, S.; Dahotre, N.; Srinivasan, S. Laser surface engineering of B4C/Fe nano composite coating on low carbon steel: Experimental coupled with computational approach. *Mater. Des.* **2020**, *190*, 108576. [CrossRef]

Disclaimer/Publisher's Note: The statements, opinions and data contained in all publications are solely those of the individual author(s) and contributor(s) and not of MDPI and/or the editor(s). MDPI and/or the editor(s) disclaim responsibility for any injury to people or property resulting from any ideas, methods, instructions or products referred to in the content.

coatings

MDPI

Article

Performance Evaluation of PVD and CVD Multilayer-Coated Tools in Machining High-Strength Steel

Saima Yaqoob [1,2], Jaharah A. Ghani [1], Nabil Jouini [3,4,*] and Afifah Z. Juri [1]

[1] Department of Mechanical and Manufacturing Engineering, Faculty of Engineering and Built Environment, Universiti Kebangsaan Malaysia, Bangi 43600, Selangor, Malaysia; engg_saima@hotmail.com (S.Y.); jaharahaghani@ukm.edu.my (J.A.G.); afifahjuri@ukm.edu.my (A.Z.J.)
[2] Department of Industrial and Manufacturing Engineering, NED University of Engineering and Technology, University Road, Karachi 75270, Pakistan
[3] Mechanical Engineering Department, College of Engineering, Prince Sattam Bin Abdulaziz University, Alkharj 11942, Saudi Arabia
[4] Laboratoire de Mécanique, Matériaux et Procédés (LR99ES05), École Nationale Supérieure d'Ingénieurs de Tunis, Université de Tunis, Tunis 1008, Tunisia
* Correspondence: n.jouini@psau.edu.sa

Abstract: To curtail the negative effects of traditional flood machining, dry cutting using carbide tools has emerged as a prominent alternative for manufacturers, owing to its low cost and phenomenal surface qualities. In line with this view, high-speed machining of high-strength AISI 4340 alloy steel was carried out using multilayer Al_2O_3/TiCN-CVD and TiAlN/AlCrN-PVD carbide tools in a dry environment. The experimental scheme was adopted, as per Taguchi's L_{18} orthogonal array, to investigate the two most crucial machinability aspects, namely tool life and surface roughness. An analysis of variance (ANOVA) was performed on the obtained data, and it was inferred that the feed rate exhibited the strongest effects on both the tool life and surface roughness, with corresponding percentage contributions of 46.22% and 68.96%, respectively. The longest tool lives of 14.75 min and 10.08 min were obtained at a low cutting speed and feed rate for CVD and PVD tools, respectively. However, the lowest surface roughness of 0.276 µm and 0.307 µm was achieved at a high cutting speed and low feed rate for PVD and CVD tools, respectively. The evolution of tool wear, studied through the microscopic images of the worn tools, revealed that a high cutting speed and feed rate accelerated the flank wear for both types of tools. Nevertheless, the CVD tool exhibited better results due to the thick and effective Al_2O_3/TiCN coating layer, which protected the carbide substrate against thermal–mechanical loads. Moreover, scanning electron microscopy (SEM) and energy-dispersive X-ray spectroscopy (EDX) performed on the worn tools revealed that adhesion, oxidation, diffusion, and abrasion were the main wear mechanisms for both types of tools.

Keywords: high-speed machining; multilayer-coated carbide tool; AISI 4340; surface roughness; tool wear; tool life

1. Introduction

In this era of rapid development, manufacturing industries remain the main source of environmental pollution. The precarious effluents produced by the industrial sector, when released into the atmosphere, pose serious environmental and health hazards. Metal cutting is a critical manufacturing process that relies heavily on lubricants. However, conventional metal-cutting fluids, while effective at suppressing heat, pose severe medical and ecological risks. Studies have linked exposure to conventional metal-cutting fluids to an increased risk of various types of cancer, skin allergies, and even physical disabilities [1]. Moreover, their chemical dissolution after disposal is a potential cause of soil contamination and water pollution, emphasizing the need for expensive, yet necessary, pre-disposal treatment [2]. According to statistics presented by a leading German automobile company, the

procurement and disposal expenses associated with cutting fluids make up approximately 7% to 17% of the direct labor cost [3]. Due to these ecological and economic challenges, dry cutting has emerged as a growing field of research. Dry cutting, being carried out without coolants or lubricants, offers significant environmental advantages over flood machining. However, the involvement of high thermal–mechanical loads, particularly in the machining of difficult-to-cut materials, such as titanium, nickel, and high-strength steel, compromises surface quality and the dimensional accuracy of machined components in a dry environment [4]. To address these challenges, advanced tool materials and coatings possessing excellent tribological properties and wear resistance have been introduced. Although the application of advanced materials such as ceramics, cubic boron nitride (CBN), and polycrystalline cubic boron nitride (PCBN) have substantially improved the chemical, mechanical, and cutting capabilities of cutting tools, cemented carbide tools, due to their cost-effectiveness, still capture a major share (~53%) of the market [5]. Among these, 80%–90% are categorized with single- or multilayer-coated carbide tools [6]. Thin films covering the surface of a carbide substrate function as hard coatings and serve various purposes. For instance, coating a substrate with a highly thermally resistant material can protect it from temperature-driven damage in applications involving elevated temperatures [7]. Grigoriev et al. [2] reported that Ti-based coatings can withstand high machining temperatures and considerably inhibit the diffusion and oxidation wear mechanism.

The most common types of hard coatings that are applied to cutting tools are TiCN, HSN^2, Al_2O_3, TiN, TiAlN, TiB_2, TiBN, and AlTiCrN [8]. The synthesis of coatings can generally be achieved through physical vapor deposition (PVD) and chemical vapor deposition (CVD) processes. Both techniques differ in their method of application and depend on the type and nature of the coating and substrate material. PVD refers to a vacuum-coating process that allows for the deposition of solid material as a thin film layer on the substrate body through vaporization and condensation [9]. The coating temperature in PVD remains lower than 500 °C, and a thin layer of coated material is deposited on the base material, making it mostly suitable for finishing applications [7]. On the other hand, CVD is a heat-activated process in which gaseous precursors are injected into a reaction chamber for chemical surface reaction and dissociation, resulting in the formation of a potential coating. The temperature of the substrate is maintained between 800 °C and 1150 °C [10]. Both deposition methods can form single-layer and multilayer coatings. The effectiveness of single- and multilayer coating has also been investigated by many researchers; multilayer coatings have been claimed to be more effective when machining difficult-to-cut materials. Chinchanikar and Choudhury [11] reported that coated tools can substantially reduce tool wear mechanisms. They noticed a significant reduction in tool wear when a single-layer TiAlN-coated tool was compared with an uncoated tool while machining hardened steel, demonstrating satisfactory performance in increasing cutting from 62 to 200 m/min. However, the cutting efficiency of multilayer $TiCN/Al_2O_3/TiN$ tools was remarkably improved up to a cutting speed of 350 m/min. It was concluded that single-layer coatings could not sustain the harsh machining environment and were, thus, severely affected by accelerated crater wear, weakening the cutting edge.

High-strength steel has widespread engineering applications (e.g., transmission shafts, gears, bearings, rolling dies, building structures, pipeline transportation, etc.) due to its superior qualities, such as high hardness and torsional strength, enhanced fatigue and abrasion resistance, and excellent shock-absorbing abilities [12,13]. Moreover, its high abrasiveness, low thermal conductivity, and high plastic nature are associated with poor machining capabilities [14]. The high cutting resistance exhibited by heat-treated steel, particularly at high machining regimes, is the leading cause of intense heat generation, high power consumption, unfavorable chip formation, shorter tool life, and increased machining time and cost [15]. With advancements in coating technologies, these machinability challenges can be addressed. The literature has reported that abrasion, adhesion, and temperature-driven diffusion are the main tool wear mechanisms in the machining of AISI 4340 high-strength alloy steel [16,17]. Therefore, Al_2O_3 coatings, being thermally

and chemically resistant [18], can be paired with TiCN [19] or TiAlN coatings, which are categorized by high adhesion and corrosion resistance [20], to provide a better machinability performance. According to Li et al. [21], multilayer PVD-coated carbide tools can improve the machinability of heat-treated alloy steel during a high-speed machining process. They employed three types of PVD coatings, namely AlTiN single-layer, TiAlN/TiN bi-layer, and TiN/TiCN/TiAlN multilayer coatings, on the carbide substrate and a PVD bi-layer-TiCN/NbC composite coating on the ceramic substrate. It was reported that TiN/TiCN/TiAlN tools considerably reduced the tearing and collapse of the coatings and resulted in less plastic deformation, crack nucleation, edge chipping, and abrasive wear.

Many studies have been carried out regarding the machining of high-strength steel, with different coatings and tool materials. Das et al. [22] utilized thin multilayer Ti (C N O) PVD-coated cermet tools in machining heat-treated AISI 4340 alloy steel and achieved the lowest surface roughness of 1.065 μm in cutting speed, V = 250 m/min, feed rate, F = 0.09 mm/rev, and depth of cut, DOC = 0.4 mm. Interestingly, they found that the cutting depth was the most influential factor affecting the surface roughness, followed by the feed rate and cutting speed. However, Zheng et al. [23], in the milling of AISI 4340 (43 HRC) steel using an Al_2O_3/TiCN CVD-coated carbide tool, found considerably less surface roughness, 0.40 μm, at an identical machining speed and feed rate (V = 250 m/min, F = 0.09 mm/rev) but with a low depth of cut, DOC = 0.1 mm. The performance of a TiAlN PVD-coated tool in machining Ni-based super-alloy was evaluated in reference [24]. The results showed that the TiAlN coating initially suppressed the adherence of the work material, but, with subsequent cutting, crack initiation led to the occurrence of flaking and exposure of the substrate. The literature has also highlighted the comparative studies of different types of coatings. For instance, Sonawane and Sargade [25] compared uncoated AlTiCrN and AlTiN tungsten carbide inserts in tuning duplex stainless-steel 2205 under a dry environment. It was reported that AlTiCrN exhibited the lowest amount of tool wear, Vb = 0.16 mm, after completing 2450 mm of machining length for each tool. Likewise, Boing et al. [6] conducted a comparative assessment of TiCN/ Al_2O_3/TiN CVD and TiAlN PVD multilayer-coated tools, during which they reported the sequence of events of tool wear progression. It was observed that CVD tools were initially affected by abrasion, followed by crack nucleation and propagation, coating delamination, and, lastly, complete spalling. In contrast, the sequence of tool wear events for PVD tools included abrasion, high plastic deformation, crack nucleation, leading to weakening of the substrate and coating bonding, and, eventually, the detachment of the entire coating. In a recent study, Bag et al. [26] reported the best surface quality of machined surfaces (Ra = 0.40 μm) with a a TiN/TiCN/ Al_2O_3 CVD-coated tool at a cutting speed of 260 m/min. An ANOVA performed on surface roughness data revealed that the feed rate had the highest percentage contribution rate (PCR) of 71.93%, making it the most influential parameter. This was followed by machining speed, with a PCR of 14.8%, and depth of cut, with a PCR of 3.4%. Moreover, they analyzed worn tools and reported abrasion and adhesion as the main wear mechanisms. An ANOVA on tool wear data demonstrated the dominating effect of cutting speed, exhibiting the highest PCR of 66.06%, followed by the feed rate at 13.91% and depth of cut at 3.83%. Alok et al. [27] also acknowledged the highest statistical influence of the cutting speed on flank wear while machining AISI 4340 steel (52 HRC) using a HSN^2-coated carbide insert. Furthermore, Kumar et al. [28] investigated the influence of different lubrication conditions, namely water-soluble, nano-cutting fluid, and compressed air, on the cutting performance of uncoated cermet tools. It was determined that nano-cutting fluid effectively reduced the cutting force, produced curlier chips, and inhibited the tool flank wear compared to the other two conditions. These results were in line with the findings of Singh et al. [29], who utilized uncoated textured carbide inserts under nano-fluid-based MQL lubrication. In another study, Zenjanab et al. [30] conducted high-speed machining in a range between V = 300 and 400 m/min, F = 0.1–0.2 mm/rev, using ceramic tools under dry conditions, CuO-based cutting fluids, and soluble cutting fluids. The results revealed

that CuO-based cutting fluids exhibited better machinability under all cutting conditions due to favorable anti-friction and anti-wear properties.

Shalaby and Veldhuis [31] suggested that pure alumina + ZrO_2-based ceramic tools produced better tool life at a low machining speed, V = 150 and 250 m/min, while mixed alumina+ Al_2O_3 + TiCN-based ceramic outperformed, with a high cutting speed at V = 700 and 1000 m/min. Furthermore, Suyama and Diniz [32] performed high-speed turning of AISI 4340 using a CBN+ Al_2O_3/TiCN ceramic phase insert and obtained the longest tool life of 15 min at a low cutting speed of 300 m/min. Additionally, they studied the effect of vibration on tool wear by varying the tool overhang distance and reported that diffusion was the main wear mechanism at high vibration, while abrasion predominated at low vibration. Da Silva et al. [33] compared the results of hard turning with the traditional grinding process by using ceramic and polycrystalline cubic boron nitride (PCBN) tools. It was claimed that hard turning in dry cutting conditions with both tools produced the lowest Ra of 0.18 μm at a high cutting speed, V = 300 m/min. On the contrary, there was a comparatively high Ra in grinding (0.20 μm), suggesting that hard turning could be a potential replacement for the traditional grinding process.

After reviewing the literature, it was determined that tools made up of advanced materials such as CBN and ceramics were primarily evaluated for the high-speed hard machining of AISI 4340 alloy steel. However, the utilization of multilayer-coated carbide tools has not been investigated in detail under high machining parameters. Therefore, this study aimed to provide an in-depth analysis on the performance of multilayer CVD and PVD-coated carbide tools in a dry environment, considering two crucial machinability aspects: surface roughness and tool life. Moreover, the evolution of tool wear and the behavior of different coatings in inhibiting the wear progression, followed by a comprehensive analysis of wear mechanisms, were also included in the scope of this study. It was anticipated that this research would be of potential interest to tool manufacturers and industry professionals who are striving to achieve better product quality and machinability performance by utilizing sustainable methods of manufacturing.

2. Materials and Methods

Round cylindrical bars of AISI 4340 alloy steel having dimensions Ø60 × 120 were employed for experimentation. The work samples were heat-treated to achieve the desired hardness of 50 HRC through a series of repetitive operations, including 3 h of curing at 840 °C, followed by 1 h of quenching at 830 °C and 4 h of annealing at 400 °C. The experiments were conducted on a CNC turning machine with high cutting speed in a range between 300 and 350 m/min, feed rate 0.05–0.15 mm/rev, and depth of cut 0.1–0.3 mm according to Taguchi L_{18} orthogonal array, as presented in Table 1. The machining parameters were selected as per Ref. [30], utilizing ceramic tools in high-speed (250–400 m/min) machining of heat-treated AISI 4340 alloy steel (52 HRC), using soluble cutting fluid-based nanofluids (CuO, CuO + boric acid), which have a detrimental impact on the environment. This study was conducted to realize sustainable machining using a dry approach and aimed to evaluate the effectiveness of multilayer-coated carbide tools, which are less costly than ceramic tools.

Two multilayer-coated carbide inserts TiAlN/AlCrN with physical vapor deposition (PVD) and Al_2O_3/TiCN chemical vapor deposition (CVD) were employed for the turning experiments. The selection of tool coating was based on reviewed literature, as hard turning generates intense machining heat, which promotes temperature-driven wear mechanisms. Therefore, effective coatings were selected to provide thermal stability and chemical resistance. For instance, Al_2O_3 coating forms a thermal barrier and offers greater oxidation and wear resistance at elevated temperatures [34], TiCN exhibits resistance to shock loading [21], TiAlN coating possesses hardness and self-lubricating properties [35], and TiCrN offers good wear resistance and chemical stability [36]. The characteristics of both tools are listed in Table 2. Tool performance was evaluated by measuring tool wear and surface roughness under each experimental condition. The progression of tool wear

was tracked by capturing the wear images at different intervals using a Zeiss Stemi 2000-C optical microscope (Zeiss, Oberkochen, Germany), where an average tool life criterion of Vb $\geq$ 300 µm was used as per ISO 3685 [37] for tool life analysis. Next, the worn inserts were analyzed using a Zeiss SUPRA 55VP scanning electron microscope (SEM) and energy-dispersive spectroscopy (EDS) to determine the associated wear mechanisms. Then, the surface quality of machined samples was measured by using a Mitutotyo Surfest SJ-301 surface roughness tester (Mitutotyo, Kawasaki, Japan). Three surface roughness readings were recorded at different positions on the cylindrical workpiece, and the average value was computed. Figure 1 illustrates the experimental scheme adopted for this study.

Table 1. Experimental scheme, as per Taguchi L_{18}.

Exp. No	Tool Type (T)	Cutting Speed V (m/min)	Feed Rate F (mm/rev)	Depth of Cut DOC (mm)	Exp. No	Tool Type (T)	Cutting Speed V (m/min)	Feed Rate F (mm/rev)	Depth of Cut DOC (mm)
E1	PVD	300	0.05	0.1	E10	CVD	300	0.05	0.3
E2	PVD	300	0.10	0.2	E11	CVD	300	0.10	0.1
E3	PVD	300	0.15	0.3	E12	CVD	300	0.15	0.2
E4	PVD	350	0.05	0.1	E13	CVD	350	0.05	0.2
E5	PVD	350	0.10	0.2	E14	CVD	350	0.10	0.3
E6	PVD	350	0.15	0.3	E15	CVD	350	0.15	0.1
E7	PVD	400	0.05	0.2	E16	CVD	400	0.05	0.3
E8	PVD	400	0.10	0.3	E17	CVD	400	0.10	0.1
E9	PVD	400	0.15	0.1	E18	CVD	400	0.15	0.2

Table 2. Characteristics of PVD and CVD tools [38].

Characteristics	PVD Tool	CVD Tool
Grade	H-grade	P-grade
Coating	TiAlN/AlCrN	Al_2O_3/TiCN
Coating thickness	3 µm	18 µm
Hardness of substrate	93.2 HRA	90.5 HRA
Nose radius	0.4 mm	0.4 mm
Rake angle	−6°	−6°
Cutting edge angle	95°	95°

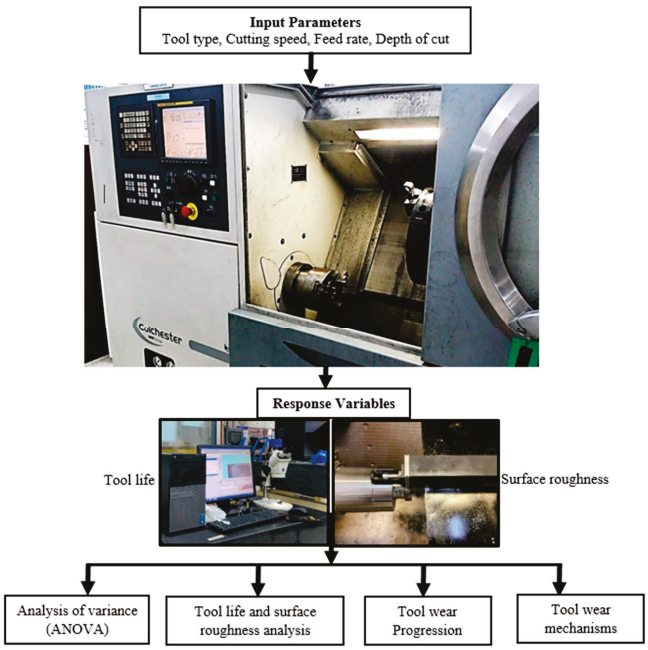


Figure 1. Experimental setup adopted for machining.

3. Results and Discussion

This section presents a comprehensive discussion on the crucial machinability aspects when high-strength steel was machined with Al_2O_3/TiCN-CVD and TiAlN/AlCrN-PVD carbide tools: tool life, tool wear progression, tool wear mechanisms, and surface roughness.

3.1. Statistical Analysis of Tool Life and Surface Roughness

The output variables tool life and surface roughness for each experimental run are tabulated in Table 3. Analysis of variance (ANOVA) was performed to infer meaningful information from the obtained data, and the most significant factors with their percentage contributions were determined by using Minitab 17 statistical software.

Table 3. Results obtained for each experimental run.

Exp. No	Tool Type	Surface Roughness	Tool Life	Exp. No	Tool Type	Surface Roughness	Tool Life
E1		0.3490	10.080	E10		0.4910	14.750
E2		1.0800	6.590	E11		0.8320	10.570
E3		1.9723	2.980	E12		1.2110	4.540
E4		0.2755	7.830	E13		0.3050	14.110
E5	PVD	1.1660	3.290	E14	CVD	0.7190	6.850
E6		1.7430	1.940	E15		0.9920	2.840
E7		0.2940	4.530	E16		0.3070	4.830
E8		0.7210	0.943	E17		0.5820	4.230
E9		1.2060	0.493	E18		0.7940	2.510

3.1.1. Tool Life

Based on the ANOVA results (Table 4), it was revealed that the feed rate, cutting speed, and tool type were the most influential parameters for tool life, with corresponding percentage contributions of 46.22%, 28.50%, and 12.92%, respectively. However, the depth of cut with $p = 0.828$ was found to be insignificant, and its contribution was only 0.46%. Similar results could also be deduced from the main effect plot of the means in Figure 2a, where the depth of cut showed a relatively shorter spread in comparison to other parameters. The result of the present study was unexpected based on the previous literature, where, generally, the cutting speed was the governing factor for tool life. The appreciable variation in tool life with changing feed rates can be justified by the fact that raising the feed rate leads to an increased tool–workpiece contact area, resulting in a high material removal rate. This exerts more force on the tool, in addition to a colossal increase in friction between the contacting surfaces. These factors substantially contributed in hastening the tool wear, particularly in the hard turning operation, which unequivocally involves high thermal stresses. Therefore, the range of variation in tool life was sufficient to contribute greater weight to the feed rate, and this nullified the presumed dominating influence of machining speed. The results obtained in this research were similar to López-Luiz et al. [39], who performed hard turning of AISI D2 steel with carbide inserts and found the feed rate to be the most controlling factor affecting the tool wear/life. Moreover, a recent study carried out by Fedai [40] in turning AISI 4340 alloy steel also found the feed rate to be a statistically significant exerting dominating effect on tool wear rather than cutting speed. Overall, the upward trend demonstrated by the CVD-coated tools in the main effect plot of tool type in Figure 2a showed that they outperformed in extending tool life within the conducted experimental scheme.

Table 4. ANOVA table for response variables.

Source	DF	Seq SS	Adj SS	Adj MS	F	*p*	% Cont.	Significance
Tool life (T) (R-Sq 86.62%)								
T	1	39.144	39.144	39.144	10.85	0.008 *	12.92%	Significant
V	2	86.382	86.382	43.191	11.97	0.002 *	28.50%	Significant
F	2	140.08	140.080	70.040	19.41	0.000 *	46.22%	Significant
DOC	2	1.386	1.386	0.6928	0.19	0.828	0.46%	Insignificant
Residual Error	10	36.075	36.075	3.6075				
Total	17	303.067						
Surface Roughness (R_a) (R-Sq 88.09%)								
T	1	0.3680	0.3680	0.36802	11.13	0.008 *	8.75%	Significant
V	2	0.3526	0.3526	0.17631	5.33	0.027 *	8.38%	Significant
F	2	2.8996	2.8996	1.44978	43.83	0.000 *	68.98%	Significant
DOC	2	0.2523	0.2523	0.12614	3.81	0.059	6.002%	Insignificant
Residual Error	10	0.3308	0.3308	0.03308				
Total	17	4.2033						

* Significant factor.

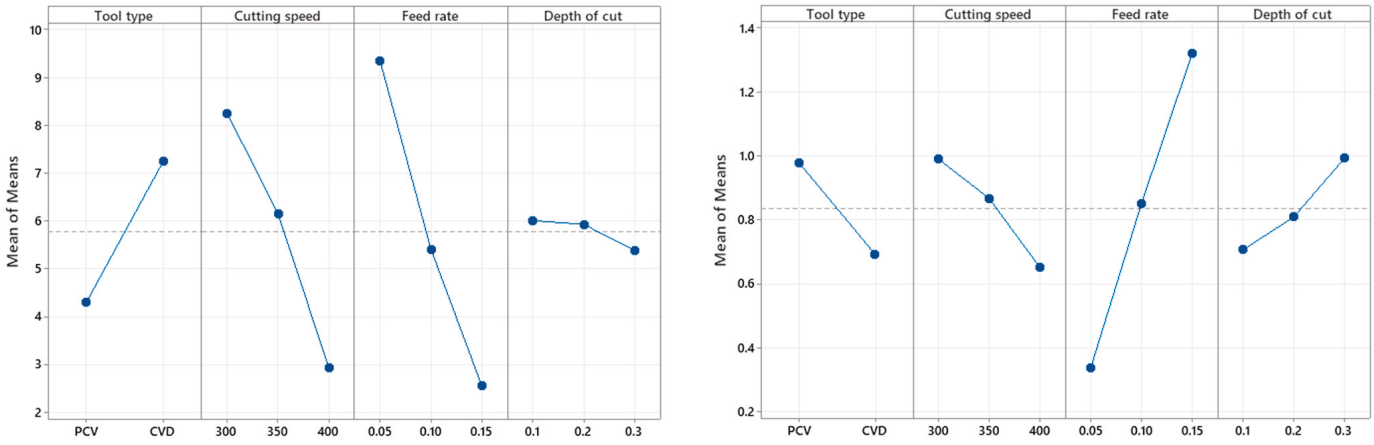


Figure 2. Main effect plot of (**a**) mean of tool life and (**b**) mean of surface roughness.

3.1.2. Surface Roughness

The results presented in Table 4 indicate that the feed rate continued to be the most significant factor affecting the surface roughness, exhibiting a percentage contribution of 68.98%. This was followed by cutting speed and tool types, with respective contributions of 8.75 % and 8.38%. However, depth of cut, with *p*-value = 0.059 and contributing 6%, remained the least significant factor in this study. The main effect plot of the mean in Figure 2b also supports these findings, showing that the graph of feed rate, cutting speed, and tool type exhibited a relatively broader spread compared to the depth of cut. The apparent reason for the increasing surface roughness with increasing feed rate is associated with the high chip volume and thrust force, which can lead to increased vibration and, consequently, decreased surface quality. This result is similar to the observation of Mia et al. [41] while machining heat-treated AISI 1060 steel. According to them, the feed rate and then the cutting speed were the most significant governing variables for surface roughness. The lowest mean value exhibited by CVD tools in Figure 2b indicated their superior performance within the conducted experimental scheme.

3.2. Analysis of Tool Life/Wear for PVD- and CVD-Coated Carbide Tool

3.2.1. Tool Life and Tool Wear Progression

From the results illustrated in Figure 3, it was determined that the CVD-coated tool demonstrated the longest tool life of 14.75 min in experiment 10. However, at an identical machining speed (V = 300 m/min) and feed rate (F = 0.05 mm/rev), the useful life of the PVD-coated tool was 10.08 min, which was 31.3% less than the CVD tool. The trend of decreasing tool life was noticed when increasing the speed and feed for both types of tools. The higher order of both parameters produced significant heat generation and plastic deformation [42]. Overall, CVD-coated tools outperformed PVD tools in all experimental runs, as deduced from Figure 2. The obtained results of tool life can be comprehensively explained by analyzing the tool wear progression and mechanism with different parametric settings. Thorough analysis of tool wear progression can provide valuable insights into potential tool failures. The effects of significant input variables for a comparative assessment of tool wear were evaluated from the Taguchi L_{18} orthogonal array. As in Taguchi's L_{18} design of experiment, only one factor varied, while others remained the same. Since, the depth of cut had been identified as the least influential variable, as per the discussion in Section 3.1.1, its variation was not expected to significantly influence the accuracy of the comparative assessment. Hence, the assessments of tool wear for both CVD and PVD tools were performed by examining the microscopic images of the tool with increasing machining time.

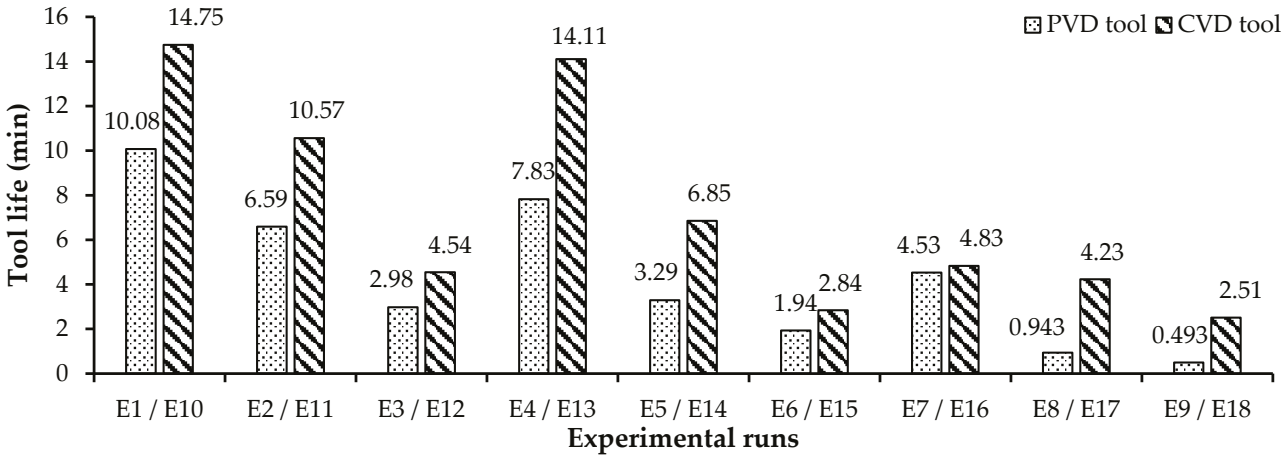
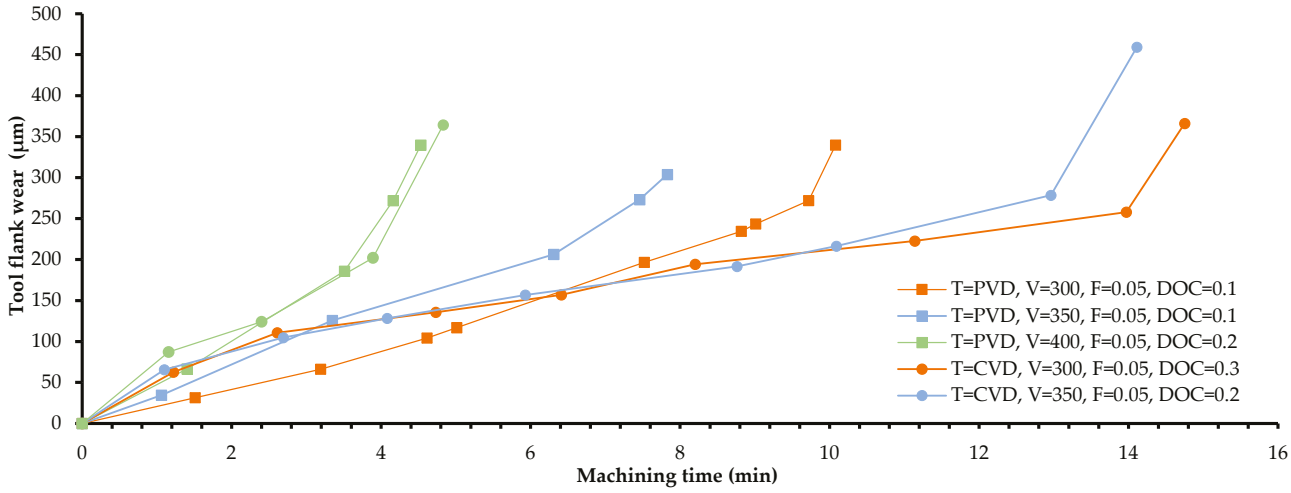


Figure 3. Tool life results for CVD and PVD tools in different experimental runs.

It is evident from Figure 4 that variation in machining parameters can substantially influence the evaluation of tool wear. Most particularly, as the level of cutting speed and feed rate increases, the tool wear accelerates and rapidly progresses towards the severe wear stage for both types of tools. The corresponding wear graphs in Figure 4a–c were, therefore, more skewed towards the left side as the cutting speed increased from 300 to 400 m/min and feed rate increased from 0.05 to 0.15 mm/rev. The most critical reason for this behavior was the excess heat generation with increasing cutting speed, resulting in plastic deformation and thermal softening of the tool material. Even a small rise in the feed rate in this scenario resulted in a proportional increase in the tool's transverse speed across the rotating workpiece, causing friction between the tool and the workpiece, ultimately leading to degradation of the tool [43]. It was noticed that the progression of wear in the case of CVD tools remained nearly steady in all cutting speed and feed rate combinations. However, it notably accelerated for PVD tools when the feed value was raised to 0.1 mm/rev and 0.15 mm/rev, as evident from Figure 4b,c. In order to determine why CVD tools outperformed PVD tools, microscopic and SEM images of worn tools were analyzed with respect to machining time for low and high parametric settings, as shown in Figure 5. It was discernible that PVD tools in both cutting conditions (experiment 1 and 9)

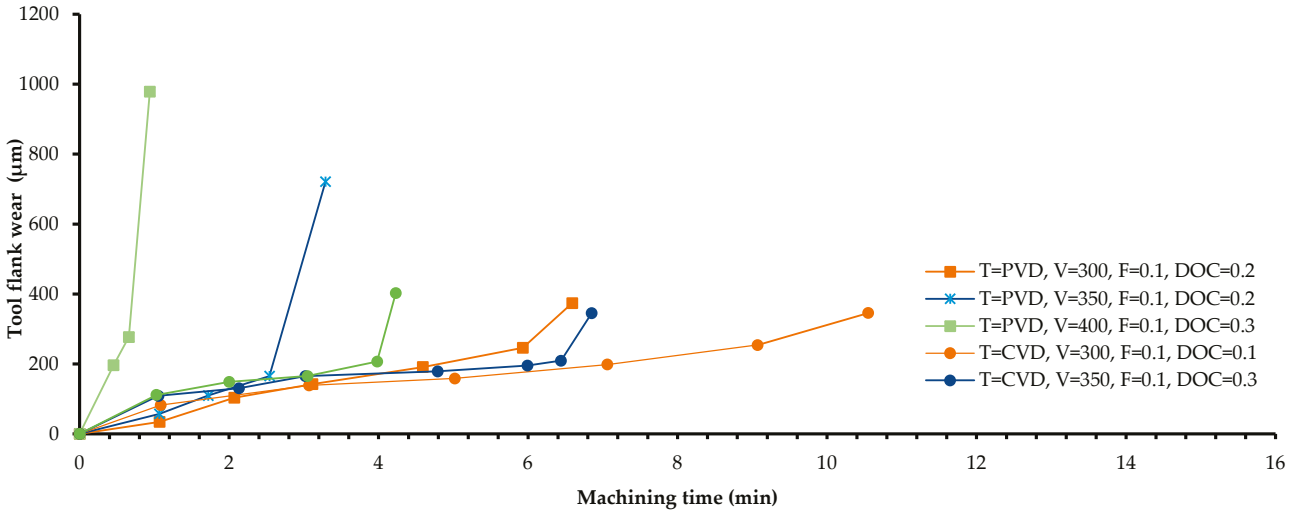
were highly affected by excessive chipping and abrasion, even during the initial wear stage (Vb $\geq$ 66.21 µm), indicating that the thin layer of the TiAlN/AlCrN coating (3 µm) could not protect the tool against thermal–mechanical loads. On the contrary, the double thick layer of the Al_2O_3/TiCN coating (18 µm) showed better resistance to chipping during the initial and gradual wear stages. It could also be observed from the tool cutting geometry in Figure 5 that it was relatively more stable at high wear width, Vb $\leq$ 194.14 µm @ 8.2 min in experiment 10 and at Vb $\leq$ 167.33 µm @ 1.83 min in experiment 18. According to Sonawane and Sargade [25], thicker coatings have low thermal conductivity, which plays a crucial role in protecting the carbide substrate from exposure to temperature variation. However, soon after the deterioration of the coating, the carbide substrate of both tools could not withstand the thermal–mechanical variations imposed by harsh machining conditions. Thus, they experienced faster progression towards the failure region. It is worth noting that PVD tools exhibited less flank wear width than CVD tools in experiment 1 (Vb = 339.70 µm < Vb = 366.18 µm) and experiment 9 (Vb = 415.2 µm < Vb = 841.12 µm). This behavior could be attributed to the following reasons:

- Comparatively lower depth of cut of 0.1 mm for the PVD tool, which exerted less mechanical load on the tool edge, eventually causing less damage.
- The higher hardness possessed by the PVD tool (93.2 HRA) compared to the CVD tool (90.5 HRA), which provided stability against thermal–mechanical loads.
- The high thermal expansion coefficient of the inner coating in case of the CVD tool (TiCN~7.8 $\times$ 10^{-6} K^{-1} [44] > AlCrN ~6 $\times$ 10^{-6} K^{-1} [45]) compared to the carbide substrate (5.7–6.9 $\times$ 10^{-6} K^{-1} [46]), causing the coating to expand more than the carbide substrate. Consequently, this exerted compressive stresses and damaged the tool.
- The high thermal conductivity of the TiCN coating (30 W/mk [47]) compared to AlCrN (4.63 W/mk [48]), causing excess heat to transfer to the carbide substrate, thereby weakening the base material of the tool and resulting in extensive flank wear.

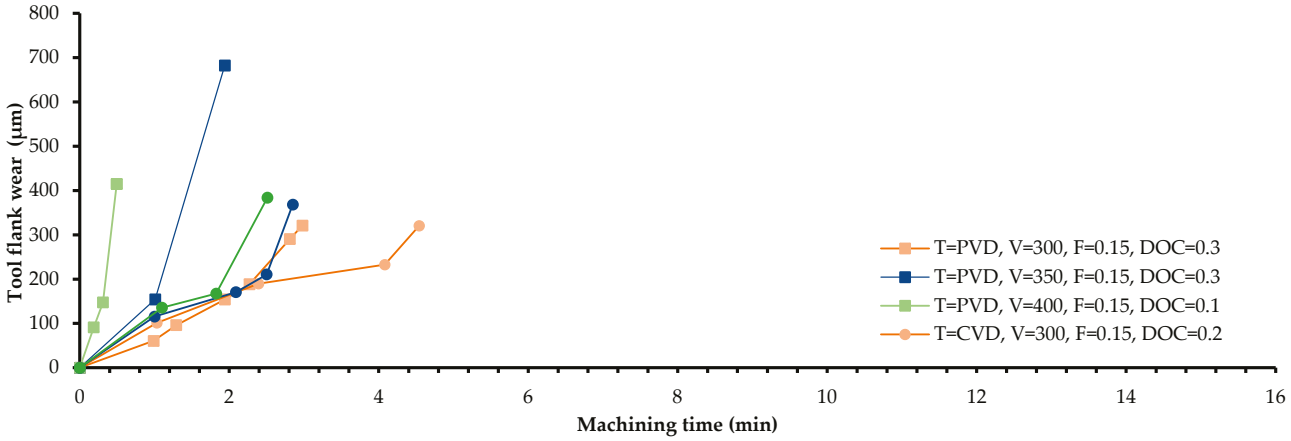


(**a**)

Figure 4. *Cont.*



(**b**)



(**c**)

Figure 4. Wear progression for PVD and CVD tools at feed rates of (**a**) 0.05 mm/rev, (**b**) 0.1 mm/rev, and (**c**) 0.15 mm/rev.

3.2.2. Tool Wear Mechanisms

To comprehend the wear mechanisms for both types of tools, SEM analysis was performed on the worn tool from experiments 1 and 10. Three regions of the worn tools were also examined in detail for SEM and EDX analysis: (a) crater face, (b) cutting edge, and (c) flank face. Figure 6a represented the high crater formation of the PVD tool, indicating a severe tribological condition between the flowing chips and the tool rake face. Reis et al. [49] stated that the combined effect of diffusion and adhesion caused the evolution of crater wear. Traces of elemental composition in spectra 1 and 2 showed the strong peaks of Fe and an appreciable amount of oxygen. This confirmed the adherence of the workpiece material, as well as elemental diffusion and oxidation, which were likely caused by the formation of iron oxide and a high-stress field at elevated temperature. Since the machining was performed in a high-speed regime, the generation of intense heat was inevitable. The rough surface on the crater surface also indicated diffusion. Moreover, chipping and abrasion were also noticed near the cutting edge. The presence of a few traces of Ti and Al elements in all spectra suggested that the tool coating had deteriorated. However, a noticeable percentage of W in spectra 1 and 2 represented exposure to the carbide substrate. It was expected that the periodic entry of the tool during the cutting cycle may have smashed the adhered material onto the tool, thereby leading to carbide breakage in the form of chipping. Das et al. [50] stated that stress concentration and uneven force distribution near the cutting

edge increase the possibility of chipping followed by tool fracture. Parallel friction marks in the direction of material flow indicated abrasion, which was identifiable on the tool flank face near the main cutting edge. The hard carbide micro-inclusion in the workpiece material rubbed against the tool, which caused abrasive wear. Furthermore, a significant percentage of workpiece material in spectra 1 and 2 indicated serious adhesion and was a possible cause of accelerated tool flank wear in the case of the PVD tool.

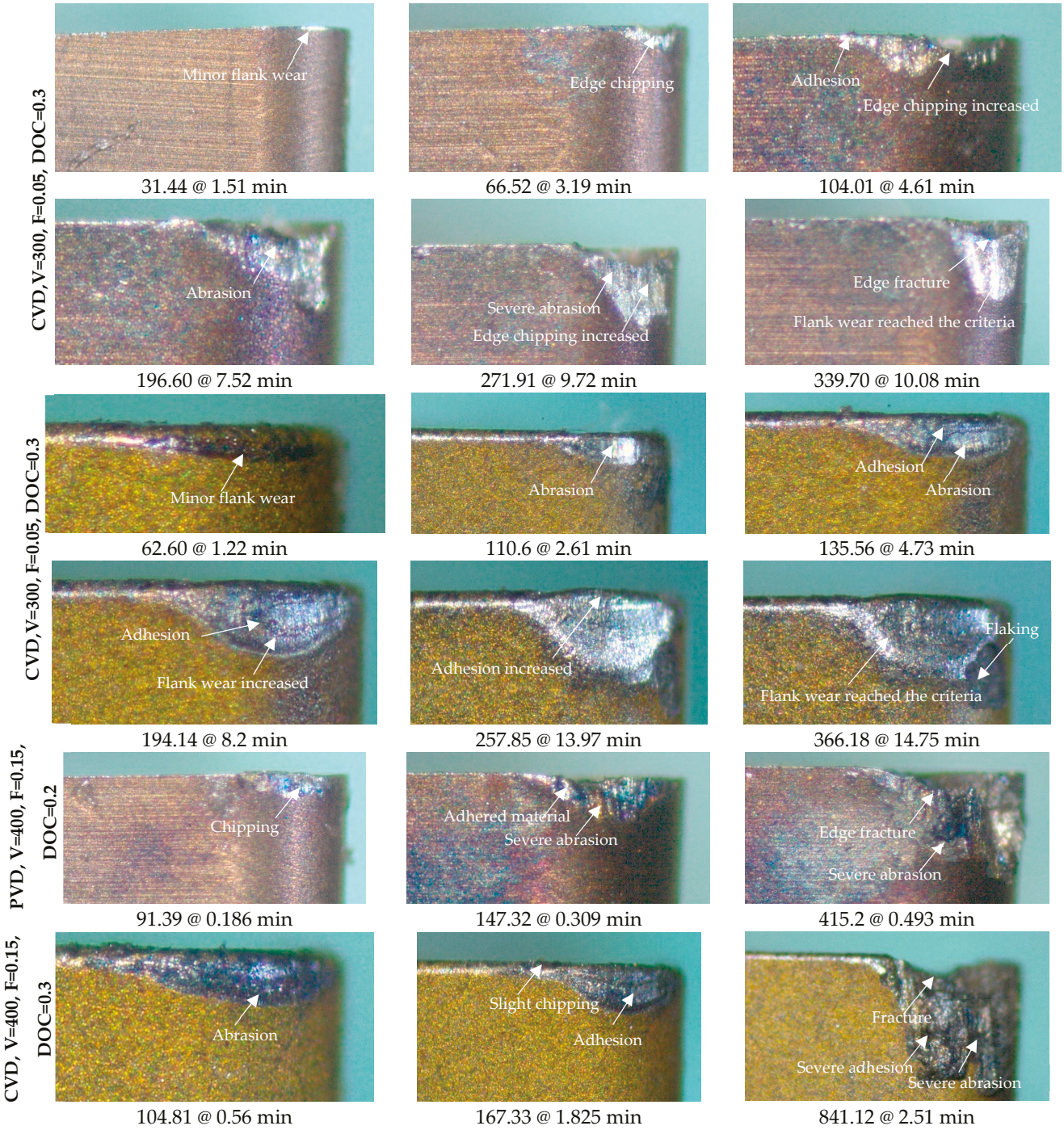
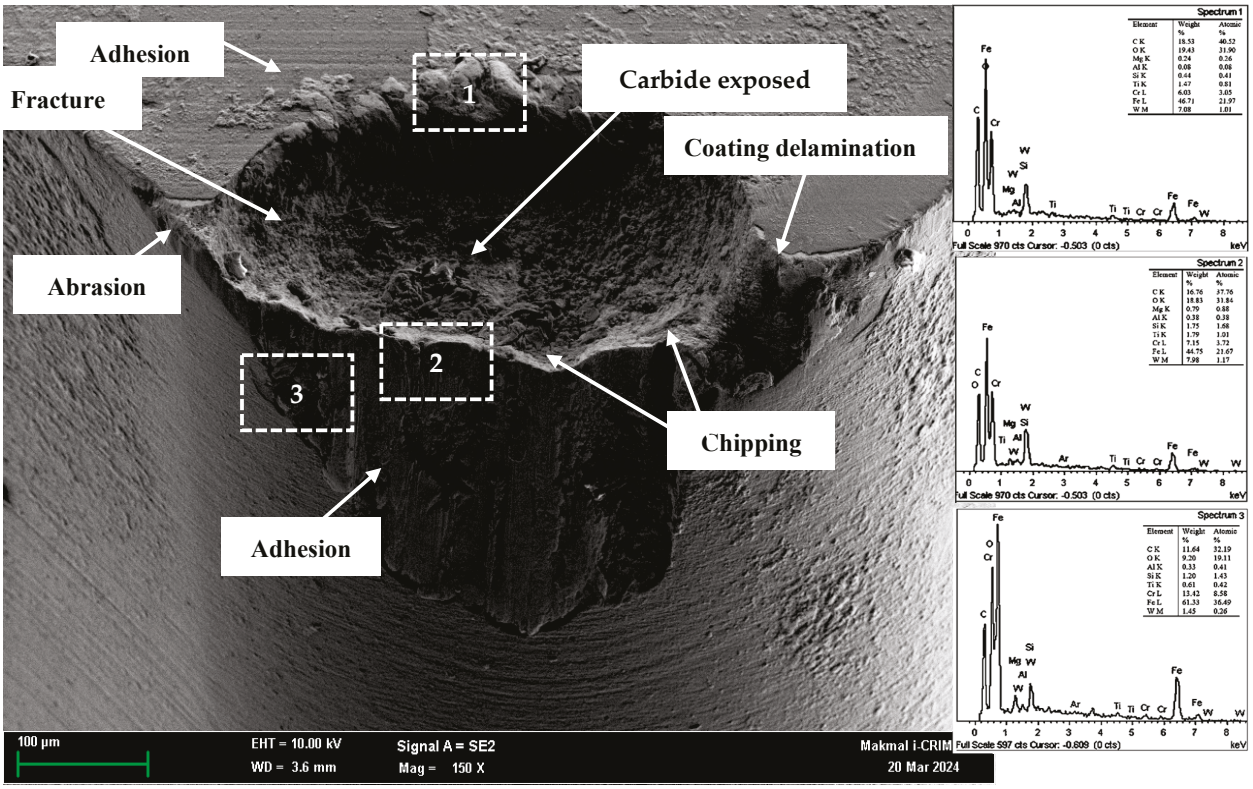
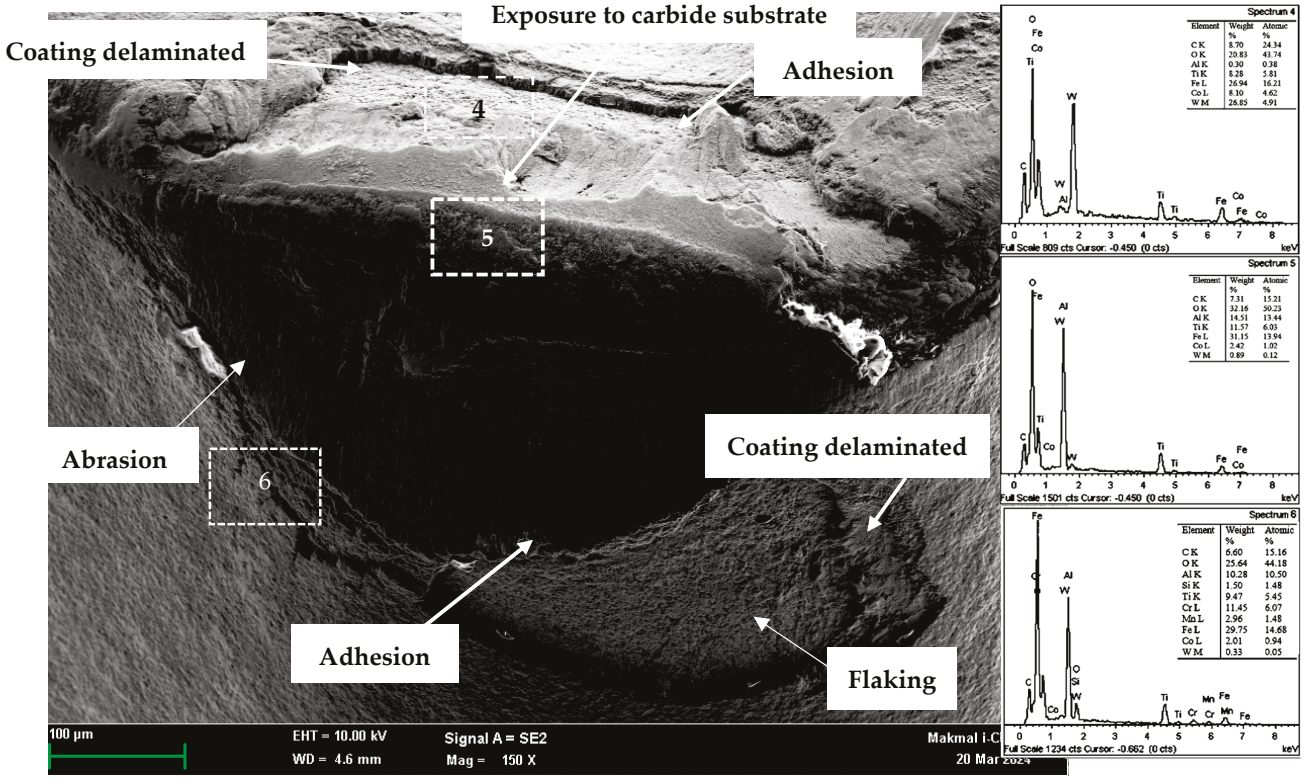


Figure 5. Wear images of both tools with the machining time at low and high parametric settings.



(**a**)



(**b**)

Figure 6. SEM and EDX analysis of the worn tools at V = 300 m/min and F = 0.05 mm/rev. (**a**) PVD tool; (**b**) CVD tool.

In comparison, the CVD tool exhibited a shallower crater depth, as shown in Figure 6b. This was due to the effective multilayer coating, which substantially minimized the wear and friction in comparison to the PVD tools. However, the EDX analysis of spectrum 4 showed high percentages of W, Co, and O, with a few traces of Al, suggesting the deterioration of the Al_2O_3 coating and the occurrence of oxidation wear. Interestingly, the presence of the inner TiCN coating on the rake face benefitted the carbide substrate against the varied thermo-mechanical loads and caused less damage, as compared to the PVD tool. Therefore, the profile of the main edge was relatively more stable. Previous studies have also reported that the TiCN coating exhibits excellent shock resistance capabilities [51]. The EDX analysis on the cutting edge (spectrum 5) revealed the existence of the Al_2O_3/TiCN coating, which effectively prevented material adhesion and chipping, thereby maintaining a stable cutting-edge geometry. Bjerke et al. [52] stated that the outer layer of the Al_2O_3 coating can form a protective layer of aluminum oxide during the machining process, thus providing thermal stability and abrasion resistance to the cutting edge. The wear morphology at the flank face represents abrasion and adhesion to the tool due to constant rubbing of hard micro-inclusions from the workpiece and carbide substrate. Meanwhile, the adherence on the flank face (as evident from spectrum 6) was an extrusion of flowing chips between the tool and workpiece. Due to the strong chemical affinity of the work material with the tool substrate, further adherence led to the weakening of the binder in the carbide matrix, while the adhered material, being unstable in nature, was continuously dislodged from the tool surface, promoting a traction effect, causing interlayer coating delamination [53]. Considering this fact, it was expected that the high depth of cut in this scenario exerted an increased cutting force, which was sufficiently high to cause tool flaking and ultimately led to the complete tool life criteria.

Based on SEM and EDX analysis, it is summarized that adhesion, oxidation, and abrasion constituted the primary wear mechanisms for both Al_2O_3/TiCN-CVD- and TiAlN/AlCrN-PVD-coated tools. However, excessive chipping on the main cutting edge and severe diffusion on the crater face were the contributing factors that accelerated wear mechanisms in the case of the PVD-coated tools.

3.3. Analysis of Surface Roughness for PVD- and CVD-Coated Carbide Tool

A pictorial representation of average surface roughness (R_a) for PVD and CVD tools is shown in Figure 7. It can be seen that the best surface roughness of 0.276 μm was obtained with the PVD tool in experiment 4 at V = 350 m/min, F = 0.05 mm/rev, and DOC = 0.1 mm. However, the minimum R_a of 0.307 μm in the case of the CVD tool was obtained at a cutting speed of 400 m/min, feed rate of 0.05 mm/rev, and depth of cut of 0.3 mm. Overall, CVD tools outperformed in delivering the best surface quality, showing 66.6% better results than PVD tools. These results were consistent with the tool wear/life findings discussed in Section 3.2, where the thick layer of the Al_2O_3/TiCN coating effectively decreased the coefficient of friction and resulted in lower surface roughness. On the contrary, the PVD tool was only 33.33% effective in delivering a better surface finish, as per the results of experiments 1, 4, and 7. This meant that the PVD tool with high hardness and a thin coating (TiAlN/AlCrN) was merely effective at low machining parameters because all these experiments were conducted at a low machining speed V = 300 m/min, low feed rate 0.05 mm/rev, and low depth of cut, DOC = 0.2–0.3 mm.

From Figure 7, it is also inferred that with an increase in the machining speed, there was a decrease in surface roughness. This is because increasing the speed minimizes the tool–chip contact area, thereby lowering the friction, and this produces better surface quality. Thermal softening of the work material by increasing the cutting speed is one of the governing factors, contributing to a decreasing cutting force as well as decreasing peaks and valleys present in the work surface, thereby allowing for a better surface finish [27]. It was also revealed that the surface roughness for both tools substantially increased with an increment in the feed rate. Most importantly, the value of R_a was augmented at a higher feed F = 0.15 mm/rev for both tools due to higher undeformed chip thickness,

which exerted a load on the cutting edge, leading to tool wear and increased surface roughness. The highest R_a of 1.97 μm and 1.211 μm were observed at low machining speeds V = 300 m/min and the highest feed rate F = 0.15 mm/rev for the PVD and CVD tools, respectively, in experiments 3 and 12. Though the effect of the cutting depth was not statistically significant, as discussed in Section 3.1.2, its higher value with high feed rates (0.1 mm/rev and 0.15 mm/rev) considerably increased the surface roughness. A combination of higher feed rate and depth of cut resulted in an increase in the chip cross-sectional area, which is associated with a higher force requirement to shear the material, resulting in chatter and a subsequent deterioration in surface quality [54]. Hence, it is suggested that a high machining speed with a low feed rate and depth of cut is favorable for lower surface roughness.

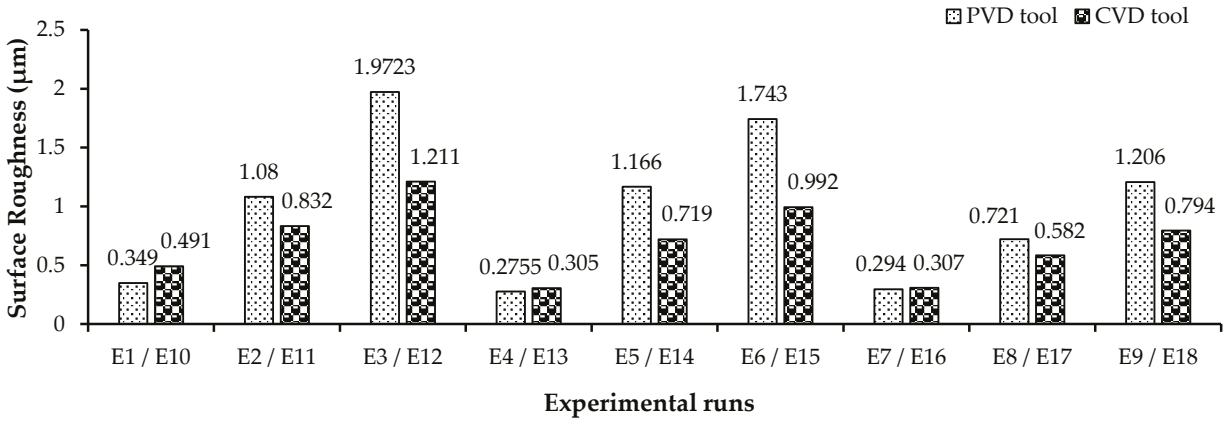


Figure 7. Surface roughness results for PVD and CVD tools in different experimental runs.

4. Conclusions

In this study, the performance of PVD and CVD multilayer-coated tools was analyzed with respect to the tool life, tool wear, and surface roughness undergoing high-speed turning under a dry environment. The following conclusions can be drawn based on this analysis:

1. Based on the ANOVA results, it was found that the feed rate, cutting speed, and tool type significantly influence both the tool life and surface roughness. The feed rate exhibited the highest percentage contributions of 46.22% and 68.96% for tool life and surface roughness, respectively, thereby establishing it as the most influential parameter in this study. However, the cutting depth, with a high *p*-value (>0.05), was found to be insignificant for both response variables.
2. The highest tool lives of 14.75 min and 10.08 min were obtained at a low cutting speed (300 m/min) and low feed rate (0.05 mm/rev) for CVD- and PVD-coated tools, respectively. The wear progression graph for both tools skewed towards the left as the machining speed and feed rate increased. Additionally, optical microscopic images captured at different time intervals of the worn tool indicated that the CVD-coated tool with the Al_2O_3/TiCN coating protected the tool from thermal–mechanical loads, thus maintaining the cutting-edge geometry, despite high flank wear width at the end of the tool life. Conversely, the PVD tool with the TiAlN/AlCrN coating exhibited excessive chipping in the early phases of cutting, resulting in a comparatively shorter tool life.
3. SEM and EDX analysis revealed that adhesion, oxidation, and abrasion constituted the primary wear mechanisms for both types of tools. Furthermore, excessive chipping on the main cutting edge and severe diffusion on the crater face were also identified as contributing factors to the wear mechanisms in the case of PVD-coated tools.
4. The best surface roughness of 0.276 μm and 0.307 μm was achieved at a high cutting speed and low feed rate for both PVD and CVD tools, respectively. Remarkably,

the CVD-coated tool exhibited the most favorable outcomes in terms of low surface roughness due to the reduced thermal conductivity of the Al_2O_3/TiCN coating, which notably reduced the coefficient of friction.

5. From the perspective of future research, a more comprehensive understanding of tool wear mechanisms can be achieved by analyzing the cutting force, chip formation, and cutting temperature. This deeper knowledge is crucial for optimizing the tool life and surface integrity in high-speed machining applications. Additionally, emerging trends in the field of tool coating, for instance, advanced multilayer composite coatings and nano-structural hard coatings, can offer outstanding tribological features and wear resistance to cutting tools. Thus, research in this domain can improve the cutting performances of the PVD- and CVD-coated tools during the machining of high-strength steel. Lastly, the cost quantification and sustainability assessment of coated carbide tools in machining high-strength steel could demonstrate significant economic and environmental benefits, motivating manufacturers to implement these tools in wide-scale industrial applications.

Author Contributions: S.Y.: Methodology, investigation, data curation, writing—original draft. J.A.G.: Methodology, investigation, data curation, writing—review and editing, supervision. N.J.: Writing—review and editing, funding acquisition. A.Z.J.: Writing—review and editing, supervision. All authors have read and agreed to the published version of the manuscript.

Funding: The authors extend their appreciation to Prince Sattam bin Abdulaziz University for funding this research, with project number (PSAU/2024/01/29747).

Institutional Review Board Statement: Not applicable.

Informed Consent Statement: Not applicable.

Data Availability Statement: Data are contained within the article.

Conflicts of Interest: The authors declare no conflicts of interest.

References

1. Musavi, S.H.; Davoodi, B. Risk Assessment for Hazardous Lubricants in Machining Industry. *Environ. Sci. Pollut. Res.* **2021**, *28*, 625–634. [CrossRef]
2. Naveed, M.; Arslan, A.; Javed, H.M.A.; Manzoor, T.; Quazi, M.M.; Imran, T.; Zulfattah, Z.M.; Khurram, M.; Fattah, I.M.R. State-of-the-Art and Future Perspectives of Environmentally Friendly Machining Using Biodegradable Cutting Fluids. *Energies* **2021**, *14*, 4816. [CrossRef]
3. Bagaber, S.A.; Yusoff, A.R. Multi-Objective Optimization of Cutting Parameters to Minimize Power Consumption in Dry Turning of Stainless Steel 316. *J. Clean. Prod.* **2017**, *157*, 30–46. [CrossRef]
4. Yaqoob, S.; Ghani, J.A.; Juri, A.Z.; Muhamad, S.S.; Haron, C.H.C.; Jouini, N. A Review of Sustainable Hybrid Lubrication (Cryo-MQL) Techniques in Machining Processes. *Int. J. Adv. Manuf. Technol.* **2024**, *131*, 151–169. [CrossRef]
5. Dedalus Consulting. Global Market Research End User Analysis Database. 2022. Available online: https://www.dedalusconsulting.com/index.php (accessed on 20 January 2024).
6. Boing, D.; De Oliveira, A.J.; Schroeter, R.B. Evaluation of Wear Mechanisms of PVD and CVD Coatings Deposited on Cemented Carbide Substrates Applied to Hard Turning. *Int. J. Adv. Manuf. Technol.* **2020**, *106*, 5441–5451. [CrossRef]
7. Dabees, S.; Mirzaei, S.; Kaspar, P.; Holcman, V.; Sobola, D. Characterization and Evaluation of Engineered Coating Techniques for Different Cutting Tools—Review. *Materials* **2022**, *15*, 5633. [CrossRef]
8. Sousa, V.F.C.; Silva, F.J.G. Recent Advances in Turning Processes Using Coated Tools—A Comprehensive Review. *Metals* **2020**, *10*, 170. [CrossRef]
9. Panjan, P.; Drnovšek, A.; Terek, P.; Miletić, A.; Čekada, M.; Panjan, M. Comparative Study of Tribological Behavior of TiN Hard Coatings Deposited by Various PVD Deposition Techniques. *Coatings* **2022**, *12*, 294. [CrossRef]
10. Von Fieandt, L.; Johansson, K.; Larsson, T.; Boman, M.; Lindahl, E. On the Growth, Orientation and Hardness of Chemical Vapor Deposited Ti (C, N). *Thin Solid Film.* **2018**, *645*, 19–26. [CrossRef]
11. Chinchanikar, S.; Choudhury, S.K. Wear Behaviors of Single-Layer and Multi-Layer Coated Carbide Inserts in High Speed Machining of Hardened AISI 4340 Steel. *J. Mech. Sci. Technol.* **2013**, *27*, 1451–1459. [CrossRef]
12. Feng, R.; Pan, J.; Zhang, J.; Shao, Y.; Chen, B.; Fang, Z.; Roy, K.; Lim, J.B.P. Effects of Corrosion Morphology on the Fatigue Life of Corroded Q235B and 42CrMo Steels: Numerical Modelling and Proposed Design Rules. *Structures* **2023**, *57*, 105136. [CrossRef]
13. Feng, R.; Yang, F.; Shao, Y.; Roy, K.; Lim, J.; Chen, B. Experimental Study on High-Cycle Fatigue Behaviour of Butt Welds Made of Corroded AISI 304 Stainless Steel and Q460 High-Strength Steel. *Structures* **2024**, *62*, 106141. [CrossRef]

14. Muhamad, S.S.; Ghani, J.A.; Che Haron, C.H.; Yazid, H. Wear Mechanism of Multilayer Coated Carbide Cutting Tool in the Milling Process of AISI 4340 under Cryogenic Environment. *Materials* **2022**, *15*, 524. [CrossRef] [PubMed]
15. Yap, P.H.; Ghani, J.A.; Wan Mahmood, W.M.F. Optimisation on the Performance of Bubble-Bursting Atomisation for Minimum Quantity Lubrication with Vegetable Oil Using Computational Fluid Dynamics Simulation. *Materials* **2022**, *15*, 4355. [CrossRef] [PubMed]
16. Abu Bakar, H.N.; Ghani, J.A.; Haron, C.H.C.; Ghazali, M.J.; Kasim, M.S.; Al-Zubaidi, S.; Jouini, N. Wear Mechanisms of Solid Carbide Cutting Tools in Dry and Cryogenic Machining of AISI H13 Steel with Varying Cutting-Edge Radius. *Wear* **2023**, *523*, 204758. [CrossRef]
17. Xu, Q.; Zhao, J.; Ai, X. Cutting Performance of Tools Made of Different Materials in the Machining of 42CrMo4 High-Strength Steel: A Comparative Study. *Int. J. Adv. Manuf. Technol.* **2017**, *93*, 2061–2069. [CrossRef]
18. Ahmad, A.A.; Ghani, J.A.; Che Haron, C.H. Effect of Cutting Parameters on Tool Life during End Milling of AISI 4340 under MQL Condition. *Ind. Lubr. Tribol.* **2022**, *74*, 392–401. [CrossRef]
19. Yang, W.; Xiong, J.; Guo, Z.; Du, H.; Yang, T.; Tang, J.; Wen, B. Structure and Properties of PVD TiAlN and TiAlN/CrAlN Coated Ti (C, N)-Based Cermets. *Ceram. Int.* **2017**, *43*, 1911–1915. [CrossRef]
20. Kenzhegulov, A.; Mamaeva, A.; Panichkin, A.; Alibekov, Z.; Kshibekova, B.; Bakhytuly, N.; Wieleba, W. Comparative Study of Tribological and Corrosion Characteristics of TiCN, TiCrCN, and TiZrCN Coatings. *Coatings* **2022**, *12*, 564. [CrossRef]
21. Li, Y.; Zheng, G.; Cheng, X.; Yang, X.; Xu, R.; Zhang, H. Cutting Performance Evaluation of the Coated Tools in High-Speed Milling of AISI 4340 Steel. *Materials* **2019**, *12*, 3266. [CrossRef]
22. Das, A.; Patel, S.K.; Hotta, T.K.; Biswal, B.B. Statistical Analysis of Different Machining Characteristics of EN-24 Alloy Steel during Dry Hard Turning with Multilayer Coated Cermet Inserts. *Measurement* **2019**, *134*, 123–141. [CrossRef]
23. Zheng, G.; Cheng, X.; Li, L.; Xu, R.; Tian, Y. Experimental Investigation of Cutting Force, Surface Roughness and Tool Wear in High-Speed Dry Milling of AISI 4340 Steel. *J. Mech. Sci. Technol.* **2019**, *33*, 341–349. [CrossRef]
24. Davoodi, B.; Eskandari, B. Tool Wear Mechanisms and Multi-Response Optimization of Tool Life and Volume of Material Removed in Turning of N-155 Iron–Nickel-Base Superalloy Using RSM. *Measurement* **2015**, *68*, 286–294. [CrossRef]
25. Sonawane, G.D.; Sargade, V.G. Machinability Study of Duplex Stainless Steel 2205 During Dry Turning. *Int. J. Precis. Eng. Manuf.* **2020**, *21*, 969–981. [CrossRef]
26. Bag, R.; Panda, A.; Sahoo, A.K.; Kumar, R. Sustainable High-Speed Hard Machining of AISI 4340 Steel under Dry Environment. *Arab. J. Sci. Eng.* **2022**, *48*, 3073–3096. [CrossRef]
27. Alok, A.; Kumar, A.; Das, M. Hard Turning with a New HSN2-Coated Carbide Insert and Optimization of Process Parameter. *Trans. Indian. Inst. Met.* **2021**, *74*, 1577–1591. [CrossRef]
28. Kumar, S.; Singh, D.; Kalsi, N.S. Performance Evaluation of TiN-Coated CBN Tools During Turning of Variable Hardened AISI 4340 Steel. In *Advanced Engineering Optimization through Intelligent Techniques*; Venkata Rao, R., Taler, J., Eds.; Advances in Intelligent Systems and Computing; Springer: Singapore, 2020; Volume 949, pp. 847–857. ISBN 9789811381959.
29. Singh, R.; Dureja, J.S.; Dogra, M. Performance Evaluation of Textured Carbide Tools under Environment-Friendly Minimum Quantity Lubrication Turning Strategies. *J. Braz. Soc. Mech. Sci. Eng.* **2019**, *41*, 87. [CrossRef]
30. Jafarian Zenjanab, M.; Pedrammehr, S.; Chalak Qazani, M.R.; Shabgard, M.R. Influence of Cutting Fluid-Based CuO-Nanofluid with Boric Acid-Nanoparticles Additives on Machining Performances of AISI 4340 Tool Steel in High-Speed Turning Operation. *Iran. J. Sci. Technol. Trans. Mech. Eng.* **2022**, *46*, 335–345. [CrossRef]
31. Shalaby, M.; Veldhuis, S. New Observations on High-Speed Machining of Hardened AISI 4340 Steel Using Alumina-Based Ceramic Tools. *J. Manuf. Mater. Process.* **2018**, *2*, 27. [CrossRef]
32. Suyama, D.I.; Diniz, A.E. Influence of Tool Vibrations on Tool Wear Mechanisms in Internal Turning of Hardened Steel. *J. Braz. Soc. Mech. Sci. Eng.* **2020**, *42*, 370. [CrossRef]
33. Da Silva, L.R.; Couto, D.A.; Dos Santo, F.V.; Duarte, F.J.; Mazzaro, R.S.; Veloso, G.V. Evaluation of Machined Surface of the Hardened AISI 4340 Steel through Roughness and Residual Stress Parameters in Turning and Grinding. *Int. J. Adv. Manuf. Technol.* **2020**, *107*, 791–803. [CrossRef]
34. Tang, S.; Liu, P.; Su, Z.; Lei, Y.; Liu, Q.; Liu, D. Preparation and Cutting Performance of Nano-Scaled Al_2O_3-Coated Micro-Textured Cutting Tool Prepared by Atomic Layer Deposition. *High Temp. Mater. Process.* **2021**, *40*, 77–86. [CrossRef]
35. Gupta, K.M.; Ramdev, K.; Dharmateja, S.; Sivarajan, S. Cutting Characteristics of PVD Coated Cutting Tools. *Mater. Today Proc.* **2018**, *5*, 11260–11267. [CrossRef]
36. Alaksanasuwan, S.; Buranawong, A.; Witit-Anun, N. Preparation and Characterization of Nanostructured TiCrN Thin Films Deposited from Ti-Cr Mosaic Target by Reactive DC Magnetron Sputtering. *J. Phys. Conf. Ser.* **2021**, *1719*, 012072. [CrossRef]
37. *ISO 3685:1993*; Tool-Life Testing with Single-Point Turning Tools. International Organization for Standardization (ISO): Geneva, Switzerland, 1993.
38. Sumitomo, E. Sumitomo Cutting Tools General Catalog 2023–2024. 2023. Available online: https://www.sumitool.com/en/downloads/cutting-tools/general-catalog (accessed on 15 August 2023).
39. López-Luiz, N.; Alemán, O.J.; Hernández, F.A.; Dávila, M.M.; Baltazar-Hernández, V.H. Experimentation on Tool Wear and Surface Roughness in AISI D2 Steel Turning with WC Insert. *Mod. Mech. Eng.* **2018**, *8*, 204–220. [CrossRef]
40. Fedai, Y. Exploring the Impact of the Turning of AISI 4340 Steel on Tool Wear, Surface Roughness, Sound Intensity, and Power Consumption under Dry, MQL, and Nano-MQL Conditions. *Lubricants* **2023**, *11*, 442. [CrossRef]

41. Mia, M.; Dey, P.R.; Hossain, M.S.; Arafat, M.T.; Asaduzzaman, M.; Ullah, M.S.; Zobaer, S.T. Taguchi S/N Based Optimization of Machining Parameters for Surface Roughness, Tool Wear and Material Removal Rate in Hard Turning under MQL Cutting Condition. *Measurement* **2018**, *122*, 380–391. [CrossRef]
42. Butt, M.M.; Najar, K.A.; Dar, T.H. Experimental Evaluation of Multilayered CVD-and PVD-Coated Carbide Turning Inserts in Severe Machining of AISI-4340 Steel Alloy. *J. Tribol.* **2021**, *29*, 117–143.
43. Li, Y.; Zheng, G.; Zhang, X.; Cheng, X.; Yang, X.; Xu, R. Cutting Force, Tool Wear and Surface Roughness in High-Speed Milling of High-Strength Steel with Coated Tools. *J. Mech. Sci. Technol.* **2019**, *33*, 5393–5398. [CrossRef]
44. Xian, G.; Xiong, J.; Zhao, H.; Xian, L.; Fan, H.; Li, Z.; Du, H. Study on the Growth and Wear Behavior of the TiAlN-Based Composite Coating Deposited on TiCN-Based Cermets with Different Binder Phase. *Wear* **2020**, *460–461*, 203460. [CrossRef]
45. Bartosik, M.; Daniel, R.; Mitterer, C.; Keckes, J. Thermally-Induced Formation of Hexagonal AlN in AlCrN Hard Coatings on Sapphire: Orientation Relationships and Residual Stresses. *Surf. Coat. Technol.* **2010**, *205*, 1320–1323. [CrossRef]
46. Stylianou, R.; Velic, D.; Daves, W.; Ecker, W.; Tkadletz, M.; Schalk, N.; Czettl, C.; Mitterer, C. Thermal Crack Formation in TiCN/α-Al_2O_3 Bilayer Coatings Grown by Thermal CVD on WC-Co Substrates with Varied Co Content. *Surf. Coat. Technol.* **2020**, *392*, 125687. [CrossRef]
47. Kone, F.; Czarnota, C.; Haddag, B.; Nouari, M. Finite Element Modelling of the Thermo-Mechanical Behavior of Coatings under Extreme Contact Loading in Dry Machining. *Surf. Coat. Technol.* **2011**, *205*, 3559–3566. [CrossRef]
48. Samani, M.K.; Chen, G.C.K.; Ding, X.Z.; Zeng, X.T. Thermal Conductivity of CrAlN and TiAlN Coatings Deposited by Lateral Rotating Cathode Arc. *Key Eng. Mater.* **2010**, *447–448*, 705–709. [CrossRef]
49. Reis, B.C.M.; Dos Santos, A.J.; Dos Santos, N.F.P.; Câmara, M.A.; De Faria, P.E.; Abrão, A.M. Cutting Performance and Wear Behavior of Coated Cermet and Coated Carbide Tools When Turning AISI 4340 Steel. *Int. J. Adv. Manuf. Technol.* **2019**, *105*, 1655–1663. [CrossRef]
50. Das, A.; Gupta, M.K.; Das, S.R.; Panda, A.; Patel, S.K.; Padhan, S. Hard Turning of AISI D6 Steel with Recently Developed HSN2-TiAlxN and Conventional TiCN Coated Carbide Tools: Comparative Machinability Investigation and Sustainability Assessment. *J. Braz. Soc. Mech. Sci. Eng.* **2022**, *44*, 138. [CrossRef]
51. Patil, P.; Karande, P. Performance Analysis of Twin-Layer AlTiN and TiCN Coated Inserts during High Speed Turning of SS304 with Synthetic Coolant at 0 °C. *Tribol.—Mater. Surf. Interfaces* **2024**, *18*, 53–62. [CrossRef]
52. Bjerke, A.; Lenrick, F.; Norgren, S.; Larsson, H.; Markström, A.; M'Saoubi, R.; Petrusha, I.; Bushlya, V. Understanding Wear and Interaction between CVD α-Al_2O_3 Coated Tools, Steel, and Non-Metallic Inclusions in Machining. *Surf. Coat. Technol.* **2022**, *450*, 128997. [CrossRef]
53. Hassan, S.; Khan, S.A.; Naveed, R.; Saleem, M.Q.; Mufti, N.A.; Farooq, M.U. Investigation on Tool Wear Mechanisms and Machining Tribology of Hardened DC53 Steel through Modified CBN Tooling Geometry in Hard Turning. *Int. J. Adv. Manuf. Technol.* **2023**, *127*, 547–564. [CrossRef]
54. Saleem, M.Q.; Mumtaz, S. Face Milling of Inconel 625 via Wiper Inserts: Evaluation of Tool Life and Workpiece Surface Integrity. *J. Manuf. Process.* **2020**, *56*, 322–336. [CrossRef]

Disclaimer/Publisher's Note: The statements, opinions and data contained in all publications are solely those of the individual author(s) and contributor(s) and not of MDPI and/or the editor(s). MDPI and/or the editor(s) disclaim responsibility for any injury to people or property resulting from any ideas, methods, instructions or products referred to in the content.

coatings

MDPI

Article

Friction and Wear Behavior of 3D-Printed Inconel 718 Alloy under Dry Sliding Conditions

Ioannis Karagiannidis [1,*], Athanasios Tzanis [2,3,*], Dirk Drees [4], Lais Lopes [4], Georgios Chondrakis [2], Maria Myrto Dardavila [3], Emmanuel Georgiou [1] and Angelos Koutsomichalis [1]

[1] Laboratory of Materials, Hellenic Airforce Academy, Dekelia Air Base, 13671 Acharnes, Attikis, Greece; emmanouil.georgiou@hafa.haf.gr (E.G.); a.koutsomichalis@gmail.com (A.K.)
[2] Laboratory of Materials, Electronics Depot-R&T Centre, 16562 Glyfada, Attikis, Greece; geochondrakis@gmail.com
[3] Laboratory of General Chemistry, School of Chemical Engineering, National Technical University of Athens, 15772 Zografou, Attikis, Greece; mirtodar@mail.ntua.gr
[4] Falex Tribology NV, Wingepark 23B, 3110 Rotselaar, Belgium; ddrees@falex.eu (D.D.); lais.lopes@falex.eu (L.L.)
* Correspondence: johnkarag5@gmail.com (I.K.); ttzanis@hotmail.com (A.T.)

Abstract: Tailor-made materials used for advanced applications are nowadays of great research interest in various industrial and technological fields, ranging from aerospace and automotive applications to consumer goods and biomedical components. In the present research, Inconel 718 superalloy specimens were fabricated by the selective laser melting (SLM) technique. Structural characterization of the 3D-printed samples showed that they consisted of γ solid solution along with spherical carbide particles. To explore the applicability of these materials in abrasive tribological applications, reciprocating sliding tests were performed under dry conditions versus an Al_2O_3 counter-body. A 3D representation (triboscopy) of the tangential force during each sliding cycle was carried out in order to obtain better insight on the evolution of friction and to visualize localized tribological phenomena. Quantification of wear was performed with confocal microscopy and the wear mechanisms were analyzed with SEM and EDS techniques. Furthermore, the effect of surface finishing (as-printed and polished) on friction and wear were also investigated, and a comparison with other industrial materials is also included to evaluate the applicability of these alloys. The results indicated that surface finishing had an effect on friction during the run-in stage, whereas in steady-state conditions, no significant differences were observed between the as-printed and polished specimens. In all cases, the main wear mechanisms observed were a mixture of two-body and three-body abrasion, along with oxidative wear (indicated by the formation of an oxide-based tribo-layer).

Keywords: Inconel 718; selective laser melting; triboscopy; wear; friction

1. Introduction

Additive manufacturing (AM) has emerged as a modern manufacturing method since its introduction in the late 1990s [1]. Despite being relatively young, AM has rapidly evolved, becoming a versatile technique applicable to various materials [2]. Nowadays, it is widely recognized as a promising approach for fabricating complex mechanical components across diverse industrial sectors, including aerospace, automotive, civil engineering, and biomedical fields [3]. Selective laser melting (SLM) has gained prominence among AM methods for its ability to produce intricate metallic parts [4]. However, a notable drawback of SLM is the presence of defects, often necessitating post-processing thermal treatments [5].

However, despite these existing drawbacks, SLM metal printing has revolutionized the materials manufacturing industry, particularly in aeronautics, by enabling the creation of lightweight, high-strength components that are crucial for enhancing performance, fuel efficiency, and safety [6]. On a daily basis, engineers utilize this technology to design and

produce components with challenging geometries and improved mechanical properties, while at the same time achieving a reduction in weight without compromising structural integrity [7]. Additionally, it facilitates rapid prototyping and iteration, accelerating innovation and reducing development time for new aerospace components [8], whereas at the same time, it offers the flexibility to produce on-demand and low-volume parts, eliminating the need for expensive tooling and long lead times associated with traditional manufacturing methods [9]. These features are of vital importance, especially for the aeronautical industry, where sourcing expensive spare parts can be challenging (e.g., due to aging phenomena and/or environmental degradation) and costly.

Among the various aeronautical materials, Inconel alloys hold a prominent position as they combine high temperature [10] and corrosion [11] resistance with excellent mechanical characteristics [12]. Thus, metal 3D-printing Inconel alloy components have great potential in the aeronautical industry as they offer design flexibility and enhance manufacturing versatility and efficiency. The most widely used Inconel alloy in AM is 718, as it finds applications in aircrafts, gas turbines, turbocharger rotors, and various other corrosive and structural contexts where temperatures reach up to approximately 700 °C [13]. The high research interest in this alloy is confirmed by the increased number of publications, focusing mainly on its mechanical properties, as explained in the review article of Hosseini and Popovich [13]. Extensive work has also been performed on the corrosion behavior of this alloy produced with different AM methods and tested under different environments and temperatures [14–18]. In addition, AM Inconel alloys are increasingly used in tribological applications [19]. Indeed, there are several recent articles on this topic concerning the tribological behavior of 3D-printed 718 Inconel alloys [20–26].

In these articles, the friction and wear of this material are evaluated under different conditions, including dry wear versus hard abrasive carbides [20], high temperatures [21], and lubricated environments [22]. The performance of the alloy was linked to both its intrinsic characteristics and structure, which are determined by the manufacturing conditions [23], as well as its ability to form oxide-based tribo-layers and debris in the contacting interface [24]. The presence of corrosive environments was also reported [25] to significantly affect and accelerate material loss, mainly due to the synergism between wear and corrosion phenomena. Currently, further optimization of tribological properties of AM 718 Inconel alloys is explored by performing various post-processing treatments such as nitriding [26], etc. However, there is still a lack of comprehensive information regarding the tribological performance of these alloys, especially in SLM-manufactured components. The main issue stems from the fact that friction and wear are systemic properties that depend on the contact geometry and conditions, counter-body, environment, etc. This means that results cannot be extrapolated from one tribo-system to another. Thus, this research article aims to establish a structure–property relationship and understand dominant wear mechanisms under dry reciprocating conditions, against an oxide abrasive countermaterial. The influence of surface finishing was also considered and studied via triboscopy analysis, whereas a comparison with other widely used industrial materials was also included to provide a direct tribological ranking of materials under the test conditions.

2. Materials and Methods

A commercially supplied Inconel 718 alloy powder, consisting of particles with spherical morphology and size ranging between 15 μm and 45 μm, was utilized to fabricate rectangular-shaped specimens (30 mm × 30 mm × 2 mm) with the SLM technique.

The SLM apparatus utilized for the additive manufacturing procedure was a Print Sharp 150, equipped with a single-mode fiber laser which operates in the IR region, at a power of 120 W, and a scanning speed of 1200 mm/s. During the manufacturing process, the chamber operated under an inert nitrogen atmosphere, while the building platform temperature was held constant at 60 °C. The residual oxygen level was kept below 500 ppm, as stated by the technical capabilities of the apparatus. The layer thickness and the hatch spacing were 30 μm

and 50 μm, respectively. The scanning strategy that was followed was stripes with horizontal orientation. The specimens were not subjected to subsequent heat treatment.

To investigate the microstructure of the material, a metallographic sample was prepared from cross-sections of the fabricated SLM specimens by grinding with SiC papers and polishing with 3 μm and 1 μm diamond suspension, followed by 0.1 μm aluminum oxide polishing. Finally, the metallographic sample was etched by swabbing with a chemical solution consisting of 60 mL of lactic acid, 20 mL of HNO_3, and 10 mL of HF.

The microstructure was investigated with optical microscopy (OM) and scanning electron microscopy (SEM, JEOL IT500LV, Tokyo, Japan), while the stoichiometry was analyzed with an energy-dispersive spectrometer (EDS, Oxford Instruments X-Max Extreme, Oxford, UK). The crystallographic structure was studied by means of the X-ray diffraction technique (XRD, Bruker D8 Advance, Ettlingen, Germany), operating with a CuK_α X-ray source (λ = 0.154 nm) and a step size of 0.1°.

Vickers microhardness measurements were performed by applying a load of 1 kg for a duration of 12 s with a Duramin-5 (Struers, Copenhagen, Denmark) apparatus. The average microhardness value was obtained from five indentations.

A ball-on-disk tribometer (BASALT-N2, TETRA, Ilmenau, Germany) was utilized to carry out the friction and wear reciprocating sliding experiments in ambient conditions. An Al_2O_3 ball (hardness 2000 HV0.5, Rα = 0.2 μm) with a diameter of 6 mm was utilized as a counter-body. The applied load was set at 10 N, the stroke length at 2 mm, and the speed at 20 mm/s. On each track, the friction experiment was repeated for 10,000 cycles. For the tribo-tests, two sets of surface finishing were considered; one was the as-prepared (Samples "A" and "B") and the other with surface finishing with SiC papers of 120, 320, 400, 600, 800, and 1200 grit (Samples "C" to "F"). For the polished specimens, four different samples were considered, and, on each sample, duplicate tribo-tests were performed. In addition, for the as-prepared specimens, two samples were evaluated again by carrying out duplicate tests.

To explore the applicability of the 3D-printed Inconel alloys, triplicate tribological tests were carried out for the same experimental conditions in order to have a direct and meaningful comparison with reference materials, namely commercially supplied 100Cr6 bearing steel, commercially supplied Ag-coated steel, electroless Ni-P-coated steel [27], electrodeposited hard Cr and Cr(III)-coated steels [27], and atmospheric plasma sprayed titania and chromia coatings [28].

A NanoFocus μSurf Explorer (NanoFocus AG, Oberhausen, Germany) confocal microscope was utilized to measure the surface roughness of the specimens prior to the friction test, as well as to carry out a subsequent wear depth analysis. Between 200 and 400 confocal images per second were acquired with a ×10 magnifying lens in order to fully resolve the topographical features, which were in the micrometer range. Finally, the wear mechanisms were analyzed with the SEM and EDS configuration described previously.

3. Results and Discussion

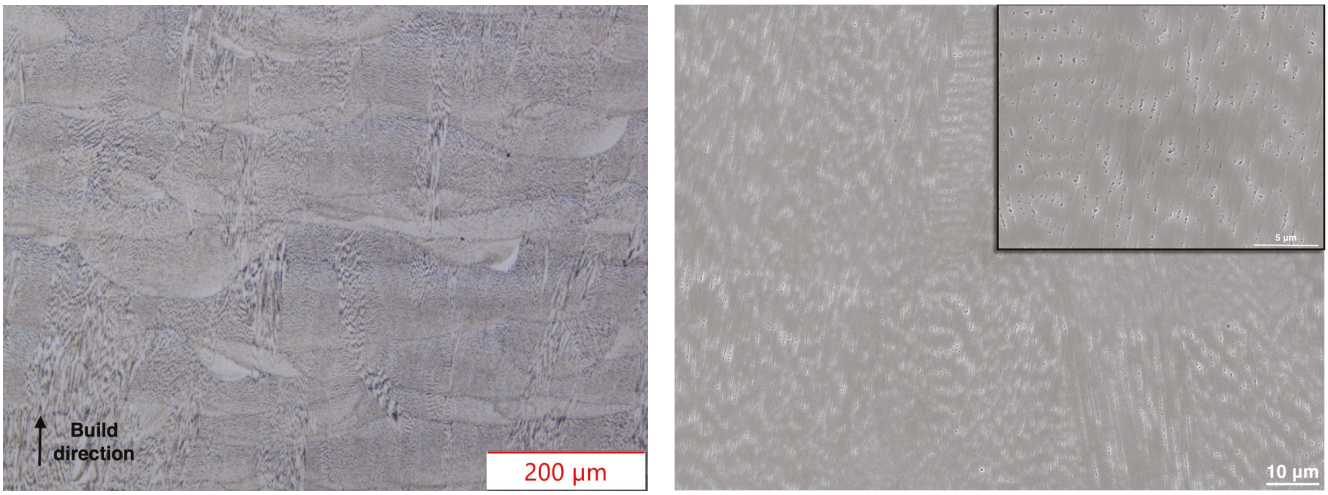
3.1. Specimen Characterization

The fabricated specimens have the typical stoichiometric composition (wt. %), which is presented in Table 1 along with the nominal composition of the nickel-based 718 superalloy according to aerospace material specification (AMS) 5662.

Table 1. Stoichiometric composition of the fabricated specimens.

Element	Ni	Cr	Nb	Mo	Ti	Al	Fe
Content in wt. %	52.5	19.5	5.2	2.9	1.1	0.7	Remainder
Nominal composition	50–55	17–21	4.8–5.5	2.8–3.3	0.7–1.2	0.2–0.8	Remainder

In Figure 1a, the OM microstructure of the specimens is represented after chemical etching. Melt pool boundaries, as well as columnar grains, can be seen in the OM micrograph, as it was also observed in as-prepared specimens by other scientific groups [29–32]. Black regions in Figure 1b correspond to carbides (likely of MC type), Laves phase, and defects (microporosity and non-fused regions) [29,30,32,33].



(**a**) (**b**)

Figure 1. As-prepared specimen: (**a**) optical micrograph; (**b**) SEM magnified micrographs.

The microhardness of the material was measured at 284 ± 15 HV, the typical value for the as-prepared AM 718 alloy [31,32].

As it is shown in the XRD spectrum in Figure 2, the as-prepared specimens show the diffracting peaks (111), (200), (220), (311), and (222) that are attributed to the γ solid solution [29].

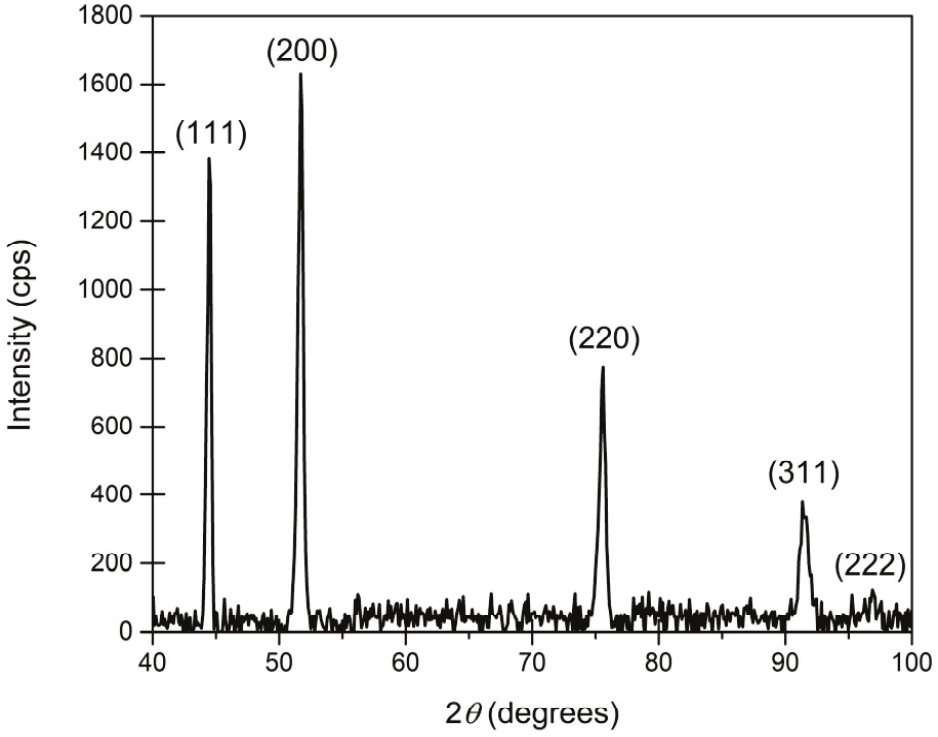
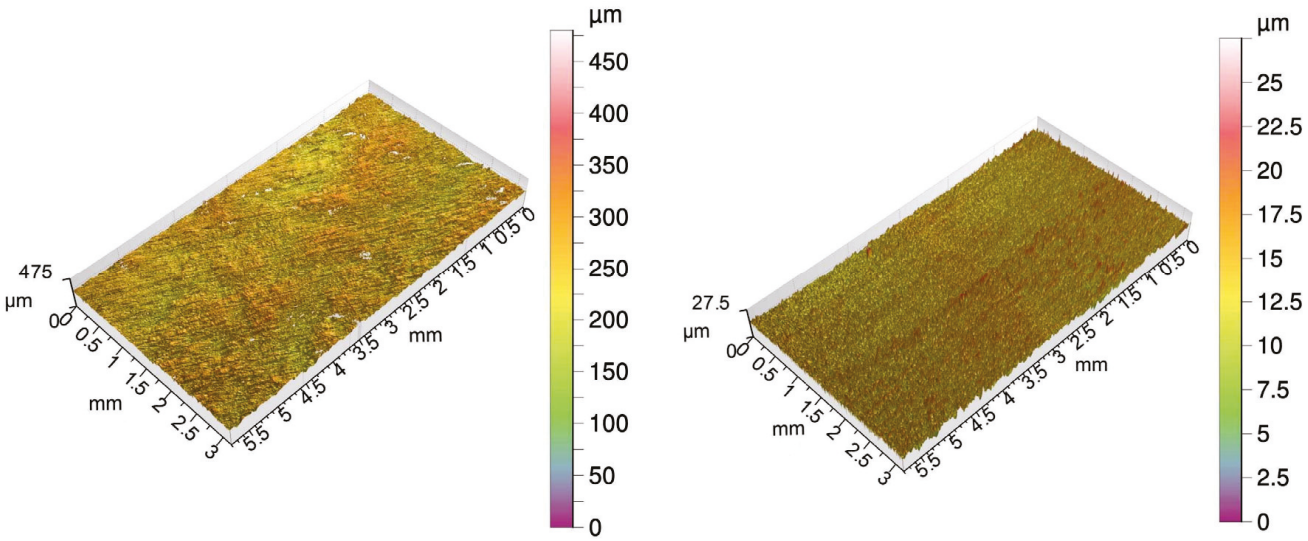


Figure 2. X-ray diffractogram of the SLM specimen.

SEM analysis did not reveal the strengthening phases of γ' and γ'' particles due to either their nanometer-scale size or their very small quantity. Also, from the diffractogram it can be derived that the γ' and γ'' phases were not distinguishable or detected due to the overlapping of their corresponding peaks with the ones of the γ phase and/or due to their concentration being below the detection limit of this method [34], possibly indicating a very small quantity in the prepared samples. Furthermore, according to the literature, the decreased microhardness values show that no strengthening mechanism is achieved. The aforementioned statements point towards the fact that the γ' and γ'' phases were either in very small quantity or not present in the as-prepared samples [33,35].

The surface roughness was measured both for the as-prepared and for the polished specimens prior to the friction experiment. Indicative 3D surface topographies are shown in Figure 3.



(**a**) (**b**)

Figure 3. Characteristic examples of the 3D surface roughness for the two types of specimens: (**a**) as-prepared; (**b**) polished.

The as-prepared specimens exhibit a mean surface roughness of 15.8 µm, whereas the polished ones show a much-reduced roughness with an average value of 1.56 µm.

The skewness and kurtosis parameters were derived from the surface roughness analysis. The as-prepared specimens exhibit a height distribution which was above the mean plane and almost normal, as it was derived from the skewness parameter Ssk and the kurtosis parameter Sku, which were −0.165 and 3.63, respectively. The values of Ssk and Sku for the polished specimens were −0.029 and 4.15, respectively, showing an almost symmetrical form around the mean plane and leptokurtic (spiked) height distribution.

3.2. Triboscopical Performance

The evolution of the coefficient of friction (COF) μ per cycle is depicted in Figure 4a for the as-prepared "A" and "B" specimens and in Figure 4b for the polished "C" to "F" specimens.

The COF of the polished specimens shows a smoother evolution per cycle compared to the as-prepared specimens, especially during the run-in stage. The higher fluctuation in the COF of the as-prepared samples is mainly ascribed to localized changes and/or reduction of the initial asperities [36], and to the generation of debris at the tribo-contact. However, the nature of run-in and COF fluctuations is often much more complicated as other factors such as sub-surface deformation and localized heating-up and oxidation are also associated [37]. To draw safe conclusions, post analysis of the wear tracks was performed to identify surface interactions and will be presented later on.

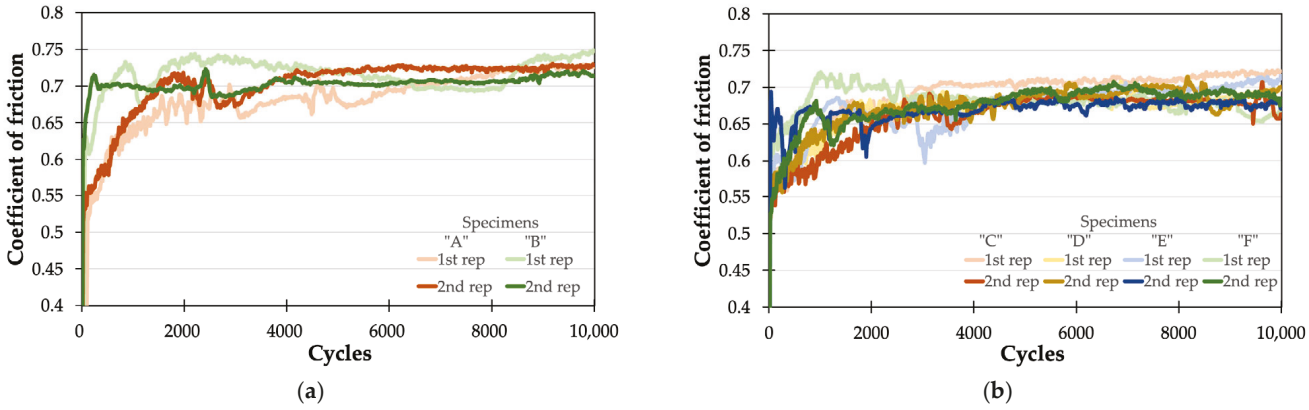


Figure 4. Evolution of the COF per cycle for the (**a**) as-prepared specimens and (**b**) polished specimens.

The as-prepared specimens presented an average COF value of $\mu = 0.709 \pm 0.016$, while the polished specimens had an average COF value of $\mu = 0.689 \pm 0.019$. For both types of specimens, the very low standard deviation from the average COF values shows a very good repeatability between the experiments. Furthermore, the two types of specimens show an almost identical steady-state value of COF.

In order to further evaluate the triboscopical properties of the two types of specimens, the evolution of friction force versus the displacement is plotted for each sliding cycle. Characteristic 3D curves for both types are presented in Figure 5.

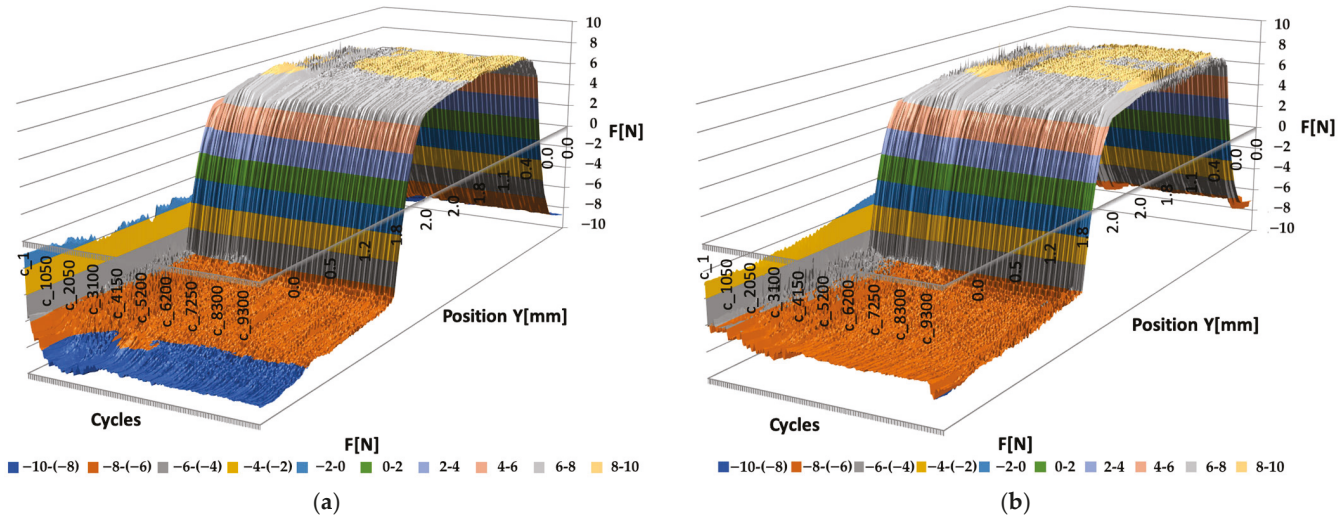
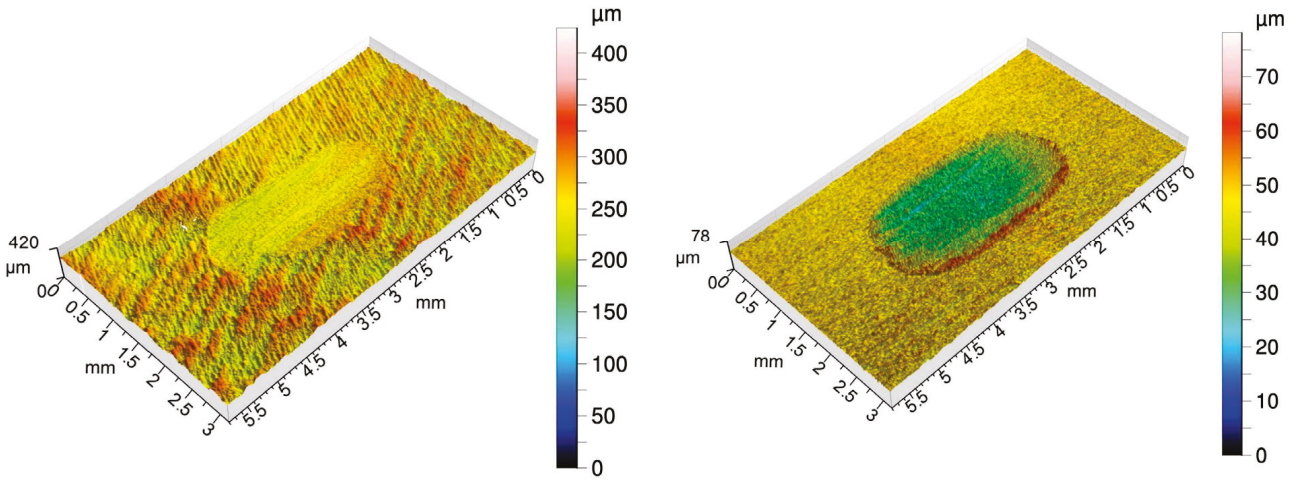


Figure 5. Indicative examples of 3D triboscopy patterns showing the evolution of frictional force during every sliding cycle for the (**a**) as-prepared specimen; (**b**) polished specimen.

Although both the as-prepared and the polished specimens have the same steady-state friction COF, they exhibit quite different transition behavior regarding the friction force. The early intense fluctuating phenomena are also depicted in the 3D triboscopical curve of the as-prepared specimen (Figure 5a). Furthermore, emphasizing at the as-prepared specimen, it was observed that peaks of friction force appear at the edges of the cycles, appearing in Figure 5a with blue color representing forces between −10 and −8 N. This increase in friction force is indicative of debris pile-up in the edges of the sliding track, which result in adhesion phenomena with the alumina counter-body. The high amount of debris can be ascribed to the much higher average roughness (one order of magnitude) and to the height distribution of the as-prepared specimen being skewed above the mean plane.

3.3. Wear Behavior

Indicative 3D confocal microscopy images for the as-prepared and polished specimens are presented in Figure 6.



(**a**) (**b**)

Figure 6. Three-dimensional confocal microscopy images of the wear track after the tribo-experiments of the (**a**) as-prepared specimen; (**b**) polished specimen.

The wear track of the as-prepared specimens exhibits a mean volume loss of 0.069 mm^3 and a mean depth from the surface of about 17.2 µm. Material pile-up at the edges of the wear track is observed by confocal microscopy and shows a mean volume above the surface of the specimen of about 0.023 mm^3 and a mean height above the surface of about 12.6 µm. In contrast, the wear tracks of the polished specimens show a mean volume loss of 0.03 mm^3 and a mean depth from the surface of about 7.7 µm. The debris pile-up shows a mean volume and height above the surface of about 0.006 mm^3 and 3.3 µm, respectively. It is deduced that an almost doubled wear loss accompanies the as-prepared specimens. As for the polished specimens, it should also be noted that the mean maximum values of depth (43.8 $\pm$ 7.3 µm) and height (30.8 $\pm$ 5.9 µm) distances from the surface show a good homogeneity. This case is not observed for the as-prepared specimens. In particular, the wear track in Figure 6a exhibits a maximum depth from the surface of about 250 µm and a maximum height of 166 µm, while the average values of the as-prepared specimens are 139.1 $\pm$ 77.5 µm and 93.4 $\pm$ 49.4 µm, respectively. This fact shows that the produced debris from the friction experiment are of higher amount and larger in size, and can damage the surface following three-body abrasion.

In order to obtain a more precise understanding of the wear behavior of the polished specimens in particular, SEM analysis was conducted at their corresponding wear tracks. Indicative micrographs are depicted in Figure 7.

Figure 7a is a backscatter electron micrograph near the edge of the wear track. Abrasive lines from the counter-body are clearly depicted in the wear groove. Areas of black color indicate the presence of lighter elements present in the surface. At such elongated black areas, the formation of parallel micro-cracks is observed, which are perpendicular to the sliding direction, indicating the growth of excessive strains during the reciprocating counter-body motion [38].

Figure 7b is a higher-magnification backscatter micrograph at the black areas spotted. EDS analysis performed at these black areas revealed a high increase in the oxygen concentration and a slight increase in aluminum content, indicating the formation of a mixture of oxides. In the secondary electron micrograph of Figure 7c, it can be observed that these oxidation products exhibit also a mud-cracking morphology [39] and appear to be adhered on the specimen's surface. The formation of oxides and their adhesion on the

specimen's surface indicate elevated temperatures during the reciprocating movement of the counter-body [40].

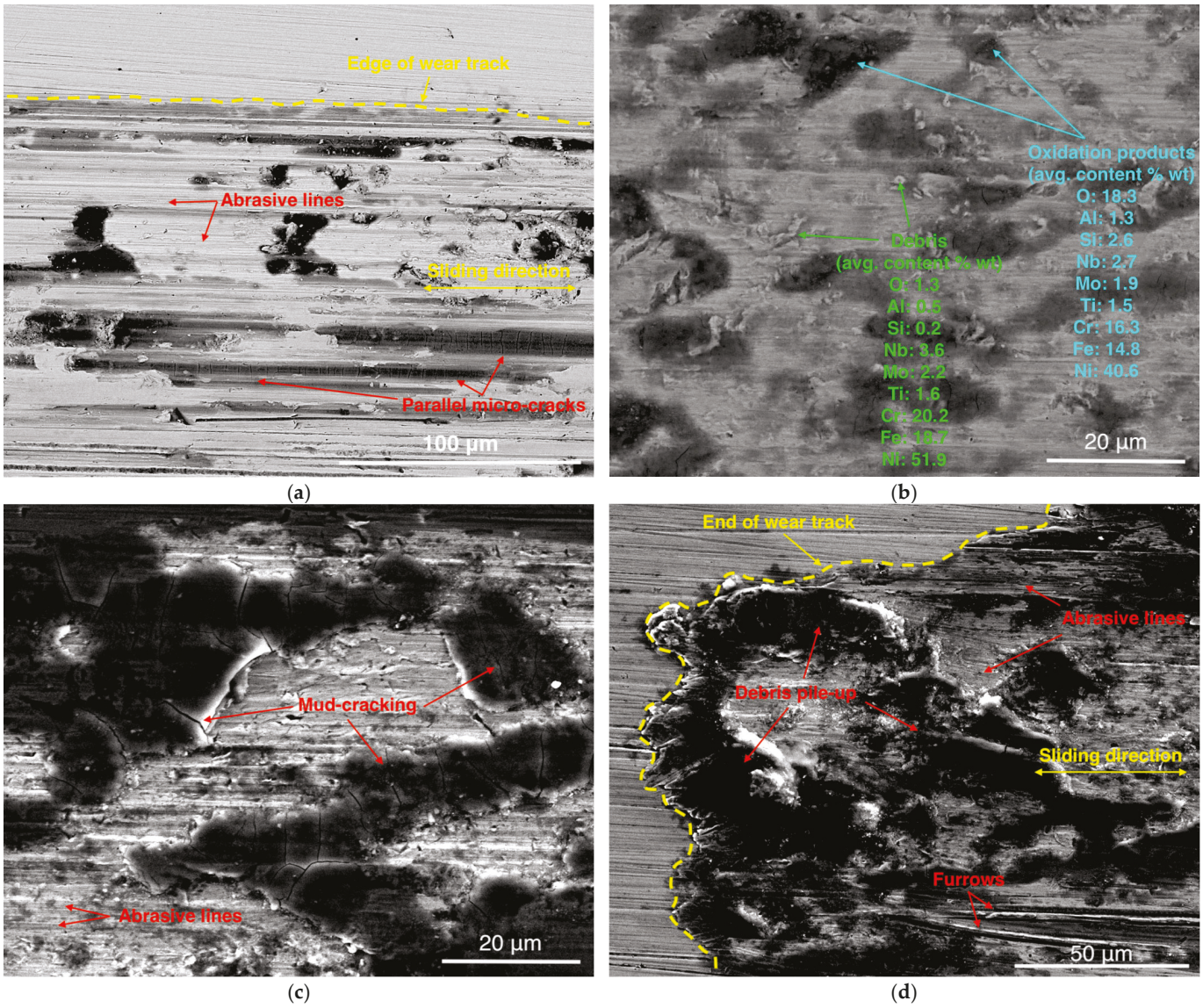


Figure 7. SEM micrographs of indicative areas in the wear track of the polished specimens: (**a**,**b**) backscatter electron micrographs; (**c**,**d**) secondary electron micrographs.

In the secondary electron image of Figure 7d, it can be observed that the specimen has undergone plastic deformation with material removal. There is debris pile-up at the end of the wear track. Also, abrasive lines are apparent in the wear groove, but also large furrows that point to the edge and have formed due to debris abrasion, indicative of the three-body abrasion wear mechanism.

To explore the applicability of the AM 718 Inconel alloy under dry sliding abrasive conditions, the friction (in steady-state conditions) and wear per cycle are compared to different reference materials used in tribological applications and tested under the same operating conditions (Figure 8). In terms of wear resistance, the AM printed alloy has similar wear resistance to the ceramic-based chromia- and titania-sprayed coatings which are made especially for abrasive applications, whereas it has superior wear resistance to conventional metallic-based materials and coatings. Only hard chrome coatings have clearly higher resistance, but these coatings are being restricted by the European Commission due to the negative environmental impact of hard chromium plating processes [41]. Further,

optimization of AM 718 Inconel alloy can potentially be an alternative to hard chrome coatings. Concerning friction, the majority of these materials have a high COF, which is due to the aggressive abrasive conditions, which result in the generation of debris particles in the tribo-contact. Indeed, it is known that the higher the amount of debris generated in the contact, the higher the friction [42]. Therefore, lubrication and/or further surface modification seem essential in order to reduce friction.

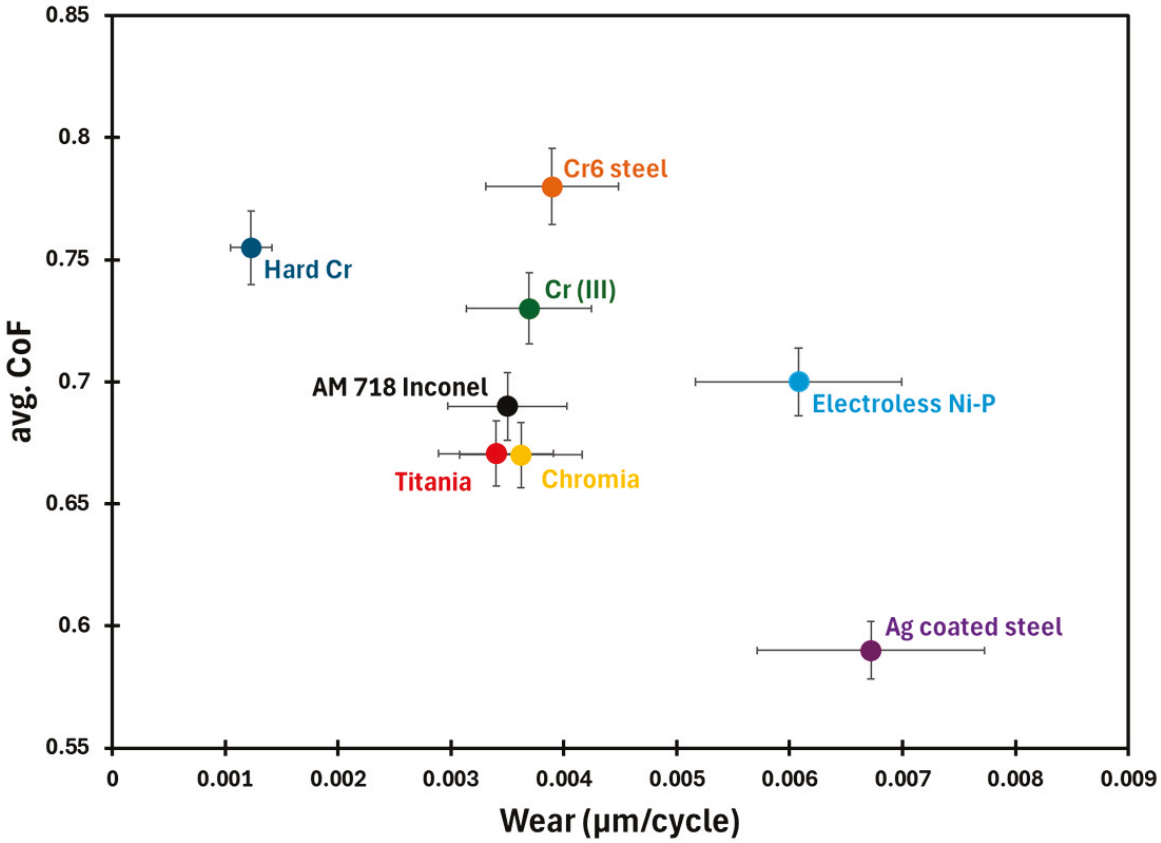


Figure 8. Comparison of average COF and wear per cycle between AM 718 Inconel and other industrial material.

Apart from lubrication, another approach to enhancing the tribological properties of additive manufactured (AM) materials is through advanced post-processing surface treatments. Recent review articles [43–46] have demonstrated that thermal, mechanical, and chemical post-treatments can significantly improve the surface properties of AM metallic parts. These enhancements are achieved by reducing surface roughness and residual stresses, altering the microstructure, and eliminating structural defects in the surface layers. A wide variety of surface post-treatments are now utilized, categorized by the intrinsic characteristics of the applied technology and the resultant effects on the AM part's surface [46]. These treatments include processes with and without material removal, coatings, and hybrid treatments. For AM post-processing of the 718 Inconel alloy, current notable treatments include heat treatments [47,48], shot peening [49], laser shock peening [50], finish machining (FM) [51], drag finishing (DF) [51], and vibratory surface finishing (VSF) [51]. When optimized processing conditions are applied [47,48,50,51], improvements in friction and wear performance can be achieved. However, the success and impact of these post-processes also depend on the tribo-chemistry, contact conditions, contact geometry, and environment of the tribo-system, as tribology is a systemic property [52]. Therefore, further research into post-processes and their influence on friction and wear is crucial for expanding the application of AM in industries where high-performance materials are essential.

4. Conclusions

The triboscopical properties of both as-prepared and polished SLM Inconel 718 specimens were examined in the present work.

OM, SEM, EDS, and XRD analysis show that the specimens have the typical microstructure and stoichiometry of an as-prepared AM nickel-based 718 superalloy. It should be noted that no further heat treatment was applied to the specimens. Confocal microscopy verified the finer surface roughness of the polished specimens.

Both types of specimens exhibit almost the same values of COF, namely 0.709 and 0.689 for the as-prepared and polished specimens, respectively. In comparison to the as-prepared specimens, the COF of the polished ones shows a relatively smoother transition during the run-in stage. Also, an almost halved wear volume was recorded for the polished specimens. From the SEM-EDS analysis, it was possible to address the existence of three wear mechanisms, namely abrasive (both two-body and three-body), adhesive, and oxidative wear.

Depending on the intended performance of the final product, as-prepared AM Inconel 718 materials are potential candidates for utilization in wear-resistant applications.

Surface polishing had an influence during the run-in stage, mainly due to topographical changes and the subsequent formation of debris in the tribo-contact. However, depending on the selected post-treatment, various topographical and/or structural changes can occur, and the surface properties may vary considerably. Thus, further research is needed to establish a better correlation between surface finishing processes such as remelting, shot or laser peening, etc., and their influence on the microstructure and properties (mechanical and/or electrochemical) of this AM alloy.

Author Contributions: Formal analysis, I.K., A.T. and A.K.; investigation, I.K., A.T., D.D., L.L., G.C., M.M.D. and E.G.; writing—original draft, I.K. and A.T.; writing—review and editing, E.G. and A.K. All authors have read and agreed to the published version of the manuscript.

Funding: This research received no external funding.

Institutional Review Board Statement: Not applicable.

Informed Consent Statement: Not applicable.

Data Availability Statement: Data are contained within the article.

Conflicts of Interest: The authors declare no conflicts of interest.

References

1. Afkhami, S.; Amraei, M.; Unt, A.; Piili, H.; Björk, T. *Metal Additive Manufacturing for Industrial Applications*; LUT University: Lappeenranta, Finland, 2021.
2. Gu, D.; Shi, X.; Poprawe, R.; Bourell, D.L.; Setchi, R.; Zhu, J. Material-structure-performance integrated laser-metal additive manufacturing. *Science* **2021**, *372*, 1487. [CrossRef] [PubMed]
3. Kant, R. *Modern Materials and Manufacturing Techniques*; CRC Press: Boca Raton, FL, USA, 2024.
4. Gao, B.; Zhao, H.; Peng, L.; Sun, Z. A review of research progress in selective laser melting (SLM). *Micromachines* **2022**, *14*, 57. [CrossRef]
5. Singla, A.K.; Banerjee, M.; Sharma, A.; Singh, J.; Bansal, A.; Gupta, M.K.; Khanna, N.; Shahi, A.S.; Goyal, D.K. Selective laser melting of Ti6Al4V alloy: Process parameters, defects and post-treatments. *J. Manuf. Process.* **2021**, *64*, 161–187. [CrossRef]
6. Bhate, D. *Design for Additive Manufacturing: Concepts and Considerations for the Aerospace Industry*; SAE International: Warrendale, PA, USA, 2018.
7. Raja, S.; Al-Tmimi, H.M.; Ghadir, G.K.; Mustafa, M.A.; Alani, Z.K.; Rusho, M.A.; Rajeswari, N. An analysis of polymer material selection and design optimization to improve Structural Integrity in 3D printed aerospace components. *Appl. Chem. Eng.* **2024**, *7*, 1875.
8. Madhavadas, V.; Srivastava, D.; Chadha, U.; Raj, S.A.; Sultan, M.T.H.; Shahar, F.S.; Shah, A.U.M. A review on metal additive manufacturing for intricately shaped aerospace components. *CIRP J. Manuf. Sci. Technol.* **2022**, *39*, 18. [CrossRef]
9. Jordan, J.M. *3D Printing*; MIT Press: Cambridge, MA, USA, 2019.
10. Greene, G.A.; Finfrock, C.C. Oxidation of Inconel 718 in air at high temperatures. *Oxid. Met.* **2001**, *55*, 505–521. [CrossRef]
11. Zhao, S.; Xie, X.; Smith, G.D.; Patel, S.J. Research and improvement on structure stability and corrosion resistance of nickel-base superalloy INCONEL alloy 740. *Mater. Des.* **2006**, *27*, 1120–1127. [CrossRef]

12. Shankar, V.; Rao, K.B.S.; Mannan, S.L. Microstructure and mechanical properties of Inconel 625 superalloy. *J. Nucl. Mater.* **2001**, *288*, 222–232. [CrossRef]
13. Hosseini, E.; Popovich, V.A. A review of mechanical properties of additively manufactured Inconel 718. *Addit. Manuf.* **2019**, *30*, 100877. [CrossRef]
14. Tang, Y.; Shen, X.; Liu, Z.; Qiao, Y.; Yang, L.; Lu, D.; Zou, J.; Xu, J. Corrosion behaviors of selective laser melted inconel 718 alloy in NaOH solution. *Acta Met. Sin.* **2021**, *58*, 324–333.
15. Zhang, Q.; Zhang, J.; Zhuang, Y.; Lu, J.; Yao, J. Hot corrosion and mechanical performance of repaired Inconel 718 components via laser additive manufacturing. *Materials* **2020**, *13*, 2128. [CrossRef] [PubMed]
16. Luo, S.; Huang, W.; Yang, H.; Yang, J.; Wang, Z.; Zeng, X. Microstructural evolution and corrosion behaviors of Inconel 718 alloy produced by selective laser melting following different heat treatments. *Addit. Manuf.* **2019**, *30*, 100875. [CrossRef]
17. Zhang, L.N.; Ojo, O.A. Corrosion behavior of wire arc additive manufactured Inconel 718 superalloy. *J. Alloys Compd.* **2020**, *829*, 154455. [CrossRef]
18. Sanviemvongsak, T.; Monceau, D.; Desgranges, C.; Macquaire, B. Intergranular oxidation of Ni-base alloy 718 with a focus on additive manufacturing. *Corros. Sci.* **2020**, *170*, 108684. [CrossRef]
19. Ur Rahman, N.; Matthews, D.T.A.; De Rooij, M.; Khorasani, A.M.; Gibson, I.; Cordova, L.; Römer, G.W. An overview: Laser-based additive manufacturing for high temperature tribology. *Front. Mech. Eng.* **2019**, *5*, 16. [CrossRef]
20. Basha, M.M.; Sankar, M.R. Experimental tribological study on additive manufactured Inconel 718 features against the hard carbide counter bodies. *J. Tribol.* **2023**, *145*, 121702. [CrossRef]
21. Peng, J.; Lv, X.; Lu, Z.; Liu, X.; Li, Z.; Xu, Z. Investigations of the mechanical and high-temperature tribological properties of the Inconel 718 alloy formed by selective laser melting. *Tribol. Int.* **2023**, *188*, 108813. [CrossRef]
22. Zhang, Y.; Pan, Q.; Yang, L.; Li, R.; Dai, J. Tribological behavior of IN718 superalloy coating fabricated by laser additive manufacturing. *Lasers Manuf. Mater. Process.* **2017**, *4*, 153–167. [CrossRef]
23. Tombakti, I.A.; Adesina, A.Y.; Alharith, A.; Attallah, M.M.; AlMangour, B. Effect of Laser Mode and Power on the Tribological Behavior of Additively Manufactured Inconel 718 Alloy. *J. Tribol.* **2023**, *145*, 101703. [CrossRef]
24. Basha, M.M.; Sankar, M.R.; Murthy, T.C.; Sahu, A.K.; Majumdar, S. Tribological Investigations on Additively Manufactured Inconel 718 Features with Silicon Carbide Ball: Role of the Tribo-Oxide Layer. *Tribol. Lett.* **2024**, *72*, 59. [CrossRef]
25. Siddaiah, A.; Kasar, A.; Kumar, P.; Akram, J.; Misra, M.; Menezes, P.L. Tribocorrosion behavior of inconel 718 fabricated by laser powder bed fusion-based additive manufacturing. *Coatings* **2021**, *11*, 195. [CrossRef]
26. Mondragón-Rodríguez, G.C.; Torres-Padilla, N.; Camacho, N.; Espinosa-Arbeláez, D.G.; de León-Nope, G.V.; González-Carmona, J.M.; Alvarado-Orozco, J.M. Surface modification and tribological behavior of plasma nitrided Inconel 718 manufactured via direct melting laser sintering method. *Surf. Coat. Technol.* **2020**, *387*, 125526. [CrossRef]
27. Georgiou, E.P.; Drees, D.; Timmermans, G.; Zoikis-Karathanasis, A.; Pérez-Fernández, M.; Magagnin, L.; Celis, J.-P. High Performance Accelerated Tests to Evaluate Hard Cr Replacements for Hydraulic Cylinders. *Coatings* **2021**, *11*, 1511. [CrossRef]
28. Koutsomichalis, A.; Lontos, A.; Loukas, G.; Vardavoulias, M.; Vaxevanidis, N. Fatigue behaviour of plasma sprayed titania and chromia coatings. *MATEC Web Conf.* **2021**, *349*, 02009. [CrossRef]
29. Calandri, M.; Yin, S.; Aldwell, B.; Calignano, F.; Lupoi, R.; Ugues, D. Texture and microstructural features at different length scales in Inconel 718 produced by selective laser melting. *Materials* **2019**, *12*, 1293. [CrossRef]
30. Moussaoui, K.; Rubio, W.; Mousseigne, M.; Sultan, T.; Rezai, F. Effects of Selective Laser Melting additive manufacturing parameters of Inconel 718 on porosity, microstructure and mechanical properties. *Mater. Sci. Eng. A* **2018**, *735*, 182–190. [CrossRef]
31. Zhao, J.-R.; Hung, F.-Y.; Lui, T.-S. Microstructure and tensile fracture behavior of three-stage heat treated Inconel 718 alloy produced via laser powder bed fusion process. *J. Mater. Res. Technol.* **2020**, *9*, 3357–3367. [CrossRef]
32. Popovich, V.A.; Borisov, E.V.; Heurtebise, V.; Riemslag, T.; Popovich, A.A.; Sufiiarov, V.S. Creep and thermomechanical fatigue of functionally graded Inconel 718 produced by additive manufacturing. In *TMS 2018 147th Annual Meeting & Exhibition Supplemental Proceedings*; Springer International Publishing: Cham, Switzerland, 2018; pp. 85–97.
33. Popovich, V.A.; Borisov, E.V.; Popovich, A.A.; Sufiiarov, V.S.; Masaylo, D.V.; Alzina, L. Impact of heat treatment on mechanical behaviour of Inconel 718 processed with tailored microstructure by selective laser melting. *Mater. Des.* **2017**, *131*, 12–22. [CrossRef]
34. Khan, H.; Yerramilli, A.S.; D'Oliveira, A.; Alford, T.L.; Boffito, D.C.; Patience, G.S. Experimental methods in chemical engineering: X-ray diffraction spectroscopy-XRD. *Can. J. Chem. Eng.* **2020**, *98*, 1255–1266. [CrossRef]
35. Zhao, Y.; Guan, K.; Yang, Z.; Hu, Z.; Wang, H.; Ma, Z. The effect of subsequent heat treatment on the evolution behavior of second phase particles and mechanical properties of the Inconel 718 superalloy manufactured by selective laser melting. *Mater. Sci. Eng. A* **2020**, *794*, 139931. [CrossRef]
36. Blau, P.J. On the nature of running-in. *Tribol. Int.* **2005**, *38*, 1007–1012. [CrossRef]
37. Blau, P.J. Running-in: Art or engineering? *J. Mater. Eng.* **1991**, *13*, 47–53. [CrossRef]
38. Totten, G.E. Friction, Lubrication, and Wear Technology. In *ASM Handbook*; ASM International: Materials Park, OH, USA, 1992; Volume 18.
39. Schroeder, C.J.; Parrington, R.J.; Maciejewski, J.O.; Lane, J.F. Fractography. In *ASM Handbook*; Prepared under the Direction of the ASM Handbook Committee; ASM International: Materials Park, OH, USA, 1987; Volume 12.
40. Becker, W.T.; Shipley, R.J. Failure Analysis and Prevention. In *ASM Handbook*; ASM International: Materials Park, OH, USA, 2002; Volume 11.

41. Zarogiannis, P. *Environmental Risk Reduction Strategy and Analysis of Advantages and Drawbacks for Hexavalent Chromium*; Risk & Policy Analysts Ltd.: Norwich, UK, 2005.
42. Sherrington, I.; Hayhurst, P. Simultaneous observation of the evolution of debris density and friction coefficient in dry sliding steel contacts. *Wear* **2001**, *249*, 182–187. [CrossRef]
43. Arif Mahmood, M.; Chioibasu, D.; Ur Rehman, A.; Mihai, S.; Popescu, A.C. Post-Processing Techniques to Enhance the Quality of Metallic Parts Produced by Additive Manufacturing. *Metals* **2022**, *12*, 77. [CrossRef]
44. Malakizadi, A.; Mallipeddi, D.; Dadbakhsh, S.; M'Saoubi, R.; Krajnik, P. Post-processing of additively manufactured metallic alloys—A review. *Int. J. Mach. Tools Manuf.* **2022**, *179*, 103908. [CrossRef]
45. Mahmood Khan, M.; Karabulut, Y.; Kitay, O.; Kaynak, Y.; Jawahir, I.S. Influence of the post-processing operations on surface integrity of metal components produced by laser powder bed fusion additive manufacturing: A review. *Mach. Sci. Technol.* **2021**, *25*, 118–176. [CrossRef]
46. Maleki, E.; Bagherifard, S.; Bandini, M.; Guagliano, M. Surface post-treatments for metal additive manufacturing: Progress, challenges, and opportunities. *Addit. Manuf.* **2021**, *37*, 101619. [CrossRef]
47. Careri, F.; Umbrello, D.; Essa, K.; Attallah, M.M.; Imbrogno, S. The effect of the heat treatments on the tool wear of hybrid Additive Manufacturing of IN718. *Wear* **2021**, *470–471*, 203617. [CrossRef]
48. Karabulut, Y.; Tascioglu, E.; Kaynak, Y. Heat treatment temperature-induced microstructure, microhardness and wear resistance of Inconel 718 produced by selective laser melting additive manufacturing. *Optik* **2021**, *227*, 163907. [CrossRef]
49. Lesyk, D.A.; Dzhemelinskyi, V.V.; Martinez, S.; Mordyuk, B.N.; Lamikiz, A. Surface Shot Peening Post-processing of Inconel 718 Alloy Parts Printed by Laser Powder Bed Fusion Additive Manufacturing. *J. Mater. Eng. Perform.* **2021**, *30*, 6982–6995. [CrossRef]
50. Jinoop, A.N.; Subbu, S.K.; Paul, C.P.; Palani, I.A. Post-processing of Laser Additive Manufactured Inconel 718 Using Laser Shock Peening. *Int. J. Precis. Eng. Manuf.* **2019**, *20*, 1621–1628. [CrossRef]
51. Kaynak, Y.; Tascioglu, E. Post-processing effects on the surface characteristics of Inconel 718 alloy fabricated by selective laser melting additive manufacturing. *Prog. Addit. Manuf.* **2020**, *5*, 221–234. [CrossRef]
52. Kato, K. Wear in relation to friction—A review. *Wear* **2000**, *241*, 151–157. [CrossRef]

Disclaimer/Publisher's Note: The statements, opinions and data contained in all publications are solely those of the individual author(s) and contributor(s) and not of MDPI and/or the editor(s). MDPI and/or the editor(s) disclaim responsibility for any injury to people or property resulting from any ideas, methods, instructions or products referred to in the content.

coatings

MDPI

Article

Design and Application of Driving Resistance Test Device for Aircraft Tire and Soil Pavement

Zihan Wang, Xiaolei Chong *, Lei Liang, Zhenglei Chen and Chaojia Liu

College of Aeronautical Engineering, Air Force Engineering University, Xi'an 710038, China
* Correspondence: kgy_zxl@163.com

Abstract: In view of the lack of soil bins for studying the surface interaction between aircraft wheels and soil, this study designed an indoor test bench for aircraft wheels and soil, including a soil container, loading vehicle, and intelligent measurement and control system, to test key parameters such as tire speed and wheel frictional resistance. The test system is capable of achieving speed regulation ranging from 0 to 30 km/h. The vertical load adjustment range with an adjustment interval of 10 kg spans from 90 to 140 kg. The soil type, compaction degree, and other conditions can be modified as per requirements to vary multiple test conditions, thereby enabling us to explore their influence on the driving resistance of the wheels. Moreover, the test data can be collected and processed in real time. A performance test of a wheel–soil table was carried out. The results show that the wheel–soil table test system is stable and reliable and can determine the relationship between the tire and soil, and the structural design of the test system meets the use requirements. In addition, it achieves the target test speed, data acquisition frequency, and stability. In terms of functionality and operational difficulty, the data acquisition of the entire test process is automated, and the test system achieves better informationization than previous methods. The overall operation of the wheel–soil platform is stable and powerful; thus, the model test platform design goal is achieved, and the testing requirements are met.

Keywords: soil pavement; unsurfaced airfields; aircraft driving resistance; wheel–soil model test; surface interaction; soil bin test system

1. Introduction

Soil pavement has attracted global attention because of its low construction cost, fast construction speed, and ability to meet the emergency take-off and landing requirements of transport aircraft [1,2]. The driving resistance of the aircraft wheels on the soil pavement is one of the most important sources of resistance from the aircraft during take-off and landing [3,4]. It not only affects the surface performance of the soil pavement, but also affects the length of the soil runway. Therefore, it is very important to determine the driving resistance of the wheels on the soil pavement [5]. In order to obtain this information, we must first clarify the interaction between the wheel and the soil.

In previous research, the main way to study the interaction between aircraft tires and the soil runway was to carry out theoretical calculations and full-scale tests of ground vehicles [6,7]. In reality, the driving environment of the aircraft is more complex than can be represented using this method: soil in nature is heterogeneous and non-isotropic, so it is difficult to study this interaction through theoretical derivation. There are some differences between the motion principles of the full-scale testing of the vehicle and those of the testing of the real machine [8], and the running speed of the simulation is much lower than that of the aircraft. Although the accuracy of this method is high, there are still some errors compared with the real situation. Therefore, a wheel–soil table model test is necessary to study the relationship between the aircraft wheels and the soil. Tire–soil model testing is an important means to study the relationship between tires and soil. It

has many advantages, including cost efficiency, high test accuracy, fast data acquisition speed, and strong repeatability [9]. In general, it is more efficient than a full-scale test. In a full-scale test, the test involving soil is greatly affected by natural conditions and weather, and the repeatability of the test is low. Through a wheel–soil table model test, the research parameters can be strictly controlled according to the research needs without the limitation of external conditions, to accurately explore the internal mechanisms of the interaction [10].

The wheel–soil test-bed model is widely used in agricultural machinery [11], lunar exploration robots [12,13], and other fields. The test results have great guiding significance for design, performance evaluation, and design optimization [14]. In 1914, George Kuehne first proposed the use of the soil bin test to study tire–soil interaction. Since then, there has been a surge in research on soil bin testing [15]. The initial soil bin has a high input cost and weak power, which represent considerable limitations in the test. Siemens (1964) [16] designed a small soil bin that can test the performance of agricultural machinery. This equipment requires high investment and cannot perform many full-scale tests. Godwin (1980) [17] constructed and designed a multi-purpose soil bin to meet the needs of their test model, which can be used for the testing of full-scale and model agricultural machinery. However, the operation speed of the silo is very slow, only reaching 3 m/s. The University of Botka, Malaysia, designed a soil bin with a mobile frame with a cantilever-mounted tire (2007) [18], which can be used to test the effects of different parameters, including soil conditions, dynamic load, driving speed, and tire pressure. It is a relatively powerful soil bin, but it did not make a considerable breakthrough in test speed. The University of Urmia in Iran built a 23 × 2 × 1 m soil tank (2013) [19] capable of performing single-wheel tests on agricultural vehicle tires. The maximum speed of the test can reach 5.55 m/s, and the maximum vertical load can reach 5 kN, which can enable the measurement of driving resistance. The Federal Technical University of Akure, Nigeria, built a soil bin that can be tested under specific soil conditions (2010) [20], which enables the performance evaluation of reduced models of agricultural tillage tools in terms of drought and soil disturbance.

China's soil bin testing started later than that of other countries, mainly in the field of agricultural machinery and lunar rovers. The size of the soil bin in the field of agricultural machinery is larger, while that of the soil bin in the field of lunar rovers is smaller, due to the different needs of machinery in different fields. The first soil bin in China was built at the Luoyang Tractor Research Institute. Due to the limitations of the conditions, the test equipment was simple and its function was weak. With the accelerated pace of scientific and technological progress, the soil trough test equipment industry has developed rapidly. Jilin University has developed a series of soil bin test systems since the 1950s [21], which can enable the measurement of subsidence, wheel speed, driving speed, and other parameters, so as to explore tire–soil relationships. Beijing University of Aeronautics and Astronautics designed a soil bin test system for studying wheel–soil interaction, whereby the test platform enables the interconnection of sensors, computers, and control systems (2010) [22]. The Harbin Institute of Technology developed a soil bin for studying the wheel–ground interaction of planetary exploration rovers (2011) [23]. The soil bin is small, and the side wall is made of tempered glass. In the experiment, the influence of the wheels on the soil particles was observed. Li [24] designed an indoor soil bin for testing rotary tillage components, which can be used to explore the relationship between traction resistance, torque, and other parameters and test rate.

In recent years, with the development of and research on soil trough test benches, the soil trough has gradually developed to become intelligent, precise, and fully functioning. The running speed of agricultural machinery and lunar rovers is low, so the soil bin designed to test them is not high and cannot be effectively applied to aircraft tires. The speed of an aircraft running on the ground during take-off and landing can reach more than 60 m/s, which introduces many new requirements regarding the operating speed and test sampling frequency of the soil bin used to simulate the changes in the wheels' landing parameters. Based on the real-life needs of aircraft, this study designed a wheel–

soil platform suitable for exploring the relationship between the wheels and the soil during take-off and landing.

2. Materials and Methods

2.1. Design and Analysis of Soil Bin

The operation of an aircraft on a soil runway is an extremely complex process; thus, in this study, it was simplified to a tire–soil model for analysis. The principle of the wheels running on a soil runway is similar to that of the wheels running on soil ground, and the same principle can be used for this analysis. When driving on soil roads, for the convenience of research, it is assumed that the tire works like a rigid wheel [25], and thus, Bekker's pressure–sinkage relationship equation should be used, as shown in Equation (1). The theoretical model is shown in Figure 1 below.

$$p = (\frac{k_c}{b} + k_\phi)z^n \tag{1}$$

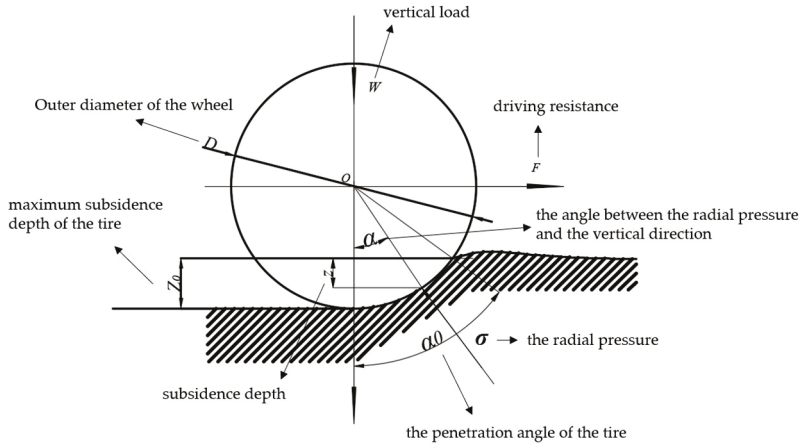


Figure 1. Simplified tire–soil interaction model.

In this equation, p is pressure, b is tire width, z is sinkage, and n, k_c, and k_ϕ are parameters describing the relationship between pressure and sinkage.

According to the balance equation of the driven rigid wheel, combined with the subsidence theory and the geometric relationship in Figure 1, the following driving resistance equation can be obtained. The specific calculation process is shown in [25].

$$F = \frac{1}{(3-n)^{\frac{2n+2}{2n+1}}(n+1)b^{\frac{1}{(2n+1)}} \cdot (k_C/b + k_\varphi)^{\frac{1}{2n+1}}}(\frac{3W}{\sqrt{D}})^{\frac{2n+2}{2n+1}} \tag{2}$$

The above is the theoretical calculation of driving resistance, but the real situation is more complicated than Equation (2) suggests. Therefore, it is necessary to carry out a model test to verify the driving resistance in real life. The aircraft on the soil road surface is summarized as moving with fast speed and a large vertical load, and the influencing factors of its movement are many and complicated [26,27]. Therefore, it is necessary to design a powerful soil tank for the model test. The soil trough in the field of agricultural machinery is close to our goal in terms of function, but it still has some shortcomings, including running speed, test frequency, accuracy, etc. [28,29].

Based on the influencing factors of exploration, this paper designs a soil bin with complete test functions. The established soil bin needs to increase the speed of the tire to 30 km/h in a 14-m-long acceleration channel, that is, 8.3 m/s, and then stop the test at the end of a 7-m pavement. The pavement can be replaced according to the needs of the test. The direction of the vehicle is one-way, and it undergoes free deceleration after the acceleration section. The width of the pavement is about 1 m, which ensures that the tire

can run normally, and the depth of the pavement is greater than 0.6 m, which is the general influence depth of the vertical load.

In view of the above requirements, the soil test bench is designed. The wheel–soil model test bench (hereinafter referred to as the test bench) is mainly used to simulate the interaction between the wheels and the pavement when the aircraft lands. The pavement type can be designed and replaced according to our needs to enable the testing and analysis of the interaction between the wheels and different pavements.

The test platform includes each platform and track. The platform base adopts a reinforced concrete structure, which has sufficient strength and stiffness, and can ensure that cracking, slip, local settlement, and permanent deformation do not occur. The platform base is designed to include each test platform, track, and loading test mechanism. The test platform and track provide safe and reliable structural support for the loading test mechanism. The guide rail provides three dimensions of guidance and support for the driving of the loading vehicle. The functional components of the test platform are shown in Figure 2.

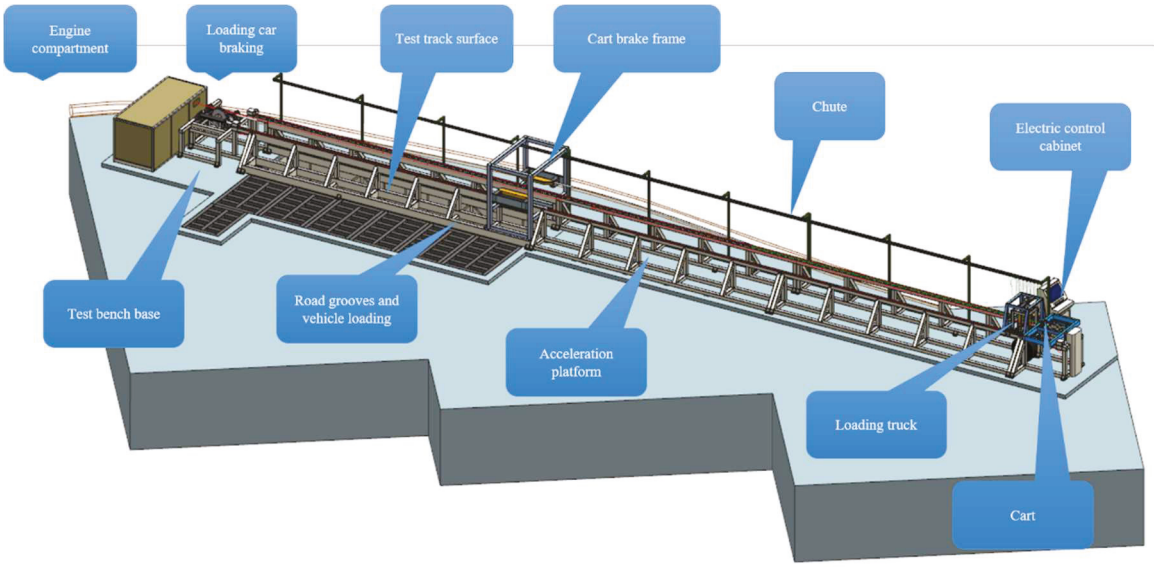


Figure 2. Diagram of main functional components of wheel–soil platform (the designs are not to scale).

The overall design of the test platform is divided into several areas, including the power cabin, braking section, test section, acceleration section, and starting section. The division of the test platform is shown in Figure 3:

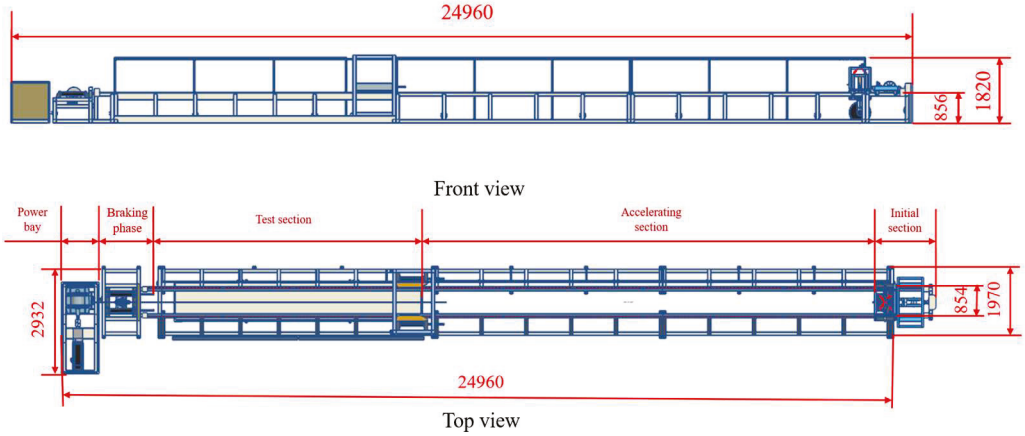


Figure 3. The division of the test platform (the designs are not to scale, mm).

The dimensions (length × width × height), shown in Figure 3, are 24.96 m × 2.932 m × 1.82 m, and the track width is 854 mm.

2.1.1. Bearing Platform

The platform is divided into four sections: starting, accelerating, testing, and braking. The starting section is used to park the loading vehicle and is the initial position of the loading mechanism. The purpose of the accelerating section is to accelerate the test wheel to the initial speed required for the test, to achieve the speed and kinetic energy required for the test, and to ensure the safe and reliable braking of the cart at the end of this section. The test pavement is used to read the test data and observe the interaction between the wheels and the pavement. The purpose of the braking section after the wheel test is to ensure the safe and reliable braking of the loading vehicle. The bearing platform provides a load-bearing and fixed locking interface for track installation, and ensures firmness and reliability between the track and the platform. The installation interface of the loading mechanism provides the load-bearing and fixed locking interface for the installation of the loading mechanism, and ensures that the position of the driving mechanism relative to the track and the pavement is consistent.

2.1.2. Test Track Surface

The vehicle on the test pavement adopts the structure of a box combining a rail and a roller, and the vehicle adopts a welded steel skeleton. The dimensions of the vehicle box are 7000 mm × 1000 mm × 650 mm, and the steel sealing plate is welded inside to accommodate different pavements, such as gravel, soil, and hard pavements. A standard rail is selected for the track, and the roller, made of a steel alloy, is designed according to its structural form. The roller shaft core is designed with a rolling bearing, and the driving force required to move the vehicle is small. The vehicle is moved out of the designed electric steel wire winch drive. When it is necessary to replace the test pavement material, the road surface vehicle starts to drive the electric hinge plate. The vehicle moves with the rail until the signal feedback stops. At this time, the vehicle is parked in the sinking groove of the pavement base.

2.1.3. Power Bay

The power cabin is composed of a servo motor, an electric winch, a wire device, a traction rope, etc., which provides reliable power for the movement of the loading mechanism. When the test is completed, the traction trolley is driven back to the starting position of the test bench by controlling the reverse rotation of the motor. For the servo motor to obtain better starting performance, the winch needs to be lightweight. The winch is made of 2A12-T4 aluminum alloy, which has a light weight, a small moment of inertia, and good starting performance.

The servo motor is the power source of the soil bin. Because of its high cost, it should be practical and economical. The performance requirements of the motor are related to the mass, acceleration distance, and target speed of the loading device, which are analyzed one by one in this study. The mass statistics of the relevant components of the loading device are shown in Table 1.

Table 1. Mass of loading device-related parts.

Name	Mass (kg)
Loading frame car	62.9
Loading car (including counterweight block)	103.7
Trolley	50.2
Test wheel	30
Total	246.8

The contact mode between the loading vehicle and the trolley device on the guide rail is rolling friction, and the friction coefficient μ is 0.1; the total length of the acceleration section is 12.9 m, the acceleration distance is 11 m, and 1.9 m is reserved for motor deceleration shutdown. The trolley device pushes the loading vehicle to accelerate at 11 m to reach 30 km/h (8.33 m/s). A 10% margin is reserved according to the instantaneous speed of 33 km/h (9.16 m/s). Assuming that the acceleration of the loading vehicle on the track is uniform, the uniform acceleration equation is shown in Equation (3):

$$2aS = v^2 - v_0^2 \tag{3}$$

The acceleration section S = 7 m, v = 33 km/h (10 m/s) is substituted into the above equation to obtain a = 3.81 m/s^2. The rolling friction resistance f of the loading device on the acceleration section is shown in Equation (4).

$$f = \sum mg\mu = 242.1 \text{ N} \tag{4}$$

The traction force of the loading device on the acceleration section is F, as shown in Equation (5).

$$F = ma + f = 1182.4 \text{ N} \tag{5}$$

According to the technical requirements, when the loading vehicle enters the test section at an instantaneous speed of no less than 30 km/h, the design value of the scheme is 33 km/h according to the instantaneous speed. In actual use, the speed of the servo motor can be adjusted according to the user's needs. The linear speed of the rope on the winch is v_J, and the linear speed of the trolley is equal to this value, so the reel speed n_J is shown in Equation (6).

$$n_J = \frac{60v_J}{2\pi r} = 437 \text{ RPM} \tag{6}$$

In this equation, r is the radius of the winch drum, which is 0.2 m.

According to the torque equation, the output torque T is shown in Equation (7).

$$T = Fr = 236.5 \text{ N} \cdot \text{m} \tag{7}$$

According to the equation calculating the output power of the motor, when the loading vehicle and the trolley device reach a speed of 33 km/h in the acceleration section, the maximum output power required for the motor output is shown in Equation (8).

$$P = \frac{Tn_J}{9550\eta} = 22.1 \text{ kW} \tag{8}$$

In this equation, the transmission efficiency of the reducer is 0.9 and that of the traction rope is 0.625 (with reference to the driving traction), the motor efficiency is 0.87, and the actual total transmission efficiency of the system η is about 0.49. According to the technical parameters of the motor, a Suzhou Tongjin 200MAH115020 servo motor (Suzhou, China) is selected. The rated power of the servo motor is 24.1 kW, the rated torque is 115 Nm, and the maximum speed is 2500 RPM.

2.1.4. Charger

The loading device is composed of a loading frame car, a loading car, and a trolley. The trolley drives the loading car to move by driving the traction rope. The loading car is composed of a frame car, a loading car, and a hand-operated winch, and the frame moves on the guide rail. The driving mechanism provides the necessary test speed for the loading car, and provides the required loading capacity for the test wheel by increasing or decreasing the counterweight block.

The loading frame vehicle is the carrier of the loading vehicle. The wheel provides reliable structural support for the loading vehicle in the acceleration, test, and braking

stages, and transmits the load of the loading vehicle to the track support. The loading frame car is designed with a guide pulley block and a linear slider guided by the loading vehicle, and loading vehicle dials. When working, the guide pulley block ensures that the frame moves on the guide rail to provide guidance for the acceleration, testing, and braking of the loading vehicle. When the loading vehicle is under extreme working conditions (such as the wheel being embedded in the test surface), the guide pulley block's anti-overturning and anti-torsion abilities can offset the impact load. The guide pulley block can ensure the safe and reliable operation of the wheel acceleration section, the test surface, and the braking section. The loading frame vehicle adopts a lightweight design, with a size of 1000 mm × 616 mm × 900 mm. 6061T6 aluminum alloy profile pipe fittings are used to weld the frame. A manual steel wire hinge plate is installed at the top to enable the loading vehicle to rise, and a guide seat is placed in the middle to facilitate the passage of a traction rope. A limit dial is placed on both sides of the loading frame vehicle, and the other end of the dial is used to support the loading vehicle. In the acceleration section, the dial supports the loading vehicle to ensure that the distance between the wheel and the test road surface is no less than 20 mm.

The loading vehicle adopts a 6061T6 aluminum alloy profile welded frame, with an overall size of 480 mm × 460 mm × 1175 mm. An adjustable limit block is placed on both sides to accommodate the replacement of various wheel specifications. A wheel locking handle is placed on the wheel mounting frame to lock the wheel, and a four-corner linear guide rail installation is match with the slider on the loading frame vehicle.

The cart adopts a 6061T6 aluminum alloy profile welding frame, with an overall size of 1370 mm × 755 mm × 370 mm. An aluminum alloy hinge plate is installed in the middle of the cart to facilitate the return of the loading car. The rear part is the shear pin interface, and the front part is equipped with a shock absorber to enable soft contact with the loading frame car.

Due to the large load on the loading device during the test, in order to carry out the test smoothly, preserve the service life of the test bench, and determine whether the safety standard is met, it is necessary to simulate the key parts of the system.

(1) Loading Frame Vehicle and Loading Vehicle Landing Stiffness and Strength Analysis

Considering the limit condition, after the loading vehicle arrives on the experimental road surface, the impact of the wheel and the test road surface is completely stopped within 0.1 s. A simplified model of the frame, loading vehicle, loading wheel, and axle is established using ANSYS software (ANSYS 2021 R1) [30], and the direct connection of the three-axis force sensor is canceled. The frame and loading vehicle are made of a 6061T6 aluminum alloy material, and the axle is made of a 40Cr material. A coordinate system is established, with the reverse direction of the loading vehicle in the x-positive direction, the right side of the loading vehicle body in the y-positive direction, and the vertical direction being the z-positive direction.

The following settings are established for the boundary conditions:

1. Apply 500 N on the counterweight-fixed surface to simulate 5 counterweight loads;
2. Apply -83 m/s^2 acceleration in the x-positive direction to simulate the emergency stopping of the loading vehicle, and apply 0.4 g acceleration in the z-positive direction to simulate the emergency stopping of the loading vehicle after the dial is opened;
3. Apply gravity acceleration of 1 g;
4. The fixed-constraint loading wheel touches the ground;
5. Restrain the degree of freedom in the y and z directions of the installation surface of the horizontal guide slider on the frame, and release the degree of freedom in the x direction;
6. Define the frame and the loading car slider guide rail as having non-separable contact.

The boundary conditions are set as shown in Figure 4:

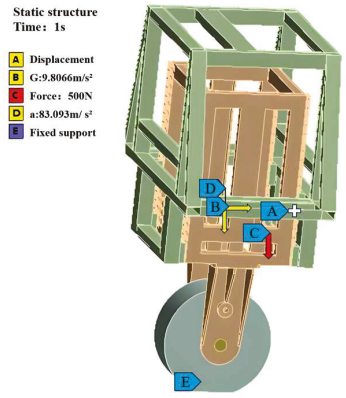


Figure 4. Loading vehicle boundary conditions.

As shown in Figures 5 and 6, the maximum stress (77 MPa) of the loading vehicle appears at the axle mounting hole; the safety factor is 3.1; the maximum cumulative total displacement of the loading vehicle, which is located in the upper skeleton of the loading vehicle, is about 2.9 mm; and the maximum displacement of the loading vehicle in the *x*-axis direction, which is located in the upper skeleton of the frame, is about 2.8 mm. The maximum displacement of the loading vehicle in the z direction, which is located in the front vertical guide rail of the installation skeleton, is about 0.65 mm. The maximum stress of the wheel axle appears at the installation with the loading vehicle. The maximum stress is 108 MPa, and the safety factor is 7.2, which meets the design requirements.

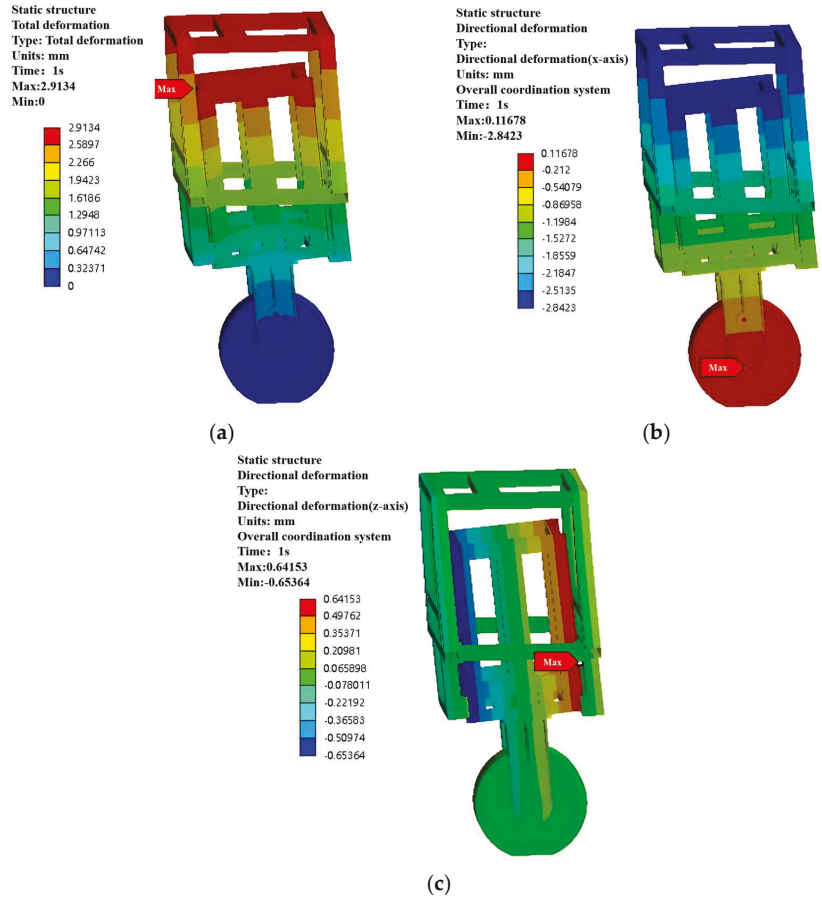


Figure 5. Displacement simulation result diagram. (**a**) Overall displacement cloud diagram of loading vehicle and lifting vehicle; (**b**) loading vehicle and trolley *x*-axis displacement cloud diagram; (**c**) loading car and car *z*-axis displacement cloud diagram.

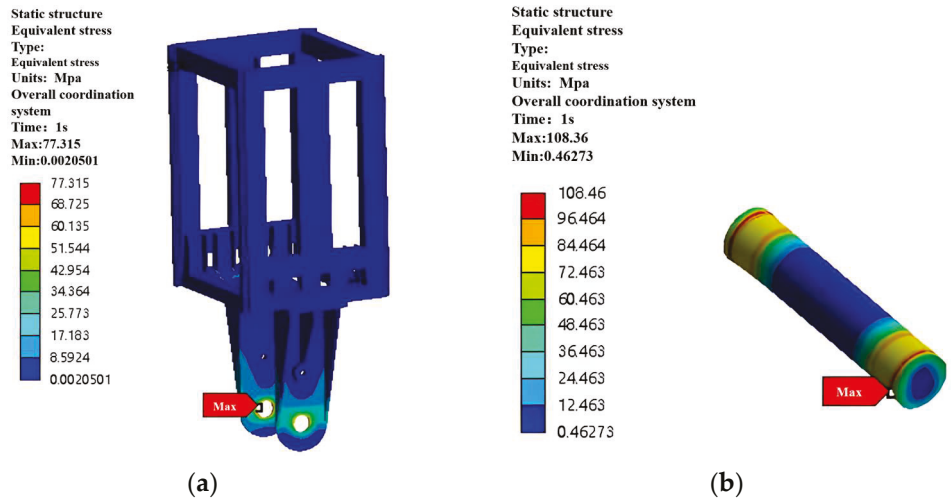


Figure 6. Stress simulation result diagram. (**a**) Loading vehicle stress cloud diagram; (**b**) wheel shaft stress cloud diagram.

The maximum stress of the loading frame car appears at the axle mounting hole (see Figure 7). The maximum stress is 42 MPa; the safety factor is 5.7; and the total displacement of the loading frame car, which is located in the upper skeleton of the frame, is about 2.9 mm. The maximum displacement of the frame in the *x*-axis direction, which is located in the upper skeleton of the frame, is about 2.8 mm. The maximum displacement of the loading vehicle in the z direction, which is located on the rear side of the skeleton, is about 0.2 mm, which meets the design requirements.

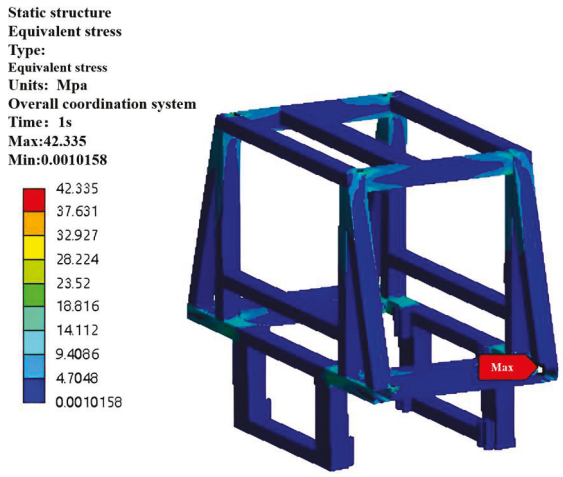


Figure 7. Loading frame car stress nephogram.

(2) Brake Stiffness and Strength Analysis of Cart

Considering the extreme working conditions, after the loading vehicle enters the experimental road surface, the trolley stops completely within 0.1 s when braking, and a simplified model of the trolley is established. The trolley adopts a 6061T6 aluminum alloy material. A coordinate system is established, with the reverse direction of the trolley in the x-positive direction, the right side of the trolley body in the y-positive direction, and the vertical direction being the z-positive direction.

The following settings are established for the boundary conditions:

1. Apply -83 m/s^2 acceleration in x-positive direction to simulate the emergency stopping of the loading vehicle;
2. Apply gravity acceleration of 1 g;
3. Fix the contact surface between the constraint cart and the buffer.

4. Restrain the degrees of freedom in the y and z directions of the horizontal guide slider's installation surface on the trolley, and release the degree of freedom in the x direction.

The boundary conditions of the cart are set as shown in Figure 8:

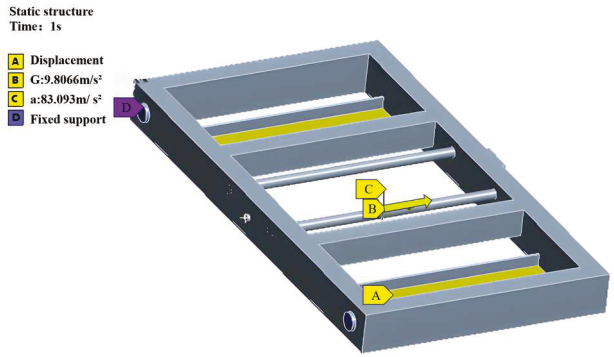
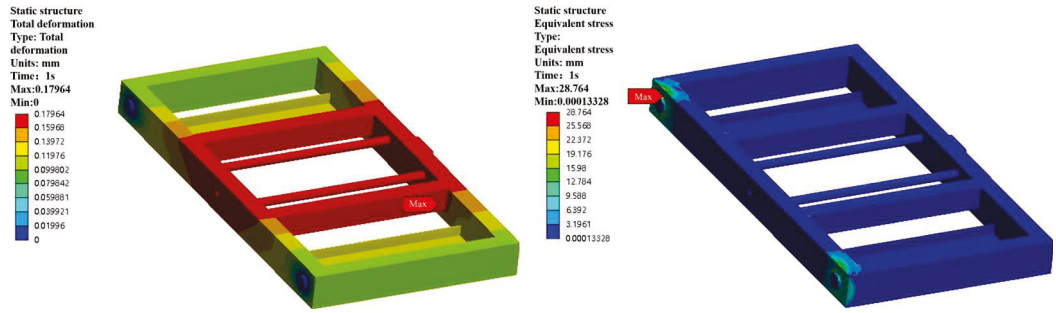


Figure 8. Boundary conditions of cart.

As shown in Figure 9, the maximum stress of the cart appears at the point of contact with the retarder; the maximum stress is 29 Mpa; the safety factor is 8.2; and the maximum total displacement of the cart, which is located in the middle of the cart, is about 0.18 mm, which meets the design requirements.



(**a**) (**b**)

Figure 9. Trolley simulation result diagrams. (**a**) Pusher displacement cloud map; (**b**) Stress cloud diagram of cart.

According to the above simulation results, the stiffness of the loading device meets the use requirements and can ensure the smooth running of the test.

2.1.5. Stopping Gear

The braking system includes two parts: loading vehicle braking and pushing vehicle braking. As shown in Figure 10, in the part of pushing vehicle braking, the cart and the loading car are separated, the cart stops, and the loading car continues to move forward. In the loading vehicle braking section, the loading vehicle stops. The braking device adopts the combination of an airbag hydraulic buffer and a protective wall panel. The airbag hydraulic buffer can absorb the kinetic energy of the loading vehicle after driving on the test pavement within a distance of 0.5 m. The buffer wall acts as an auxiliary protection function. When the airbag buffer works normally, the buffer wall can absorb a small amount of energy and play a secondary protective role. When the airbag hydraulic buffer fails, the loading vehicle stops safely and smoothly under the action of the damping spring arranged on the buffer wall to protect personnel and equipment.



Figure 10. Stopping gear diagram.

2.1.6. Control and Data Acquisition System

The control and data acquisition system consists of a servo motor driver and a sensor data acquisition and processing module. The servo driver provides the necessary power support for the loading vehicle on a specific pavement by controlling the rotation of the servo motor. The data acquisition and processing module can collect, process, display, and store the data of the speed sensor and the three-dimensional force sensor. The electric control cabinet is designed to operate and display the whole test system for the display and input terminals.

2.2. Sensor Placement

2.2.1. Three-Axis Sensor

A Shenzhen New Transform Technology Co., LTD (Shenzhen, China) 3KD170 three-axis force sensor is used in this study. When the wheel is driving in the test section, the three-axis force sensor (see Figure 11) can accurately output the force value in the horizontal and vertical directions of the wheel. The three-axis force sensor has a simple structure and a small volume. It converts the mechanical energy of the measured object into an electrical signal output. It has strong anti-interference ability, a wide temperature range, and is not affected by air pollution, oil pollution, and other media at the test site. It is commonly used in electronically controlled engines to determine the current crankshaft speed and position. Through the rotation of the signal disk, cutting of the magnetic field line is achieved, the core body is induced, and the signal output is obtained. This signal is modulated by the internal modulation of the electronic control unit to obtain a square-wave signal with high precision. The measured data can be automatically recorded and stored during the test, and are easy to export.

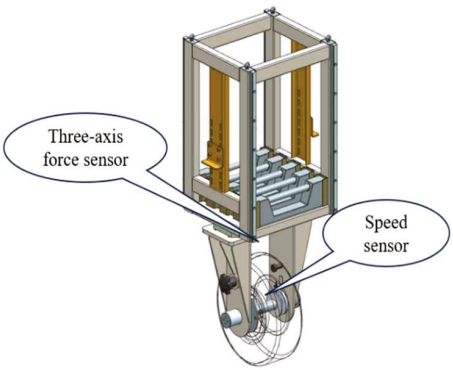


Figure 11. Triaxial force sensor layout.

2.2.2. Speed Sensor

In order to accurately output the driving speed of the loading wheel, the error is set such that it does not exceed 5%. At the maximum speed, the speed acquisition frequency is set to no less than 100 Hz. SPHZ18-2FS speed sensors (see Figure 11) are arranged near the loading vehicle and the wheel to obtain the driving speed of the loading vehicle and the

wheel during the test. An SPHZ18-2FS Hall gear speed sensor is small and does not need a power supply, and it can directly absorb mechanical energy from the measured object and convert it into an electrical signal output.

3. Results and Discussion

In this paper, a wheel–soil test bench is designed and tested, as shown in Figure 12. After the construction of the test bench, it is necessary to carry out tests to evaluate its performance. The main test pertained to the software system and its functionality, including the acceleration performance of the trolley, the contact between the loading vehicle and the pavement, the stop performance of the loading vehicle, and the effectiveness of the intelligent data acquisition system.



(**a**) (**b**)

Figure 12. Soil bin. (**a**) Panoramic view of the soil bin; (**b**) close-up view of the soil bin.

3.1. Design of Experiments

The soil of the test pavement is loess from the Xi'an area. Before the test, the soil is turned and dried so that the physical properties, such as the water content, of each part of the soil remain uniform. The compaction degree of the pavement is determined by different compaction processes and is formulated according to the test plan. A test operation is carried out according to the test process. In order to make the conditions of the pavement test close to the real conditions of a soil pavement, the compaction degree is set at more than 90% and placed in the natural environment for five days. During this five-day period, the average temperature is 35 °C, and there is no wind or rain. Four experiments were carried out under loads of 93 kg, 113 kg, and 143 kg, respectively. The instantaneous speed of the trolley is greater than 20 km/h at the moment of launching the loading car, and the loading car can stop at the end of the pavement with the help of a deceleration device.

3.2. Principle of Operation

During the test, the trolley transfers power to the loading vehicle under the pulling of the traction rope and enters the test platform after acceleration. Before entering the test platform, the loading frame vehicle drives the loading vehicle to unlock the limit through the support handle on the frame of the kinetic energy collision. The loading vehicle falls freely in the frame through the combination of the linear guide rail and slider until the wheel contacts the test pavement. At this time, the servo motor obtains signal feedback and brakes in response to a signal from the sensor. The trolley is limited by the braking torque of the servo motor to absorb the kinetic energy of the vehicle through the extension of the traction rope and the hydraulic buffer cylinder, so that the trolley and the frame are separated and stopped.

After the acceleration process ends, the wheel falls into and interacts with the test pavement. The average duration of the interaction can be recorded by the speed sensor. The interaction force between the wheel and the test pavement can be obtained by the three-dimensional force sensor installed on the wheel shaft. The speed and force can be recorded by a recording device.

3.3. Analysis of Test Results

During the test, the acceleration and stopping performance of the loading vehicle are good, and the test is carried out smoothly. From Figure 13, it can be seen that the tire of the loading vehicle is in good contact with the road surface, leaving a wheel trace. Figure 14 shows an information acquisition diagram of the driving resistance data acquisition system with 200 Hz acquisition frequency. The data in the figure are divided into two stages, the first stage is the stage where the resistance caused by the bounce of the tire when it has just landed has a large fluctuation. The second stage is the resistance image formed when the tire is rolling steadily, which is also the focus of the article.



Figure 13. Wheel rut diagram.

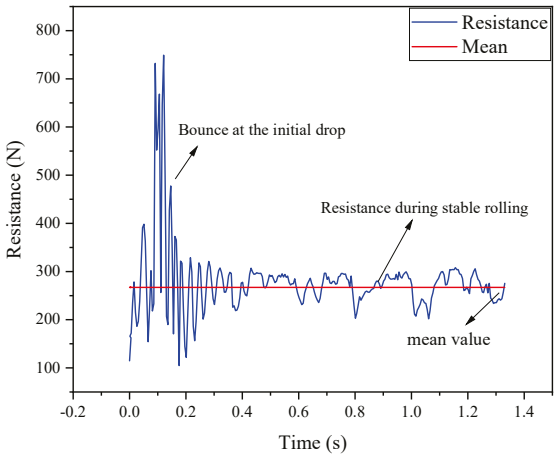


Figure 14. Variation diagram of driving resistance of a fully loaded vehicle running at a speed of 20 km/h.

Figures 15 and 16 reflect the characteristics of 12 sets of test data. It can be found from this figure that the data of the four consecutive tests under the same test conditions have large variation, but the overall data characteristics are similar, and most of the data are between 200 and 300 N. From the analysis of the box plot in Figure 15, it can verify the fluctuation range of the data, and there are fewer outliers. The fluctuation range in a single set of data is large, but this is caused by the nature of the soil. It can be found from the box diagram that the mean values of each group of data under the same load conditions are similar. The driving resistance values under 93 kg, 113 kg, and 143 kg are 152 N, 180 N, and 265 N, respectively. After testing the model, it is found that the intelligent data acquisition system is stable, the signal transmission is continuous and normal, and the working performance is good.

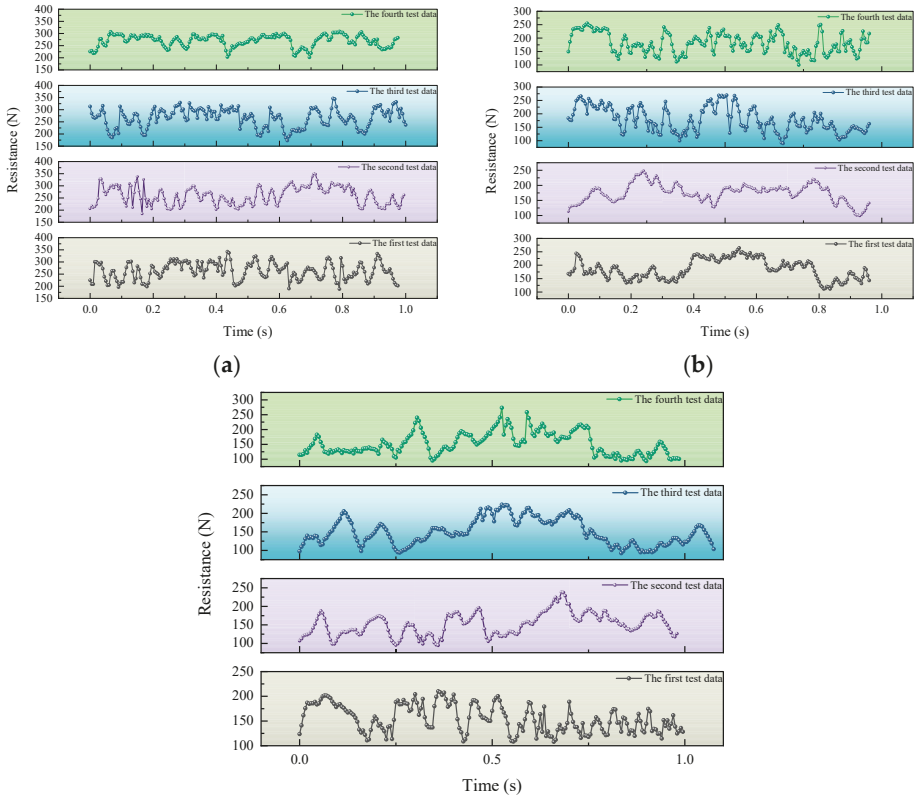


Figure 15. Variation diagram of wheel driving resistance under different loads. (**a**) 143 kg load; (**b**) 113 kg load; (**c**) 93 kg load.

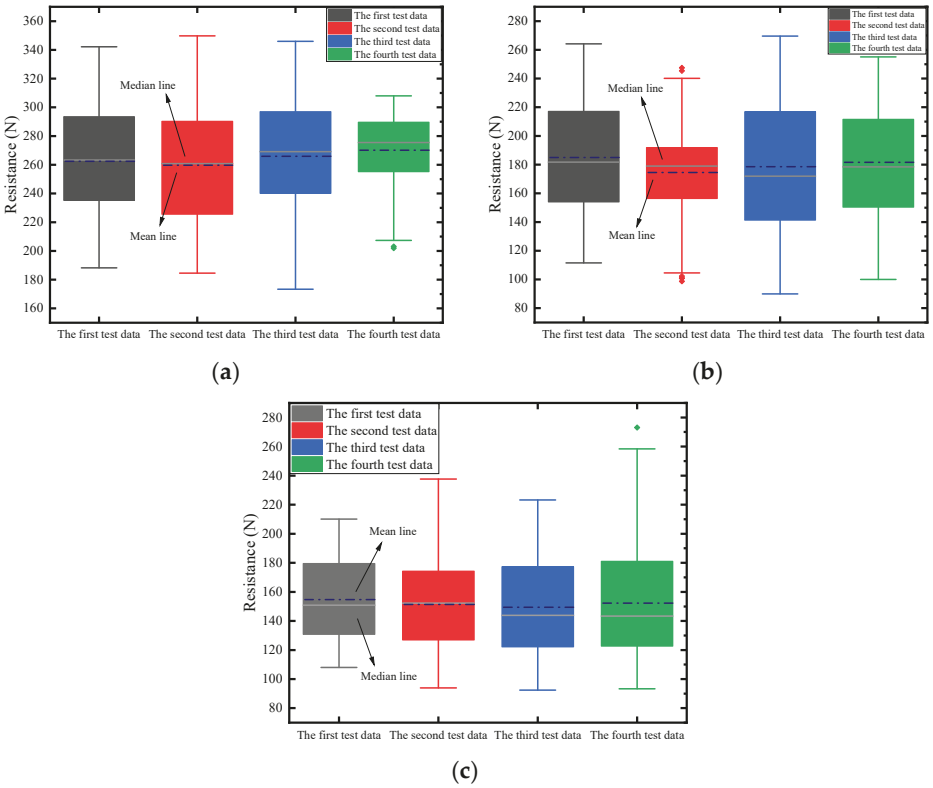


Figure 16. Wheel resistance test box diagram under different loads. (**a**) 143 kg load; (**b**) 113 kg load; (**c**) 93 kg load.

4. Conclusions

(1) In this study, a wheel–soil test bench composed of a power cabin, a braking section, a test section, an acceleration section, and a starting section was designed, with each section mainly composed of a soil tank and a loading device. The test bench uses a servo motor with a rated power of 24.1 kW and a rated torque of 115 Nm as a power drive, which can achieve a speed adjustment of 0~30 km/h. The range of vertical load is 90~140 kg, with 10 kg as the adjustment interval. ANASYS software was used to simulate and analyze the part of the loading vehicle with a large load in the soil bin. The simulation results show that the design strength meets the use requirements.

(2) The control system of the wheel–soil test-bed monitors the current speed of the test-bed cart, the current speed of the tire, the starting position of the cart, the middle position, the swing rod state of the frame, and the frame state in real time. The intelligent data acquisition system is powerful, and its test operation is simple. This system can perform many functions, such as data acquisition, data storage, and data analysis.

(3) A performance test was carried out on the wheel–soil platform. The mean values of driving resistance test under 93 kg, 113 kg, and 143 kg loads are 152 N, 180 N, and 265 N, respectively, and the mean value of resistance test under the same load does not change significantly. The results show that the wheel–soil platform test system is stable and reliable, and the structural design of the test system meets the use requirements. The target test speed, data acquisition frequency, and stability are achieved. In terms of functionality and operational difficulty, the pavement can be replaced according to the research objective, and the entire data acquisition process of the test is automated. This test system achieves better informationization that previous methods. The overall operation of the wheel–soil platform is stable and powerful, enabling it to meet the needs of the test.

Author Contributions: Conceptualization, Z.W. and X.C.; methodology, C.L.; software, X.C.; validation, X.C.; formal analysis, C.L.; investigation, L.L.; resources, X.C.; data curation, C.L.; writing—original draft preparation, Z.W.; writing—review and editing, X.C.; visualization, Z.C.; supervision, Z.C.; project administration, L.L.; funding acquisition, Z.W. All authors have read and agreed to the published version of the manuscript.

Funding: This research received no external funding.

Institutional Review Board Statement: Not applicable.

Informed Consent Statement: Not applicable.

Data Availability Statement: Data are contained within the article.

Conflicts of Interest: The authors declare no conflict of interest.

References

1. US, Air Force Flight Test Center. *Aircraft Operations on Unsurfaced Soil, Soil Measurements and Analyses*; Army Engineer Waterways Experiment Station: Vicksburg, MS, USA, 1963; pp. 12–54.
2. Abeyratne, R.I.R. Search and Rescue Operations of Aircraft in Africa: Some Compelling Issues. *J. Air Transp. World Wide* **2002**, *7*, 2–3.
3. Gong, Z.; Miao, Y.; Lantieri, C. Review of Research on Tire–Pavement Contact Behavior. *Coatings* **2024**, *14*, 157. [CrossRef]
4. Wang, Z.; Chong, X.; Wang, G.; Liu, C.; Zhang, J. Research on the Measurement and Estimation Method of Wheel Resistance on a Soil Runway. *Coatings* **2024**, *14*, 1062. [CrossRef]
5. Pytka, J.A. Identification of Rolling Resistance Coefficients for Aircraft Tires on Unsurfaced Airfields. *J. Aircr.* **2014**, *51*, 353–360. [CrossRef]
6. Ward, A.B.; Falls, A.J.; Rutland, C.A. Development of Deceleration-Based Friction Prediction Models and Methods on Semiprepared Runway Surfaces. *Transp. Res. Rec. J. Transp. Res. Board* **2023**, *1*, 036119812311536. [CrossRef]
7. Pytka, J.A. Semiempirical Model of a Wheel-Soil System. *Int. J. Automot. Technol.* **2010**, *11*, 681–690. [CrossRef]
8. Liu, C.; Chong, X.; Liang, L.; Chen, Z.; Wang, Z.; Li, Y.; Liu, W. Improved Design, Development and Field Investigation of the Wheel-Soil Interaction Measurement System under Aircraft Load. *Meas. J. Int. Meas. Confed.* **2024**, *236*, 115117. [CrossRef]
9. Kumar, S.; Noori, M.T.; Pandey, K.P. Performance Characteristics of Mode of Ballast on Energy Efficiency Indices of Agricultural Tyre in Different Terrain Condition in Controlled Soil Bin Environment. *Energy* **2019**, *182*, 48–56. [CrossRef]

10. Bahrami, M.; Naderi-Boldaji, M.; Ghanbarian, D.; Keller, T. Discrete Element Modelling of Stress Propagation in Soil under a Rigid Wheel in a Soil Bin: A Simulation of Probe Inducing Stress Deviation and Wheel Speed. *Biosyst. Eng.* **2023**, *230*, 159–170. [CrossRef]
11. Tagar, A.A.; Changying, J.; Adamowski, J.; Malard, J.; Qi, C.S.; Qishuo, D.; Abbasi, N.A. Finite Element Simulation of Soil Failure Patterns under Soil Bin and Field Testing Conditions. *Soil Tillage Res.* **2015**, *145*, 157–170. [CrossRef]
12. Zou Meng, Z.M.; Li JianQiao, L.J.; Li YinWu, L.Y.; Jia Yang, J.Y.; Ma WenZhe, M.W. Prediction Model and Experimental Study on the Interaction of Rigid-Wheel and Lunar Soil. *Trans. Chin. Soc. Agric. Eng.* **2007**, *23*, 119–123.
13. Wang, Y.; Huang, H.; Li, J.; Chen, B.; Zou, M. Experiment on Lunar Rover's Trafficability on Slope Terrain Based on Similarity Theory. *Trans. Chin. Soc. Agric. Mach.* **2017**, *48*, 406–412.
14. Ani, O.A.; Uzoejinwa, B.B.; Ezeama, A.O.; Onwualu, A.P.; Ugwu, S.N.; Ohagwu, C.J. Overview of Soil-Machine Interaction Studies in Soil Bins. *Soil Tillage Res.* **2018**, *175*, 13–27. [CrossRef]
15. Ademosun, O.C. Soil Tillage Dynamics in Nigeria: Potentials Prospects and Challenges. In Proceedings of the Nigerian Branch of International Soil Tillage Research Organisation, ISTRO-Nigeria Symposium, Akure, Nigeria, 3–6 November 2014; pp. 26–31.
16. Siemens, J.C.; Weber, J.A. Soil Bin for Model Studies on Tillage Tools & Traction Devices. *J. Terramech.* **1964**, *1*, 56–67.
17. Godwin, R.J.; Spoor, G.; Kilgour, J. The Design and Operation of a Simple Low Cost Soil Bin. *J. Agric. Eng. Res.* **1980**, *25*, 99–104. [CrossRef]
18. Yahya, A.; Zohadie, M.; Ahmad, D.; Elwaleed, A.K.; Kheiralla, A.F. UPM Indoor Tyre Traction Testing Facility. *J. Terramech.* **2007**, *44*, 293–301. [CrossRef]
19. Taghavifar, H.; Mardani, A. A Knowledge-Based Mamdani Fuzzy Logic Prediction of the Motion Resistance Coefficient in a Soil Bin Facility for Clay Loam Soil. *Neural Comput. Appl.* **2013**, *23*, 293–302. [CrossRef]
20. Agbetoye, L.A.S.; Manuwa, S.I.; Ademosun, O.C.; Adesina, A. Development of Below-Floor Level Soil Bin System for Soil Tillage Dynamics Research at the Federal University of Technology Akure, Nigeria. In Proceedings of the Nigeria 17th World Congress of the International Commission of Agricultural and Biosystems Engineering (CIGR), Québec City, QC, Canada, 13–17 June 2010.
21. Li, J.; Huang, H.; Wang, Y.; Tian, L.; Ren, L. Development on Research of Soft-Terrain Machine Systems. *Trans. Chin. Soc. Agric. Mach.* **2015**, *46*, 306–320.
22. Sun, P.; Gao, F.; Yao, S.; Li, W. Interaction between Lunar Rover Wheel and Simulant Lunar Soil by Experiment. *J. Beijing Univ. Aeronaut. Astronaut.* **2010**, *36*, 757–761.
23. Ding, L.; Gao, H.; Deng, Z.; Nagatani, K.; Yoshida, K. Experimental Study and Analysis on Driving Wheels' Performance for Planetary Exploration Rovers Moving in Deformable Soil. *J. Terramech.* **2011**, *48*, 27–45. [CrossRef]
24. Li, Y.; Song, J.; Dong, X.; Zhang, J.; Wang, J. Design of Test Device for Rotary Tiller Components Based on Soil Bin. *Trans. Chin. Soc. Agric. Eng.* **2012**, *28*, 38–43.
25. Wong, J.Y. *Theory of Ground Vehicles*; John Wiley & Sons: Hoboken, NJ, USA, 2022; ISBN 1119719704.
26. Meng, Q.; Zhong, K.; Sun, M. Dynamic Response Analysis of Airport Pavement under Impact Loading. *Appl. Sci.* **2023**, *13*, 5723. [CrossRef]
27. Zhang, D.; Cai, L.; Zhou, S. An Airfield Soil Pavement Design Method Based on Rut Depth and Cumulative Fatigue. *J. Adv. Transp.* **2019**, *2019*, 6032305. [CrossRef]
28. Mardani, A.; Golanbari, B. Indoor Measurement and Analysis on Soil-Traction Device Interaction Using a Soil Bin. *Sci. Rep.* **2024**, *14*, 10077. [CrossRef]
29. Chen, L.; Zou, M.; Chen, Z.; Liu, Y.; Xie, H.; Qi, Y.; He, L. The Applications of Soil Bin Test Facilities to Terramechanics: A Review. *Rend. Lincei* **2024**, *7*, 1–21. [CrossRef]
30. Silori, P.; Shaikh, A.; Nithin Kumar, K.C.; Tandon, T. Finite Element Analysis of Traction Gear Using ANSYS. *Mater. Today Proc.* **2015**, *2*, 2236–2245. [CrossRef]

Disclaimer/Publisher's Note: The statements, opinions and data contained in all publications are solely those of the individual author(s) and contributor(s) and not of MDPI and/or the editor(s). MDPI and/or the editor(s) disclaim responsibility for any injury to people or property resulting from any ideas, methods, instructions or products referred to in the content.

coatings

MDPI

Article

Interfacial Diffusion and Copper Alloy Layer Wear Mechanism in Cu-20Pb-5Sn/45 Steel Bimetallic Composites

Yuanyuan Kang [1,*], Guowei Zhang [2], Yanling Hu [3] and Yue Liu [1]

[1] Engineering Training Center, Taiyuan University, Taiyuan 030032, China; 2023515002@tyu.edu.cn
[2] School of Material Science and Engineering, North University of China, Taiyuan 030051, China; 20030358@nuc.edu.cn
[3] China Shipbuilding Group Fenxi Heavy Industry Co., Ltd., Taiyuan 030027, China; 15333004112@163.com
* Correspondence: 2022515003@tyu.edu.cn

Abstract

Cu-20Pb-5Sn/45 steel bimetallic composites were prepared using the solid–liquid composite method. The interfacial microstructure, bonding strength, and wear performance were systematically characterized to elucidate the mechanisms governing the solid-solution interface and copper alloy layer wear behavior. The results reveal that mutual diffusion of Cu and Fe forms a metallurgically bonded α-(Cu,Ni)/α-Fe interface with a diffusion layer thickness of approximately 10.7 μm and an interfacial shear strength of 227.58 MPa. Under dry sliding conditions, the average coefficient of friction was 0.145, with a wear rate of 7.3665×10^{-6} $mm^3/(N \cdot m)$. The α-(Cu,Ni) matrix was reinforced by hard Cu_3P and Ni-rich phases, which resist frictional shear stresses, while dispersed Pb particles provide self-lubricating properties, while the solid-solution interface hindered dislocation propagation, reducing dislocation pile-up and ensuring stable frictional performance.

Keywords: Cu-20Pb-5Sn/45 steel; interface; wear; microstructure

1. Introduction

Copper alloy/steel bimetallic composites are commonly utilized in low-to-medium load hydraulic pump cylinders, where the copper alloy layer forms a friction pair with the pump plunger for power transmission, while the steel layer provides high-strength mechanical support in coordination with the pump body [1–4]. During the startup phase, the copper alloy layer and plunger friction pair operate under dry or intermittent lubrication conditions, relying on the material's inherent wear resistance [2,5]. The Cu-20Pb-5Sn alloy, known for its excellent self-lubricating properties, is typically used as the friction material metallurgically bonded with steel to form bimetallic composites [6]. In tribological studies of copper alloy/steel bimetals, Pervikov et al. employed electric explosion and magnetic pulse techniques to fabricate bimetallic materials, achieving reduced friction and wear through magnetic pulsing [7]. Zykova et al. used electron beam additive manufacturing combined with friction stir processing, reporting a 25% reduction in the friction coefficient post-processing [8]. Zhang et al. investigated the effect of varying Ag content in bimetals prepared via the solid–liquid composite method, finding that Ag addition enhanced interfacial shear strength by 58.3% and significantly improved wear resistance [9]. Similarly, Shi et al. optimized the comprehensive performance of copper alloy/steel bimetals using electromagnetic stirring, identifying optimal process parameters for superior tribological properties [10].

Existing literature often treats the interface and friction layer of bimetallic materials as separate entities. However, beyond the wear resistance and stable frictional performance of the copper alloy layer, the integrity of the bimetallic interface is critical to prevent delamination under shear stress [11,12]. Engineering practices have confirmed that weak interfacial bonding is a primary cause of bimetallic material failure [13,14]. Furthermore, Wang et al. compared single-metal lead bronze, brass, and bimetallic bronze/steel materials prepared via vacuum diffusion welding, finding that the presence of the steel layer reduced plastic deformation of the bronze during wear, resulting in superior tribological performance [15]. This indicates that the tribological properties of copper alloy/steel bimetallic composites are not solely determined by the copper alloy layer. During wear, frictional shear stress transfers through the copper alloy layer to the interface [16,17]. The interfacial microstructure, including the diffusion layer and grain boundaries, inevitably influences dislocation propagation and stress distribution during wear, thereby affecting surface deformation and overall stability of the copper alloy layer [18]. Additionally, wear-induced microstructural evolution in the friction layer, such as work hardening and dislocation pile-up, impacts the stress state at the interface [19,20]. These complex interactions are crucial for preventing material failure.

Despite numerous recent reports on the preparation, interface, and properties of copper alloy/steel bimetallic composites, research on the mechanisms linking interfacial microstructural features with the wear behavior of the copper alloy layer under sliding friction conditions remains limited [21–23]. Therefore, this study aims to fabricate Cu-20Pb-5Sn/45 steel bimetallic composites using the solid–liquid composite method. The microstructure, bonding strength, and tribological performance of the interface and copper alloy layer were systematically investigated, elucidating their interaction mechanisms under tribological loads. These findings offer a novel design strategy for layered bimetallic materials, particularly in applications requiring synergistic high strength and wear resistance.

2. Materials and Methods

2.1. Preparation of Bimetallic Specimens

The Cu-20Pb-5Sn/45 Steel bimetallic material was prepared by the solid–liquid composite method. 45 steel was used as the solid matrix material, and the original microstructure was mainly composed of polygonal ferrite and pearlite. The Cu-20Pb-5Sn was used as the liquid material. Table 1 shows the actual composition of the bimetallic determined by the Germany SPECTRO-MAXX (SPECTRO Analytical Instruments, Kleve, Germany) type direct reading spectrometer.

Table 1. Main chemical composition of bimetallic materials (wt.%).

Component	C	Si	Mn	Pb	Sn	Zn	P	Ni	Cu	Fe
Cu-20Pb-5Sn	0	0	0	19.85	4.73	1.75	0.08	2.38	Bal.	0
45 Steel	0.45	0.21	0.68	0	0	0	0	0	0	Bal.

Figure 1a shows the process route of this experiment. The surface of the 45 steel substrate is contaminated with oil, rust, and oxide films, etc. Therefore, the surface of the substrate needs to be pre-treated before the solid–liquid composite process. Firstly, the steel substrate is ground with 240 # sandpaper to remove the rust and oxide films on the bonding surface. Then, it is immersed in NaOH (10%–15%) and HCL (10%–20%) solutions for 10 min each and subsequently cleaned with alcohol and dried. After the pre-treatment, a high-temperature active anti-oxidation coating ($Na_2B_4O_7$:$(CH_2OH)_2$ = 20:13) is applied to the surface of the steel substrate to prevent oxidation of the steel substrate during the

high-temperature preheating process. The preheating temperature of the steel substrate is 1150 ± 30 °C, and the preheating time is 30 ± 5 min. The pouring volume of each sample of copper alloy liquid is 500 g. The melting temperature is 1200 ± 30 °C. After the pure copper is melted, Ni, Zn, Pb, and Sn are added to the molten metal in sequence at intervals of 3–5 min according to their melting points from high to low. P is added to the copper liquid in the proportion of 1/3 for deoxidation and gas removal first. After adding all the other alloy elements, stirring is carried out with a graphite rod, and the remaining 2/3 is added to the alloy liquid. The bimetallic composite, prepared via the solid–liquid composite method, was sequentially cut from bottom to top into samples with thicknesses of 12.32 mm and 10 mm for microstructural analysis, friction performance testing, and shear strength evaluation. Figure 1b illustrates the sampling method for evaluating the microstructure and friction properties of the bimetallic material.

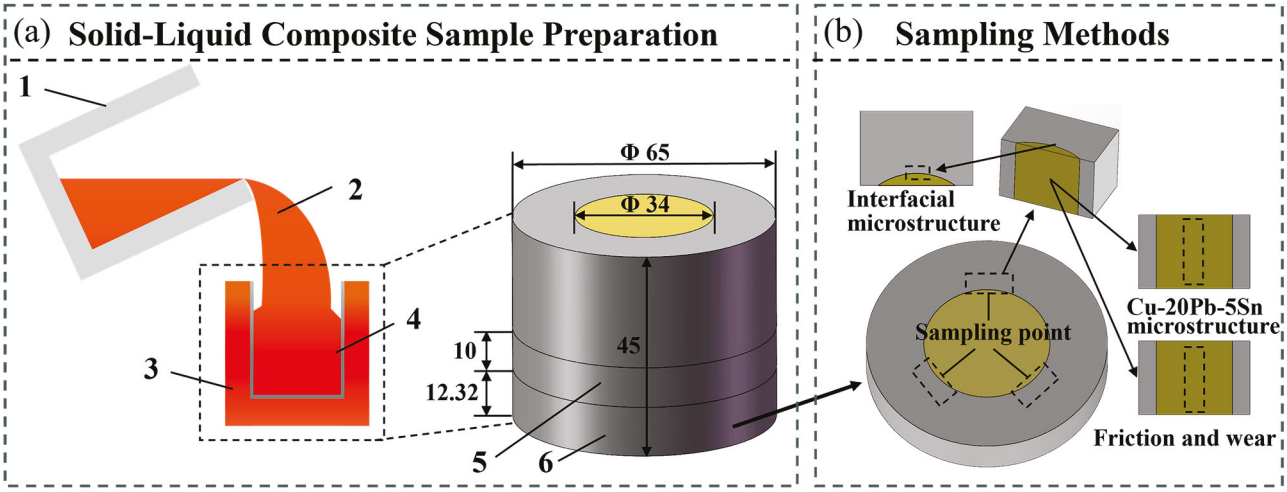


Figure 1. Schematic diagram for fabrication of Cu-20Pb-5Sn/45 Steel bimetallic composite materials: (**a**) Process route of the experiment; (**b**) Sampling methods. 1. Crucible; 2. Cu-20Pb-5Sn alloy liquid; 3. 45 Steel; 4. Active agent coating; 5. Shear strength test sample; 6. Microstructure and friction test sample.

2.2. Microstructure and Performance Characterization

The copper alloy layer of the bimetallic composite was etched for 90–120 s using a 1:3 ammonia ($NH_3 \cdot H_2O$) and hydrogen peroxide (H_2O_2) solution, while the steel side was wiped with a 5% nitric acid alcohol solution for 5 s. OM (Zeiss AXIO Scope.A1, Carl Zeiss Microscopy GmbH, Oberkochen, Germany) was performed to observe the microstructure of the bimetallic interface and copper alloy layer. SEM (Hitachi SU5000, Hitachi High-Tech Corporation, Tokyo, Japan) was carried out using a 20 kV accelerating voltage and 50 nA probe current to study the microstructural features of the interface and copper alloy layer. EDS (X-Max^n 50, Oxford Instruments, Oxford, United Kingdom) was employed to analyze atomic diffusion and phase distribution at the interface. EBSD (Symmetry S2, Oxford Instruments, Oxford, United Kingdom) was conducted using a 20 kV accelerating voltage, 10 nA probe current, and 0.5 μm step size to investigate crystal orientation, grain boundary angles, and grain size at the interface. TEM (FEI Titan Cubed Themis G2 300, Thermo Fisher Scientific, Hillsboro, OR, United States) was performed using a 300 kV accelerating voltage and 0.07 nm point resolution to characterize the crystal structure, solid-solution phases, and dislocation behavior at the interface.

Figure 2 illustrates the schematic for friction and wear testing and interfacial shear strength testing of the bimetallic samples. Friction tests were conducted using a ring-on-block configuration (MRH-3A friction testing machine, Jinan Hensgrand Instrument Co.,

Ltd., Jinan, China) under dry sliding conditions to evaluate the tribological performance of the copper alloy layer. As shown in Figure 2a, the copper alloy/steel bimetallic sample, a rectangular block, contacts a rotating ring-shaped counterbody. The copper alloy layer surface slides against the outer surface of the counterbody, with a normal load applied to the top of the sample perpendicular to the contact surface, generating friction force along the sliding. In the ring-on-block friction test, the maximum thickness of the copper alloy layer was maintained at 2 mm. The test conditions were as follows: ambient temperature, contact pressure of 0.66 MPa, sliding speed of 3.87 m/s, and test duration of 10 min. The counterbody was a GCr15 steel ring (HRC 60–62) with the following chemical composition (wt.%): C: 0.95%–1.05%, Si: 0.15%–0.35%, Mn: 0.25%–0.45%, Cr: 1.40%–1.65%, Fe: balance. The test aimed to simulate the dry friction conditions of a plunger pump cylinder during startup and early operation. The friction coefficient was recorded in real-time using a force sensor, and the wear rate was calculated using the formula $W = V/(F \cdot L)$, where V is the wear volume, F is the load, and L is the sliding distance. Each sample group was tested three times, and the average values were taken to minimize errors.

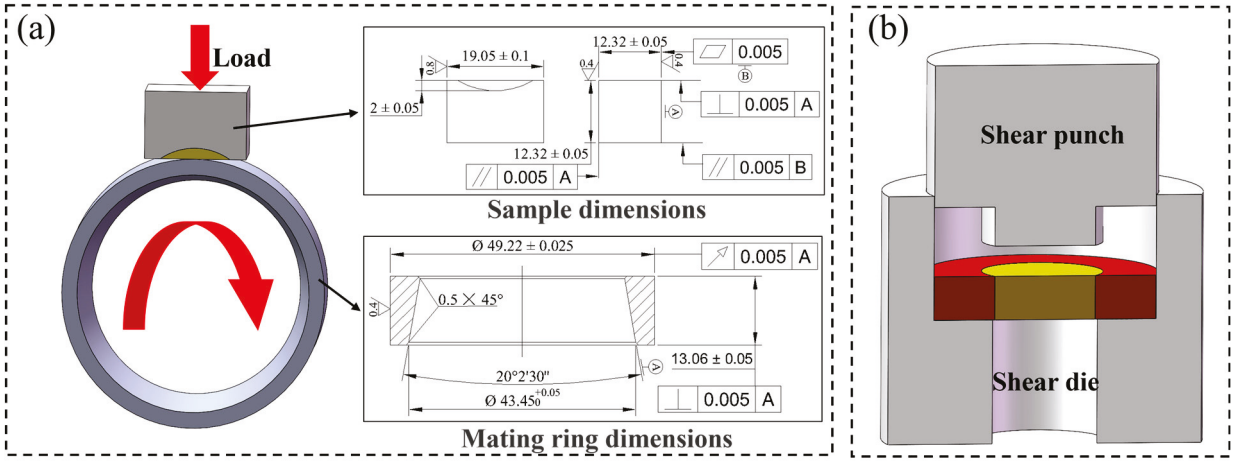


Figure 2. Schematic of friction and interfacial shear strength testing for bimetallic samples: (**a**) Schematic of the friction test; (**b**) Schematic of the shear test.

Shear strength testing at ambient temperature was conducted using a universal material testing machine (SUNS WAW-D, Shenzhen SUNS Technology Stock Co., Ltd., Shenzhen, China) to evaluate the bonding strength of the Cu-20Pb-5Sn/45 steel interface. The loading rate was maintained at $\leq$1 kN/s, and the interfacial shear strength was determined by averaging three test measurements. The shear strength was calculated using the formula $\tau = F/(\pi \cdot d \cdot h)$, where F is the maximum load, d is the interface diameter, and h is the thickness of the bimetallic sample, as illustrated in Figure 2b.

3. Results

3.1. Microstructure and Properties of Cu-20Pb-5Sn/45 Steel Bimetallic Interface

Figure 3 presents the microstructure of the Cu-20Pb-5Sn/45 Steel bimetallic composite fabricated via the solid–liquid composite method. A continuous, defect-free interface (free of inclusions, pores, or other defects) is formed between the copper alloy and steel layers. The microstructure on the steel side consists of a network of ferrite and lamellar pearlite. Additionally, a minor fraction of bainite is present, attributed to the rapid and non-uniform cooling conditions. The copper alloy layer is primarily composed of the copper-rich matrix, dendritic features, and free lead particles phases.

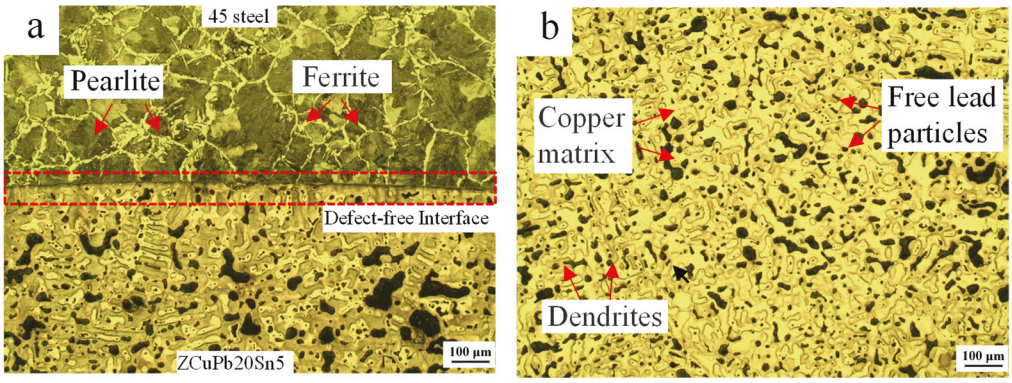


Figure 3. Cu-20Pb-5Sn/45 Steel interface and copper alloy layer microstructure: (**a**) Metallography at Cu-20Pb-5Sn/45 Steel interface; (**b**) Metallography at Cu-20Pb-5Sn alloy layer.

Figure 4 presents elemental line profiles of Cu and Fe concentrations across the Cu-20Pb-5Sn/45 Steel bimetallic interface, alongside the corresponding grain boundary distribution and grain size statistics. As evident in Figure 4a, mutual atomic diffusion occurs, forming a diffusion layer with an approximate thickness of 10.7 μm. Diffusion is predominantly characterized by Fe atoms migrating into the Cu side. The inverse pole figure (IPF) map in Figure 4b reveals that the diffusion layer forms a solid-solution interface, exhibiting an absence of pronounced crystallographic texture. Adjacent to the interface on the copper alloy side, the microstructure consists of columnar grains growing perpendicular to the interface. Furthermore, the average grain size in the copper alloy is significantly larger than that in the iron. Figure 4c displays the grain boundary misorientation angle distribution. Low-angle grain boundaries (LAGBs), represented by green lines, account for 62.2% of the total, while high-angle grain boundaries (HAGBs), indicated by black lines, constitute 37.8%. During shear deformation, LAGBs effectively dissipate dislocation propagation energy, whereas HAGBs impede dislocation transmission across the interface. This synergistic interaction contributes to enhanced interfacial strength [24]. During the solidification and cooling process, mutual diffusion of Fe and Cu atoms occurs at the interface. The increasing Fe concentration within the copper alloy layer near the interface refines its microstructure [18]. Which aligns with the finer grain structure observed in the copper alloy layer proximal to the interface in the IPF map.

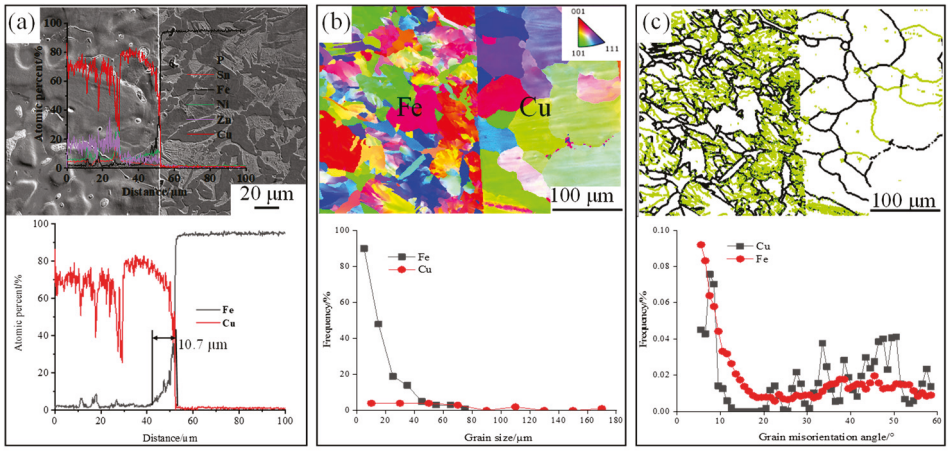


Figure 4. Microscopic characterization of the Cu-20Pb-5Sn/45 Steel interface: (**a**) Interface diffusion line scanning; (**b**) Grain size distribution; (**c**) Grain boundary orientation difference distribution.

Figure 5 presents the interfacial shear strength test results. The measured interfacial shear strength between the copper alloy and steel layers was 227.58 MPa. The shear

force-time curve reveals that the interfacial shear force increased gradually during the initial steady-state phase. This robust initial performance is attributed to the solid-solution diffusion layer, its refined microstructure featuring columnar grains oriented perpendicular to the interface, and the synergistic effect of high-angle and low-angle grain boundaries, collectively contributing to the high interfacial bond strength.

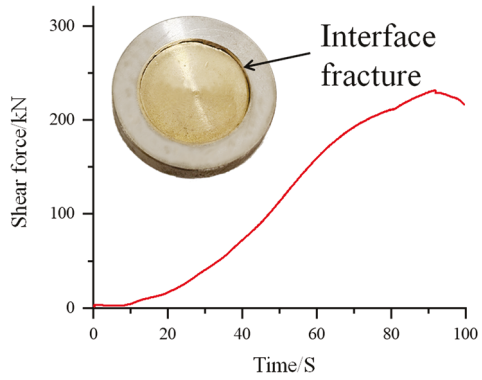


Figure 5. Cu-20Pb-5Sn/45 Steel interfacial shear strength.

3.2. Microstructure and Properties of Cu-20Pb-5Sn/45 Steel Bimetallic Copper Alloy Layer

Figure 6 shows the EDS mapping of element distributions in the copper alloy layer of the bimetallic composite. P and Ni exhibit dispersed dot and strip features, with closely aligned distributions. Pb is distributed as free particles within the matrix, Sn displays dendritic or segregated morphology, and Zn is uniformly distributed but at low concentration. Elemental compositions measured at different regions marked in Figure 6a are presented in Table 2. Location 1 corresponds to the Pb phase; at location 2, Sn has an atomic fraction of 15.19%, compared to 3.88% at location 4, indicating significant Sn segregation during solidification. At location 3, P combines with Cu to form the Cu_3P phase, which also contains a high Ni content. At location 4, Ni and Cu form a continuous solid-solution phase, identified as α-(Cu, Ni).

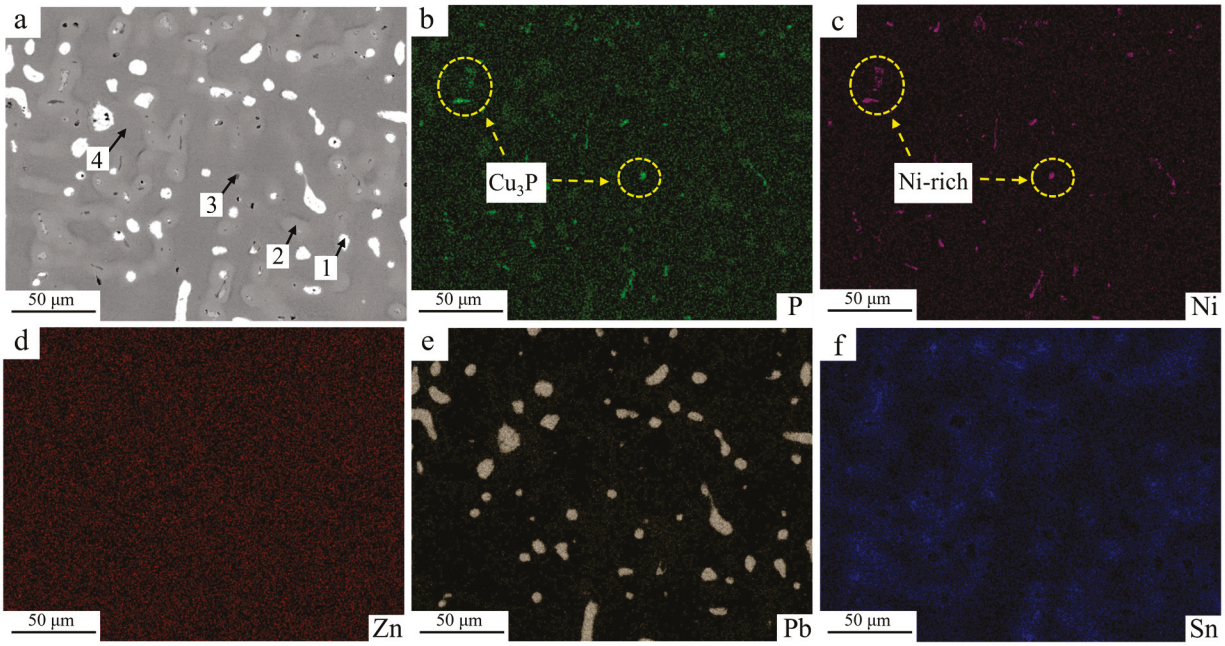


Figure 6. EDS element mapping of different element distributions in bimetallic copper alloy layer: (**a**) SEM morphology; (**b**) P surface distribution; (**c**) Ni surface distribution; (**d**) Zn surface distribution; (**e**) Pb surface distribution; (**f**) Sn surface distribution.

Table 2. Elemental content at different positions in Figure 6a.

Location	at.%					
	Cu	**Zn**	**Sn**	**P**	**Ni**	**Pb**
1	12.8	1.34	1.42	5.04	3.45	75.95
2	77.31	1.06	15.19	4.39	1.82	0.23
3	65.12	0.26	0.36	24.77	9.46	0.03
4	83.2	1.9	3.88	0.31	10.66	0.05

In the molten state, the atomic radius of P (0.17 Å) is smaller than that of Cu (1.57 Å), facilitating preferential diffusion toward primary dendrite arms [25]. During solidification, the Cu_3P phase precipitates at the liquid front, influenced by the non-equilibrium solidification of the solid–liquid composite method, leading to Ni segregation from the α-(Cu,Ni) phase and precipitation of a Ni-rich phase near Cu_3P. Consequently, the distributions of P and Ni are closely aligned, as observed in Figure 6b,c.

To prevent interference from thermal effects or debris accumulation caused by extended wear testing, the tribological properties of the copper alloy layer in the Cu-20Pb-5Sn/45 steel bimetallic composite were assessed under dry sliding conditions over a 10 min duration. As depicted in Figure 7, the friction coefficient stabilizes at 0.14–0.15 after an initial run-in period of approximately 2 min, maintaining consistency for the remaining 8 min. This stability signifies the establishment of a uniform frictional interface following the run-in phase. The wear rate was 7.3665×10^{-6} $mm^3/(N \cdot m)$, indicating that no significant material loss occurred within 10 min, consistent with the characteristics of stable contact under low-pressure post–run-in conditions.

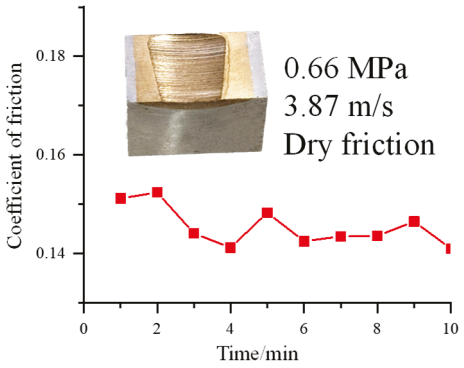


Figure 7. Copper alloy layer friction coefficient curve.

Figure 8 presents the elemental mapping of the copper alloy layer surface after wear testing. Figure 8a shows the SEM morphology of the copper alloy layer, revealing parallel and continuous grooves on the worn surface, with no deep pits or cracks. A small amount of detached particles or wear debris is observed between the grooves, indicating uniform wear tracks without large-scale delamination or adhesive marks. Figure 8b illustrates the distribution of Pb, which appears as dispersed white spots, with some Pb particles embedded within the grooves or at surface protrusions. The absence of significant Pb detachment or aggregation suggests the formation of a Pb film during friction, contributing to self-lubrication. Figure 8c,d show relatively uniform distributions of Cu_3P and Ni-rich phases, with minimal overlap with the grooves, indicating that these hard phases form a composite structure that resists wear. The elemental distributions reveal that Pb acts as a soft phase dispersed throughout the matrix, while P and Ni form hard phase agglomerates. No significant oxide or transfer layers are observed on the post-wear surface, indicating mild wear. The cutting and plowing actions of the counterbody on the copper alloy layer during sliding confirm abrasive wear as the dominant wear mechanism.

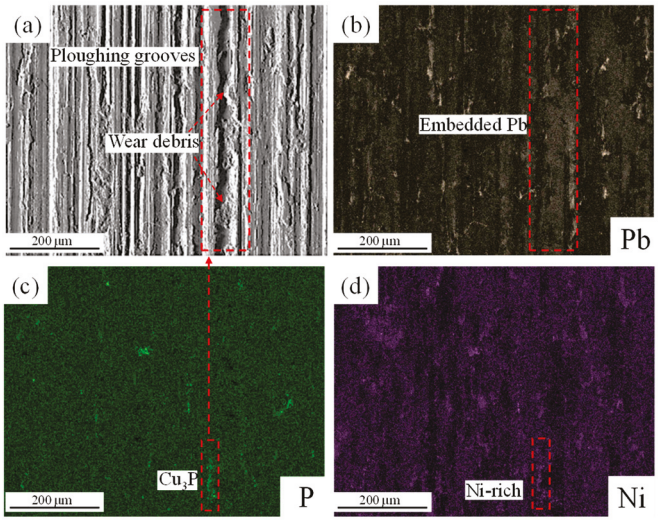
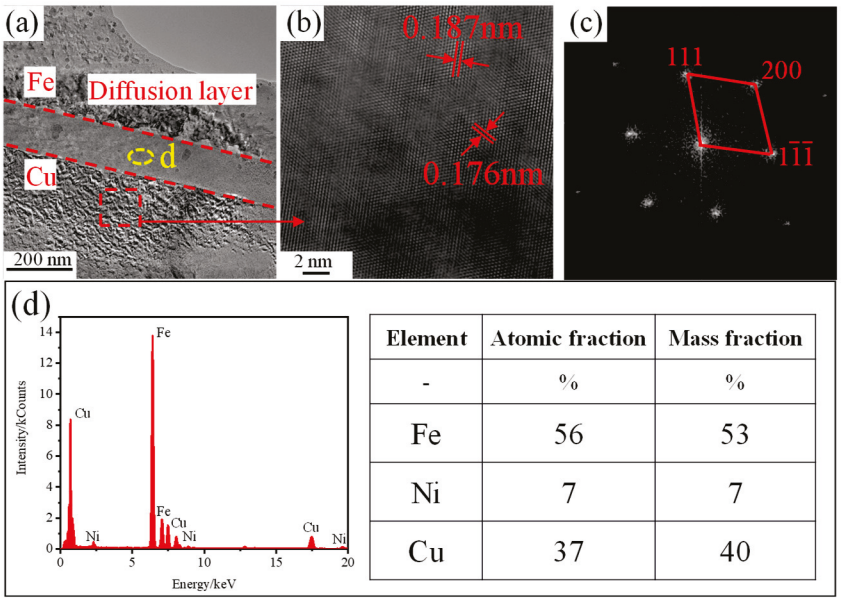


Figure 8. Scanning of the elemental surface of the copper alloy layer after friction: (**a**) SEM morphology; (**b**) Pb surface distribution; (**c**) P surface distribution; (**d**) Ni surface distribution.

3.3. Interface Diffusion and Copper Alloy Layer Wear of the Mechanism Behavior

The microstructure and morphology of the interfacial diffusion layer were characterized using bright-field transmission electron microscopy (TEM), as shown in Figure 9. Figure 9b,c reveal variations in lattice constants across different orientations, indicating the formation of an α-(Cu,Ni) phase due to Ni solid solution in the Cu matrix. Point-scan analysis of the interfacial diffusion layer, presented in Figure 9d, confirms the presence of both α-(Cu,Ni) and α-Fe phases. During the solid–liquid composite process, Ni, with an atomic radius of 1.62 Å, closely matches that of Cu (1.57 Å), facilitating its solid solution in the Cu matrix and enhancing the lattice stability of the Cu-based phase [26]. Mutual diffusion of Fe and Cu atoms occurs at the interface, resulting in partial dissolution of Fe atoms into the copper alloy matrix, forming a metallurgically bonded α-(Cu,Ni)/α-Fe solid-solution interface.



Element	Atomic fraction	Mass fraction
-	%	%
Fe	56	53
Ni	7	7
Cu	37	40

Figure 9. TEM bright field image and calibration of solid solution interface: (**a**) TEM bright field image; (**b**) High-resolution imaging of the copper alloy side at the interface; (**c**) Selected area electron diffraction; (**d**) Point-scan analysis of the diffusion layer.

Figure 10 illustrates the schematic architecture of the Cu-20Pb-5Sn/45 steel bimetallic system under frictional conditions. The combined effects of applied load and transient frictional heating induce several phenomena at the contact surface of the copper alloy layer, including plastic deformation, grain refinement, work hardening, oxidation reactions, and phase transformations [27,28]. These near-surface modifications impose significant transient shear stresses on the underlying interface, requiring robust interfacial bond strength to prevent catastrophic instantaneous fracture at the interface.

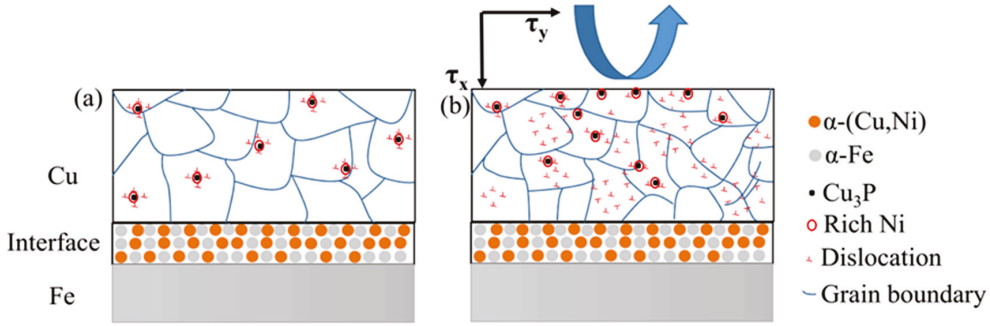


Figure 10. Frictional microstructural evolution of Cu-20Pb-5Sn/45 Steel bimaterial system: (**a**) Structure before wear; (**b**) Structure after wear.

The presence of the α-(Cu,Ni)/α-Fe solid-solution interface creates a natural barrier to dislocation propagation. Under frictional loads, shear stresses are transmitted through the copper alloy layer to the interface, inducing dislocation motion and accumulation [29]. The incorporation of Ni increases lattice distortion in the α-(Cu,Ni) phase, impeding further dislocation transmission toward the 45 steel side. This dislocation-blocking effect reduces stress concentration at the interface, ensuring structural integrity under high shear stresses and significantly enhancing interfacial bonding strength. As friction progresses, the increasing dislocation density leads to accumulation and entanglement within the copper alloy matrix [30,31]. When these stresses propagate to the interface, the solid-solution layer effectively hinders further dislocation transmission, as evidenced by the observed dislocation pile-up at the α-(Cu,Ni)/α-Fe boundary, shown in Figure 11. This blocking mechanism minimizes the risk of interfacial delamination, ensuring stable frictional behavior.

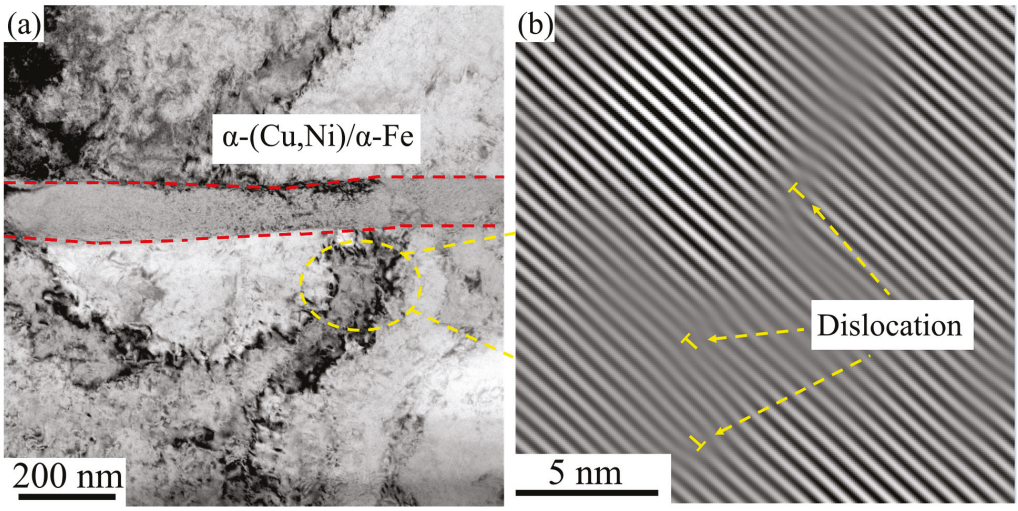


Figure 11. TEM observation of dislocation propagation hindered by solid-solution interface: (**a**) α-(Cu,Ni)/α-Fe interface exhibiting dislocation distribution; (**b**) High-resolution view of dislocation propagation within the structure.

4. Conclusions

The Cu-20Pb-5Sn/45 steel bimetallic composites, fabricated via the solid–liquid composite method, were systematically investigated for their interfacial and copper alloy layer microstructure and performance, yielding the following conclusions:

(1) The Cu-20Pb-5Sn/45 steel interface forms a metallurgically bonded α-(Cu,Ni)/α-Fe diffusion layer with an interfacial shear strength of 227.58 MPa. This high bonding strength results from the synergistic contribution of fine columnar grains in the diffusion layer and the interplay of high- and low-angle grain boundaries.

(2) Under dry sliding conditions, the copper alloy layer exhibits a stable friction coefficient of 0.145 and a low wear rate of 7.3665×10^{-6} $mm^3/(N \cdot m)$. The excellent tribological performance is primarily attributed to the α-(Cu,Ni) matrix reinforced by hard Cu_3P and Ni-rich phases, which resist frictional shear stresses, while dispersed Pb particles provide self-lubricating properties.

(3) The α-(Cu,Ni)/α-Fe solid-solution interface effectively impedes dislocation propagation to the diffusion layer under frictional loads, reducing dislocation pile-up. This interfacial blocking effect, combined with the hard phases and self-lubricating Pb particles in the copper alloy layer, ensures stable frictional behavior during sliding.

Significant challenges remain in quantitatively correlating the microstructural evolution at the interface with friction-induced dynamic stresses in Cu-20Pb-5Sn/45 steel bimetallic composites. Real-time characterization of the dynamic microstructural changes in the copper alloy layer and interface under frictional loads is critical yet complex, limiting the broader application of these materials. Future research should integrate advanced in situ characterization techniques with multi-scale simulation methods to capture the real-time interactions between dislocations and the interface. Additionally, exploring lead-free alloying strategies and innovative interface design approaches could enable the simultaneous achievement of high strength and long-term tribological stability.

Author Contributions: Conceptualization, Y.K. and G.Z.; data curation, Y.L.; formal analysis, Y.K. and Y.H.; funding acquisition, Y.K.; investigation., Y.L. and Y.H.; project administration, Y.H.; validation, Y.K. and Y.H.; writing—original draft, Y.K., G.Z. and Y.L.; writing—review and editing, Y.K., G.Z., Y.L. and Y.H. All authors have read and agreed to the published version of the manuscript.

Funding: This research was funded by the Shanxi Provincial Basic Research Program Young Scientists Fund (Grant No. 202303021222228) and the Scientific and Technological Innovation Programs of Higher Education Institutions in Shanxi (Grant No. 2023L381).

Institutional Review Board Statement: Not applicable.

Informed Consent Statement: Not applicable.

Data Availability Statement: All data generated or analyzed during this study are included in this published article.

Conflicts of Interest: Author Yanling Hu was employed by the company China Shipbuilding Group Fenxi Heavy Industry Co., Ltd. The remaining authors declare that the research was conducted in the absence of any commercial or financial relationships that could be construed as a potential conflict of interest.

References

1. Osipovich, K.; Vorontsov, A.; Chumaevskii, A.; Gurianov, D.; Shamarin, N.; Savchenko, N.; Kolubaev, E. Characterization of a Bimetallic Multilayered Composite "Stainless Steel/Copper" Fabricated with Wire-Feed Electron Beam Additive Manufacturing. *Metals* **2021**, *11*, 1151. [CrossRef]
2. Senatore, A.; Risitano, G.; Scappaticci, L.; D'andrea, D. Investigation of the Tribological Properties of Different Textured Lead Bronze Coatings under Severe Load Conditions. *Lubricants* **2021**, *9*, 34. [CrossRef]

3. Schlegel, F.; Schmitz, K. Geometric design of axial piston machine slipper-bearings made of high-performance plastics. *Forsch. Ingenieurwesen* **2025**, *89*, 1–12. [CrossRef]
4. Bandyopadhyay, A.; Zhang, Y.; Onuike, B. Additive manufacturing of bimetallic structures. *Virtual Phys. Prototyping.* **2022**, *17*, 256–294. [CrossRef]
5. Anand, A.; Sharma, S.M. High Temperature Friction and Wear Characteristics of Fe–Cu–C Based Self-Lubricating Material. *Trans. Indian Inst. Met.* **2017**, *70*, 2641–2650. [CrossRef]
6. Perini, M.; Silvestri, A.T. Multi-material bronze-steel plain bearings produced by laser-directed energy deposition. *Rapid Prototyp. J.* **2024**, *30*, 325–335. [CrossRef]
7. Pervikov, A.; Khrustalyov, A.; Filippov, A.; Mironov, Y.; Lozhkomoev, A.; Lerner, M.; Tarasov, S. Structural, Mechanical, and Tribological Characterization of Magnetic Pulse Compacted Fe–Cu Bimetallic Particles Produced by Electric Explosion of Dissimilar Metal Wires. *Metals* **2019**, *9*, 1287. [CrossRef]
8. Zykova, A.; Chumaevskii, A.; Vorontsov, A.; Kalashnikov, K.; Gurianov, D.; Gusarova, A.; Kolubaev, E. Evolution of microstructure and properties of Fe-Cu, manufactured by electron beam additive manufacturing with subsequent friction stir processing. *Mater. Lett.* **2022**, *307*, 131023. [CrossRef]
9. Zhang, Y.; Shi, Z.; Wang, Z.; Chen, H.; Zhao, L.; Li, Y.; Zhang, G.; Xing, M.; Ren, X.; Xu, H. Study on the bonding mechanism and performance optimization of Cu-12Sn-2Ni/42CrMo bimetallic interface controlled by Ag doping. *J. Mater. Res. Technol.* **2025**, *38*, 3277–3290. [CrossRef]
10. Shi, Z.; Zhang, Y.; Zhang, G.; Xu, H.; Ren, X. Effect of electromagnetic stirring current on the microstructure, mechanical and tribological properties of copper/steel bimetal. *Mater. Today Commun.* **2025**, *47*, 113126. [CrossRef]
11. Peng, T.; Yan, Q.; Li, G.; Zhang, X. The Influence of Cu/Fe Ratio on the Tribological Behavior of Brake Friction Materials. *Tribol. Lett.* **2017**, *66*, 18. [CrossRef]
12. Singh, V.; Raja, P.; Katiyar, J.K.; Ramkumar, P. Effect of friction modifiers compositions on tribological properties of Cu-Sn alloy/Al_2O_3 brake composite material. *Proc. Inst. Mech. Eng. Part J J. Eng. Tribol.* **2020**, *235*, 1541–1550. [CrossRef]
13. D'ANdrea, D.; Epasto, G.; Bonanno, A.; Guglielmino, E.; Benazzi, G. Failure analysis of anti-friction coating for cylinder blocks in axial piston pumps. *Eng. Fail. Anal.* **2019**, *104*, 126–138. [CrossRef]
14. Equey, S.; Houriet, A.; Mischler, S. Wear and frictional mechanisms of copper-based bearing alloys. *Wear* **2011**, *273*, 9–16. [CrossRef]
15. Wang, X.; Tang, B.; Wang, L.; Wang, D.; Dong, W.; Li, X. Microstructure, Microhardness and Tribological Properties of Bronze–Steel Bimetallic Composite Produced by Vacuum Diffusion Welding. *Materials* **2022**, *15*, 1588. [CrossRef]
16. Liu, J.; Miao, Y.; Wang, Z.; Zhao, Y.; Wu, Y.; Li, C. Improved interfacial strength in bimetallic additive manufacturing of aluminum bronze/steel by controlling interface melting. *J. Manuf. Process.* **2024**, *121*, 333–342. [CrossRef]
17. Mašović, R.; Miler, D.; Čular, I.; Jakovljević, S.; Šercer, M.; Žeželj, D. The Effect of Steel Electropolishing on the Tribological Behavior of a Steel–Bronze Pair in the Mixed and Boundary Lubrication Regimes. *Lubricants* **2023**, *11*, 325. [CrossRef]
18. Rodrigues, T.A.; Bairrão, N.; Farias, F.W.C.; Shamsolhodaei, A.; Shen, J.; Zhou, N.; Maawad, E.; Schell, N.; Santos, T.G.; Oliveira, J. Steel-copper functionally graded material produced by twin-wire and arc additive manufacturing (T-WAAM). *Mater. Des.* **2022**, *213*, 110270. [CrossRef]
19. El-Husseiny, M.M.; Baraka, A.A.; Oraby, O.; El-Danaf, E.A.; Salem, H.G. Fabrication of Bimetallic High-Strength Low-Alloy Steel/Si-Bronze Functionally Graded Materials Using Wire Arc Additive Manufacturing. *J. Manuf. Mater. Process.* **2023**, *7*, 138. [CrossRef]
20. Demirsöz, R. Wear Behavior of Bronze vs. 100Cr6 Friction Pairs under Different Lubrication Conditions for Bearing Applications. *Lubricants* **2022**, *10*, 212. [CrossRef]
21. Wang, Y.; Gao, Y.; Li, Y.; Zhai, W.; Sun, L.; Zhang, C. Review of preparation and application of copper–steel bimetal composites. *Emerg. Mater. Res.* **2019**, *8*, 538–551. [CrossRef]
22. Jadhav, S.; Kusekar, S.; Belure, A.; Digole, S.; Mali, A.; Cheepu, M.; Mugale, M.; Alkunte, S.; Kim, D. Recent Progress and Scientific Challenges in Wire-Arc Additive Manufacturing of Metallic Multi-Material Structures. *J. Manuf. Mater. Process.* **2025**, *9*, 284. [CrossRef]
23. Yi, H.; Meng, X.; Chen, Y.; Cao, H. A review of multi-material composite gears: Integration of lightweight and transmission performance. *Thin-Walled Struct.* **2025**, *216*, 113666. [CrossRef]
24. Kondo, S.; Mitsuma, T.; Shibata, N.; Ikuhara, Y. Direct observation of individual dislocation interaction processes with grain boundaries. *Sci. Adv.* **2016**, *2*, e1501926. [CrossRef] [PubMed]
25. Dudina, D.V.; Tokarev, V.G. Copper matrix composites with metallic reinforcements. *Trans. Indian Inst. Met.* **2025**, *78*, 113. [CrossRef]
26. Drescher, S.; Kuzmin, A.; Welter, E.; Freudenberger, J.; Smekhova, A. Component-dependent lattice distortions and atomic scale insights in multi-component Au-Cu-Ni-Pd-Pt based alloys. *Nano Res.* **2025**, *18*, 94907122. [CrossRef]

27. Rau, J.S.; Balachandran, S.; Schneider, R.; Gumbsch, P.; Gault, B.; Greiner, C. High diffusivity pathways govern massively enhanced oxidation during tribological sliding. *Acta Mater.* **2021**, *221*, 117353. [CrossRef]
28. Greiner, C.; Liu, Z.; Schneider, R.; Pastewka, L.; Gumbsch, P. The origin of surface microstructure evolution in sliding friction. *Scr. Mater.* **2018**, *153*, 63–67. [CrossRef]
29. Haug, C.; Ruebeling, F.; Kashiwar, A.; Gumbsch, P.; Kübel, C.; Greiner, C. Early deformation mechanisms in the shear affected region underneath a copper sliding contact. *Nat. Commun.* **2020**, *11*, 1–8. [CrossRef]
30. Ruebeling, F.; Xu, Y.; Richter, G.; Dini, D.; Gumbsch, P.; Greiner, C. Normal Load and Counter Body Size Influence the Initiation of Microstructural Discontinuities in Copper during Sliding. *ACS Appl. Mater. Interfaces* **2021**, *13*, 4750–4760. [CrossRef]
31. Singh, A.; Dao, M.; Lu, L.; Suresh, S. Deformation, structural changes and damage evolution in nanotwinned copper under repeated frictional contact sliding. *Acta Mater.* **2011**, *59*, 7311–7324. [CrossRef]

Disclaimer/Publisher's Note: The statements, opinions and data contained in all publications are solely those of the individual author(s) and contributor(s) and not of MDPI and/or the editor(s). MDPI and/or the editor(s) disclaim responsibility for any injury to people or property resulting from any ideas, methods, instructions or products referred to in the content.

coatings

MDPI

Article

Study of Surface Wear of Punches and Molds for Optimization of Nuclear Fuel Production

Bauyrzhan Rakhadilov [1,2], Nurtoleu Magazov [1,2], Aidar Kengesbekov [1,2,*], Manarbek Kylyshkanov [3] and Arystanbek Kussainov [1,2]

[1] Plasma Science LLP, Ust-Kamenogorsk 070000, Kazakhstan; rakhadilovb@gmail.com (B.R.); magazovn@gmail.com (N.M.); arys20055@gmail.com (A.K.)
[2] Scientific Center "Protective and Functional Coatings", D. Serikbayev East Kazakhstan Technical University, Ust-Kamenogorsk 070000, Kazakhstan
[3] Ulba Metallurgical Plant JSC, Ust-Kamenogorsk 070000, Kazakhstan; kylyshkanov@mail.ru
* Correspondence: aidar.94.01@mail.ru; Tel.: +7-777-245-2066

Abstract

This paper presents the results of a comprehensive study of the wear processes of press tools used in the molding of uranium dioxide (UO_2) nuclear fuel pellets. Particular attention is paid to the analysis of the influence of operating conditions on changes in microstructure, geometry and physical and mechanical properties of working surfaces of molds and punches. The studies using scanning electron microscopy (SEM), X-ray fluorescence (XRF) and X-ray phase analysis (XRD) methods, as well as evaluation of microhardness and roughness, allowed to identify the dominant failure mechanisms—abrasive and adhesive wear, microcrack formation and local degradation of coatings. The results of the experiments confirmed the presence of progressive changes on the working surfaces of the tool, affecting the formation of defects of fuel pellets and reducing the service life of the press equipment. This work allows us to not only better understand the wear patterns in the batch production of nuclear fuel, but also to formulate practical recommendations to increase tool life by optimizing pressing modes and using wear-resistant coatings.

Keywords: mold; punch; uranium dioxide; wear; metallography; X-ray fluorescence analysis

1. Introduction

The development of nuclear power requires the improvement of operational reliability and economic efficiency of all stages of the nuclear fuel cycle. The wear of press tools used in the molding of UO_2 pellets has a significant impact on product quality, increasing the probability of defects and increasing the reject rate. These problems can reduce the efficiency of the production process and increase the risk of fuel failures in the reactor [1].

Although there is a large amount of research devoted to the thermal and structural characteristics of fuel pellets, a comprehensive study of mechanical factors such as punch and die wear is not sufficiently covered. Given the importance of ensuring accurate pellet geometry, especially when using advanced fuel additives and coatings, this work fills an existing gap [2]. As part of the global transition to higher efficiency and more sustainable fuel solutions (e.g., with improved thermal conductivity or the addition of neutron absorbers), attention to the details of the manufacturing process, including the condition of the press tool, becomes paramount [3].

There are several nuclear fuel materials available worldwide. The most utilized fuel material is uranium, and it is most often utilized in the oxide form in pellet form. These

fuel pellets are placed inside thin metal tubes that are assembled in bundles to become the fuel elements for the core of the reactor. UO_2 has a very high melting point—2865 °C (compared with uranium metal—1132 °C)—which allows nuclear reactors to operate much hotter. UO_2 is chemically and physically more stable in reactor environments. A key disadvantage of UO_2 is its low thermal conductivity at high temperatures and its reduction in radiation damage (burnup). The most common form of uranium in a light-water reactor is as UO_2. The enriched UF6 is transported to a fuel fabrication plant where the UF6, in solid form in containers, is again heated to its gaseous form and the UF6 gas is chemically processed to form uranium dioxide (UO_2) powder. This powder is then mixed with various additives to enable achievement of the final required fuel pellet density. Additives may be U3O8, lubricants, pore formers, and burnable poisons such as gadolinium. The topic is undoubtedly relevant since there is a large amount of research into uranium-based nuclear fuel [4–9].

Nuclear fuel is a carefully manufactured solid substance of a certain shape and size. The process begins by pressing either natural or enriched UO_2 powder into small cylindrical shapes, measuring about 10–13 mm in length and 8–13.5 mm in diameter. In addition, the commercial tablets have a unique end face geometry. The end face is designed with a recess called a "plate" in the center to accommodate differential thermal expansion and plastic flow in the center of the cylinder due to the high internal temperature of the pellet during reactor operation. In addition, the edges of the pellet are beveled to reduce chipping and stress concentration in the shell when the pellet expands and interacts with the surrounding shell. This geometry is incorporated into the tablet during the manufacturing process and is not machined after the tablet is manufactured. Currently, uranium dioxide (UO_2) is used as the standard nuclear fuel in fission nuclear reactors and has been extensively studied since the sixties [10]. During the formation of nuclear fuel pellets from uranium dioxide powders, continuity failures (cracks) may occur, which leads to pellet rejects and increases their production cost. In works, the profile of the inner cavity of matrices for forming of products was substantiated and it was revealed that inhomogeneous character of the process of molding of presses (discontinuous, stepwise) can determine the appearance of cracks, and homogeneous character contributes to the reduction in the number of rejected products and creates prerequisites for increasing productivity at the molding operation. However, at certain modes of molding with the subsequent ejection of pressings, cracks are formed on their ends, which contribute to the appearance of spalling on the side of the ejector (lower) punch (Figure 1).

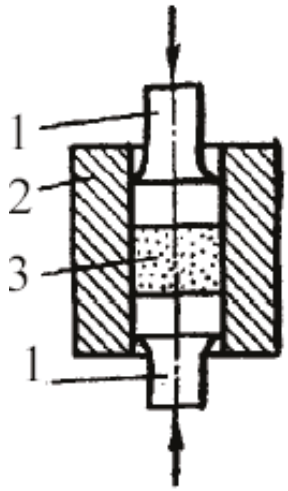


Figure 1. Scheme of double-sided pressing 1—Punches, 2—Mold, 3—Press powder.

The process of molding of nuclear fuel pellets is an important stage of production as the operational reliability of the final product depends on its quality. The main problem is the wear of molds and punches (Figure 1), which leads to an increased reject rate, deterioration of geometry and mechanical characteristics of pellets. It is important to understand the mechanisms of wear, assess their impact on the quality of molded products and develop methods to minimize them.

The purpose of this work is to analyze the wear of the inner cavity of the matrix and punch faces after their long-term operation to identify the main mechanisms of destruction and to develop recommendations for extending the service life of the press tool.

2. Materials and Methods

2.1. Materials

As the material of the study was chosen, the matrix (steel 45) of the press mold as well as the upper and lower punch were coated with Xtv9 (Figure 2) after cyclic loading of nuclear fuel pellets. Steel 45 is a medium carbon structural steel, often used in mechanical engineering for stressed parts. Chemical composition: Carbon (C)—0.45%–0.50%, Silicon (Si)—up to 0.40%, Manganese (Mn)—0.50%–0.80%, Sulfur (S) and Phosphorus (P)—no more than 0.035% in total, Other elements (iron)—up to 100%. Tensile strength—about 600–750 MPa depending on heat treatment. Yield strength is 400–500 MPa. After normalization and hardening, steel 45 has a hardness of about 170–250 HB. Impact toughness: 30–50 J/cm^2, which makes the material quite resistant to fracture under impact loads. Figure 3 shows a schematic of the matrix drawing. Examples of studies in which steel 45 was used are given in [11–13].

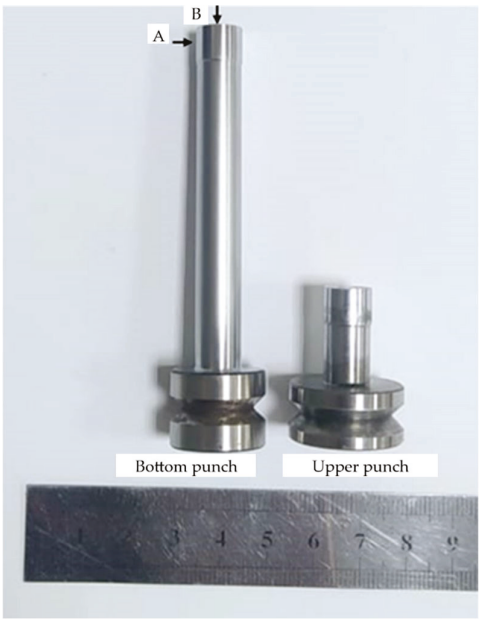


Figure 2. Punch coated with Xtv9 working face (A) and side surface (B).

Xtv9 coating is a thermodiffusion coating that is applied to parts subjected to high wear and thermal loads, such as punches and dies in the process of pressing nuclear fuel pellets. Chemical composition: Titanium (Ti) is the main chemical substance that gives the coating high strength. Cobalt (Co) is used to improve heat resistance. Chromium (Cr) improves wear resistance. Nickel (Ni) improves overall corrosion resistance and adhesion of the coating to the substrate. Xtv9 coating is characterized by high hardness, reaching 850–1000 HV (depending on the coating thickness). This allows for significantly improving the wear resistance of molds and punches, which are subjected to prolonged

cyclic loading. The coating is able to withstand temperatures up to 800–900 °C, which is important for high temperature applications typical of pressing nuclear fuel pellets. Xtv9 significantly improves the wear resistance of the material, making it ideal for use under cyclic mechanical loading conditions. This coating reduces the number of defects on the surface of the punches and dies, which in turn reduces the likelihood of defects in the pellets themselves. The coating also protects the metal from corrosive substances, which is important when working with nuclear fuel materials that can be chemically active. Examples of work with used Xtv9 [14–17].

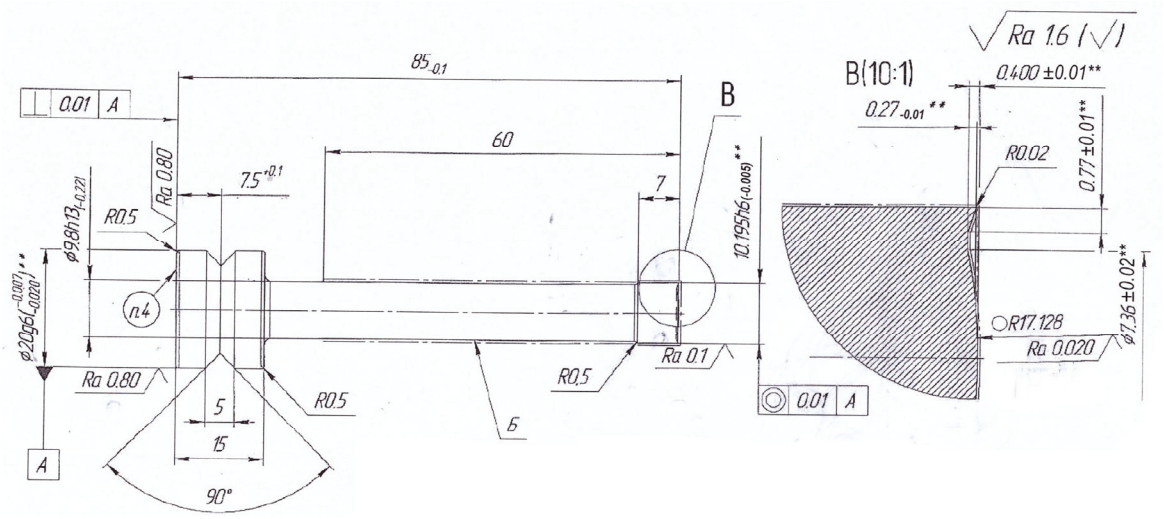


Figure 3. Schematic drawing of poisson lower. ** marks critical, tightly-toleranced dimensions.

2.2. Research Methods

For the cross-sectional study and coating thickness analysis, the punch was cut using a precision cutting machine to minimize deformation and damage to the structure. Fragments including the working face and side surface (sections A and B) were cast in epoxy resin for ease of further processing. After polymerization of the resin, a standard metallographic preparation procedure was performed, including sequential grinding on abrasive paper and polishing using diamond suspensions to obtain a mirror-like surface.

Metallographic studies were performed to analyze the surface wear, microstructural defects, microcracks and local plastic deformations of the punch. Using a metallographic microscope model Altami MET 5S (Altami, Russia, Moscow), the surface of the sample was photographed at 5 times optical magnification.

For detailed analysis of the morphology of worn surfaces, detection of local defects, mechanical damage and wear fractions, a JEOL JSM-6610LV (JEOL Ltd. Akishima, Tokyo, Japan) scanning electron microscope with energy dispersive analysis at an accelerating voltage of 15 kV was used. There is an example of work with this microscope [18] and also works where many results with SEM are shown [19,20]. To prepare the material for the study, the samples were fixed on a conductive tape. Since the samples under study were on epoxy resin, a conductive carbon layer was applied on them using a Quorum Q150R ES (Quorum technologies Ltd. Ashford, Kent, UK) sputtering machine.

Roughness plays a key role in wear assessment as changes in surface microrelief directly affect press quality and tool life. Roughness was evaluated via the standard method (GOST-2789-73 [21]) using a profilometer model 130. Roughness parameters were used to describe surface microgeometry: Rt—total profile height, Rz—maximum profile height, Ra—average deviation of profile from the center line. The measurement was carried out in 3 places 10 times along the entire length of the matrix circumference with a step—2.669 mm, ϑ = 0.5 mm/s, Rt = 500 μm, L = 15 mm as shown in Figure 4.

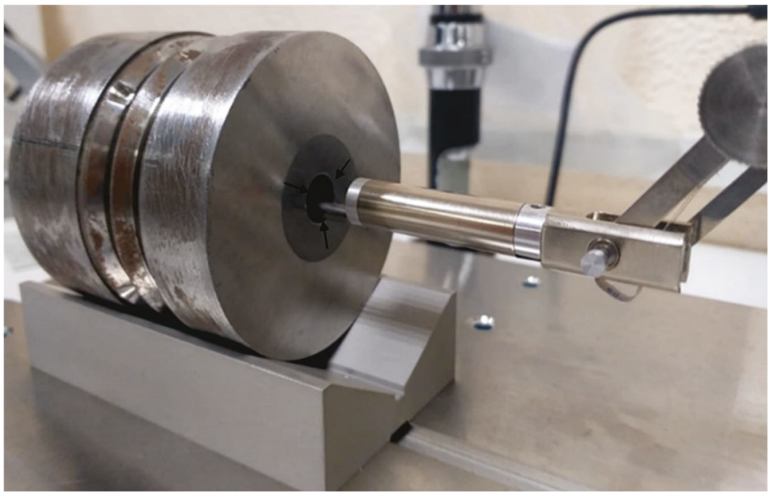


Figure 4. The process of matrix examination on the profilometer.

Important information about the fracture mechanism is provided by analyzing the structure of the wear groove (on the sample). Tribological testing. Ball-on-disk tests (Anton Paar TRB3) were performed at room temperature in dry conditions using a 100Cr6 ball (radius 6 mm). The normal load was 2 N; the wear track radius R = 3 mm. The prescribed sliding distance was S = 50 m, corresponding to N $\approx$ 2653 revolutions (circumference $2\pi R$ = 18.85 mm), with a linear speed of v = 30 mm·s^{-1}, giving a test duration of ~1667 s (~27.8 min). The wear scar width/depth were quantified ex situ; the coefficient of friction was recorded in situ. Testing followed ASTM G99/G133 guidance [22].

Further, in order to measure the degree of hardening or softening of the tool material as a result of operation, microhardness measurement was carried out. Vickers microhardness (HV0.05/10) was measured per GOST 9450-76/ISO 6507-1 [23,24] on a METOLAB-502 tester (Metolab, Moskow, Russia): 0.05 kgf load, 10 s dwell. In each zone (A, B), n = 10 indents were made with spacing $\geq$3d to avoid interaction. Results are reported as mean $\pm$ SD (95% CI).

To identify changes in the chemical composition of the working surface and to assess the possible loss of alloying elements, X-ray fluorescence analysis of the surface of the samples was carried out. The research was carried out on the X-ray fluorescence spectrometer S1 TITAN (Bruker, Billerica, MA, USA) (50 kV, 40 μA, Metals mode, 8 mm collimator), based on the use of miniature X-ray tube technology, which is an automated autonomous portable device that provides measurement, information processing, its registration and storage, and is designed to work in laboratory and field conditions. The operating principle of the device is based on the energy dispersive X-ray fluorescence spectral method of analysis. To study the samples we select the mode of metals on the device. We examine each sample by bringing the instrument close to the sample, perpendicular to the sample. Each examination takes 60 s before the instrument signals its completion. In studying the capabilities of this method, the punch before and after operation were selected as objects of study. The measurement was carried out at 3 locations as shown in Figure 5.

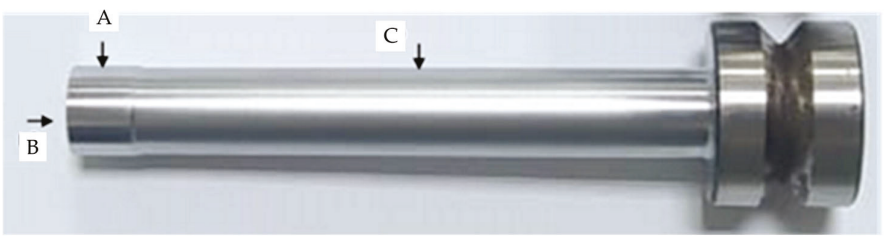


Figure 5. Top punch working face (A), side surface (B) and not working surface (C).

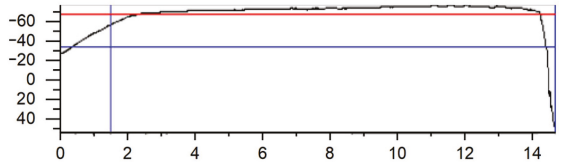
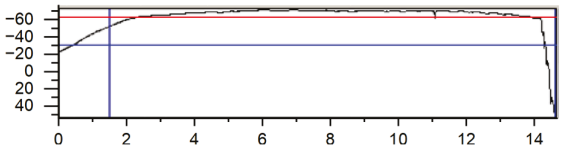
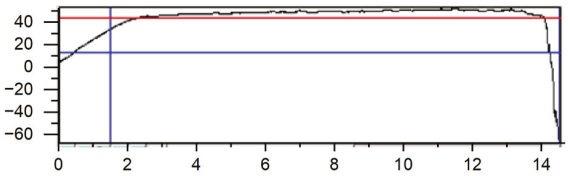
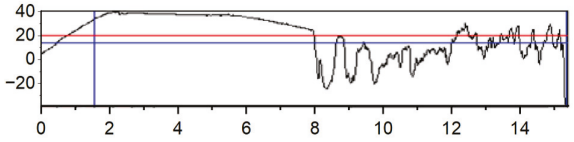
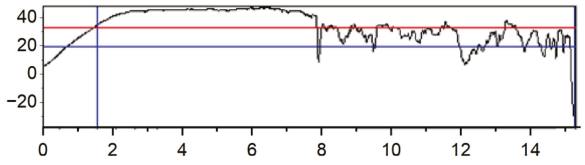
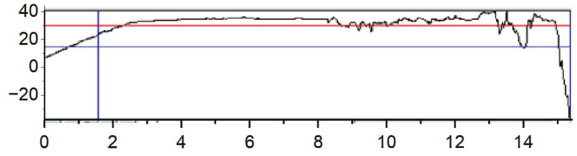
In order to determine the phase composition of the sample, XRD patterns were collected on a PANalytical X'Pert Pro (Malvern Panalytical, Almelo, The Netherlands) diffractometer using Cu Kα (λ = 1.5406 Å) operated at 40 kV, 30 mA. Data were acquired over 2θ = 20–90° with a 0.02° step and 1 s counting time per step. Examples of the application of this analysis method are described in detail in [25–27].

3. Research Results

3.1. Surface Roughness Analysis

Surface roughness was evaluated using the standard method (GOST 2789-73) with the results displayed on a PC monitor (Figure 4), using a profilometer. As a result of processing the profilograms, the following characteristics of the roughness of the samples were obtained (Table 1).

Table 1. Results of evaluation of roughness of the inner hole of the surface matrix.

Sample	Profile Along the Punch Length	Parameters, Microns
Matrix before operation		R_a = 0.0559 R_z = 0.125 R_q = 0.0779 R_v = 0.119
		R_a = 0.0623 R_z = 0.143 R_q = 0.0881 R_v = 0.125
		R_a = 0.0573 R_z = 0.131 R_q = 0.0837 R_v = 0.125
Matrix after operation		R_a = 0.150 R_z = 0.474 R_q = 0.212 R_v = 0.354
		R_a = 0.206 R_z = 0.549 R_q = 0.261 R_v = 0.455
		R_a = 0.161 R_z = 0.493 R_q = 0.234 R_v = 0.395

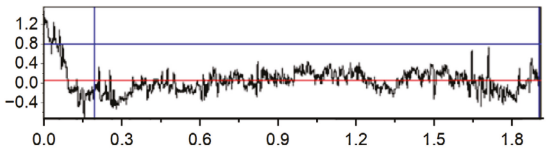
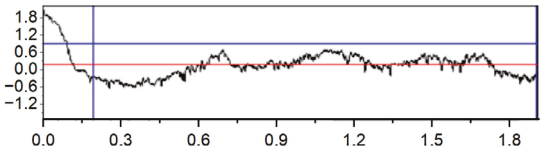
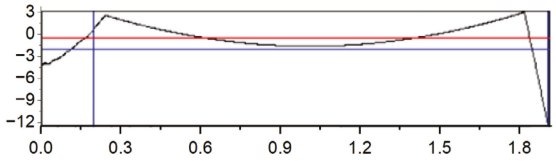
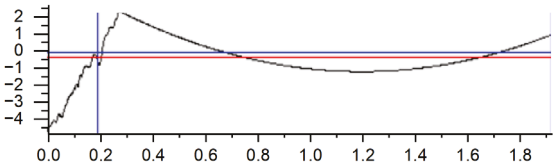
The conducted studies have shown that the friction surface has sufficient cleanliness and is characterized by wear of traces of damage, in section (B) of contact interaction, arising in the given conditions of friction, localized in thin surface layers annihilate in the process of cyclic loading.

To increase the informativeness of the study we noted several parameters, such as R_q as the mean square deviation of the profile and R_v is the depth of the largest depression of the profile, but the main parameter was R_a.

The analysis of the table shows that as a result of working out of the inner holes of the matrix for pressing, R_a is the average deviation of the profile from the middle line, increased 3 times from the initial value of the roughness of the matrix (Table 1). Roughness of surfaces after running-in indicates the formation of microgeometry, explained by significant wear, the inner hole of the matrix.

Table 2 shows the profilograms of the punch surface before and after pressing of uranium dioxide tablets. The measurement was carried out at two locations (A and B).

Table 2. Results of punch roughness evaluation.

Sample	Punch Length Profile	Parameters, Microns
Punch before operation (side A)		R_a = 0.140 R_z = 1.11 R_t = 1.62 R_q = 0.192 R_v = 0.659
Punch after operation, (side A)		R_a = 0.212 R_z = 1.21 R_t = 1.75 R_q = 0.285 R_v = 0.772
Punch before operation (side B)		R_a = 0.158 R_z = 0.914 R_t = 9.96 R_q = 0.243 R_v = 0.586
Punch after operation (side B)		R_a = 0.368 R_z = 2.23 R_t = 4.42 R_q = 0.529 R_v = 0.937

After pressing under real shop conditions, the surface profile changes. The roughness of the surface increases and its wear occurs. Also the working surface in zone B is worn, which negatively affects its performance characteristics.

3.2. Microhardness

The obtained results showed a decrease in microhardness at the working areas by 25%–30%, which indicates the degradation of the structure of the protective coating and local accumulation of damage in the surface layers of steel. Before operation, the microhardness averaged 875 HV, while after long-term operation—635 HV. The most pronounced decrease was observed in the zone of active contact with press powder (section B), which correlates with the results of visual observations and profilometric data. The observed decrease in microhardness indicates the beginning of wear and fatigue processes of the tool material. In particular, the accumulation of plastic deformations, the formation of microcracks and the destruction of the protective layer significantly weaken the ability of the surface to resist contact loads. In this paper [28] it is stated that a decrease in surface

microhardness is an early sign of fatigue degradation of mold surfaces used in pressing nuclear fuel. This pattern is confirmed in the present work (Figure 6).

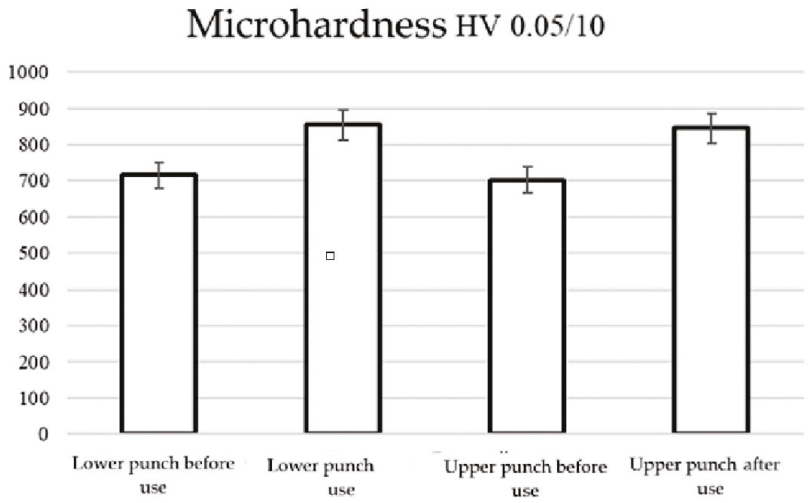


Figure 6. Microhardness of the samples.

3.3. Analysis of Tribological Tests

The results of tribological tests of the sample at room temperature are shown in Figure 7. All of them had a consistently low coefficient of friction and a short run-in period (>5 m), the one tested paired with a 100Cr6 ball had a friction path of 50 m and a stable coefficient of friction. Evaluating the wear resistance of the specimens based on the geometric parameters of the wear groove, it can be said that the width of the groove of the specimen after operation is significantly larger compared to the original specimen.

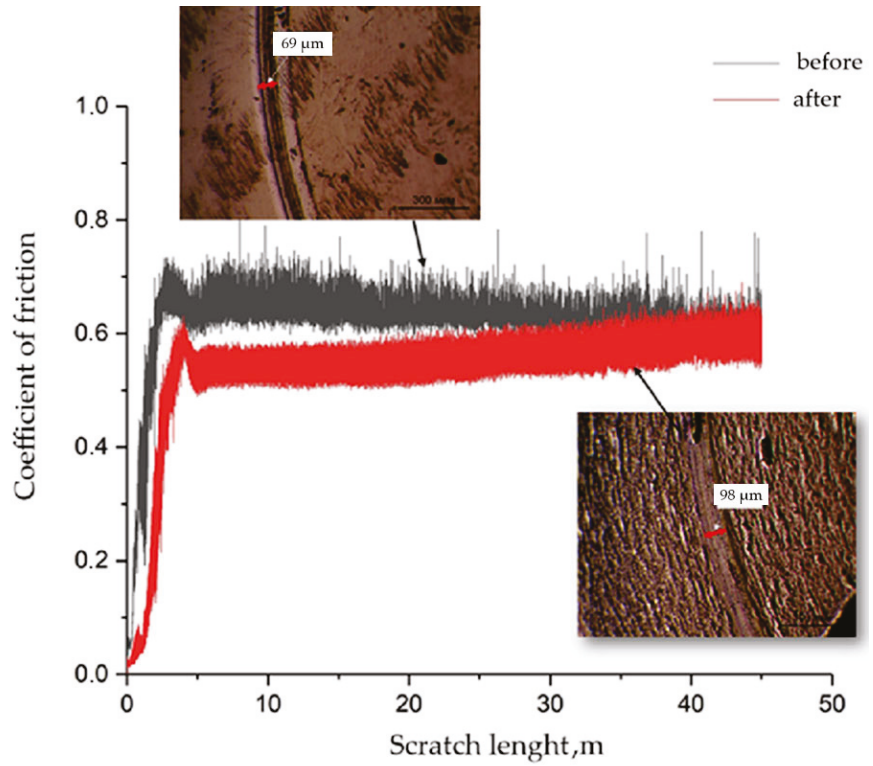


Figure 7. Tribological tests of the punch before and after operation.

After operation, visible pores are observed on the surface, indicating surface wear of the sample. Measurement of the coefficient of friction showed an increase of 20% after

operation, indicating deterioration of the antifriction properties of the punch surface. The wear depth increased, which confirms the high tool loading during pressing.

3.4. Xrf (X-Ray Fluorescence) Results

The results of X-ray fluorescence analysis showed the change in elemental composition of different sections of the punch before and after operation (Table 3). At section "B" after operation, an increased iron content was recorded due to wear of Xtv9 coatings. A comparatively small change in the elemental composition is observed at the site "A".

Table 3. Results of analysis of elemental composition of the sample.

Punch / Element	Punch Before Operation (Side B)		Punch After Operation (Side B)		Punch Before Operation (Side A)		Punch After Operation (Side A)	
	%	%	%	+/−[×]	%	+/−[×]	%	+/−[×]
Fe	60.1404	81.1313	81.1313	0.6170	26.7715	0.6170	39.4792	0.7736
Cr	38.4234	17.7758	17.7758	0.6626	71.7405	0.6626	58.7249	0.6478
Co	1.1787	0.7074	0.7074	0.1623	1.1837	0.1623	1.2483	0.1922
As	0.1516	0.2501	0.2501	0.0548	0.0729	0.0548	0.1686	0.0890
Cu	0.0702	0.0981	0.0981	0.0190	0.0395	0.0190	0.0416	0.0236
Mo	0.0156	0.0173	0.0173	0.0090	0.0148	0.0090	0.00473	0.00135
Au	-	-	-	0.0450	0.1017	0.0450	-	-
V	-	-	-	0.0443	0.0470	0.0443	0.2246	0.0641
Ni	-	-	-	-	-	-	-	-
Zn	-	0.0041	0.0041	-	-	-	-	-

A decrease in the concentration of alloying elements such as chromium and molybdenum was recorded, indicating leaching of the protective layer and loss of corrosion resistance. Surfaces subjected to prolonged contact with uranium dioxide powder showed accumulation of oxide compounds, which is confirmed by an increase in the intensity of oxygen and uranium lines in the spectra.

3.5. X-Ray Phase Analysis (XRD—X-Ray Diffraction)

X-ray phase analysis (XRD) of the samples showed pronounced changes in the condition of the punch surface layer before and after operation. Intense peaks corresponding to chromium-containing phases were registered on the diffractograms of the new tool, which confirms the presence of a protective coating. After operation, broadening of diffraction lines and decrease in their intensity were observed, which indicates accumulation of defects in the crystal lattice, internal stress and possible amorphization of a part of the surface layer (Figure 8).

In addition, the appearance of additional weak peaks corresponding to oxide phases (e.g., Cr_2O_3) indicates oxidation of the surface under friction and temperature stresses. As emphasized in [26]:

"X-ray diffraction provides critical insight into residual stresses and defect accumulation in surface-engineered components, often preceding visible wear damage". This is consistent with the results of SEM and XRF analysis, which showed evidence of coating failure and exposure of the underlying metallic material of the punch.

3.6. Results of M Croscopic Analysis

Figure 9 shows the SEM image of the cross-section of the punch. The results of the study confirm the results of the XRF analysis. The examination showed the absence of Xtv9 coating at section "B" (Figure 10B). At site "A" the thickness of the layer was $\sim$ 6.50 μm (Figure 10A).

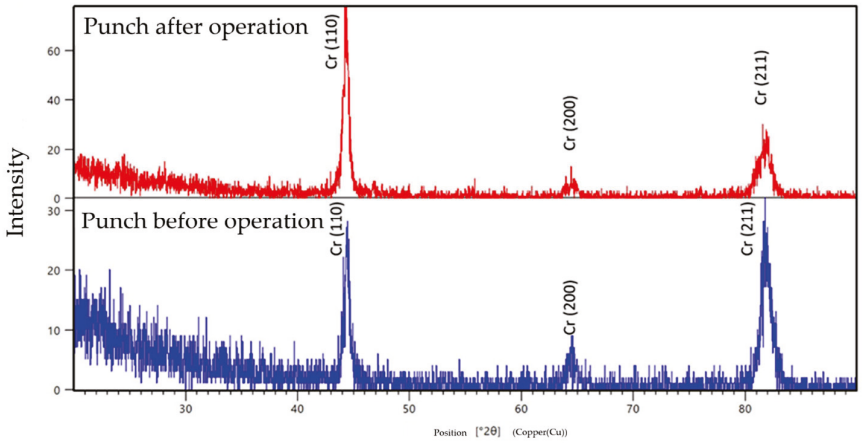


Figure 8. Diffractogram.

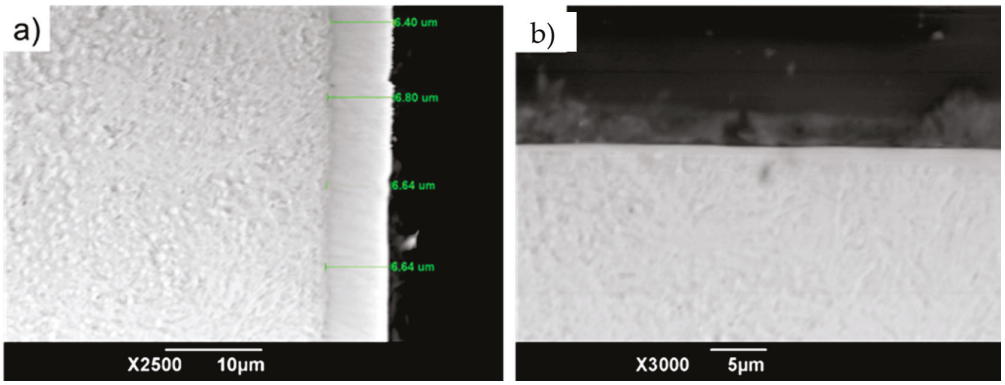


Figure 9. SEM image of the cross-section of the punch. (**a**) Section A; (**b**) section B.

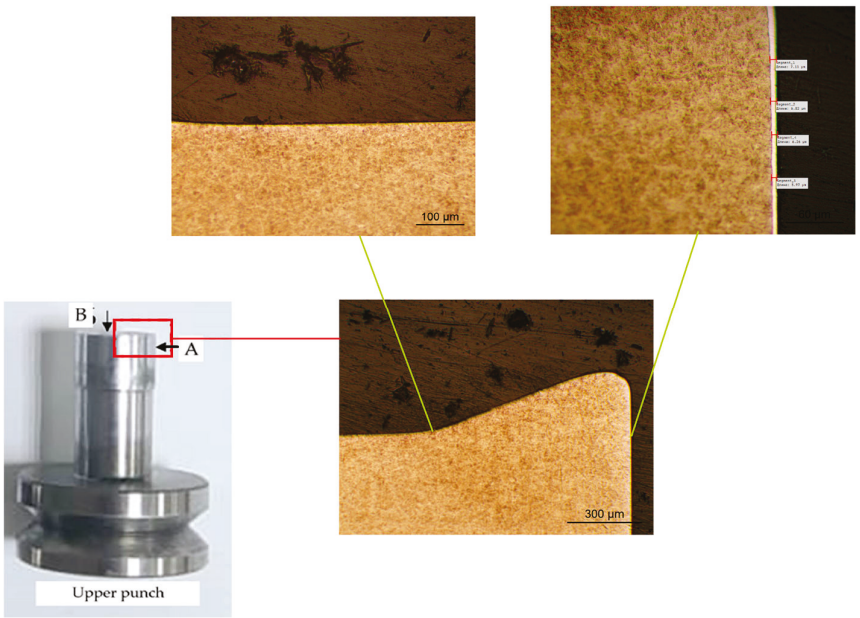


Figure 10. Optical image of the punch cross-section working face (B) and side surface (A).

Optical image of the punch cross-section (Figure 11) Metallographic analysis of the cross-section of the working edge of the top punch after operation, showing different wear mechanisms. Enlarged slice (A) shows the side surface subjected to frictional and abrasive wear from contact with the die. Figure 10B illustrates the area of the working face and

edge where the most intense failure has occurred, including degradation of the protective coating and base material, resulting from complex impact-abrasion and fatigue wear.

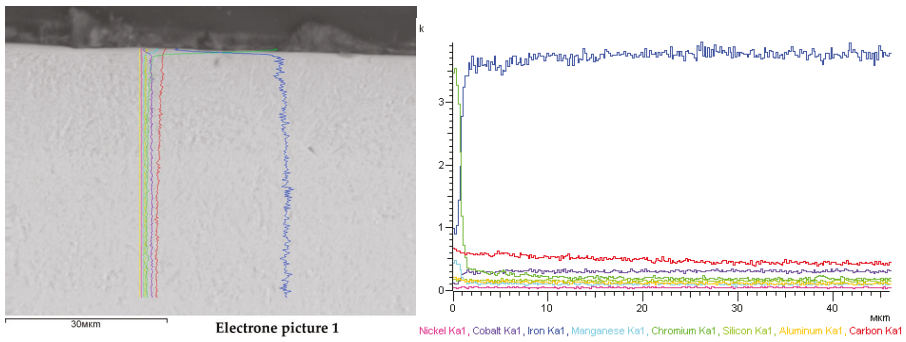


Figure 11. SEM image of the cross punch of section "B".

Figure 11 shows the distribution of elements across the cross-section of the punch at section "B". The EDS data indicate a thin layer of Xtv9 coatings. The concentration of chromium in the coating is 3.3–3.8 weight, %.

The SEM image of the cross-section of the original punch (before operation) shows (Figure 12) that the chrome layer has a thickness of ~6.50 µm and is characterized by a dense structure. Based on the analysis of the elemental composition of the surface, it can be said that the wear of the punch occurs in sections "A" and "B".

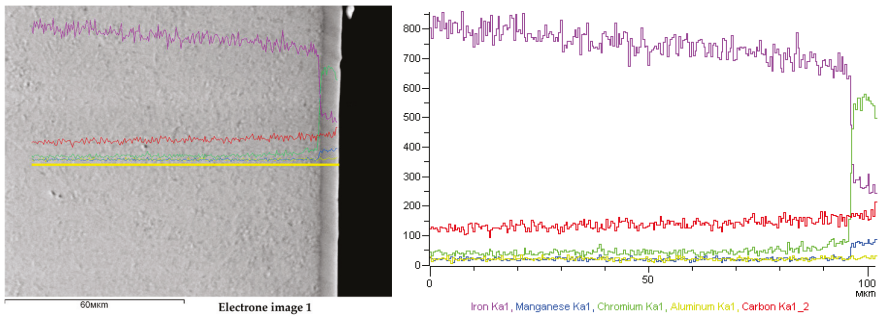


Figure 12. SEM image of the cross punch before operation.

Elemental analysis was performed for five sections (points) of the punch surface after operation. Figure 13 shows microphotographs of the surface and elemental analysis data of the punch (Table 4), indicating a satisfactory match of the composition with the chrome plated coating.

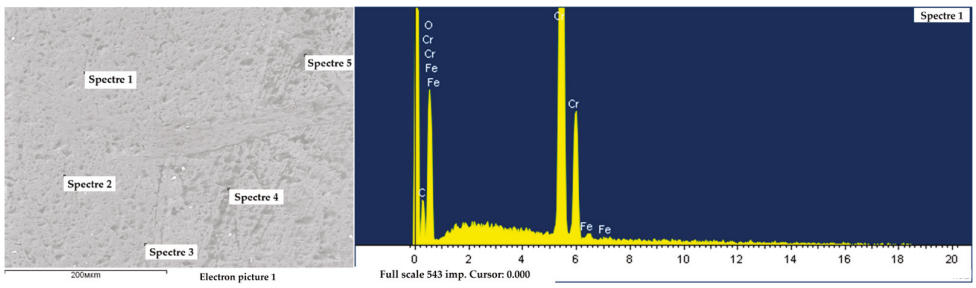


Figure 13. SEM image of cross punch.

Table 4. Results of analysis of elemental composition of sample.

Spectrum	In Stat.	O	Cr	Fe	Total
Spectrum 1	Yes	4.54	94.71	0.75	100.00
Spectrum 2	Yes	5.28	94.21	0.51	100.00
Spectrum 3	Yes	2.79	96.17	1.05	100.00
Spectrum 4	Yes	2.91	95.74	1.36	100.00
Spectrum 5	Yes	3.30	95.77	0.93	100.00
Average		3.76	95.32	0.92	100.00
Standard deviation		1.10	0.82	0.32	
Max.		5.28	96.17	1.36	
Min.		2.79	94.21	0.51	

Analysis of worn areas of molds and punches using SEM showed the presence of mechanical damage to the surface. Zones of plastic deformation, microcracks and areas of adhesive material transfer were identified. It was found that in the areas of contact with uranium dioxide powder there is localized destruction of the coating with the formation of micro-defects, which contributes to further wear progression. As emphasized in the study "Scanning electron microscopy revealed extensive microstructural damage, including crack propagation and material transfer, which are indicative of combined adhesive-abrasive wear mechanisms under cyclic loading conditions". At $\times$5000 magnification, fine wear particles were detected, indicative of a combined abrasive and adhesive wear mechanism. Areas with oxide phase layering were also observed, which is confirmed by X-ray fluorescence analysis data.

4. Discussion

The study confirmed that press tool wear during UO_2 tablet molding is manifested through complex degradation mechanisms involving both abrasive and adhesive wear. The decrease in microhardness detected in the active contact zone indicates the accumulation of plastic deformations and destruction of the protective layer of the Xtv9 coating. These changes correlate with the growth of roughness on the tool surface, which is established by profilometric analysis, and indicate the impact of high cyclic loads and temperatures.

X-ray fluorescence analysis data demonstrate the loss of alloying elements (Cr, Mo) in the contact zone, which is associated with the destruction of the surface layer and partial diffusion as a result of friction. X-ray phase analysis showed a decrease in the intensity and broadening of diffraction peaks, indicating the formation of defective sites and internal stresses in the crystal lattice. The appearance of oxide phases (Cr_2O_3) on the surface additionally confirms thermo-oxidative degradation of the coating under operating conditions.

SEM analysis allowed for visualizing microcracks, zones of plastic deformation, traces of abrasive interaction and material transfer. There were also recorded signs of local destruction of chrome coating and formation of micro voids, which reduces the efficiency of tool operation and increases the probability of defective products. The totality of the observed defects indicates a combined wear mechanism, where both mechanical and chemical–temperature factors play a role.

These data support the need to optimize pressing parameters, tool and coating material selection and technical inspection regulations. The proposed evaluation methods (XRF, XRD, SEM, microhardness, profilometry) have demonstrated high efficiency for comprehensive tool condition analysis.

5. Conclusions

A multi-modal analysis of die/punch wear in UO_2 pellet pressing shows a combined abrasive–adhesive wear mechanism accompanied by microcrack formation and localized coating degradation. Quantitatively, the microhardness drops from 875 to 635 HV (−27.4%) in the active contact zone, while surface roughness increases (matrix Ra $\approx 0.058 \rightarrow 0.172$ μm, ≈3×; punch Ra increases by 51%–133% depending on location). Tribometry (2 N, R = 3 mm, 50 m sliding) indicates a ~20% rise in the coefficient of friction after service. XRF confirms chromium depletion and iron exposure in worn regions, whereas XRD reveals peak broadening and weak oxide reflections (e.g., Cr_2O_3), consistent with defect accumulation and thermo-oxidative degradation.

The proposed methods of analysis can be used in industrial conditions to assess the residual life of press tools and to develop recommendations for their restoration or replacement. Further research should be directed to the study of alternative coatings resistant to radiation-temperature loading, as well as to the introduction of intelligent systems for real-time tool condition monitoring.

Author Contributions: Conceptualization, B.R.; Methodology, A.K. (Aidar Kengesbekov) and M.K.; Formal analysis, N.M.; Investigation, N.M., A.K. (Aidar Kengesbekov) and A.K. (Arystanbek Kussainov); Writing—original draft, N.M. and A.K. (Aidar Kengesbekov); Writing—review & editing, B.R. and M.K.; Visualization, A.K. (Aidar Kengesbekov) and A.K. (Arystanbek Kussainov); Supervision, B.R.; Project administration, B.R. All authors have read and agreed to the published version of the manuscript.

Funding: This research has been funded by the Committee of Science of the Ministry of Science and Higher Education of the Republic of Kazakhstan (Grant No. BR24992854).

Institutional Review Board Statement: Not applicable.

Informed Consent Statement: Informed consent was obtained from all the subjects involved in this study.

Data Availability Statement: Data are contained within the article.

Conflicts of Interest: Authors Bauyrzhan Rakhadilov, Nurtoleu Magazov, Aidar Kengesbekov and Arystanbek Kussainov were employed by the company Plasma Science LLP. Author Manarbek Kylyshkanov was employed by the company Ulba Metallurgical Plant JSC.

References

1. Santra, N. Advances in Process Materials for Production of UO2. 2021. Available online: https://www.academia.edu/56709344/Advances_in_Process_Materials_for_Production_of_Uo (accessed on 19 August 2025).
2. Jeon, S.-C.; Lee, J.-W.; Lee, J.-H.; Kang, S.-J.; Lee, K.-Y.; Cho, Y.-Z.; Ahn, D.-H.; Song, K.-C. Fabrication of UO_2 Porous Pellets on a Scale of 30 kg-U/Batch at the PRIDE Facility. *Adv. Mater. Sci. Eng.* **2015**, *2015*, 376173. [CrossRef]
3. Tyrpekl, V.; Cologna, M.; Vigier, J.-F.; Cambriani, A.; De Weerd, W.; Somers, J. Preparation of bulk-nanostructured UO_2 pellets using high-pressure spark plasma sintering for LWR fuel safety assessment. *J. Am. Ceram. Soc.* **2017**, *100*, 1269–1274. [CrossRef]
4. Li, B.; Yang, Z.; Wang, Z.; Huang, Q.; Zhang, D.; Xu, Q.; Xie, L.; Zhong, Y.; Wang, Y.; Duan, L.; et al. Thermal conductivity of UO2 pellets enhanced by a semi-continuous structure of Ti_3SiC_2. *Ceram. Int.* **2023**, *49*, 26049–26056. [CrossRef]
5. Gorton, J.P.; McDuffee, J.L.; Snarr, P.L.; Petrie, C.M.; Nelson, A.T. Heat transfer optimization of uo2-mo fuel using genetic algorithms. *Nucl. Eng. Des.* **2024**, *418*, 112861. [CrossRef]
6. Fu, J.; Li, J.; Wang, Z.; Cong, T.; Guo, H.; Xiao, Y.; Gu, H. Numerical study of the effect of helical fuel rod geometry on single-phase flow and heat transfer characteristics. *Ann. Nucl. Energy* **2024**, *205*, 110574. [CrossRef]
7. Sedgi, I.; Moyal, A.; Assulin, M.; Rubinstein, A.; Brandis, M.; Gershinsky, G.; Edry, I.; Halevy, I.; Fruchter, N.; Zakon, Y.; et al. Nuclear forensic signatures of UO2 fuel pellets for differentiation and provenance determination illustrated using synthetic database. *J. Nucl. Mater.* **2023**, *587*, 154730. [CrossRef]
8. Dooley, P.; Contryman, D.; Hervey, A.; Ivers, R.; Reddish, I.; Song, Y. Design of an optimized nuclear fuel pellet. *Nucl. Sci. Technol. Open Res.* **2024**, *2*, 1. [CrossRef]
9. Rakhadilov, B.K.; Kurbanbekov, S.R.; Kilishkhanov, M.K.; Kenesbekov, A.B.; Amanzholov, S. Changing the structure and phasestates and the microhardness of the R6M5 steel surface layer after electrolytic-plasma nitriding. *Eurasian J. Phys. Funct. Mater.* **2018**, *2*, 259–266. [CrossRef]

10. Balboa, H.; Van Brutzel, L.; Chartier, A.; Le Bouar, Y. Assessment of empirical potential for MOX nuclear fuels and thermomechanical properties. *J. Nucl. Mater.* **2017**, *495*, 67–77. [CrossRef]
11. Cheng, J.; Zhao, J.-H.; Zhang, J.-Y.; Guo, Y.; He, K.; Shang-guan, J.-J.; Wen, F.-L. Microstructure and Mechanical Properties of Galvanized-45 Steel/AZ91D Bimetallic Material by Liquid-Solid Compound Casting. *Materials* **2019**, *12*, 1651. [CrossRef]
12. Bai, X.; Jiang, J.; Li, C.H.; Dong, L.; Duan, Z.; Zhang, H. Lubrication Performance of Different Concentrations of Al_2O_3 Nanofluids on Minimum Quantity Lubrication Milling. *Res. Sq.* **2021**. [CrossRef]
13. Rakhadilov, B.; Kengesbekov, A.; Zhurerova, L.; Kozhanova, R.; Sagdoldina, Z. Impact of electronic radiation on the morphology of the fine structure of the surface layer of R6M5 steel. *Machines* **2021**, *9*, 24. [CrossRef]
14. El-Atwani, O.; Kim, H.; Gigax, J.G.; Harvey, C.; Aytuna, B.; Efe, M.; Maloy, S.A. Stable, Ductile and Strong Ultrafine HT-9 Steels via Large Strain Machining. *Nanomaterials* **2021**, *11*, 2538. [CrossRef]
15. Chen, Y. Irradiation Effects Of Ht-9 Martensitic Steel. *Nucl. Eng. Technol.* **2013**, *45*, 311–322. [CrossRef]
16. Sprouster, D.J.; Adam, B.; Koziol, A.; Rolly, L.; Huotilainen, C.; Tucker, J.D. Long-term thermal aging effects in ferritic-martensitic steel HT9. *Mater. Charact.* **2024**, *217*, 114418. [CrossRef]
17. Byun, T.S.; Collins, D.A.; Lach, T.G.; Choi, J.P.; Maloy, S.A. Thermomechanical Processing for Improved Mechanical Properties of HT9 Steels. *Materials* **2024**, *17*, 3803. [CrossRef] [PubMed]
18. Kengesbekov, A.; Rakhadilov, B.; Satbaeva, Z.; Kambarov, Y. Effect of Helium Plasma Irradiation on Microstructures and Mechanical Properties of Tungsten. *Adv. Mater. Sci. Eng.* **2024**, *2024*, 1968615. [CrossRef]
19. Kengesbekov, A. Influence of Plasma Arc Current and Gas Flow on the Structural and Tribological Properties of TiN Coatings Obtained by Plasma Spraying. *Coatings* **2024**, *14*, 1404. [CrossRef]
20. Xie, Z.; Yin, C.; Zhang, J.; Jiao, Y.; Ding, G.; Yang, Q.; Ding, S.; Chen, P. On the creep mechanisms and macroscopic creep rate modeling of high-uranium-density composite fuels. *J. Nucl. Mater.* **2023**, *586*, 154679. [CrossRef]
21. *GOST-2789-73*; Surface Roughness. Parameters and Characteristics. In Consulting: Ukraine, Russia, 2006.
22. *ASTM G99/G133-22*; Standard Test Method for Linearly Reciprocating Ball-on-Flat Sliding Wear. ASTM: West Conshohocken, PA, USA, 2022.
23. *GOST 9450-76*; Measurement of Microhardness by Indentation of Diamond Tips. In Consulting: Ukraine, Russia, 1977.
24. *ISO 6507-1:2023*; Metallic Materials—Vickers Hardness Test. Part 1: Test method. ISO: Geneva, Switzerland, 2023.
25. Kolyvanov, E.L.; Afonikova, N.S.; Kobelev, N.P. X-ray Diffraction Tests of Near-Surface Layer of Copper Treated by Ball Rolling. *Inorg. Mater. Appl. Res.* **2018**, *9*, 699–702. [CrossRef]
26. Harrington, G.F.; Santiso, J. Back-to-Basics tutorial: X-ray diffraction of thin films. *J. Electroceram.* **2021**, *47*, 141–163. [CrossRef]
27. Rizal, C. Microstructure, Surface Plasmon, Magneto-optic Surface Plasmon, and Sensitivity Properties of Magneto-plasmonic Co/Au Multilayers. *IEEE Trans. Magn.* **2018**, *54*, 5300309. [CrossRef]
28. Bai, X.; Jiang, J.; Li, C.; Dong, L.; Ali, H.M.; Sharma, S. Tribological Performance of Different Concentrations of Al_2O_3 Nanofluids on Minimum Quantity Lubrication Milling. *Chin. J. Mech. Eng.* **2023**, *36*, 11. [CrossRef]

Disclaimer/Publisher's Note: The statements, opinions and data contained in all publications are solely those of the individual author(s) and contributor(s) and not of MDPI and/or the editor(s). MDPI and/or the editor(s) disclaim responsibility for any injury to people or property resulting from any ideas, methods, instructions or products referred to in the content.

coatings

MDPI

Article

POSS-Grafted PI/MoS_2 Gradient Composite Coatings with Enhanced Tribological Properties Under Atomic Oxygen Irradiation

Chuanyong Yu [1], Peng Zhang [2], Min Wei [1,*], Qiwei Wang [2,*] and Wei Zhang [1]

[1] School of Mechatronic Engineering and Automation, Foshan University, Foshan 528225, China; yucy14@163.com (C.Y.); zhangwei18@fosu.edu.cn (W.Z.)
[2] Institute of Advanced Wear & Corrosion Resistant and Functional Materials, Jinan University, Guangzhou 510632, China; tzhangpeng@jnu.edu.cn
* Correspondence: weimin@fosu.edu.cn (M.W.); wangqiwei@jnu.edu.cn (Q.W.); Tel.: +86-18511795731 (M.W.); +86-13929565955 (Q.W.)

Abstract

The irradiation of atomic oxygen (AO) severely restricts the application of polymeric lubricating coatings in low Earth orbit (LEO). Herein, octa- and mono-amino polyhedral oligomeric silsesquioxanes (POSSs) were chemically bonded onto polyimide/molybdenum disulfide (PI/MoS_2) composite coatings with a gradient structure based on Si density. The gradient coatings presented better wear resistance under different loads; notably, the wear rate decreased by 83.5%. Additionally, the effects of AO exposure on the surface morphologies, chemical structure, and tribological properties of the gradient coatings were investigated in detail. The results indicated that the mass loss and wear rates under AO irradiation decreased significantly, which can be attributed to the passivated network-like SiO_2 layer that covered the coating surface after AO irradiation. As a result, the addition of POSS significantly improved the tribological properties and AO resistance.

Keywords: polyhedral oligomeric silsesquioxane; gradient composite coatings; polyimide; atomic oxygen resistance; tribological properties

1. Introduction

Generally, spacecraft face harsh conditions in the space environment, which consists of high-vacuum, ultraviolet (UV), atomic oxygen (AO), electron, and strong radiation during service in low Earth orbit (LEO), which has led to the failure of lubricating materials and has seriously affected the service life of these spacecraft [1–3]. In particular, the major component of AO, playing an important role in the atmosphere, can collide with space materials at high velocities of 8 km/s, with 5 eV of kinetic energy. In addition, AO has strong oxidizability and can cause considerable erosion, degradation, and oxidation of polymeric lubrication materials, resulting in the dramatic deterioration of their mechanical and tribological properties [4–6].

Polyimide (Kapton (PI), with excellent mechanical properties and space radiation resistance) [7–9] and molybdenum disulfide (MoS_2, with excellent low-friction characteristics and wear resistance) [10–12] have become indispensable high-performance structural or coating materials in the aerospace industry due to their excellent inherent characteristics. Nevertheless, the increasing life-duration requirements and harsh service conditions of new spacecraft (such as those used in space stations and lunar exploration projects) demand a

higher performance of lubricating materials. Traditional polymeric lubricating coatings can no longer meet the ever-increasing multifunctional demands for high AO resistance, excellent tribology properties, and long life.

A general approach to producing polymeric materials with great AO resistance is copolymerization or coating with an inorganic protective layer to yield a hybrid composite material that can resist AO erosion [13–16]. In previous research, many surface-protective AO-resistant inorganic coatings were deposited on polymeric surfaces via methods such as surface silanization, ion implantation, and vapor deposition [17–20]. However, inorganic surface coatings are prone to cracking or peeling during transport and can easily develop small cracks when subjected to thermal cycling or repeated shear stress during service, leading to 'drilling' of the underlying polymer. In an effort to address this, internal matrix strengthening has received more attention; this strengthening is achieved by adding inorganic nanoparticles or organic compounds containing Si and P elements to a polymeric system to improve its surface protection properties [21–23]. Moreover, by introducing organic–inorganic hybrid materials to construct a gradient composite structure, the interfacial bonding between inorganic and organic components can be significantly enhanced, and the coating can be endowed with excellent surface-protective performance. The introduction of organic–inorganic hybrid silicon nanomaterials has especially led to excellent AO resistance and structural advantage.

Polyhedral oligomeric sesquisiloxane (POSS) has attracted widespread attention, as it has been found to act as a novel organic/inorganic hybrid nanomaterial, containing a hollow, cage-like inorganic backbone that consists of Si-O-Si bonds surrounded with different inert or functional groups [24–27]. Additionally, the POSS monomer can be chemically bonded in polymeric materials as a cross-linking agent, side group, or end-capping agent, and is enriched on the inside or surface of the polymeric system [6,28]. Many scholars have made extensive efforts to develop POSS-reinforced polymeric materials, demonstrating that the introduction of moderate POSS could improve their mechanical properties and significantly increase AO resistance [14,24,29]. Similarly, in our previous work, we systematically studied the effect of POSS on the tribological properties of lubricating coatings, and the results indicated that adding multifunctional POSS improved the cross-linking, hardness, strength, and wear resistance of the coatings [2,30]. However, the coating surface faced erosion and oxidation under AO irradiation caused by insufficient silicon on the coating surface. Therefore, it is of great significance to enhance the protective capability of coating surfaces through the construction of a gradient structure.

In this work, the octa- and mono-amino POSSs were grafted onto a PI matrix according to the molecular structure of the POSS. Then, POSS-modified PI/MoS_2 composite coatings with a double-deck structure were prepared, and the effects of applied load on the friction and wear behaviors were investigated. On this basis, the effects of AO on the surface morphologies, chemical structure, elementary composition, and tribological properties were also investigated. The results suggested that the POSS-modified composite coatings with a double-deck structure exhibited excellent AO resistance and tribological properties in the LEO. Therefore, hopefully, research into the evolution mechanisms of the POSS-modified gradient structure and its tribological properties under AO irradiation could constitute an efficient direction for fabricating advanced lubricating coatings with excellent AO resistance and tribological properties in LEO.

2. Materials and Methods

2.1. Materials

The octa-amino and mono-amino seven-isobutyl polyhedral oligomeric sesquisiloxane (POSS) materials were purchased from the Beijing HWRK Chemical Company (Beijing,

https://doi.org/10.3390/coatings16010073

China). The pyromellitic dianhydride (PMDA) materials were obtained from the Sinopharm Group Chemical Reagent Company, whereas the 4,4-diaminodiphenyl ether (ODA) was sourced from Shanghai Kefeng Chemical Reagent Company (Shanghai, China). The MoS_2 powder, with an average particle size of 2.5 μm after planetary ball milling, was supplied by Shanghai Research Institute of Synthetic Resins (Shanghai, China). Other reagents, including ethanol, hydrochloric acid, and N, N-dimethylacetamide (DMAc), were commercially provided by East Instrument Chemical Glass Company Limited (Shanghai, China). All chemicals were of analytical grade.

2.2. Preparation of POSS/PI/MoS_2 Coatings

First, 1.5 g of ODA was dissolved in 30 mL of DMAc under stirring for 30 min. After the ODA was fully dissolved, the reaction setup was transferred to an ice-water bath in a three-necked flask, and 1.65 g of PMDA was added slowly within 5 min. As the reaction proceeded, the viscosity of the solution gradually increased, and its appearance changed from transparent to pale yellow. This mixture was stirred continuously for 6 h, ultimately yielding a poly(amic acid) (PAA) solution. Then, the octa-amino POSSs (5 wt% of the system) were added into the solution, and stirring was continued 10 min. And the mono-amino POSSs (5 wt% of the system) were added and stirred for another 20 min to ensure thorough reaction. POSS nanomaterials can be incorporated into the main chain of the polyimide (PI) resin or as a side or end-group, as shown in Figure 1.

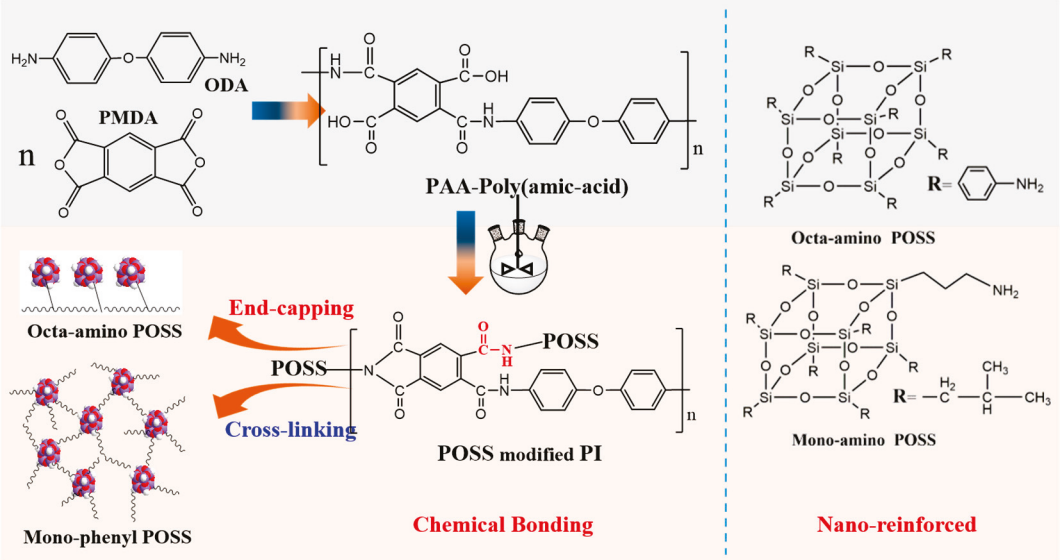


Figure 1. Preparation procedure of the composite coatings.

The octa- and mono-amino POSS-PI composites and MoS_2 were mechanically mixed with a certain proportion, as shown in Table 1. The lubricating coatings were fabricated by sequentially spraying the composite slurries onto steel substrates. First, a layer of octa-amino POSS-PI/MoS_2 slurry was sprayed onto a steel substrate with a thickness of approximately 25 ± 3 μm, followed by a layer of octa- and mono-amino POSS-PI/MoS_2 at about 10 ± 2 μm. The as-sprayed gradient coatings were then pre-dried at 150 °C for 1 h in an electric oven and subsequently cured at 280 °C for 1 h, resulting in a final coating thickness of 35 ± 3 μm.

https://doi.org/10.3390/coatings16010073

Table 1. Weight compositions of the POSS-PI/MoS_2 composite coatings.

Coatings	Weight Compositions (g)				
	PMDA	**ODA**	**MoS_2**	**Octa-POSS**	**Mono-POSS**
PI/MoS_2	1.65	1.5	3.0	0	0
POSS-PI/MoS_2	1.65	1.5	3.0	0.15	0.15

2.3. AO Exposure Experiment

The AO exposure experiments were performed using a space environment ground simulation device (purchased from Yanfei Electrical Technology Company Limited, Hefei, China) under vacuum (<1.5×10^{-2} Pa). In these experiments, AO with an average kinetic energy of approximately 5 eV struck the lubricating coatings, and the AO flux was approximately 1.23×10^{16} AO/cm^2·s. The AO erosion experiment was conducted from 5 h to 20 h.

The effective AO *flux* can be calculated by Equation (1).

$$AO\ flux = \frac{\Delta M}{\rho \times A \times t \times AORC} \quad (1)$$

where ρ is the density of Kapton, A is the exposed surface area, t is the exposure time, and $AORC$ is the AO reactivity coefficient of Kapton with an AO reactivity of 3.0×10^{-24} cm^3/atom. Additionally, ΔM is the mass loss of Kapton after AO irradiation [2,24].

2.4. Structural Characterizations of the Coatings

The microhardness of these composite lubricating coatings was investigated using a microhardness tester (HXS-1000, Caikon, Shanghai, China) under an applied load of 10 g and a loading time of 5 s. To evaluate the interfacial bonding strength, adhesion tests were performed at least in triplicate on each specimen using a QFZ-II tester according to the standard cross-hatch method (GB/T 4893.4-85 [31]).

To analyze the chemical structure evolution induced by AO irradiation, the coatings were examined using Fourier-transform infrared spectroscopy (FTIR-ATR, Nexus 870, Thermo Nicolet Corporation, Madison, WI, USA), X-ray diffraction (XRD, Bruker D8 Discover 25, Karlsruhe, Germany), and X-ray photoelectron spectroscopy (XPS, ESCA-LAB 250Xi, Thermo Fisher Scientific, Portland, OR, USA). To investigate the morphological and compositional changes on the surface and within wear tracks, scanning electron microscopy (SEM, JSM-5600LV, JEOL, Tokyo, Japan) coupled with energy-dispersive spectroscopy (EDS) was employed. Furthermore, micro-Raman spectroscopy (HORIBA Jobin LabRAM HR Evolution, Paris, France) was utilized to probe the chemical structures of the worn surfaces across the 100–1100 cm^{-1} spectral range.

2.5. Friction and Wear Behavior

The tribological properties of the POSS-PI/MoS_2 composite coatings, both before and after AO irradiation, were comparatively evaluated using a ball-on-disk vacuum tribometer (CSM, Anton Paar, Graz, Austria) at room temperature. The vacuum degree was less than 5×10^{-5} mbar, and a GCr15 steel ball (diameter: 6 mm; hardness: 58–62 HRC) served as the counterpart. Prior to AO irradiation, the counter balls slid against the coatings at a speed of 10 cm/s (amplitude: 2.5 mm) with the applied load ranging from 5 N to 20 N, and the friction distance was 100 m. After AO erosion, the friction tests were conducted under 5 N at a speed of 10 cm/s (amplitude: 2.5 mm), with 100 m distance. In addition, the lifetime was tested under 5 N at a speed of 1000 rpm, with a distance 6.5 × 105 r. The

https://doi.org/10.3390/coatings16010073

wear volume of each track was measured using a Micro-XAM-3D non-contact surface profiler (AEP, R-tec instruments, San Jose, CA, USA) to calculate the wear rate, thereby evaluating the anti-wear performance. A specific wear rate (W) was calculated according to the following formula:

$$W = \frac{V}{F \cdot D}$$

where V, F, and D represent the wear volume (mm^3), normal load (N), and wear distance (m), respectively. All experiments were repeated three times to ensure reproducibility.

3. Results and Discussion

3.1. Tribological Properties of the Lubricating Coatings Under Different Loads

Figure 2 shows the SEM morphology and element mapping of the composite coatings. As can be observed from the figure, the surfaces of both PI/MoS_2 and POSS-PI/MoS_2 composite coatings exhibited a relatively uniform surface (Figure 2a,b). The surface roughness of the PI/MoS_2 coating was relatively low; however, the POSS-modified composite coating exhibited greater roughness compared to the original PI/MoS_2 coating. The low surface energy of POSS resulted in a surface migration effect, and the mono-amino POSS acted as the side or end group, leading to an increase in surface roughness [27]. This observation is supported by the three-dimensional morphology and the surface roughness measured from the two-dimensional cross-sectional profiles (Figure 2c,d), and our previous work could confirm the formation of a gradient structure based on Si density [24]. Additionally, the distribution of Mo and Si elements indicated that molybdenum disulfide and POSS were uniformly dispersed within the coating.

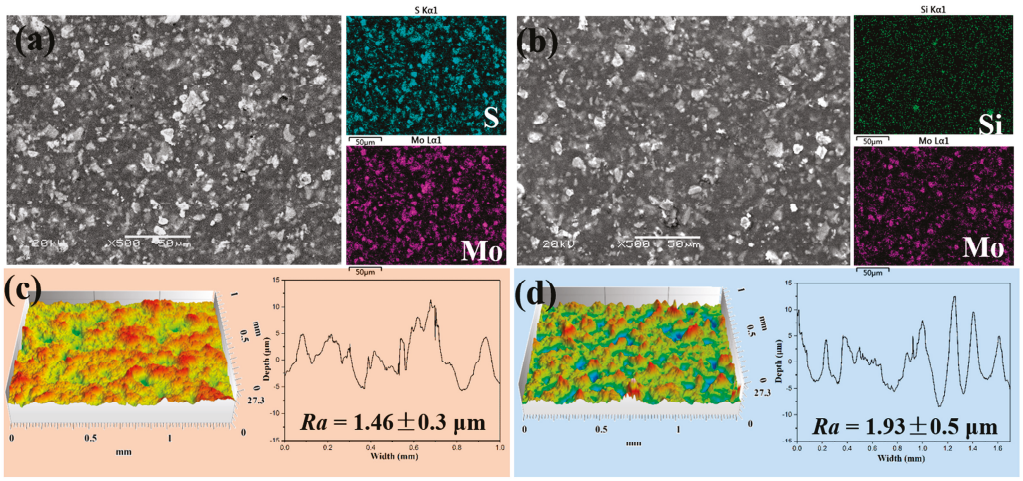


Figure 2. SEM micrographs (**a**,**b**), three-dimensional and sectional profiles (**c**,**d**) of the (**a**,**c**) PI/MoS_2, and (**b**,**d**) POSS-PI/MoS_2 lubricating coating surfaces.

Additionally, the basic physical properties of the composite coatings before and after POSS modification were measured and are listed in Table 2. As can be seen, both the original PI/MoS_2 and the POSS-modified lubricating coatings demonstrate an adhesion grade of 0, a flexibility grade of 1 mm, and an impact resistance of 50 cm, indicating that the prepared coatings possessed excellent fundamental properties and met national standards. Furthermore, the microhardness of the POSS-modified coating was improved. This improved hardness can be attributed to the incorporation of the inorganic, cage-like siloxane framework from POSS and the increased cross-linking density caused from multiple amino groups and the PI matrix [23,32]. Additionally, the mono-amino POSSs were introduced as an end-capping agent that is mainly distributed on the composite surface due to surface migration, which resulted in the gradient structure. Therefore,

https://doi.org/10.3390/coatings16010073

the synergistic effect of octa- and mono-amino POSS collectively enhanced the coating's load-bearing capacity and hardness.

Table 2. Basic physical properties of the composite coatings.

Coatings	Adhesion/ Grade	Flexibility/ Grade	Impact Resistance/cm	Microhardness/ Hv
PI/MoS_2	0	1	50	31.06
POSS-PI/MoS_2	0	1	50	36.47

The influence of different loads on the vacuum tribological performance of the POSS-modified coating was investigated, as shown in Figure 3. It is possible to observe that both the original and POSS-modified coatings maintained relatively good lubricating properties, with friction coefficients below 0.03. However, compared to the PI/MoS_2 coating, the modified coating exhibited a decrease in friction coefficient (Figure 3a), although this reduction is not significant. However, the coatings exhibited significant differences in wear rates, with the modified coatings showing a remarkable reduction in wear. The wear rate of the PI/MoS_2 composite coating exceeded 9×10^{-7} $mm^3 \cdot N^{-1} \cdot m^{-1}$ under both low (5 N) and high (20 N) loads. By contrast, the POSS-modified coating demonstrated a notably lower wear rate, which further decreases as the load increased. At a load of 15 N, the POSS-modified coating exhibits optimal wear resistance, with a wear rate as low as 2.7×10^{-7} $mm^3 \cdot N^{-1} \cdot m^{-1}$, which decreased by 83.5% compared with that of the original coating. This improvement is attributed to the incorporation of the abundant inorganic siloxane cage-like frameworks in the POSS, which enhanced the coating's hardness and load-bearing capacity. Additionally, multiple amino groups in POSS underwent cross-linking reactions with the resin, which increased the cross-linking density and thereby further improved the wear resistance of the composite coating.

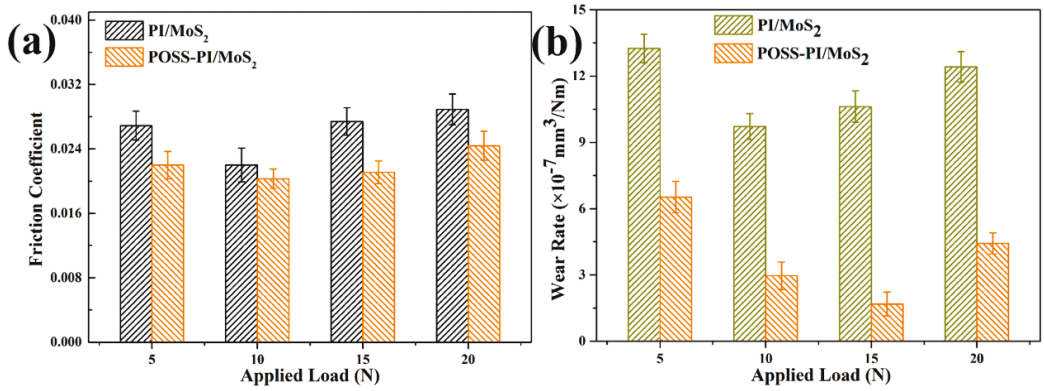


Figure 3. Average friction coefficient (**a**) and wear rates (**b**) of the composite coatings under different applied loads.

The three-dimensional (3D) topographies and cross-sectional (2D) curves of the wear tracks were also measured to further explore their wear mechanisms, and the results of these measurements are shown in Figure 4. It can be seen that the PI/MoS_2 coating experienced severe wear, with a relatively wide and deep wear scar profile measuring approximately 0.765 ± 0.08 mm in width and 21.16 ± 2 μm in depth (Figure 4a). By contrast, the POSS-modified PI/MoS_2 coating exhibited significantly reduced wear track dimensions (Figure 4b), with a width and depth measuring 0.68 ± 0.1 mm and 13.75 ± 1.5 μm, respectively. Furthermore, the surface roughness of the worn area decreased markedly, which is likely attributable to a change in the wear mechanism. Thus, the incorporation of inorganic cage-like frameworks and high cross-linking density caused by multiple func-

https://doi.org/10.3390/coatings16010073

tional groups into the coating imparted excellent load-bearing capacity, thereby enhancing wear resistance as confirmed by the results above.

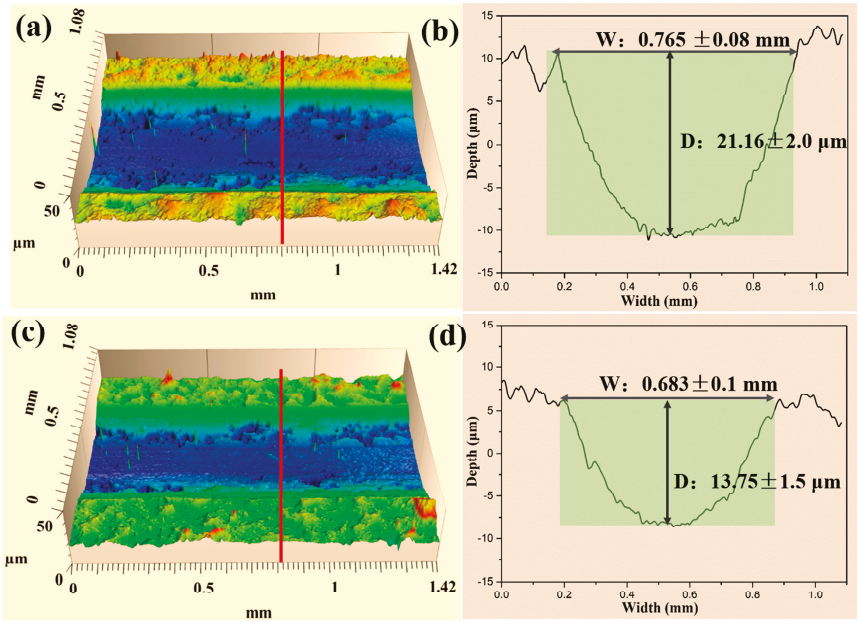


Figure 4. Three-dimensional surface morphologies (**a**,**c**) and sectional profiles (**b**,**d**) of the wear tracks of (**a**,**b**) PI/MoS_2 and (**c**,**d**) POSS-PI/MoS_2 coatings under 10 N.

The SEM morphologies and corresponding elemental mapping distributions of S, Mo, and Si on the worn surfaces are presented in Figure 5. As shown in Figure 5a, the worn surface of the PI/MoS_2 coating exhibits severe flaking, with Fe from the substrate exposed. This indicates that the coating experienced severe wear during the friction process. In addition, slight peeling appears on the worn surface, which results from the fatigue wear. However, the addition of POSS exhibits an obvious effect on the wear mechanism of the composite coating. The spalling phenomena in the wear scar morphology are significantly reduced (Figure 5b), and some scratch grooves appear on the worn surface, which can be attributed to the abrasive wear. Apart from this, the Si and Mo elements of the POSS-modified coating are uniformly distributed on the wear scar surface. This result further confirms that POSS was uniformly dispersed within the composite coating.

3.2. Evolution of Morphology and Microstructure Under AO Irradiation

The SEM micrographs of the PI/MoS_2 and POSS-PI/MoS_2 composite coatings before and after different AO exposure times are shown in Figure 6. The composite coating surfaces were relatively smooth and continuous prior to atomic oxygen (AO) irradiation (Figure 6a,d), with some MoS_2 sheets distributed both within and on the surface of the PI matrix. However, the coating surfaces became significantly roughened and developed numerous pores after AO irradiation (Figure 6e,f). Compared to the unexposed samples, all exposed coatings exhibited uneven and bumpy morphologies. This change can be attributed to severe erosion and oxidative degradation of the coating surfaces caused by AO irradiation. On the surface of the pristine PI/MoS_2 coating, molybdenum disulfide is stacked. It is noteworthy that the POSS-PI/MoS_2 composite coating developed a distinct, network-like cross-linked structure on its surface after AO exposure (Figure 6e,f). The PI resin exposed on the coating surface underwent significant oxidation and degradation upon AO exposure, which led to the surface becoming covered with Si, O, S, and Mo elements. The network-like structure observed on the modified coating surface can be attributed to the formation of SiO_2 and SiO_x residues originating from the oxidation of POSS molecules.

https://doi.org/10.3390/coatings16010073

For the specific conditions of our AO exposure experiment, this protective layer is estimated to be on the order of 100 nm [33]. Notably, due to the presence of the protective layer, the gaps between molybdenum disulfide (MoS_2) sheets (Figure 6b,c) have become significantly smaller and fewer. Additionally, the POSS-modified coatings exhibited a regular network structure, and the holes in the network (Figure 6e,f) feature sizes from 200 to 400 nm [34]. Although only partially continuous, this network-like residue can protect the underlying organic material from further AO irradiation. These morphological observations align with the measured changes in coating thickness and mass loss. Consequently, the POSS-PI/MoS_2 composite coating demonstrated strong AO resistance, which can be ascribed to the formation of a protective SiO_x network layer on its surface [2,4,35].

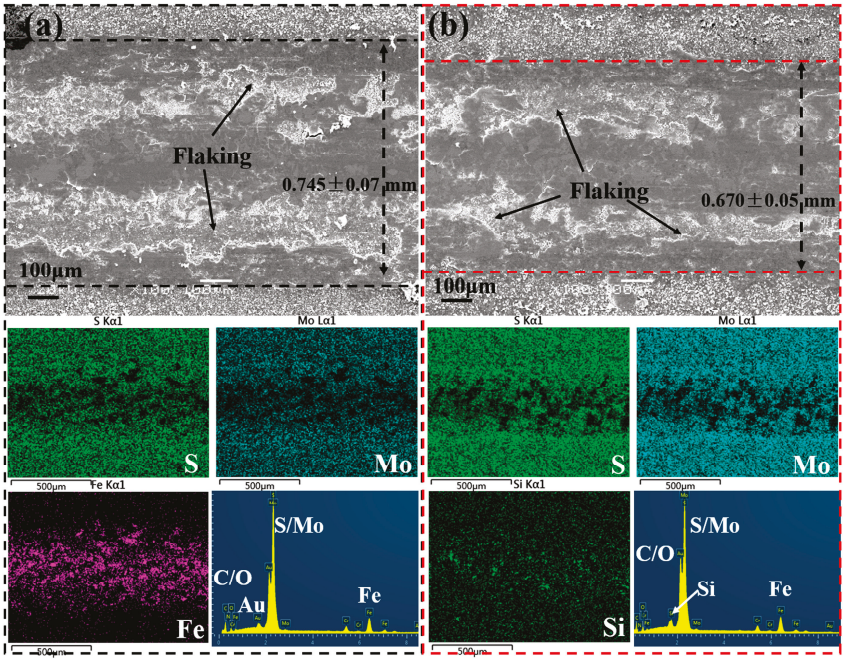


Figure 5. SEM micrographs and EDS mapping of the wear tracks of (**a**) PI/MoS_2 and (**b**) POSS-PI/MoS_2 coatings under 10 N.

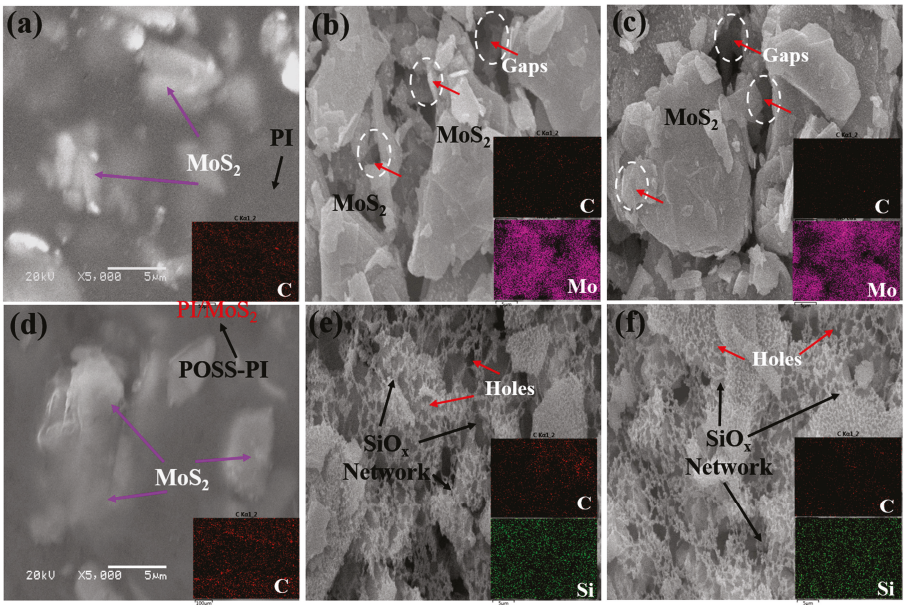


Figure 6. SEM micrographs and EDS mapping of the coating surfaces of (**a**–**c**) PI/MoS_2 and (**d**–**f**) POSS-PI/MoS_2 after AO irradiation: (**a**,**d**) 0 h; (**b**,**e**) 10 h; (**c**,**f**) 20 h.

https://doi.org/10.3390/coatings16010073

The cross-sectional SEM morphologies of the original and POSS-modified composite coatings before and after atomic oxygen (AO) exposure are shown in Figure 7. As can be observed from the figure (Figure 7a), the coating structure before AO irradiation was relatively continuous and smooth. However, after AO irradiation, the thickness of the original PI/MoS_2 coating decreased significantly and exhibited flocculent accumulation (Figure 7b,c). By contrast, the POSS-modified coating retains a relatively intact structure and a smooth cross-section after AO irradiation (Figure 7d,e).

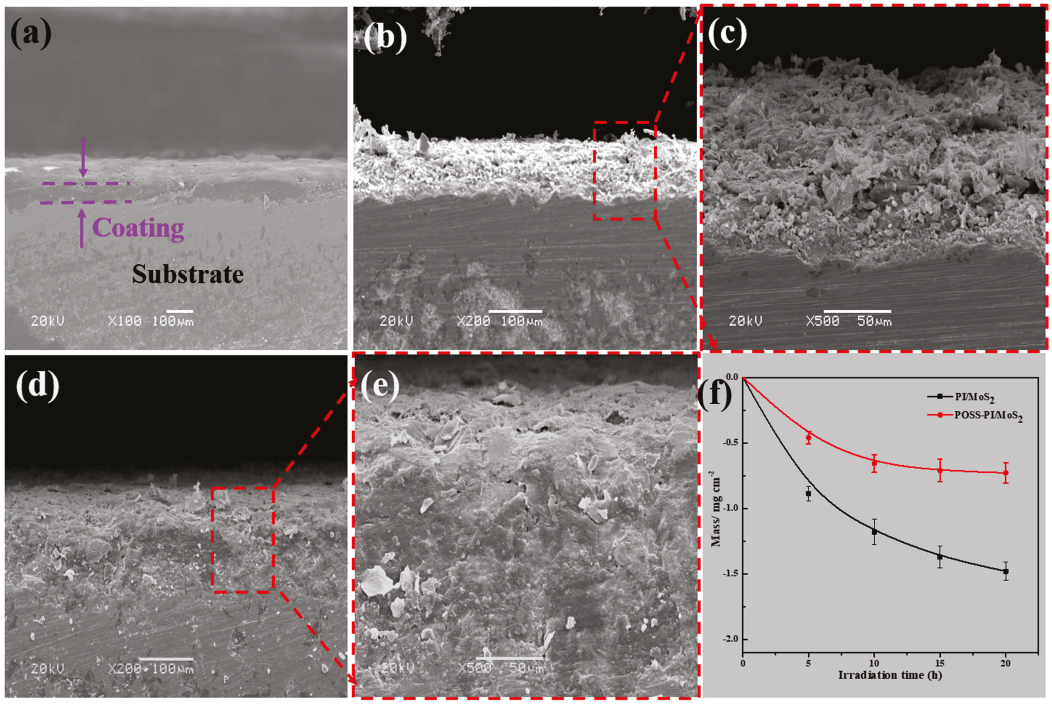


Figure 7. Cross-sectional SEM images of the (**b**,**c**) PI/MoS_2 and (**d**,**e**) POSS-PI/MoS_2 lubricating coatings before (**a**) and after (**b**–**e**) AO irradiation for 20 h; (**f**) average mass loss of the composite coatings varies from the irradiation time.

Figure 7f presents relationship curves between mass loss per unit surface area and atomic oxygen (AO) irradiation time. In the initial irradiation stage (within 5 h), the mass loss of all coatings increases rapidly due to the degradation and breakdown of the surface PI resin. Notably, the mass loss of the POSS-modified coating during this period was only 50% of that of the unmodified one. When AO irradiation exceeded 10 h, the incorporation of POSS further altered the mass loss trend in the PI-based coatings, leading to a significant reduction in mass loss. Specifically, at the same irradiation duration, the POSS-modified coating exhibited substantially lower mass loss compared to the unmodified coating. These results indicate that mass loss primarily occurred during the early stages of AO exposure, which is mainly attributed to the oxidation and degradation of surface PI resin and the organic functional groups in POSS. As irradiation continued, the mass loss rate of the composite coating gradually slowed, which can be attributed to the protective surface layer formed by MoS_2 and SiO_x.

The FTIR-ATR spectra of the PI/MoS_2 and POSS-modified composite coatings before and after atomic oxygen (AO) exposure are shown in Figure 8a. As can be observed, the irradiation of AO exposure led to significant changes in the characteristic absorption peak intensity on the coating surfaces. After AO irradiation, the absorption peaks at 1525 cm^{-1} (C=C) and 1710 cm^{-1} (C=O) and in the coatings were significantly weakened, and the intensity of the absorption peaks at 1076 cm^{-1} (C–O–C) and 2921 cm^{-1} (–NH) also decreased. The decrease in these peak intensities indicates that most of the PI resin

https://doi.org/10.3390/coatings16010073

exposed on the coating surface was subsequently oxidized and degraded. As a result, these FTIR-ATR results indicate that complex chemical reactions and degradation of the PI resin and the other organic components occurred in the PI/MoS_2 coatings after AO irradiation [2,5]. Nonetheless, the surface infrared peak intensities of the POSS-modified coating also decreased significantly, confirming that severe oxidative degradation of the organic surface components still took place.

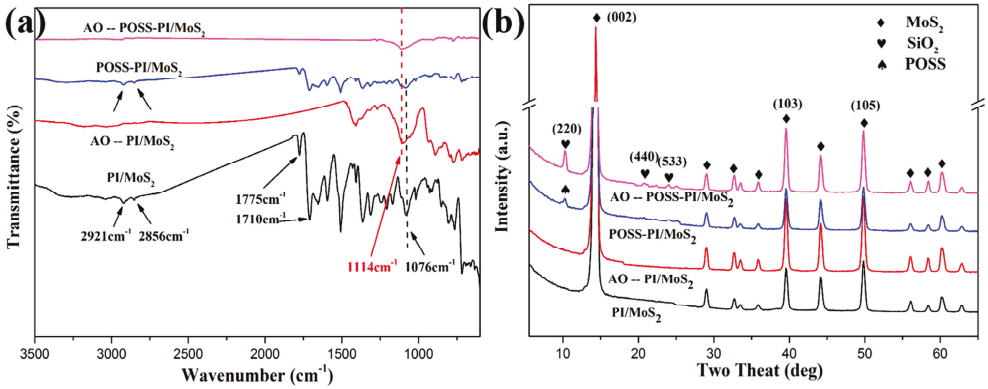


Figure 8. FTIR-ATR (**a**) and XRD (**b**) spectra of the composite coatings before and after 20 h of AO irradiation.

Additionally, the surface XRD spectra of the composite coatings, both before and after AO irradiation, are shown in Figure 8b. Compared to the pristine coating, the POSS-modified coating exhibited distinct silica peaks after AO irradiation, indicating that the POSS in the modified coating was oxidized, forming silica on the surface. This phenomenon confirms that the network structure observed on the coating surface in Figure 6 consists of silica residues.

To investigate the changes in the surface element chemical composition of the PI-based composite coatings before and after AO irradiation, XPS spectra were further employed, and the results are presented in Figure 9. It is possible to observe that the PI/MoS_2 coating displays XPS peaks for S2p, Mo3d, C1s, N1s, and O1s, whereas the POSS-modified coating exhibits an additional Si2p peak. In addition, it is worth noting that the element composition on the coating surface changed significantly, particularly with a notable decrease in C 1s element content. The changes in the element contents were mainly caused by the oxidative degradation of the PI resin on the surface, which led to the reduction in carbon content. However, the intensity of the sulfur (S) and molybdenum (Mo) elements on the coating surface increased significantly, due to the exposure of molybdenum disulfide (MoS_2) from within the coating to the surface. Additionally, the intensities of the Si2p and O1s peaks in the POSS-modified coating tended to increase after AO exposure (Figure 9b). The surface element composition of the PI-based and POSS-modified coatings before and after AO exposure derived from the XPS spectra are listed in Table 3.

It was found that the atomic oxygen (AO) could react with the PI resin and other organic components exposed on the coating surface, thus producing some volatile gases and escaping afterward. The results in Table 3 indicate that after AO irradiation, the carbon content on the coating surface significantly decreased with prolonged irradiation time, which decreased from 72.34% and 64.97% to 28.05% and 21.91%, respectively. Furthermore, due to the formation of non-volatile silica and other oxides during AO exposure, the contents of silicon and oxygen elements in the composite coatings increased markedly after AO irradiation [36]. For the POSS-PI/MoS_2 coatings, the O1s and Si2p contents increased from 21.56% and 5.5% to 39.83% and 16.2%, respectively. These results are in accordance with the surface and cross-sectional morphologies of the coating, as shown in Figures 6 and 7.

https://doi.org/10.3390/coatings16010073

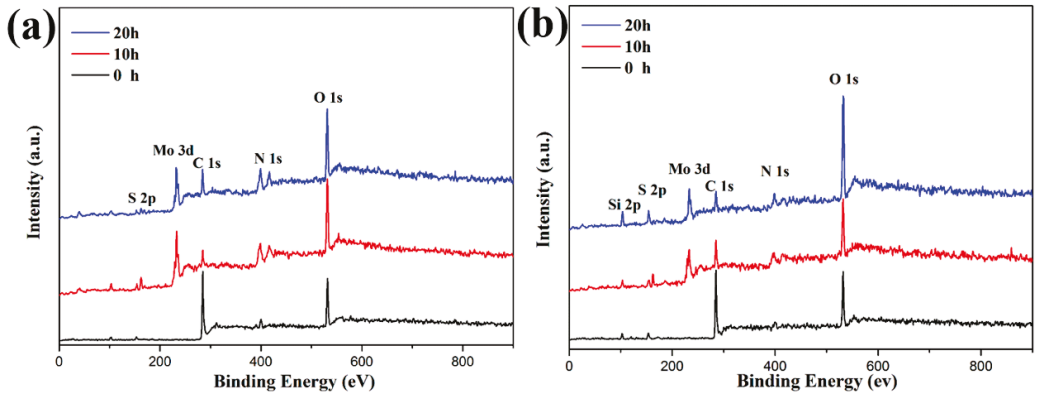


Figure 9. XPS spectra of the composite coatings (**a**) PI/MoS_2 and (**b**) POSS-PI/MoS_2 before and after AO irradiation.

Table 3. Surface composition (at. %) of the composite coatings before and after AO exposure: (a) PI/MoS_2 and (b) POSS-PI/MoS_2.

Coatings	Surface Element Composition (at. %)					
	C	N	O	S	Mo	Si
a—0 h	72.34	7.04	19.65	0.76	0.21	
a—10 h	31.18	20.23	34.66	7.37	6.56	
a—20 h	28.05	22.18	32.16	9.21	8.40	
b—0 h	64.97	6.21	21.56	1.46	0.30	5.50
b—10 h	32.95	14.08	28.27	8.14	5.73	10.82
b—20 h	21.91	13.69	39.83	4.22	4.15	16.20

Figure 10 shows high-resolution Si 2p and Mo 3d XPS spectra of the composite coating before and after AO irradiation, along with the corresponding Gaussian fitting results. As shown in Figure 10a, the intensity of the Si peak in the XPS spectra increased with the extended irradiation time. In addition, compared to the unirradiated coating, the Si 2p peak of the coating after AO exposure shifted toward a higher binding energy (Figure 10b,c), which indicated the oxidation of Si_8O_{12} to SiO_2 after AO exposure [4,24]. Furthermore, the Mo 3d XPS peaks of the PI/MoS_2 composite coating correspond to MoS_2 before exposure and transformed to MoO_3 after AO irradiation (Figure 10d–f), confirming the oxidation of MoS_2 under AO irradiation [37–39].

Additionally, after AO irradiation, the ratio of $SiO_{1.5}$ to SiO_2 in the POSS-PI/MoS_2 composite coating after 10 h of AO exposure was about 1:10.8, whereas it was 1:15.1 after 20 h of AO irradiation. The significantly increased proportion of silica on the coating surface further demonstrated the formation of surface silicon oxide. At the same time, the molybdenum disulfide (MoS_2) on the surface also oxidized to molybdenum oxide, with the valence state of molybdenum changing accordingly, and the content of molybdenum oxide increased with prolonged irradiation time.

As a result, the organic components on the coating surface were preferentially attacked by AO at the beginning of the exposure test, producing volatile gases such as CO and CO_2 that escaped from the surface. With the extended AO irradiation time, the exposed MoS_2 and POSS on the coating surface were oxidized and formed MoO_3 and SiO_2, which created an oxidized passivation layer that could protect the underlying organic material from further erosion and degradation.

https://doi.org/10.3390/coatings16010073

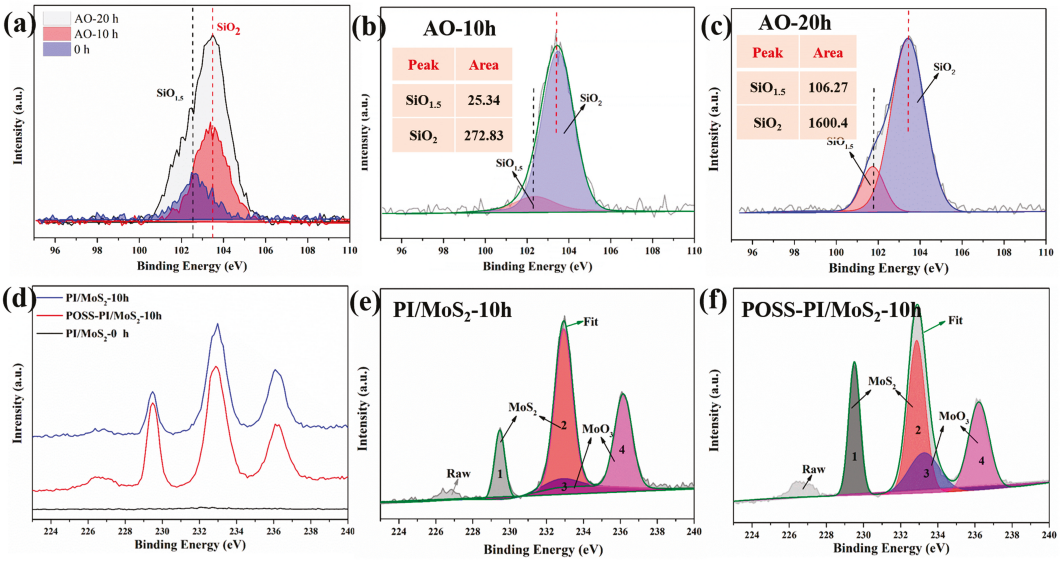


Figure 10. High-resolution Si 2p (**a**–**c**) and Mo 3d (**d**–**f**) XPS spectra of the coatings after AO irradiation.

3.3. Tribological Properties of the Composite Coatings Under AO Irradiation

According to the results above, atomic oxygen (AO) exposure led to severe oxidative degradation of the organic materials and molybdenum disulfide (MoS_2), thereby affecting the tribological properties of the composite coatings. The influence of AO irradiation on the friction and wear behaviors of POSS-modified composite coatings before and after AO exposure is shown in Figure 11.

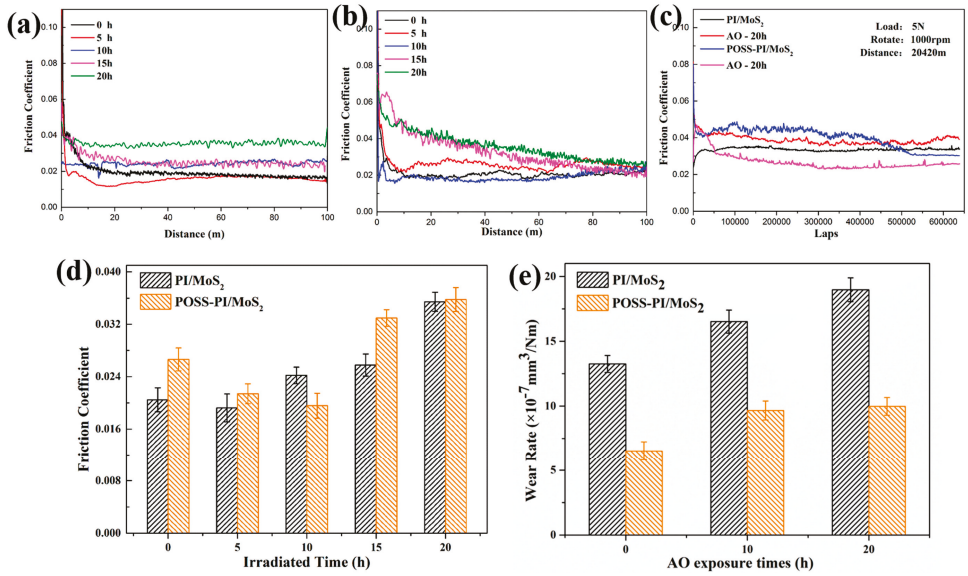


Figure 11. Friction coefficient curves (**a**–**c**), average CoF (**d**), and wear rates (**e**) of the composite coatings (**a**) PI/MoS_2 and (**b**) POSS-PI/MoS_2 before and after AO irradiation; (**c**) the standard lifetime in the space environment.

The friction coefficient (CoF) curves of the original and POSS-modified coatings under different exposure times are presented in Figure 11a,b. It can be seen that the friction coefficient decreases in the initial stage during the friction process, which was caused by the rapid formation of a transfer film composed of MoS_2 on the counterpart ball. Additionally, most of the CoFs after AO irradiation were slightly higher than those before irradiation, as shown in Figure 11c, which can be attributed to the oxidative degradation of the lubricant

https://doi.org/10.3390/coatings16010073

exposed on the surface, as shown in Figure 6, as well as the formation of a hard oxide layer consisting of SiO_2 and MoO_3.

The wear rates after AO exposure were calculated and are shown in Figure 11e. It can be seen that after AO exposure, the wear rates of the original PI/MoS_2 coatings increased with the prolonged exposure times compared with those before AO irradiation. The result was caused by the loosened and stacked molybdenum disulfide on the coating surface after AO exposure. However, it is worth noting that the POSS-modified coating after AO erosion presented a slightly higher wear rate than that before AO, which can be attributed to the AO-induced passivating layer on the coating surface. The hard SiO_2 protective layer provided a high load-bearing capacity, and prevented the inner polymeric materials from further erosion caused by AO exposure, thereby improving the wear resistance under AO irradiation.

Meanwhile, rotational friction experiments were also performed and the CoFs of the original and modified PI/MoS_2 coatings are shown in Figure 11d, both before and after AO exposure. All the composite coatings exhibit excellent wear resistance during the friction process within 6×10^5 laps. It is worth noting that the POSS-modified coating after 20 h of AO exposure presents a lower friction coefficient compared to the coating before irradiation, which confirmed the protecting and strengthening effect under AO irradiation.

The three-dimensional (3D) topographies and 2D cross-sectional profiles of the wear tracks under different irradiation times were further investigated to explore the wear mechanisms, as shown in Figure 12. Before AO irradiation, the wear tracks of both the original and POSS-modified coatings were relatively narrow and shallow (Figure 12a,b), with a depth of only 2.28 μm and 2.33 μm. However, both the depth and width of the wear tracks increased significantly after AO irradiation. This result is primarily attributed to the oxidative decomposition of the PI resin, which acted as the supporting phase in the coating. Secondly, the accumulation of MoS_2 on the surface resulted in a softer and less cohesive coating surface that notably exacerbated the wear track. In addition, the POSS-modified coating exhibited a relatively lower wear track depth and width compared to the original PI/MoS_2 coating. This improvement can be attributed to the introduction of POSS, which enhanced the cross-linking density and the AO resistance caused by the protective layer consisting of SiO_2. Additionally, the amount of the Si-O-Si inorganic framework in the POSS afforded the coating an excellent load-carrying capacity, which led to increases in wear resistance, and this result corresponds to the 3D topographies above.

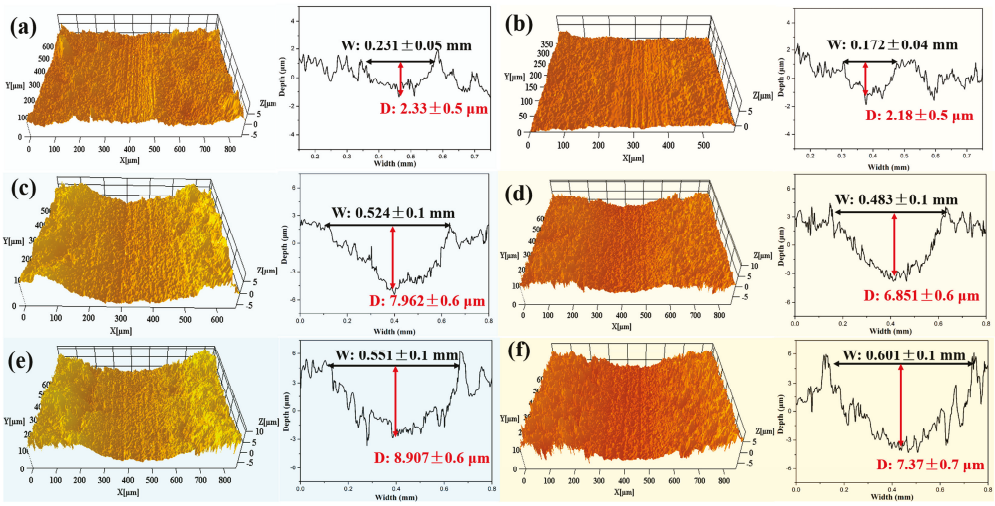


Figure 12. Three-dimensional surface morphologies and cross-sectional profiles of the composite coatings (**a**,**c**,**e**) PI/MoS_2 and (**b**,**d**,**f**) POSS-PI/MoS_2 before (**a**,**b**) and after 10 h (**c**,**d**), and 20 h (**e**,**f**) of AO irradiation.

https://doi.org/10.3390/coatings16010073

The SEM morphologies and EDS elemental distribution mapping of the worn surfaces before and after AO irradiation were investigated, and the results are shown in Figure 13. It can be seen that the composite coatings exhibited relatively narrow wear tracks before AO irradiation, which is consistent with the 3D topographies shown in Figure 12. In particular, compared to the PI/MoS_2 coating, the POSS-PI/MoS_2 coating exhibits smaller and slighter wear tracks with minor surface pits, which is consistent with the aforementioned wear morphology data. Moreover, after AO irradiation, the oxidation of surface MoS_2 generated hard MoO_3 particles, leading to some pitting and slight abrasive grooves on the worn surface (Figure 13e,f).

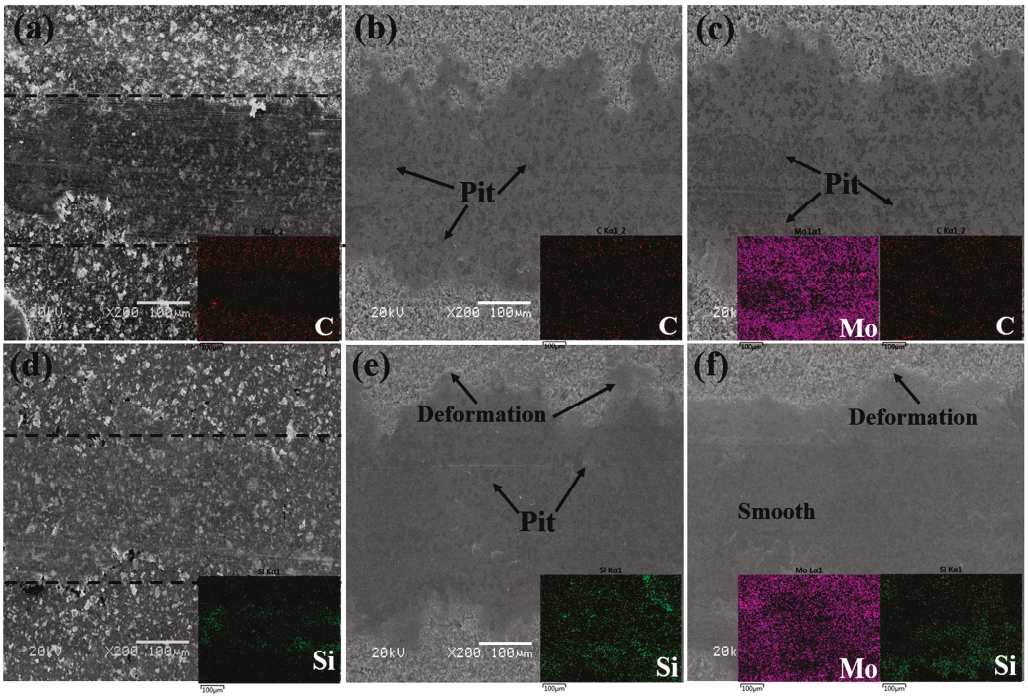


Figure 13. SEM micrographs and EDS spectra of the worn surfaces (**a**–**c**) PI/MoS_2 and (**d**–**f**) POSS-PI/MoS_2 before (**a**,**d**) and after 10 h (**b**,**e**) and 20 h (**c**,**f**) of AO irradiation.

Furthermore, the elemental distributions of the worn surface were further explored through EDS analysis, as shown in the figure. Both before and after AO irradiation, the Mo element remained uniformly dispersed on the coating surface and within the worn track, although its content within the wear track itself was relatively lower than that on the coating surface. This result was caused by the transfer of MoS_2 during the friction process, which promoted the formation of a lubricating film on the counterpart balls, thereby leading to the decrease in Mo element on the worn surface. In addition, after AO irradiation, the C content on the worn surface decreased significantly, whereas the Si content increased markedly. These changes can be attributed to the oxidation and degradation of the PI matrix, along with the surface oxidation of POSS to form a passivation layer, which have been confirmed by the results above. As a result, the incorporation of POSS enhanced both the tribological performance and AO resistance of the PI-based composite coatings. This incorporation also altered the wear mechanism, as the coating exhibited plastic deformation and fatigue wear prior to AO irradiation, whereas under AO erosion, it transitioned to mild abrasive wear.

Figure 14 shows the Raman spectra of both original and POSS-modified PI/MoS_2 composite coatings before and after AO exposure. For the PI/MoS_2 coating prior to irradiation, two strong bands are observed at 385 cm^{-1} and 408 cm^{-1} (Figure 14a), corresponding to the characteristic peaks of MoS_2 [2]. However, the intensity of these MoS_2 signals markedly decreased after AO exposure, and two new weak peaks ascribed to MoO_3 emerge at 818 and

https://doi.org/10.3390/coatings16010073

995 cm^{-1}. Moreover, the intensity of the MoO_3 peaks increases with prolonged irradiation time, indicating the partial oxidation of MoS_2.

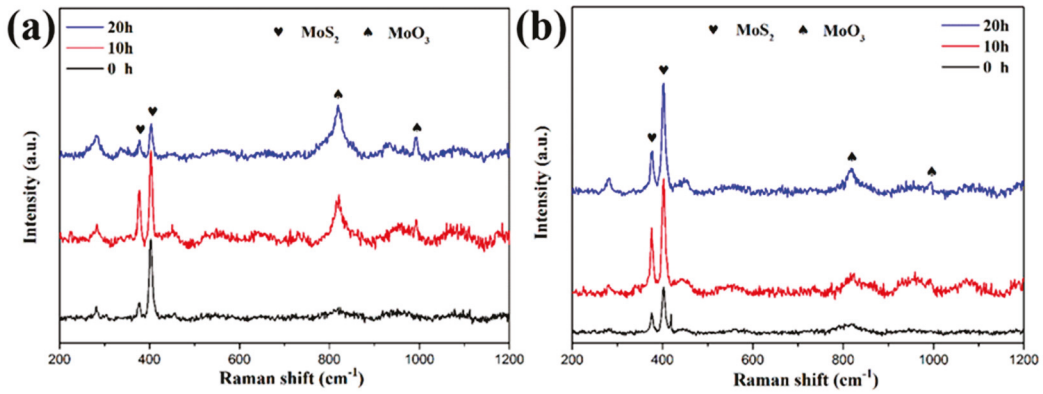


Figure 14. Raman spectra of the worn surfaces of the (**a**) PI/MoS_2 and (**b**) POSS-PI/MoS_2 composite coatings before and after AO irradiation.

In contrast, the POSS-modified coating shows little change in the MoS_2 peak intensity after AO irradiation (Figure 14b). This indicates that the incorporation of POSS effectively suppressed the oxidation of MoS_2, which can be attributed to the protective SiO_2 protective layer formed on the coating surface confirmed by the XPS spectra.

The structural evolution schematic of the original and POSS-modified coatings before and after AO exposure are shown in Figure 15. It can be seen that the incorporation of POSS enhances the cross-linking and hardness of the PI/MoS_2 composite coatings before AO irradiation and jointly improves their wear resistance. After AO exposure, the POSS-containing coatings were oxidized and a SiO_2 passivating layer was formed on the surface, which protected the underlying PI and MoS_2 from further oxidation and degradation. Compared with the original coating, the content of Si on the surface is relatively high, which results from the surface migration and enrichment of OMPOSS on the coating surface. Thus, only MoS_2 on the most superficial surface was oxidized, which corresponds to the results of Raman and XPS.

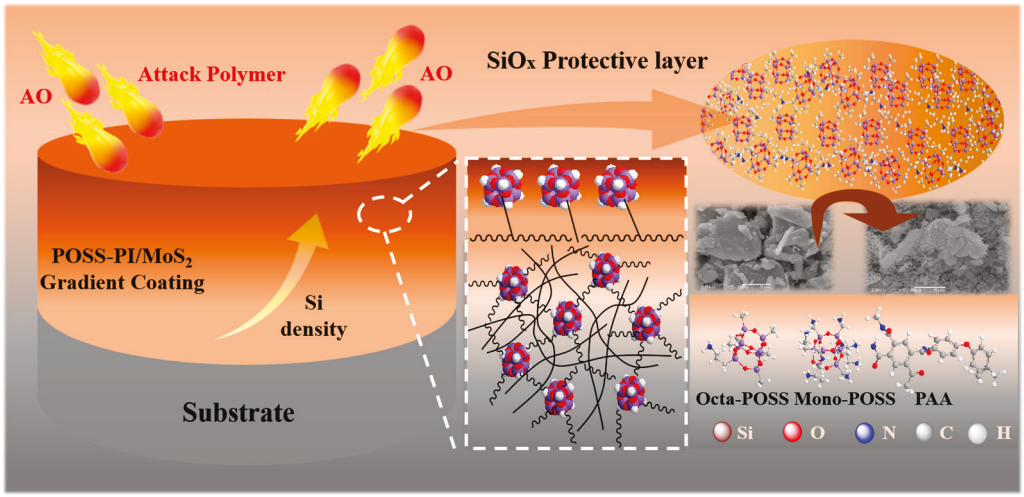


Figure 15. Schematic diagram of the structural evolution of the OMPOSS-modified PI/MoS2 composite coatings under AO irradiation.

4. Conclusions

In this work, the mono- and octa-amino POSSs were introduced into PI/MoS_2 coatings via chemical grafting, fabricating a gradient composite structure with varying silicon

https://doi.org/10.3390/coatings16010073

content. The effect of POSS on the wear resistance of PI/MoS_2 coatings before and after AO exposure was systematically investigated. The results indicated that the incorporation of multifunctional POSS provided an inorganic framework composed of Si-O-Si bonds and enhanced the cross-linking density of the PI-based composite coating, thereby enhancing both the load-bearing capacity and tribological properties of the coating. Furthermore, for the POSS-PI/MoS_2 coating, the network-like SiO_2 layer formed on its surface after AO irradiation compared with the PI/MoS_2 coating. This passivated SiO_2 layer protected the underlying organic material from further erosion and degradation, while also significantly suppressing the oxidation of the MoS_2 lubricant, as confirmed by the XPS and Raman spectra. Therefore, it is possible to conclude that the addition of multifunctional POSS endows the PI-based modified coatings with excellent AO resistance and superior tribological properties under AO irradiation. The excellent AO resistance of POSS-PI/MoS_2 coatings and their presumed mechanical and tribological properties would make them ideal as a protective coating in space environments.

Author Contributions: C.Y.: Conceptualization, Resources, Writing—Review and Editing, Supervision. P.Z.: Formal Analysis. M.W.: Methodology, Writing—Original Draft Preparation. Q.W.: Resources, Funding Acquisition. W.Z.: Formal Analysis. All authors have read and agreed to the published version of the manuscript.

Funding: This work was financially supported by the Guangdong Basic and Applied Basic Research Foundation, grant number 2022A1515110306.

Institutional Review Board Statement: Not applicable.

Informed Consent Statement: Not applicable.

Data Availability Statement: The raw data that support the findings of this study are available from the corresponding author upon reasonable request.

Acknowledgments: The authors have reviewed and edited the output and take full responsibility for the content of this publication.

Conflicts of Interest: The authors declare no conflicts of interest.

References

1. Zhang, Y.; Yuan, H.; Yan, W.; Chen, S.; Qiu, M.; Liao, B. Atomic-Oxygen-Durable and Antistatic α-AlxTiyO/γ-NiCr Coating on Kapton for Aerospace Applications. *ACS Appl. Mater. Interfaces* **2021**, *13*, 58179–58192. [CrossRef]
2. Yu, C.; Ju, P.; Wan, H.; Chen, L.; Li, H.; Zhou, H.; Chen, J. POSS-Grafted PAI/MoS_2 Coatings for Simultaneously Improved Tribological Properties and Atomic Oxygen Resistance. *Ind. Eng. Chem. Res.* **2019**, *58*, 17027–17037. [CrossRef]
3. Wang, D.; Ma, J.; Li, P.; Fan, L.; Wu, Y.; Zhang, Z.; Xu, C.; Jiang, L. Flexible Hard Coatings with Self-Evolution Behavior in a Low Earth Orbit Environment. *ACS Appl. Mater. Interfaces* **2021**, *13*, 46003–46014. [CrossRef]
4. Zhao, L.; Leng, X.; Bai, B.; Zhao, R.; Cai, Z.; He, J.; Li, J.; Chen, H. Effect of Coating Thickness on the Atomic Oxygen Resistance of Siloxane Coatings Synthesized by Plasma Polymerization Deposition Technique. *Coatings* **2023**, *13*, 153. [CrossRef]
5. Yu, C.; Ju, P.; Wan, H.; Chen, L.; Li, H.; Zhou, H.; Chen, J. Enhanced atomic oxygen resistance and tribological properties of PAI/PTFE composites reinforced by POSS. *Prog. Org. Coat.* **2020**, *139*, 105427. [CrossRef]
6. Minton, T.K.; Schwartzentruber, T.E.; Xu, C. On the Utility of Coated POSS-Polyimides for Vehicles in Very Low Earth Orbit (VLEO). *ACS Appl. Mater. Interfaces* **2021**, *13*, 51673–51684. [CrossRef]
7. Cao, L.; Dai, X.; Wu, Y.; Ba, X. Emerging Photo-Initiating Systems in Coatings from Molecular Engineering Perspectives. *Coatings* **2025**, *15*, 1028. [CrossRef]
8. Zhong, M.; Li, S.; Fan, H.; Zhang, H.; Jiang, Y.; Luo, J.; Yang, L. One-Step Fabrication of Composite Hydrophobic Electrically Heated Graphene Surface. *Coatings* **2023**, *14*, 1052. [CrossRef]
9. Yan, Y.; Zhang, B.; Wang, J.; Cao, C.; Yan, F. MWCNT–Polyimide Fiber-Reinforced Composite for High-Temperature Tribological Applications. *Coatings* **2024**, *14*, 181. [CrossRef]
10. Lee, C.; Li, Q.Y.; Kalb, W.; Liu, X.Z.; Berger, H.; Carpick, R.W.; Hone, J. Frictional Characteristics of Atomically Thin Sheets. *Science* **2010**, *328*, 76–80. [CrossRef]

11. Vellore, A.; Romero Garcia, S.; Walters, N.; Johnson, D.A.; Kennett, A.; Heverly, M.; Martini, A. Ni-Doped MoS_2 Dry Film Lubricant Life. *Adv. Mater. Interfaces* **2020**, *7*, 2001109.
12. Vellore, A.; Garcia, S.R.; Johnson, D.A.; Martini, A. Ambient and Nitrogen Environment Friction Data for Various Materials & Surface Treatments for Space Applications. *Tribol. Lett.* **2021**, *69*, 5. [CrossRef]
13. Shi, J.; Ma, G.; Han, C.; Li, G.; Liu, Y.; Liu, Q. Tribological properties and bearing application of Mo-based films in space environment. *Vacuum* **2021**, *188*, 110217. [CrossRef]
14. Goto, A.; Jorge, P.D.; Xu, C.; Gouzman, I.; Minton, T.K. Atomic-Oxygen Effects on a Siloxane-Polyimide Block-Chain Copolymer. *ACS Appl. Polym. Mater.* **2025**, *7*, 13125–13138.
15. Xu, M.; Gu, H.; Tang, D.; Zeng, B.; Sun, R.; Sun, Y.Y.; Zhang, Y.; Song, L. Graphene-wrapped Mg-Al layered double hydroxides nanosheet coating with simultaneous atomic oxygen protection and electrostatic discharge resistance on polyimide. *Compos. Part A* **2025**, *190*, 108707. [CrossRef]
16. Ouyang, Q.; Wang, W.; Fu, Q.; Dong, D. Atomic Oxygen Irradiation Resistance of Transparent Conductive Oxide Thin Films. *Thin Solid Films* **2017**, *623*, 31−39. [CrossRef]
17. Qi, H.; Qian, Y.; Xu, J.; Zuo, J.; Li, M. An AZ31 Magnesium Alloy Coating for Protecting Polyimide from Erosion-Corrosion by Atomic Oxygen. *Corros. Sci.* **2018**, *138*, 170−177. [CrossRef]
18. Sun, R.; Zhang, Y.; Gu, H.; Wang, X.; Zhang, M.; Li, H.; Ma, J.; Song, L. Property of Protection against Simultaneous Action between Atomic Oxygen Erosion and Ultraviolet Irradiation by MIL-53(Al) Coating. *ACS Omega* **2024**, *9*, 47324–47331. [CrossRef] [PubMed]
19. Yan, C.; Li, J.; Wang, H.; Tong, H.; Ye, X.; Wang, K.; Yuan, X.; Liu, C.; Li, H. Growth and atomic oxygen erosion resistance of Al_2O_3-doped TiO_2 thin film formed on polyimide by atomic layer deposition. *RSC Adv.* **2024**, *14*, 34833–34842. [CrossRef]
20. George, S.M. Atomic Layer Deposition: An Overview. *Chem. Rev.* **2010**, *110*, 111−131. [CrossRef]
21. Cooper, R.; Upadhyaya, H.P.; Minton, T.K.; Berman, M.R.; Du, X.; George, S.M. Protection of polymer from atomic-oxygen erosion using Al2O3 atomic layer deposition coatings. *Thin Solid Films* **2008**, *516*, 4036–4039.
22. Liu, B.; Pei, X.; Wang, Q.; Sun, X.; Wang, T. Effects of atomic oxygen irradiation on structural and tribological properties of polyimide/Al_2O_3 composite. *Surf. Interface Anal.* **2012**, *44*, 372–376.
23. Yu, C.; Wan, H.; Chen, L.; Li, H.; Cui, H.; Ju, P.; Zhou, H.; Chen, J. Marvelous abilities for polyhedral oligomeric silsesquioxane to improve tribological properties of polyamide-imide/polytetrafluoroethylene coatings. *J. Mater. Sci.* **2018**, *53*, 12616–12627.
24. Wang, P.; Tang, Y.; Yu, Z.; Gu, J.; Kong, J. Advanced aromatic polymers with excellent antiatomic oxygen performance derived from molecular precursor strategy and copolymerization of Polyhedraloligomeric silsesquioxane. *ACS Appl. Mater. Interfaces* **2015**, *7*, 20144.
25. Wang, X.; Zhang, C.; Zhao, C.; Liang, Y.; Zhang, M.; Yang, W.; Yu, B.; Yu, Q.; Cai, M.; Zhou, F.; et al. Modification of POSS and their tribological properties and resistant to space atomic oxygen irradiation as lubricant additive of multi-alkylated cyclopentanes. *Friction* **2024**, *12*, 884–896. [CrossRef]
26. Peng, D.; Qin, W.; Wu, X. Improvement of the atomic oxygen resistance of carbon fiber-reinforced cyanate ester composites modified by POSS-graphene-TiO_2. *Polym. Degrad. Stab.* **2016**, *133*, 211−218. [CrossRef]
27. Wright, J.S.; Jones, A.; Farmer, B.; Rodman, D.L.; Minton, T.K. POSS-Enhanced Colorless Organic/Inorganic Nanocomposite (CORIN) for Atomic Oxygen Resistance in Low Earth Orbit. *CEAS Space J.* **2021**, *13*, 399.
28. Chen, L.; Hu, Z.; Wu, Z.; Wu, G.; Ma, L.; Zhang, C.; Huang, Y. POSS-bound ZnO nanowires as interphase for enhancing interfacial strength and hydrothermal aging resistance of PBO fiber/epoxy resin composites. *Compos. Part A* **2017**, *96*, 1–8.
29. Yuan, J.; Zhang, Z.; Yang, M.; Wang, W.; Men, X.; Liu, W. POSS grafted hybrid-fabric composites with a biomimic middle layer for simultaneously improved UV resistance and tribological properties. *Compos. Sci. Technol.* **2018**, *160*, 69–78. [CrossRef]
30. Yu, C.; Zhang, P.; Wei, M.; Wang, Q.; Zhang, W. Amino-POSS grafted polyimide-based self-stratifying composite coatings for simultaneously improved mechanical and tribological properties. *Polymers* **2026**, *18*, 45. [CrossRef]
31. *TB 10099-2017*; Code for Design of Railway Station and Terminal. China Railway Publishing House: Beijing, China, 2017.
32. Liao, W.; Huang, X.; Ye, L.; Lan, S.; Fan, H. Synthesis of composite latexes of polyhedral oligomeric silsesquioxane and fluorine containing poly(styrene–acrylate) by emulsion copolymerization. *J. Appl. Polym. Sci.* **2016**, *133*, 43455. [CrossRef]
33. Minton, T.K.; Wright, M.E.; Tomczak, S.J.; Marquez, S.A.; Shen, L.; Brunsvold, A.L.; Cooper, R.; Zhang, J.; Vij, V.; Guenthner, A.J.; et al. Atomic-Oxygen Effects on POSS Polyimides in Low Earth Orbit. *ACS Appl. Mater. Interfaces* **2012**, *4*, 492–502. [CrossRef]
34. Qian, M.; Murray, V.J.; Wei, W.; Marshall, B.C.; Minton, T.K. Resistance of POSS Polyimide Blends to Hyperthermal Atomic Oxygen Attack. *ACS Appl. Mater. Interfaces* **2016**, *8*, 33982−33992. [CrossRef]
35. Qiao, S.; Jiang, H.; Zhai, R.; Liu, Y.; Li, T.; Xu, Y.; Jiang, L. Study on the Effects and Mechanism of Temperature and AO Flux Density in the AO Interaction with Upilex-S Using the ReaxFF Method. *Coatings* **2023**, *13*, 1586. [CrossRef]
36. Choi, C.; Kim, Y.; Sathish Kumar, S.K.; Kim, C.-G. Enhanced resistance to atomic oxygen of OG POSS/epoxy nanocomposites. *Compos. Struct.* **2018**, *202*, 959−966. [CrossRef]

37. Fan, X.; Shi, Y.; Cui, M.; Ren, S.; Wang, H.; Pu, J. MoS_2/WS_2 Nanosheet-Based Composite Films Irradiated by Atomic Oxygen: Implications for Lubrication in Space. *ACS Appl. Nano Mater.* **2021**, *4*, 10307−10320.
38. Zhang, X.; Xu, J.; Chai, L.; He, T.; Yu, F.; Wang, P. Carbon and Nitrogen Co-Doping Self-Assembled MoS_2 Multilayer Films. *Appl. Surf. Sci.* **2017**, *406*, 30−38.
39. Diskus, M.; Nilsen, O.; Fjellvag, H.; Diplas, S.; Beato, P.; Harvey, C.; van Schrojenstein Lantman, E.; Weckhuysen, B.M. Combination of Characterization Techniques for Atomic Layer Deposition MoO_3 Coatings: From the Amorphous to the Orthorhombic Alpha-MoO_3 Crystalline Phase. *J. Vac. Sci. Technol. B* **2012**, *30*, 01A107.

Disclaimer/Publisher's Note: The statements, opinions and data contained in all publications are solely those of the individual author(s) and contributor(s) and not of MDPI and/or the editor(s). MDPI and/or the editor(s) disclaim responsibility for any injury to people or property resulting from any ideas, methods, instructions or products referred to in the content.

https://doi.org/10.3390/coatings16010073

coatings

MDPI

Article

Tribological Performance and Microstructural Analysis of NiAl–Inconel 625 Composite Coating Produced by Wire Arc Spraying

Konstantinos Antonopoulos [1,*], Athanasios Tzanis [2], Dirk Drees [3], Michalis Vardavoulias [4], Emmanuel Georgiou [1], Angelos Koutsomichalis [1], Panagiotis Skarvelis [1] and Tom Van der Donck [5]

[1] Laboratory of Materials, Hellenic Airforce Academy, Dekelia Air Base, 136 71 Acharnes, Greece; emmanouil.georgiou@hafa.haf.gr (E.G.); a.koutsomichalis@gmail.com (A.K.); pskarv@gmail.com (P.S.)
[2] Laboratory of Materials, Electronics Depot-R&T Centre, 165 62 Glyfada, Greece; ttzanis@hotmail.com
[3] Falex Tribology NV, Wingepark 23B, 3110 Rotselaar, Belgium; ddrees@falex.eu
[4] Pyrogenesis S.A., Technological Park of Lavrio, 195 00 Lavrio, Greece; mvardavoulias@pyrogenesis-sa.gr
[5] Department Materials Engineering (MTM), KU Leuven, 3000 Leuven, Belgium; tom.vanderdonck@kuleuven.be
* Correspondence: kwnanto02@gmail.com

Abstract

Thermal spray technologies are widely used in aerospace, gas turbine, and automotive industries, where nickel-based superalloys are valued for their mechanical strength and resistance to oxidation and corrosion at elevated temperatures. This study investigates the microstructure and tribological performance of Ni–5Al/Inconel 625 composite coatings deposited on AISI 1025 steel using wire arc spraying, aiming to provide a cost-effective alternative to bulk superalloys and more advanced thermal spray techniques. Microstructural characterization was performed using optical microscopy, scanning electron microscopy, and energy-dispersive X-ray spectroscopy, while surface roughness, microhardness, and dry sliding wear behavior were evaluated using ball-on-disk tests against Al_2O_3 counterbodies. Confocal microscopy and three-dimensional triboscopic imaging were employed to analyze wear-track morphology and friction behavior. X-ray diffraction (XRD) analysis confirmed the presence of a predominantly intermetallic Ni_3Al (γ') phase with secondary NiAl in the bond coat, indicating significant interdiffusion between the NiAl bond coat and the Inconel 625 top coat. The top coat exhibited a face-centered cubic (FCC) γ Ni-based solid solution. The coatings exhibited a typical lamellar structure with low porosity (2%–3%) and oxide content of 12%–15%, primarily chromium and niobium oxides located at splat boundaries. Abrasion, combined with interlamellar decohesion, was identified as the dominant wear mechanism. Post-deposition polishing reduced surface roughness from 11.9 μm to 2.12 μm, leading to a 2.5-fold reduction in wear volume and a significant decrease in debris pile-up. The corresponding specific wear rates were approximately 9.3×10^{-5} mm^3/Nm and 3×10^{-5} mm^3/Nm for the as-prepared and polished conditions, respectively, which are within the range reported in the literature for similar coatings. These findings demonstrate that wire arc-sprayed Ni–5Al/Inconel 625 coatings, particularly after polishing, offer improved wear resistance while maintaining cost-effectiveness, making them a promising alternative for tribological applications.

Keywords: coatings; Inconel 625; NiAl; wire arc spraying; microstructure; triboscopy; wear; friction

1. Introduction

Thermal spray technologies are widely applied across numerous industrial sectors, with the aerospace, industrial gas turbine, and automotive industries representing the most economically significant markets. In addition to these major sectors, industries such as oil and gas, metal processing, and biomedical engineering increasingly benefit from advancements in thermal spray processes [1]. Engineering components operating in aggressive environments such as oil and gas, marine, and power generation systems and the aerospace industry are frequently subjected to combined wear, erosion, corrosion, and elevated temperatures. These conditions often result in accelerated surface degradation and reduced service life, highlighting the need for advanced protective coatings capable of enhancing surface durability [2] while remaining cost-effective [3,4].

Thermal spraying is a versatile surface engineering technique that enables the rapid deposition of thick protective layers. When applied as protective layers on lower-cost substrates, thermally sprayed coatings provide a cost-effective alternative to bulk materials without compromising performance or longevity. Among the available thermal spray processes, wire arc spraying (WAS) is distinguished by its high deposition efficiency, low operational cost, and suitability for large-scale and on-site applications. In this process, consumable metal wires are melted by an electric arc and atomized into fine droplets that are propelled toward the substrate, forming coatings with thicknesses up to several millimeters [3,4].

Within this context, material selection plays a critical role in achieving the desired performance of thermally sprayed coatings, particularly for demanding service environments. Nickel-based superalloys are widely used in harsh service environments due to their excellent mechanical strength and resistance to oxidation and corrosion at elevated temperatures. Inconel 625, a solid-solution-strengthened Ni–Cr–Mo alloy, exhibits outstanding resistance to pitting, crevice corrosion, and stress corrosion cracking, combined with high toughness and ductility [5]. These properties make it a preferred coating material for tribological applications under severe operating conditions.

In addition, NiAl intermetallic alloys have also attracted considerable attention owing to their low density, high melting point, and excellent oxidation resistance [6]. When combined with Inconel 625 in a composite coating system, NiAl can synergistically integrate high-temperature stability and oxidation resistance with superior corrosion resistance and mechanical toughness. This combination has the potential to enhance the overall tribological performance, making such composite coatings well-suited for demanding applications involving wear and elevated temperatures.

Although extensive studies have investigated thermally sprayed Inconel 625 coatings, most have focused on HVOF [7–9] and other thermal spray methods [10–13], with limited attention given to wire arc sprayed composite systems. Moreover, the characteristic microstructural features of WAS coatings, including lamellar splats, oxides, and porosity, play a critical role in governing wear behavior and remain insufficiently explored.

Thus, the present study investigates the tribological performance at room temperature and the microstructural characteristics of a NiAl–Inconel 625 composite coating produced by wire arc spraying. Room-temperature testing is employed as a preliminary screening approach to assess the abrasive resistance of the coating, since abrasion-induced wear represents a common failure mechanism under service conditions [14]. Particular emphasis is placed on elucidating the relationships between microstructural features, phase distribution, and the dominant wear mechanisms. The findings aim to provide deeper insight into the performance of the coating and to evaluate its suitability for demanding industrial applications.

https://doi.org/10.3390/coatings16050609

2. Materials and Methods

In this study, AISI 1025 carbon steel plate, with chemical composition which is shown in Table 1, were utilized as the base substrate materials. The specimens were machined into square coupons with dimensions of 30 mm × 30 mm, featuring thicknesses of 2 mm.

Table 1. Chemical compositions of AISI 1025.

Element	Fe	C	Mn	S	P
AISI 1025 Content in wt.%	99–99.4	0.22–0.28	0.3–0.6	0.05 max	0.04 max

Prior to coating deposition, the specimens underwent a surface preparation protocol. Initially, surface activation was achieved through a grit-blasting process conducted using commercial type, alumina (Al_2O_3) media. Alumina was chosen for its superior hardness relative to both substrates, ensuring a high-anchorage surface profile necessary for the mechanical bonding of the thermal spray coatings.

The coatings were deposited using the Wire Arc Spraying (WAS) technique. A dual-layer coating system was implemented, consisting of a primary bond coat followed by a functional topcoat. Two distinct spray systems were employed. The bond Coating Deposited using an Oerlikon-Metco system and the Main Coating Deposited using a a Metallisation Energizer 450 Series system (Metallisation Limited, Dudley, West Midlands, UK). The WAS systems utilized a twin-wire feed mechanism, where a motorized pull-and-push assembly directed the metallic wires from spools through flexible conduits into the spray gun. This configuration ensures a constant feedstock flow, which is critical for maintaining arc stability and achieving a uniform, fine-grained atomized melt stream.

The feedstock consisted of 1.6 mm diameter solid wires manufactured by Flame Spray Technologies (FST, Duiven, Gelderland, The Netherlands). For the bond coat, W-375 (Ni-5%Al) was utilized, while W-365 (Inconel 625) was used for the main functional coating. The chemical compositions of the feedstock materials are detailed in Table 2 as mentioned by FST.

Table 2. Chemical compositions of NiAl and Inconel 625.

Element	Ni	Al	Cr	Mo	Fe	Ta	Nb
NiAl Content in wt.%	Balanced	5	-	-	-	-	-
Inconel 625 Content in wt.%	58	-	21.5	9	2.5	0.1–3.5	0.1–3.5

The deposition was performed under strictly controlled parameters to ensure reproducibility. The Inconel 625 layer was deposited using a higher energy input (230 A/44 V) compared to the bond coat to ensure proper melting of the alloy. The specific operational settings for both coating layers are summarized in Table 3.

Table 3. Wire Arc Spraying Operational Parameters.

Parameter	NiAl	Inconel 625
Current (A)	180	230
Voltage (V)	33	44
Nozzle Air Pressure (bar)	6.5	6.5
Motor Pressure (bar)	-	5.5

To investigate the microstructure of the material, a metallographic sample was pre pared from cross-sections of the coated specimens by grinding with SiC papers and

https://doi.org/10.3390/coatings16050609

polishing with 3 µm and 1 µm diamond suspension, followed by 0.1 µm aluminum oxide polishing.

The coating microstructure was characterized using optical microscopy (OM) together with scanning electron microscopy (SEM, JEOL IT500LV, Tokyo, Japan). Elemental composition analysis was carried out by energy-dispersive spectroscopy (EDS, Oxford Instruments X-Max Extreme, Oxford, UK). Phase identification and crystallographic characterization were performed using X-ray diffraction (XRD, Bruker D8 Advance, Ettlingen, Germany) equipped with a CuKα radiation source (λ = 0.154 nm) and a scanning step of 0.1°.

Microhardness measurements were conducted using a Vickers indenter (Duramin-5, Struers, Copenhagen, Denmark) under a load of 0.2 kg applied for 12 s. The reported hardness values correspond to the average of five individual indentations.

Tribological experiments were performed under ambient laboratory conditions using a reciprocating ball-on-disk tribometer (BASALT-N2, TETRA, Ilmenau, Germany). An Al_2O_3 ball with a diameter of 6 mm, hardness of 2000 HV0.5, and surface roughness of Rα = 0.2 µm served as the counter material. The tests were conducted using a normal load of 10 N, a stroke length of 2 mm, a sliding speed of 20 mm/s, and a total duration of 10,000 cycles. Two different surface conditions were investigated during the wear tests. Sample "A" corresponded to the as-sprayed coating, whereas Sample "B" was mechanically polished using SiC abrasive papers with grit sizes ranging from 120 to 1200. Duplicate experiments were carried out for each condition.

Surface roughness measurements and wear-track depth evaluations were performed using a confocal microscope (NanoFocus µSurf Explorer, NanoFocus AG, Oberhausen, Germany).

3. Results and Discussion

3.1. Coating and Surface Characterization

The fabricated specimens exhibit the typical stoichiometric composition (wt.%), as presented in Table 4 and illustrated in Figure 1, together with the nominal composition of the nickel-based Inconel 625 superalloy in accordance with the aerospace material specification (AMS 5666) [15].

Table 4. Chemical compositions of Inconel 625.

Element	Ni	Al	Cr	Mo	Fe	Nb
Content in wt.%	66.4	0.3	20.6	9.1	0.4	3.2
Nominal composition	58 min	0.4 max	20–23	8–10	5 max	3.15–4.15

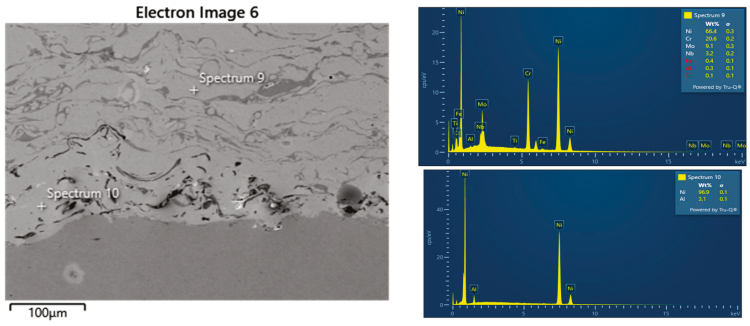
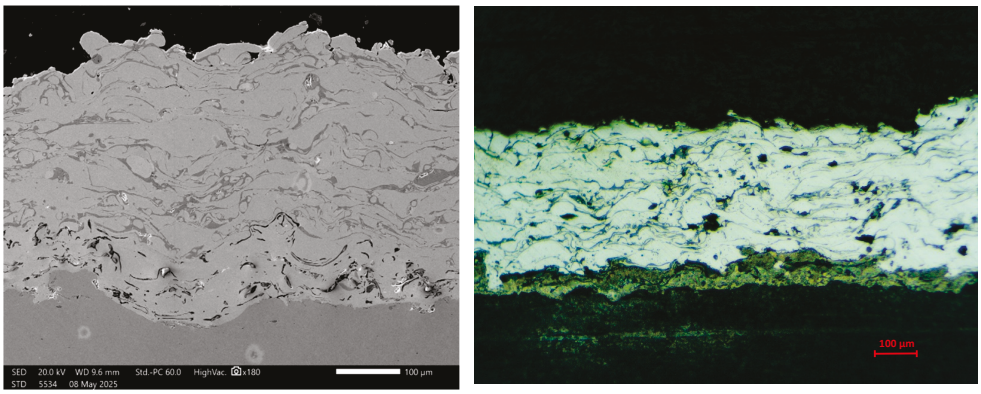


Figure 1. (**a**) Cross-sectional SEM micrograph of the NiAl–Inconel 625 composite coating (**b**) EDS spectra obtained from selected regions (Spectrum 9 and Spectrum 10), indicating the elemental composition and distribution within the coating.

Figure 2 shows a typical cross section of a coated sample where the Inconel-625 deposit is approximately 340 µm and bond coating NiAl 95 µm in thickness deposited onto the substrate. The coating porosity ranged from 2% to 3% with the noticeable presence of oxide formation, ranged from 12% to 15%, around the resolidified splats as shown in Figure 2.



(**a**) (**b**)

Figure 2. As-sprayed specimen: (**a**) SEM magnified micrographs; (**b**) Optical micrograph of the etched metallographic cross-section following swab etching using a solution containing 75 mL HCl and 25 mL HNO_3.

The coating, as shown in Figure 3, exhibits the characteristic lamellar morphology of arc-sprayed deposits, formed by the successive impingement, spreading, and rapid solidification of molten splats. Clearly defined splat boundaries are observed, along which pores and voids are preferentially distributed. These defects appear predominantly as irregularly shaped, elongated pores aligned parallel to the spraying direction, while smaller, near-spherical pores are occasionally detected within the splat interiors.

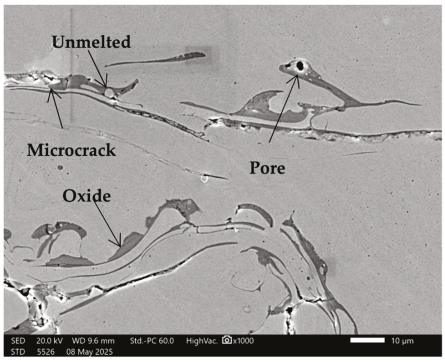


Figure 3. SEM image depicting the cross-sections of Inconel 625 coating specimen.

Regions of intermediate gray contrast are evident along several inter-splat interfaces, suggesting compositional variations induced during the spraying process, as shown in Figure 4. Elemental mapping by EDS reveals that these interfacial regions are enriched mainly in chromium, niobium, and oxygen, indicating the formation of Cr,Nb-rich oxide phases. This oxide formation is attributed to the in-flight oxidation of molten particles and subsequent oxidation during splat solidification, a phenomenon commonly associated with the Wire Arc Spraying (WAS) process. The presence of such oxide-rich inter-splat layers can influence the mechanical integrity and tribological response of the coating.

The Ni-rich regions, identified via EDS mapping, exhibit a distinct partially spherical morphology, suggesting they reached the substrate in a semi-solid or highly viscous state due to in-flight nucleation or incomplete melting at the wire arc tip. These globular nodes serve as primary sites for heterogeneous nucleation, where high thermal gradients promote

https://doi.org/10.3390/coatings16050609

rapid undercooling. Similar phenomena have also been reported in previous studies by A.H. Dent et al. [16].

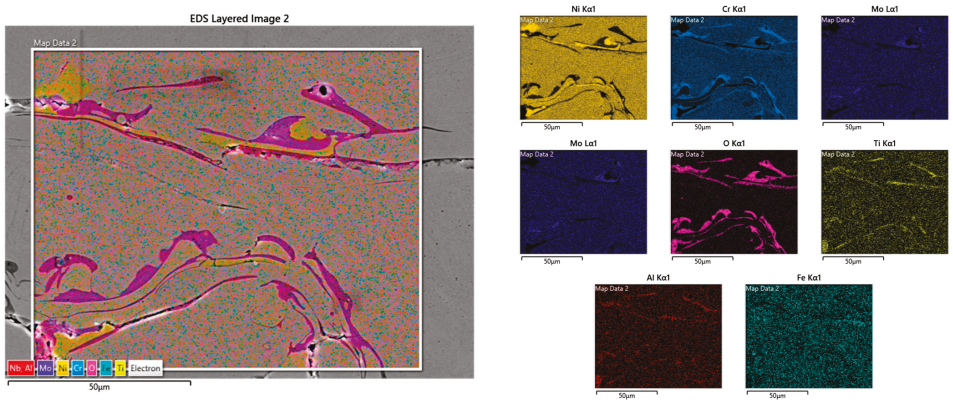


Figure 4. (**a**) Cross-sectional SEM micrograph and (**b**) corresponding EDS elemental maps of the wire arc sprayed Inconel 625 coating, illustrating the elemental distribution of the main alloying elements (Ni, Cr, Mo, Nb) as well as minor elements and substrate-related signals (Ti, O, Al, Fe).

However, the sharp geometric transition between these rigid, spherical inclusions and the surrounding flattened splats creates significant stress concentration sites. Consequently, the thermal expansion mismatch and volumetric shrinkage during quenching lead to the initiation of large micro-cracks at the interfaces of these Ni-rich phases. This localized failure highlights how the discrete distribution of Ni-rich "seeds" governs both the structural integrity and the defect density of the overall Inconel 625 coating matrix [17,18].

The microhardness of the deposited coating was measured at 444 ± 15 HV. This value represents a slight increase compared to results reported in previous studies of similar thermal spray deposits [19] and is significantly higher than the microhardness of bulk annealed Inconel 625, which typically ranges from 146 to 224 HV [20]. This enhancement in hardness is attributed to the rapid solidification and the presence of fine oxide inclusions characteristic of the wire arc spray (WAS) process (Figure 5).

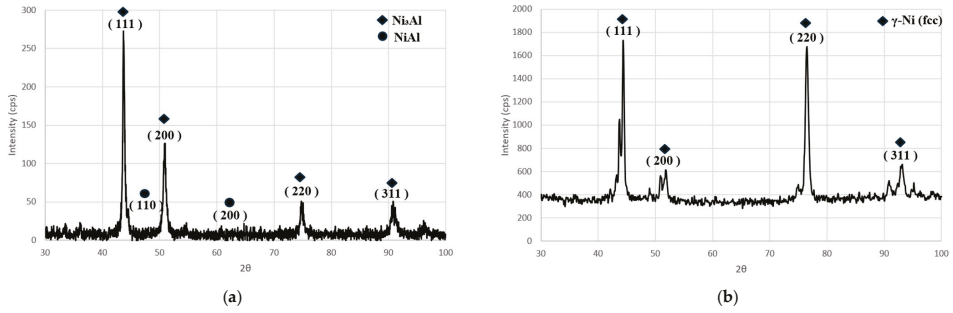


Figure 5. XRD patterns of the (**a**) NiAl Bond Coat (**b**) Inconel 625 Top coat.

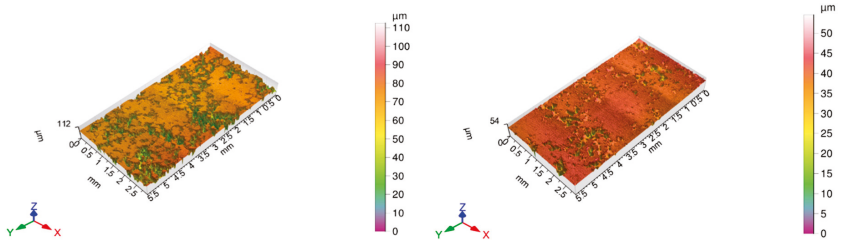
X-ray diffraction (XRD) analysis of the NiAl bond coat, as shown in Figure 5a, revealed a predominantly intermetallic microstructure, with principal reflections corresponding to Ni_3Al and secondary contributions from NiAl. The dominance of the γ' (Ni_3Al) phase indicates possible pronounced interdiffusion between the NiAl bond coat and the Inconel 625 top coat. This phase evolution is consistent with previous reports on aluminized Inconel 625 systems, where Al diffusion promotes γ'-Ni_3Al formation within the interdiffusion zone [21]. The absence of distinct γ (fcc Ni) reflections is attributed to peak overlap and the crystallographic similarity between γ and Ni_3Al.

https://doi.org/10.3390/coatings16050609

The XRD pattern of the Inconel 625 top coat, as shown in Figure 5b, is dominated by a face-centered cubic (FCC) γ solid-solution phase, with characteristic reflections indexed to the (111), (200), (220), and (311) planes of the Ni-based matrix.

Although EDS mapping indicated Nb-, Cr-, and O-enriched regions, no corresponding oxide phases were detected by XRD. This is ascribed to their low volume fraction, localized distribution, and possible amorphous or nanocrystalline nature, placing them below the detection limit of XRD [22].

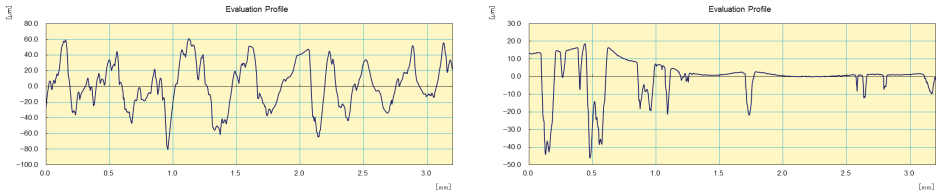
Surface roughness was characterized for both the as-sprayed and polished specimens prior to the tribological experiments. Indicative 3D surface topographies are presented in Figure 6. It is important to note that for the friction and wear tests, specific areas were selected where detached splats were absent to ensure that the results reflect the inherent wear resistance of the coating matrix rather than localized structural defects.



(**a**) (**b**)

Figure 6. Representative three-dimensional surface topographies of the two specimen conditions: (**a**) as-sprayed and (**b**) polished.

The as-sprayed specimens presented an average surface roughness of 11.9 µm, while the polished surfaces exhibited a substantially lower roughness value of 2.12 µm. In addition, skewness (Ssk) and kurtosis (Sku) parameters were evaluated to further characterize the surface topography. For the as-sprayed condition, the obtained Ssk and Sku values were −1.34 and 3.76, respectively, indicating a height distribution located slightly above the mean plane with an approximately normal profile. In contrast, the polished specimens exhibited Ssk and Sku values of −3.73 and 20.9, respectively. This pronounced negative skewness together with the elevated kurtosis value suggests that the polishing treatment effectively removed most of the prominent surface asperities while leaving isolated deep grooves across the surface as shown in Figure 7.

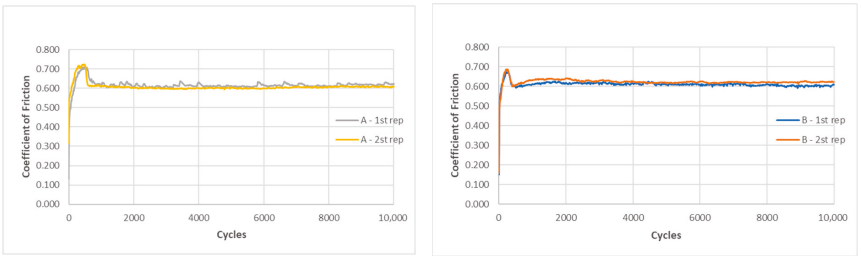


(**a**) (**b**)

Figure 7. Representative two-dimensional roughness profiles corresponding to the two surface conditions: (**a**) as-sprayed specimen and (**b**) polished specimen.

3.2. Tribological Performance

The evolution of the coefficient of friction (COF) μ per cycle is depicted in Figure 8a for the as-sprayed "A" specimen and in Figure 8b for the polished "B" specimen.



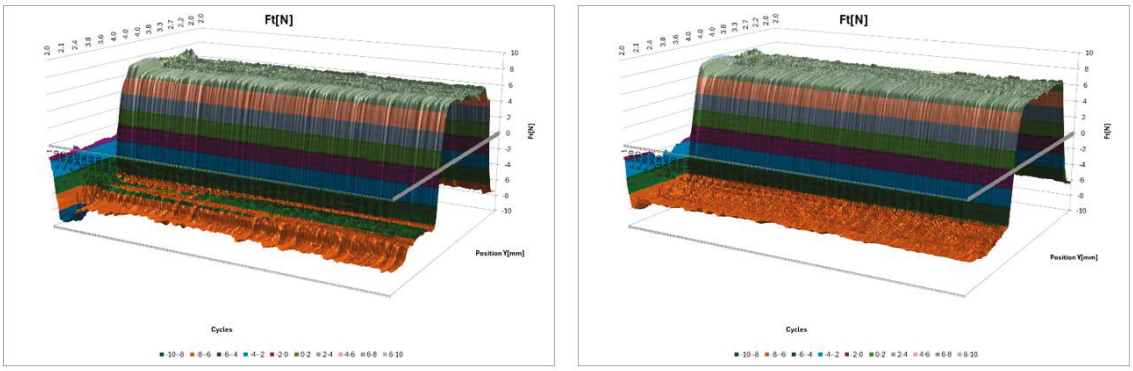
(**a**) (**b**)

Figure 8. Evolution of the COF per cycle for the (**a**) as-sprayed specimens and (**b**) polished specimens.

For the as-sprayed specimens, the run-in stage appears to extend for a higher number of cycles, until reaching steady-state. In contrast, the polished specimens exhibit a shorter transition to steady-state friction. In the fundamental work of Blau [23], such curve morphologies are associated mainly with the initial surface roughness that causes a temporary rise in friction. As the surfaces conform and smooth under sliding, friction decreases. The subsequent drop can also result from surface texturing induced by shear or from the formation of a low-shear transfer film.

The as-sprayed specimens exhibited an average steady-state coefficient of friction of $\mu = 0.611 \pm 0.008$, whereas the polished condition produced a comparable value of $\mu = 0.617 \pm 0.005$. The limited scatter observed in both datasets indicates good experimental repeatability and stable tribological behavior. Despite the significant difference in surface roughness, both specimen conditions ultimately reached nearly identical steady-state friction levels.

To further examine the sliding response of the coatings, the friction force was analyzed as a function of displacement throughout the reciprocating cycles. Representative three-dimensional triboscopic maps for both surface conditions are shown in Figure 9.



(**a**) (**b**)

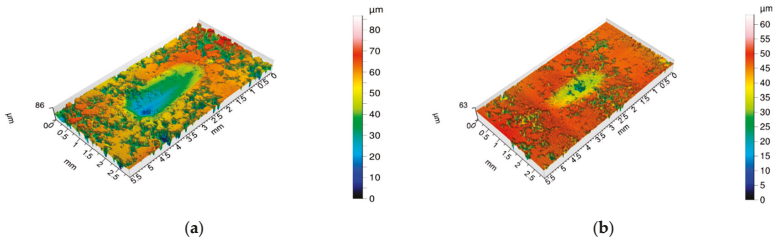
Figure 9. Representative three-dimensional triboscopy maps illustrating the variation in friction force throughout successive sliding cycles for the (**a**) as-sprayed specimen and (**b**) polished specimen.

While both the as-prepared and polished specimens eventually reach an identical steady-state coefficient of friction, their transitional friction force behaviors are markedly different. The 3D triboscopical curve for the as-prepared specimen reveals intense initial fluctuations and significant force peaks at the stroke edges, reaching values between -10 and -8 N. These peaks are believed to relate to pilling-up of debris (due to roughness removal) at the wear track edges, due to the reciprocating motion of the counter material. Thus, it is more pronounced in the as-prepared specimen's because of their higher roughness values and morphology (see Figures 6 and 7).

https://doi.org/10.3390/coatings16050609

3.3. Wear Behavior

Indicative 3D confocal microscopy images for the as-prepared and polished specimens are presented in Figure 10.



(**a**) (**b**)

Figure 10. Three-dimensional confocal microscopy images of the wear track after the tribo-experiments of the (**a**) as-prepared specimen; (**b**) polished specimen.

The wear track of the as-prepared specimen exhibits significant material removal, with a maximum depth of 50.5 μm and a maximum pile-up height of 52.7 μm at the edges of the track. This confirms the previous hypothesis, that the increase in friction at the triboscopical image at the edges of the track is mainly related to debris pile-ups. The measured wear volume was approximately 0.037 mm^3, while the debris pile-up volume (peak) was approximately 0.015 mm^3. The mean depth and height were recorded at 13.3 μm and 9.10 μm, respectively.

In contrast, the polished specimen shows enhanced wear resistance with a lower volume loss of approximately 0.012 mm^3 and a debris pile-up volume of only 0.0075 mm^3. The maximum depth and height for the polished surface were reduced to 43.0 μm and 34.3 μm, respectively, with significantly lower mean values of 5.68 μm for depth and 4.07 μm for height. This data confirms that the polished specimens exhibit approximately 2.5 times less volume loss than the as-prepared specimens, demonstrating much better surface homogeneity and reduced susceptibility to severe abrasive wear. To understand the significant differences, analysis of wear mechanisms was performed.

Thus, the specific wear rate was determined to be approximately 9.3×10^{-5} mm^3/Nm for the as-prepared specimen and 3.0×10^{-5} mm^3/Nm for the polished specimen, thereby confirming the superior wear resistance of the polished surface.

As shown in Table 5 the polished coating produced in this study exhibits one of the lowest specific wear rates among the reported deposition methods, highlighting its enhanced wear performance. Furthermore, Gao et al. [24] reported a value of approximately 1×10^{-5} mm^3/Nm untreated bulk Inconel 625 under a ball-on-disk configuration, suggesting that the present coating demonstrates comparable wear performance to bulk material.

Table 5. Comparison of specific wear rates for Inconel 625 coatings deposited by different methods.

Method of Deposition	Specific Wear Rate	Ref.
Hight Pressure Cold Spray	3×10^{-4}	[11]
Arc Spraying	4×10^{-5}	[25]
HVOF	10^{-3}	[26]
Wire Arc Spraying (Polished)	3×10^{-5}	This study

The wear observed in the specimens is primarily attributed to material loss resulting from mechanical interaction between the Inconel 625 coating and the alumina (Al_2O_3) counter-body. In the absence of significant chemical interaction and given the presence of grooves parallel to the sliding direction, as shown in Figure 11a, abrasion is identified as the dominant wear mechanism [9,27]. This occurs through both two-body abrasion, caused

by the harder asperities of the Al_2O_3 counter-body, and three-body abrasion associated with debris particles within the tribological contact.



Figure 11. SEM micrographs of the wear track after tribological testing of the polished specimen: (**a**) low magnification (500×) (**b**) higher magnification (2000×).

In addition, the presence of craters and extensive voids within the wear track suggests the concurrent action of a decohesion mechanism, where debris becomes entrapped within the contact, as shown in Figure 11b. This decohesion is likely triggered by high shear stresses acting on the pre-existing surface roughness [28] and the brittle interlamellar oxides surrounding the splats (as indicated in Figure 4). Furthermore, EDS analysis (Figure 12b) confirms the accumulation of debris within these voids and oxides, as well as the formation of tribofilms on the worn surface. The formation of such tribofilms is attributed to the compaction and oxidation of wear debris under repeated sliding, which can locally reduce direct metal-to-counter-body contact.

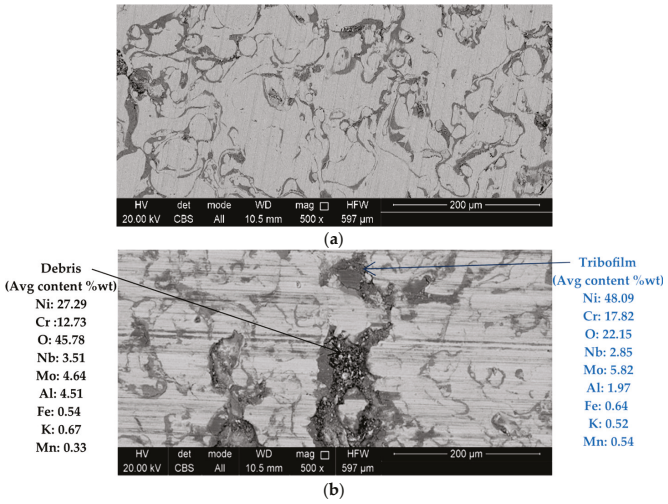


Figure 12. (**a**) SEM micrograph of the NiAl–Inconel 625 composite coating surface as polished (**b**) SEM micrograph of wear track.

While both specimen types reached a highly repeatable steady-state coefficient of friction, the as-prepared specimen exhibited significantly higher wear compared to the polished specimen. This difference emphasizes that, although polishing does not substantially alter the fundamental frictional behavior, it effectively mitigates micro-detachment of material and reduces the influence of primary topographical defects on the overall wear rate.

https://doi.org/10.3390/coatings16050609

4. Conclusions

Inconel 625 coatings were successfully deposited onto AISI 1025 steel plates via wire arc spraying (WAS). This study investigates the microstructural characteristics and tribological performance of a NiAl–Inconel 625 composite coating system. As industries increasingly demand cost-effective solutions for components operating in aggressive environments—such as marine, power generation, and aerospace—the integration of high-temperature superalloys via thermal spray processes has become a critical engineering focus.

The experimental analysis revealed that the WAS-deposited coatings exhibit a characteristic lamellar morphology, with porosity levels between 2% and 3% and oxide content ranging from 12% to 15%. Microstructural characterization via SEM and EDS identified that the formation of Cr,Nb-rich oxides and the presence of semi-solid, Ni-rich globular inclusions create significant stress concentration sites. These features lead to thermal expansion mismatch and volumetric shrinkage, which trigger inter-lamellar micro-cracking and influence the overall structural integrity of the coating. X-ray diffraction (XRD) analysis confirmed the presence of a dominant face-centered cubic (FCC) γ Ni-based solid solution in the top coat, while the bond coat consisted primarily of intermetallic γ'-Ni_3Al with secondary NiAl, indicating significant interdiffusion between layers. No oxide phases were detected by XRD, likely due to their low volume fraction and nanocrystalline or amorphous nature.

Tribological testing using a ball-on-disk reciprocating configuration demonstrated that while both as-prepared and polished surfaces achieved a consistent steady-state coefficient of friction, their wear behaviors differed significantly. The primary wear mechanism was identified as abrasion, compounded by the decohesion of brittle inter-lamellar oxides under shear stress. Post-deposition polishing reduced surface roughness from 11.9 μm to 2.12 μm, resulting in a 2.5-fold improvement in wear resistance and a substantial reduction in debris pile-up.

The corresponding specific wear rates were determined to be approximately 9.3×10^{-5} mm^3/Nm for the as-prepared condition and 3×10^{-5} mm^3/Nm for the polished surface. These values fall within the range reported in the literature for Inconel 625 coatings produced by various deposition methods and approach those of bulk Inconel 625 ($\approx 1 \times 10^{-5}$ mm^3/Nm) []. Notably, comparable wear performance is achieved using wire arc spraying, a relatively low-cost and industrially accessible technique, in contrast to more advanced deposition methods such as cold spray, highlighting its potential as a cost-effective alternative for tribological applications.

These results underscore that while wire arc spraying is an efficient method for applying protective superalloy layers, post-deposition finishing is a mandatory requirement for mitigating localized failure and maximizing service life in demanding industrial applications.

Author Contributions: Methodology, M.V., E.G. and A.K.; Validation, K.A.; Formal analysis, K.A.; Investigation, K.A. and T.V.d.D.; Writing—original draft, K.A.; Writing—review & editing, A.T., D.D., M.V., E.G., A.K. and P.S.; Supervision, E.G. and A.K. All authors have read and agreed to the published version of the manuscript.

Funding: This research received no external funding.

Institutional Review Board Statement: Not applicable.

Informed Consent Statement: Not applicable.

Data Availability Statement: The original contributions presented in this study are included in the article. Further inquiries can be directed to the corresponding author.

Conflicts of Interest: Author Dirk Drees was employed by the company Falex Tribology NV. Author Michalis Vardavoulias was employed by the company Pyrogenesis S.A. The remaining authors declare that the research was conducted in the absence of any commercial or financial relationships that could be construed as a potential conflict of interest.

References

1. Espallargas, N. *Future Development of Thermal Spray Coatings*; Elsevier: Amsterdam, The Netherlands, 2015; pp. 16–18.
2. Hawthorne, H.M.; Arsenault, B.; Immarigeon, J.P.; Legoux, J.G.; Parameswaran, V.R. Comparison of slurry and dry erosion behaviour of some HVOF thermal sprayed coatings. *Wear* **1999**, *225–229*, 825–834. [CrossRef]
3. Boulos, M.I.; Fauchais, P.L.; Heberlein, J.V.R. *Thermal Spray Fundamentals*; Springer Nature: Berlin/Heidelberg, Germany, 2021.
4. Gedzevicius, I.; Valiulis, A.V. Analysis of wire arc spraying process variables on coatings properties. *J. Mater. Process. Technol.* **2006**, *175*, 206–211. [CrossRef]
5. Reed, R.C. *The Superalloys*; Cambridge University Press: Cambridge, UK, 2008.
6. Kornienko, E.; Gulyaev, I.G.O.R.; Smirnov, A.; Nikulina, A.; Ruktuev, A.; Kuzmin, V.; Tuezov, A. Microstructure and properties of Ni-Al coatings obtained by conventional and high-velocity atmospheric plasma spraying. *Results Surf. Interfaces* **2022**, *6*, 100038. [CrossRef]
7. Zhang, D.; Harris, S.J.; McCartney, D.G. Microstructure formation and corrosion behaviour in HVOF-sprayed Inconel 625 coatings. *Mater. Sci. Eng. A* **2003**, *344*, 45–56. [CrossRef]
8. Ahmed, N.; Bakare, M.S.; McCartney, D.G.; Voisey, K.T. The effects of microstructural features on the performance gap in corrosion resistance between bulk and HVOF sprayed Inconel 625. *Surf. Coat. Technol.* **2010**, *204*, 2294–2301. [CrossRef]
9. Phiri, R.R.; Oladijo, O.P.; Maledi, N.; Akinlabi, E.T. Effect of Coating Thickness on Wear Performance of Inconel 625 coating. *IOP Conf. Ser. Mater. Sci. Eng.* **2018**, *423*, 012159. [CrossRef]
10. Vijeesh, V.P.; Ramesh, M.R.; Anoop, A.D. Inconel 625 Coatings on AISI 304 Steel using Laser Cladding: Microstructure and Hardness. *Eng. Technol. Appl. Sci. Res.* **2023**, *13*, 11911–11916. [CrossRef]
11. Wu, K.; Sun, W.; Tan, A.W.-Y.; Marinescu, I.; Liu, E.; Zhou, W. An investigation into microstructure, tribological and mechanical properties of cold sprayed Inconel 625 coatings. *Surf. Coat. Technol.* **2021**, *424*, 127660. [CrossRef]
12. Gui, W.; Zhong, C.; Gu, J.; Ding, Y.; Wang, X.; Wu, T.; Liang, Y.; Qin, J.; Qu, Y.; Lin, J. Laser-clad Inconel 625 coatings on Q245R structure steel: Microstructure, wear and corrosion resistance. *npj Mater. Degrad.* **2022**, *6*, 37. [CrossRef]
13. Scendo, M.; Staszewska-Samson, K.; Danielewski, H. Corrosion Behavior of Inconel 625 Coating Produced by Laser Cladding. *Coatings* **2021**, *11*, 759. [CrossRef]
14. Karagiannidis, I.; Tzanis, A.; Drees, D.; Lopes, L.; Chondrakis, G.; Dardavila, M.M.; Georgiou, E.; Koutsomichalis, A. Friction and Wear Behavior of 3D-Printed Inconel 718 Alloy under Dry Sliding Conditions. *Coatings* **2024**, *14*, 1029. [CrossRef]
15. SAE International | Advancing Mobility Knowledge and Solutions. *Sae.org*. 2026. Available online: https://www.sae.org/standards/ams5666k-nickel-alloy-corrosion-heat-resistant-bars-forgings-extrusions-rings-stock-forgings-extrusions-rings-62ni-215cr-90mo-365cb-nb-annealedhttps://www.sae.org/standards/ams5666k-nickel-alloy-corrosion-heat-resistant-bars-forgings-extrusions-rings-stock-forgings-extrusions-rings-62ni-215cr-90mo-365cb-nb-annealed (accessed on 24 February 2026).
16. Dent, A.H.; Horlock, A.J.; McCartney, D.G.; Harris, S.J. Microstructure formation in high velocity oxy-fuel thermally sprayed Ni–Cr–Mo–B alloys. *Mater. Sci. Eng. A* **2000**, *283*, 242–250. [CrossRef]
17. Davis and ASM International. Thermal Spray Society Training Committee. In *Handbook of Thermal Spray Technology*; ASM International: Materials Park, OH, USA, 2005; pp. 45–55.
18. Bolelli, G.; Cannillo, V.; Lusvarghi, L.; Riccò, S. Mechanical and tribological properties of electrolytic hard chrome and HVOF-sprayed coatings. *Surf. Coat. Technol.* **2006**, *200*, 2995–3009. [CrossRef]
19. Chen, T.-C.; Chou, C.-C.; Lin, H.-E.; Yung, T.-Y.; Yang, C.-T.; Tsai, Y.-W. Influence of coating microstructure on the corrosion behavior of Inconel 625 coatings fabricated by different thermal spraying processes. *Surf. Coat. Technol.* **2024**, *484*, 130674. [CrossRef]
20. INCONEL ® Alloy 625. August 2013. Available online: https://www.specialmetals.com/documents/technical-bulletins/inconel/inconel-alloy-625.pdf (accessed on 24 February 2026).
21. Bölükbaşı, Ö.S.; Serindağ, T.; Gürol, U.; Günen, A.; Çam, G. Improving oxidation resistance of wire arc additive manufactured Inconel 625 Ni-based superalloy by pack aluminizing. *CIRP J. Manuf. Sci. Technol.* **2023**, *46*, 89–97. [CrossRef]
22. Khan, H.; Yerramilli, A.S.; D'Oliveira, A.; Alford, T.L.; Boffito, D.C.; Patience, G.S. Experimental methods in chemical engineering: X-ray diffraction spectroscopy—XRD. *Can. J. Chem. Eng.* **2020**, *98*, 1255–1266. [CrossRef]
23. Blau, P.J. On the nature of running-in. *Tribol. Int.* **2005**, *38*, 1007–1012. [CrossRef]
24. Gao, Y.; Li, X.; Ma, Y.; Kitchen, M.; Ding, Y.; Luo, Q. Formation mechanism and wear behavior of gradient nanostructured Inconel 625 alloy. *Trans. Nonferrous Met. Soc. China* **2022**, *32*, 1910–1925.

25. Srichen, A.; Moonngam, S.; Linjee, S.; Banjongprasert, C. Tribological behaviors of arc sprayed NiCrMoAl alloy coating after heat treatments. *Surf. Coat. Technol.* **2022**, *437*, 128325. [CrossRef]
26. Bolelli, G.; Lusvarghi, L.; Mantini, F.P.; Barletta, M.; Casadei, F. Microstructural and tribological characterisation of as sprayed and heat treated HVOF deposited Ni alloys. *Surf. Eng.* **2007**, *23*, 355–372. [CrossRef]
27. Babu, N.N.; Kumar, S.; Govindarajan, S. Microstructural, Mechanical, and Tribological Evaluation of HVAF-Sprayed Inconel 718 Coatings. *J. Therm. Spray Technol.* **2025**, *34*, 1065–1081. [CrossRef]
28. Oladijo, O.P.; Collieus, L.L.; Obadele, B.A.; Akinlabi, E.T. Correlation between residual stresses and the tribological behaviour of Inconel 625 coatings. *Surf. Coat. Technol.* **2021**, *419*, 127288. [CrossRef]

Disclaimer/Publisher's Note: The statements, opinions and data contained in all publications are solely those of the individual author(s) and contributor(s) and not of MDPI and/or the editor(s). MDPI and/or the editor(s) disclaim responsibility for any injury to people or property resulting from any ideas, methods, instructions or products referred to in the content.

MDPI AG
Grosspeteranlage 5
4052 Basel
Switzerland
Tel.: +41 61 683 77 34

Coatings Editorial Office
E-mail: coatings@mdpi.com
www.mdpi.com/journal/coatings



Disclaimer/Publisher's Note: The title and front matter of this reprint are at the discretion of the Guest Editors. The publisher is not responsible for their content or any associated concerns. The statements, opinions and data contained in all individual articles are solely those of the individual Editors and contributors and not of MDPI. MDPI disclaims responsibility for any injury to people or property resulting from any ideas, methods, instructions or products referred to in the content.





Academic Open
Access Publishing

mdpi.com

ISBN 978-3-7258-8828-3